

# **Aerodynamic Interactions of Propulsive Deceleration and Reaction Control System Jets on Mars-Entry Aeroshells**

by

Hicham Alkandry

A dissertation submitted in partial fulfillment  
of the requirements for the degree of  
Doctor of Philosophy  
(Aerospace Engineering and Scientific Computing)  
in The University of Michigan  
2012

Doctoral Committee:

Professor Iain D. Boyd, Chair

Professor Hong G. Im

Assistant Professor Krzysztof J. Fidkowski

Professor James C. McDaniel, University of Virginia

© Hicham Alkandry 2012  
All Rights Reserved

For my family and friends.

## ACKNOWLEDGEMENTS

I would like to express my deepest gratitude and sincere appreciation to many people that have made the work presented in this document possible. It was the combined efforts of faculty, friends, and family that helped me complete this dissertation.

First and foremost, I would like to thank my advisor, Iain Boyd, for his tremendous support, encouragement, and patience throughout my graduate studies at the University of Michigan. I am truly grateful for his guidance throughout these years and I consider myself incredibly lucky and privileged to have worked with such a knowledgeable and insightful advisor. I would like to thank Professor Hong Im, Professor Krzysztof Fidkowski, and Professor James McDaniel for their willingness to serve on my committee and for providing helpful feedback and guidance on my graduate research. A special thanks goes out to Professor McDaniel and two graduate students in his group, Joshua Codoni and Erin Reed, at the University of Virginia for their collaboration that helped shape my research project. I would like to thank Dr. Ron Merski, the head of the Aerothermodynamics Branch at NASA Langley, for giving me the opportunity to work there during the summers of 2009 and 2010. I also thank all of the people in that branch, particularly Dr. William Wood, Dr. William (Bil) Kleb, and Dr. Alireza Mazaheri, as well as the FUN3D team, especially Dr. Michael Park, for all their help during my internships at Langley.

My thanks also extend to all of the current members of the Nonequilibrium Gas and Plasma Dynamics Laboratory that I have had the pleasure of working and interacting with. I am grateful to be part of a lab in which there is always someone



willing to answer questions and help with problems. I also express my thanks to some of the former members of the lab, including Tim Deschenes, Tim Holman, Alexandre Martin, and Nick Bisek. I would like to thank all of my friends at the University of Michigan that have made my time here in Ann Arbor very special. In particular, I thank Tyler Huisman and Ez Hassan for turning many long study sessions into cherishable experiences. I have also enjoyed all of the wonderful conversations that I have had with my officemates, Abhilasha Anna and Karthik Kumar, over the past few years that have covered everything from vibrational nonequilibrium to Mac vs. PC.

Last, but not least, I would like to thank my family for their help which made this dissertation possible. In particular, I thank my sister, Hind, for providing moral support. I express sincere thanks to Emily for her understanding and love during the past few years. Without her constant encouragement, this process would have been nearly impossible. Finally, my deepest love and gratitude go to my parents for all their support during the long years of my education.

This work was supported by a grant (NNX08AH37A) from the National Aeronautics and Space Administration (NASA). The use of supercomputing resources from the University of Michigan (Center for Advanced Computing) and NASA (NASA Advanced Supercomputing Division) were essential to this work and are also greatly appreciated.

# TABLE OF CONTENTS

DEDICATION . . . . .	ii
ACKNOWLEDGEMENTS . . . . .	iii
LIST OF FIGURES . . . . .	viii
LIST OF TABLES . . . . .	xv
LIST OF APPENDICES . . . . .	xvi
LIST OF NOMENCLATURE . . . . .	xvii
<b>CHAPTER</b>	
<b>I. Introduction . . . . .</b>	<b>1</b>
1.1 Motivation . . . . .	1
1.2 Mars Entry, Descent, and Landing (EDL) . . . . .	5
1.2.1 Mars EDL Challenges . . . . .	5
1.2.2 Current Mars EDL Technology Limitations . . . . .	8
1.2.3 Alternative Mars EDL Technologies . . . . .	11
1.3 Review of Related Work . . . . .	12
1.3.1 Propulsive Deceleration . . . . .	14
1.3.2 Reaction Control Systems . . . . .	17
1.4 Scope of Dissertation . . . . .	19
1.4.1 Overview . . . . .	19
1.4.2 Outline . . . . .	20
<b>II. Technical Approach . . . . .</b>	<b>23</b>
2.1 Experimental Setup . . . . .	24
2.1.1 Hypersonic Wind Tunnel . . . . .	24
2.1.2 Planar Laser-Induced Iodine Fluorescence Technique . . . . .	26
2.2 Navier-Stokes Solver . . . . .	28
2.2.1 LeMANS Overview . . . . .	29

2.3	Numerical Boundary Conditions . . . . .	33
2.3.1	Implementation in LeMANS . . . . .	33
2.3.2	Assessment of the Ashkenas and Sherman relations . . . . .	36
2.3.3	Effects of the Ashkenas and Sherman relations . . . . .	45
2.4	Summary . . . . .	48
<b>III. Central Propulsive Deceleration . . . . .</b>		<b>51</b>
3.1	Numerical Setup . . . . .	52
3.1.1	Aeroshell Geometry . . . . .	53
3.1.2	PD Jet Conditions . . . . .	55
3.2	Sonic PD Jets . . . . .	58
3.2.1	Flowfield Features . . . . .	58
3.2.2	Surface Properties . . . . .	61
3.2.3	Aerodynamic Properties . . . . .	62
3.3	Effects of the Central PD Jet Mach Number . . . . .	66
3.3.1	Flowfield Effects . . . . .	67
3.3.2	Surface Effects . . . . .	69
3.3.3	Aerodynamic Effects . . . . .	70
3.4	Summary . . . . .	74
<b>IV. Peripheral Propulsive Deceleration . . . . .</b>		<b>77</b>
4.1	Numerical Setup . . . . .	78
4.1.1	Aeroshell Geometry . . . . .	78
4.1.2	PD Jet Conditions . . . . .	80
4.2	Flowfield Features . . . . .	83
4.3	Effects of the Peripheral PD Jet Mach Number . . . . .	83
4.3.1	Flowfield Effects . . . . .	85
4.3.2	Surface Effects . . . . .	89
4.3.3	Aerodynamic Effects . . . . .	89
4.4	Comparisons Between Peripheral and Central PD Jets . . . . .	93
4.4.1	Flowfield Properties . . . . .	94
4.4.2	Aerodynamic Properties . . . . .	95
4.4.3	Deceleration Performance . . . . .	99
4.5	Summary . . . . .	99
<b>V. Reaction Control System . . . . .</b>		<b>102</b>
5.1	Numerical Setup . . . . .	103
5.1.1	Aeroshell Geometry . . . . .	104
5.1.2	RCS Jet Conditions . . . . .	105
5.2	Baseline Configuration . . . . .	108
5.3	Parallel RCS Jet . . . . .	111
5.3.1	Flowfield Properties . . . . .	111

5.3.2	Surface Properties . . . . .	113
5.3.3	Aerodynamic Properties . . . . .	116
5.4	Transverse RCS Jet . . . . .	117
5.4.1	Flowfield Properties . . . . .	117
5.4.2	Surface Properties . . . . .	119
5.4.3	Aerodynamic Properties . . . . .	122
5.5	Performance of the Parallel and Transverse RCS Jets . . . . .	123
5.6	Summary . . . . .	130
<b>VI. Comparisons with Experimental Data . . . . .</b>		<b>134</b>
6.1	Baseline Configuration . . . . .	135
6.2	Propulsive Deceleration . . . . .	140
6.2.1	Central Configuration . . . . .	140
6.2.2	Peripheral Configuration . . . . .	146
6.3	Reaction Control System . . . . .	153
6.4	Summary . . . . .	155
<b>VII. Conclusion . . . . .</b>		<b>158</b>
7.1	Summary . . . . .	158
7.2	Contributions . . . . .	162
7.3	Future Work . . . . .	165
<b>APPENDICES . . . . .</b>		<b>170</b>
<b>BIBLIOGRAPHY . . . . .</b>		<b>178</b>

## LIST OF FIGURES

### Figure

1.1	Illustration of propulsive deceleration and reaction control system . . .	3
1.2	Entry, descent, and landing sequence for MSL . . . . .	6
1.3	Earth and Mars atmospheric comparison . . . . .	7
1.4	Landing sites of the successful Mars missions . . . . .	8
1.5	Supersonic disk-gap-band parachutes for Viking, Pathfinder, and MER	9
1.6	70° blunt-cone aeroshell . . . . .	10
1.7	Alternative Mars EDL technologies . . . . .	13
1.8	Total axial force coefficient as a function of PD nozzle thrust for central and peripheral (3 jets) PD configurations . . . . .	15
1.9	Candidate EDL architectures for Exploration-class missions to Mars	17
1.10	Design process for MSL RCS thrusters layout . . . . .	19
2.1	Image of the hypersonic wind tunnel at the University of Virginia . .	25
2.2	Experimental facility . . . . .	26
2.3	Schematic of the PLIIF setup . . . . .	27
2.4	Schematic of the Ashkenas and Sherman relations . . . . .	34
2.5	Temperature and density contours around a Mars-entry aeroshell with freestream conditions calculated using the Ashkenas and Sher- man relations. . . . .	36

2.6	LeMANS boundary conditions for simulating the flow around a Mars-entry aeroshell in the experimental facility . . . . .	37
2.7	Computational grid for simulating the flow around a Mars-entry aeroshell in the experimental facility . . . . .	38
2.8	Mach number contours and velocity streamlines calculated by LeMANS around a Mars-entry aeroshell in the experimental facility . . . . .	39
2.9	Gradient-length local Knudsen number contours calculated by LeMANS around a Mars-entry aeroshell in the experimental facility . . . . .	40
2.10	Comparison of translational and rotational temperature distributions computed by LeMANS in the experimental facility . . . . .	41
2.11	Comparison of the axial and radial Mach number, temperature, and density distributions calculated by LeMANS in the experimental facility and the Ashkenas and Sherman relations . . . . .	42
2.12	Boundary conditions and mesh for simulating flow around a Mars-entry aeroshell with Ashkenas and Sherman-derived freestream conditions . . . . .	43
2.13	Comparison of Mach number and pressure contours around a Mars-entry aeroshell for the experimental facility simulation and the simulation with the Ashkenas and Sherman-derived freestream conditions . . . . .	44
2.14	Comparison of pressure and skin friction coefficients for a Mars-entry aeroshell in the underexpanded freejet and in freestream conditions provided by the Ashkenas and Sherman relations . . . . .	45
2.15	Geometry for the 10 mm diameter MSL-based aeroshell . . . . .	46
2.16	Comparison of Mach number and pressure contours around a Mars-entry aeroshell with constant and Ashkenas and Sherman-derived freestream conditions . . . . .	47
2.17	Comparison of pressure and skin friction coefficients for a Mars-entry aeroshell with constant and Ashkenas and Sherman-derived freestream conditions . . . . .	48
3.1	Aeroshell geometry with sonic and supersonic central PD jets . . . . .	54
3.2	Computational mesh for sonic and supersonic central PD jets . . . . .	55

3.3	Mach number distribution in the nozzle for sonic and supersonic central PD jets . . . . .	57
3.4	Flowfield features for sonic central PD jets . . . . .	59
3.5	Mach number contours for sonic central PD jets at various thrust coefficients . . . . .	60
3.6	PD jet species mole fraction contours for sonic central PD jets at various thrust coefficients . . . . .	61
3.7	Gradient-length local Knudsen number contours for sonic central PD jets at various thrust coefficients . . . . .	62
3.8	Coefficients of pressure and skin friction for sonic central PD jets at various thrust coefficients . . . . .	63
3.9	Drag and total axial force coefficients for sonic central PD jets . . .	64
3.10	Comparison of Mach number and pressure contours predicted by continuum and hybrid methods for $C_T = 2.0$ . . . . .	65
3.11	Mass and momentum transfer from the freestream to the surface of the aeroshell for sonic central PD jets at $C_T = 0.5$ and $C_T = 2.5$ . .	67
3.12	Comparison of Mach number contours for sonic and supersonic central PD jets at $C_T = 0.5$ and $C_T = 2.5$ . . . . .	68
3.13	Comparison of PD jet species mole fraction contours for sonic and supersonic central PD jets at $C_T = 0.5$ and $C_T = 2.5$ . . . . .	69
3.14	Comparison of gradient-length local Knudsen number contours for sonic and supersonic central PD jets at $C_T = 0.5$ and $C_T = 2.5$ . . .	70
3.15	Comparison of coefficients of pressure and skin friction for sonic and supersonic central PD jets at various thrust coefficients . . . . .	71
3.16	Comparison of drag and axial force coefficients for sonic and supersonic central PD jets . . . . .	72
3.17	Comparison of mass and momentum transfer from the freestream to the surface of the aeroshell for sonic and supersonic central PD jets at $C_T = 2.5$ . . . . .	73

3.18	Drag and thrust contributions to the axial force on the aeroshell for sonic and supersonic central PD jets . . . . .	74
4.1	Aeroshell geometry for sonic peripheral PD jets . . . . .	79
4.2	Aeroshell geometry for supersonic peripheral PD jets . . . . .	79
4.3	Surface mesh for sonic and supersonic peripheral PD jets . . . . .	80
4.4	Mach number distribution in the nozzle for the sonic and supersonic peripheral PD jets . . . . .	82
4.5	Comparison of Mach number contours for the no-jet and sonic peripheral PD jet ( $C_T = 1.5$ ) configurations . . . . .	84
4.6	Comparison of Mach number contours for sonic and supersonic peripheral PD jets at various thrust coefficients . . . . .	86
4.7	Comparison of PD jet species mole fraction contours for sonic and supersonic peripheral PD jets at various thrust coefficients . . . . .	87
4.8	Comparison of gradient-length local Knudsen number contours for sonic and supersonic peripheral PD jets at various thrust coefficients . . . . .	88
4.9	Comparison of forebody pressure coefficient contours for sonic and supersonic peripheral PD jets at various thrust coefficients . . . . .	89
4.10	Comparison of drag and axial force coefficients for sonic and supersonic peripheral PD jets . . . . .	90
4.11	Velocity streamlines along the aeroshell forebody for the no-jet and sonic peripheral jet configurations . . . . .	92
4.12	Drag and thrust contributions to the axial force on the aeroshell for sonic and supersonic peripheral PD jets . . . . .	93
4.13	Comparison of Mach number contours for sonic peripheral and central PD jets at $C_T = 0.5$ and $2.5$ . . . . .	95
4.14	Comparison of PD jet species mole fraction contours for sonic peripheral and central PD jets at $C_T = 0.5$ and $2.5$ . . . . .	96
4.15	Comparison of gradient-length local Knudsen number contours for sonic peripheral and central PD jets at $C_T = 0.5$ and $2.5$ . . . . .	96



4.16	Comparison of drag and axial force coefficients for peripheral and central PD jets . . . . .	97
4.17	Comparison of forebody pressure coefficient contours for sonic peripheral and central PD jets . . . . .	98
4.18	Deceleration performance for peripheral and central PD jets . . . . .	100
5.1	Aeroshell geometry with parallel and transverse RCS jets . . . . .	104
5.2	Surface mesh used in the RCS jet simulations . . . . .	105
5.3	Mach number distribution in the nozzle for the parallel and transverse RCS jets . . . . .	108
5.4	Mach number and gradient-length local Knudsen number contours for the no-jet case at 20° angle-of-attack . . . . .	109
5.5	Forebody and aftbody pressure coefficient contours for the no-jet case at 20° angle-of-attack . . . . .	110
5.6	Schematic of the aerodynamic forces acting on the aeroshell at 20° angle-of-attack . . . . .	111
5.7	Mach number contours for the parallel RCS jet at $C_T = 0.05$ and 1.0 . . . . .	112
5.8	RCS jet species mole fraction contours for the parallel RCS jet at $C_T = 0.05$ and 1.0 . . . . .	113
5.9	Gradient-length local Knudsen contours for the parallel RCS jet at $C_T = 0.05$ and 1.0 . . . . .	114
5.10	Forebody and aftbody pressure coefficient contours for the parallel RCS jet at $C_T = 0.05$ and 1.0 . . . . .	115
5.11	The distributions of pressure and skin friction coefficients along the centerline of the aeroshell aftbody for the parallel RCS jet at $C_T = 0.05$ and 1.0 . . . . .	116
5.12	Mach number contours for the transverse RCS jet at $C_T = 0.05$ and 1.0 . . . . .	118
5.13	RCS jet species mole fraction contours for the transverse RCS jet at $C_T = 0.05$ and 1.0 . . . . .	119

5.14	Gradient-length local Knudsen contours for the transverse RCS jet at $C_T = 0.05$ and 1.0 . . . . .	120
5.15	Forebody and aftbody pressure coefficient contours for the transverse RCS jet at $C_T = 0.05$ and 1.0 . . . . .	121
5.16	The distributions of pressure and skin friction coefficients along the centerline of the aeroshell aftbody for the transverse RCS jet at $C_T = 0.05$ and 1.0 . . . . .	122
5.17	Direction of the moment due to the thrust force from the parallel RCS jet about the center of gravity of the aeroshell . . . . .	124
5.18	Direction of the moment due to the thrust force from the transverse RCS jet about the center of gravity of the aeroshell . . . . .	126
5.19	Comparisons of the ratio of interference moment to thrust-induced moment and the RCS control gain between the parallel and transverse RCS jets at $C_T = 0.05$ and 1.0 . . . . .	127
5.20	Lengths of the moment arm with respect to the center of gravity of the aeroshell along the $X$ and $Y$ directions . . . . .	128
5.21	Comparison of the distribution of the moment per unit area along the centerline of the aeroshell aftbody between the parallel and transverse RCS jets at $C_T = 0.05$ and 1.0 . . . . .	130
6.1	Comparison of the bow shock profile for the no-jet case at $0^\circ$ angle-of-attack between the numerical and experimental results . . . . .	136
6.2	Comparison of the bow shock profile for the no-jet case at $20^\circ$ angle-of-attack between the numerical and experimental results . . . . .	137
6.3	Percent difference in the density between the Ashkenas and Sherman relations and the CFD solution of the flow in the experimental facility	138
6.4	PLIIF image of the interaction between the bow shock and the barrel shock in the experimental facility . . . . .	139
6.5	Comparison of the bow shock profile for sonic central PD jets between the numerical and experimental results . . . . .	142
6.6	Distribution of the iodine number density calculated by LeMANS along the aeroshell centerline for the sonic central PD jet at $C_T = 0.5$ and 2.5 . . . . .	143

6.7	Comparison of the bow shock profile for supersonic central PD jets between the numerical and experimental results . . . . .	144
6.8	Comparison of the bow shock standoff distance for sonic and supersonic central PD jets between numerical and experimental results . . . . .	145
6.9	Comparison of drag and total axial force coefficients for supersonic central PD jets between numerical and experimental results . . . . .	146
6.10	Comparison of the bow shock profile for sonic peripheral PD jets between the numerical and experimental results . . . . .	148
6.11	Comparison of the bow shock profile for supersonic peripheral PD jets between the numerical and experimental results . . . . .	149
6.12	Comparison of the bow shock standoff distance for sonic and supersonic peripheral PD jets between the numerical and experimental results . . . . .	150
6.13	Comparison of the PD jet I <sub>2</sub> mole fraction contours for sonic peripheral PD jet at $C_T = 1.5$ between the numerical and experimental results . . . . .	151
6.14	Comparison of PD jet I <sub>2</sub> mole fraction along extraction lines for sonic peripheral PD jet at $C_T = 1.5$ between the numerical and experimental results . . . . .	152
6.15	Comparison of the bow shock profile for the parallel RCS jet at $C_T = 1.0$ between the numerical and experimental results . . . . .	154
6.16	Comparison of bow shock profile for the transverse RCS jet at $C_T = 1.0$ between the numerical and experimental results . . . . .	155
B.1	Computational grid used to obtain preliminary numerical solutions for sonic central PD jets . . . . .	174
B.2	Preliminary numerical solution for sonic central PD jets at $C_T = 0.5$	175
B.3	Adapted computational grid for the sonic central PD jet at $C_T = 0.5$	176
B.4	Comparison of Mach number contours and surface properties between the preliminary and adapted grids for sonic central PD jet at $C_T = 0.5177$	

## LIST OF TABLES

### Table

1.1	Comparison of successful Mars entry missions . . . . .	4
2.1	Reference freestream conditions. . . . .	35
3.1	Design conditions for sonic central PD jets . . . . .	56
3.2	Design conditions for supersonic central PD jets . . . . .	56
4.1	Design conditions for sonic peripheral PD jets . . . . .	81
4.2	Design conditions for supersonic peripheral PD jets . . . . .	81
5.1	Expected freestream and RCS jet at maximum thrust conditions for MSL during flight . . . . .	106
5.2	Design conditions for the parallel and transverse RCS jets . . . . .	107
5.3	Aerodynamic properties of the no-jet case at 20° angle-of-attack . .	110
5.4	Aerodynamic properties of the aeroshell with the parallel RCS jet .	117
5.5	Aerodynamic properties of the aeroshell with the transverse RCS jet	123
5.6	Control effectiveness of the parallel RCS jet . . . . .	125
5.7	Control effectiveness of the transverse RCS jet . . . . .	125
A.1	Blottner constants for molecular nitrogen and iodine . . . . .	171
A.2	Rotational relaxation coefficients for molecular nitrogen and iodine .	172

## LIST OF APPENDICES

### Appendix

A.	Species Data . . . . .	171
B.	Manual Grid Adaptation Process . . . . .	173

## LIST OF NOMENCLATURE

### Acronyms

CFD	Computational Fluid Dynamics
DGB	Disk-Gap-Band Parachute
EDL	Entry, Descent, and Landing
MER	Mars Exploration Rover
MOLA	Mars Orbiter Laser Altitude
MSL	Mars Science Laboratory
NASA	National Aeronautics and Space Administration
PD	Propulsive Decelerator
PLIIF	Planar Laser-Induced Iodine Fluorescence
RCS	Reaction Control System
TPS	Thermal Protection System

### Latin Symbols

$C_A$	Axial Force Coefficient
$C_D$	Drag Coefficient
$C_f$	Skin Friction Coefficient
$C_M$	Moment Coefficient
$C_N$	Normal Force Coefficient
$C_P$	Pressure Coefficient
$C_T$	Thrust Coefficient
$D$	Orifice Diameter in the Experimental Facility, m
$D_{model}$	Aeroshell Diameter, m
$F_A$	Axial Force, N
$F_D$	Drag Force, N
$F_N$	Normal Force, N
$F_L$	Lift Force, N
$F_T$	Thrust Force, N
$Kn$	Knudsen Number
$Kn_{GLL}$	Gradient-Length Local Knudsen Number
$M$	Mach Number

$M_z$	Moment, Nm
$m$	Mass, kg
$\dot{m}$	Mass Flow Rate, kg/s
$n$	Number Density, 1/m <sup>3</sup>
$P$	Pressure, Pa
$q$	Dynamic Pressure, Pa
$S$	Area, m <sup>2</sup>
$T$	Temperature, K
$U$	Speed, m/s
$X$	Mole Fraction
$X_{SSD}$	Bow Shock Standoff Distance, m

### Greek Symbols

$\beta$	Ballistic Coefficient, kg/m <sup>2</sup>
$\gamma$	Ratio of Specific Heats
$\lambda$	Mean Free Path, m
$\rho$	Density, kg/m <sup>3</sup>
$\tau$	Shear Stress, Pa

### Subscripts

$(\cdot)_0$	Stagnation/Total Conditions
$(\cdot)_e$	PD or RCS Nozzle-Exit Conditions
$(\cdot)_{jet}$	PD or RCS Jet Conditions
$(\cdot)_{ref}$	Reference Freestream Conditions

# CHAPTER I

## Introduction

### 1.1 Motivation

The United States has successfully landed six robotic missions on the surface of Mars, with a seventh mission scheduled to land in 2012. These missions, which are summarized in Table 1.1, began in the 1960s and 1970s with the Viking program, which placed the Viking 1 and Viking 2 landers on the surface of Mars in 1976. The Viking landers were influenced by the design of lunar landers from the Apollo program and were not constrained by the relatively small budgets reserved for today's missions [1]. After a significant gap in NASA's surface exploration of Mars, the Mars Pathfinder resumed robotic missions to the planet in 1997. Pathfinder was influenced by the need for extreme cost saving relative to the Viking program, and consisted of a lander and a small rover. Then, after the loss of two Mars missions in 1999, the Mars Exploration Rover A (Spirit) and B (Opportunity) touched-down on Mars in 2004. These two rovers are, in fact, still operational today. The most recent mission to successfully land on Mars is Phoenix in 2008, and like the other missions, relied on Viking-era technology for atmospheric descent in order to save on cost.

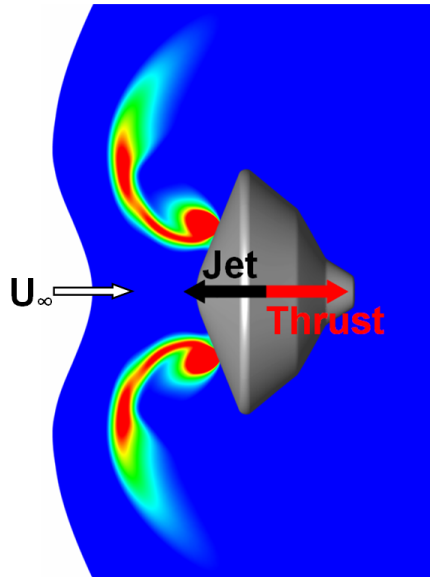
A new mission called the Mars Science Laboratory (MSL) is scheduled to land in 2012, and will achieve new breakthroughs in Mars exploration missions. At just under 1 ton and approximately the size of a compact automobile, MSL is the heaviest



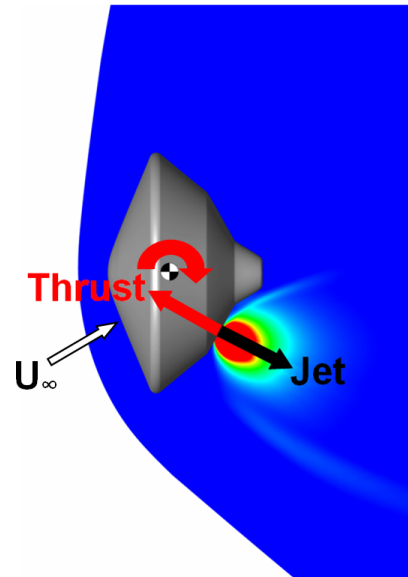
and largest mission to go to Mars. MSL is also capable of landing at sites as high as +1 km with reference to the Mars Orbiter Laser Altitude (MOLA) with the smallest landing footprint (uncertainty in landing at the target site) ever attempted on Mars of only 1 km. Similar to the other missions, MSL also relies heavily on the entry, descent, and landing technology from the Viking program. However, due to its large size and mass, MSL is pushing these technologies to the limits of their capabilities. The trend of landing more mass and larger vehicles on Mars with smaller footprints is projected to continue in order to conduct more *in situ* experiments at scientifically interesting sites. Current plans for robotic missions in the 2010 decade include landing 1 to 2 ton payloads with an accuracy better than 10 km at landing sites higher than +2 km MOLA [1]. Human exploration missions will further push the landing mass to between 40 and 80 tons with an accuracy of tens of meters at possibly high altitudes [1]. However, it may not be possible to simply extend the current Viking-era technology to these mission requirements due to the challenges of performing entry, descent, and landing on Mars.

The goal of this dissertation is to investigate the fundamental fluid interactions induced by propulsive deceleration and reaction control system thrusters for Mars-entry vehicles using computational fluid dynamics (CFD). The physical accuracy of the computational method is also assessed by comparing the numerical results to experimental measurements obtained in a wind tunnel facility at the University of Virginia. Propulsive deceleration, illustrated in Figure 1.1(a), can provide an additional component to slow the vehicle during Mars atmospheric descent by directing the thrust from engines on the entry-capsule into the incoming hypersonic or supersonic freestream. Reaction control systems (RCS), shown in Figure 1.1(b), can provide vehicle control and steering during descent by using thrusters located in the back of the entry-capsule. This research is motivated by the need to investigate alternative atmospheric entry systems that are required in order to perform pinpoint-landing of

high-mass future Mars missions.



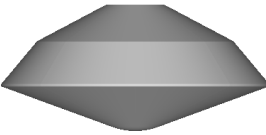
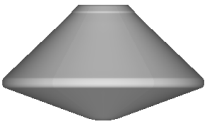
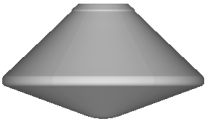
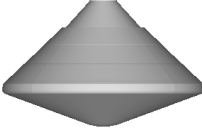
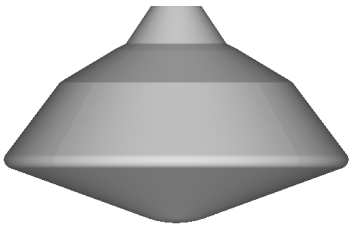
(a) Propulsive deceleration



(b) Reaction control system

Figure 1.1: Illustration of propulsive deceleration and reaction control system.

Table 1.1: Comparison of successful Mars entry missions. Data compiled from Ref.[1] and Ref. [2].

	Viking 1 & 2 1976	Pathfinder 1997	MER A & B 2004	Phoenix 2008	MSL (planned) 2012
					
Aeroshell Diameter, m	3.50	2.65	2.65	2.65	4.50
Ballistic Coefficient, $\text{kg}/\text{m}^2$	64	63	94	65	115
Entry Mass, ton	0.93	0.58	0.84	0.60	3.40
Lander/Rover Mass, ton	0.24	0.09	0.17	0.17	0.85
Landing Altitude, km	-3.5	-2.5	-1.9/-1.4	-3.5	< 1.0
Landing Ellipse, km	$280 \times 100$	$200 \times 100$	$80 \times 12$	$100 \times 21$	$20 \times 20$
Touchdown Attenuator	crushable legs	4 $\pi$ airbags	4 $\pi$ airbags	crushable legs	wheels (Sky Crane)

## 1.2 Mars Entry, Descent, and Landing (EDL)

Entry, descent, and landing is the phase during a mission to Mars (or other planets) that begins when the spacecraft reaches the edge of the atmosphere and terminates when the lander or rover safely touches down on the surface. During the EDL phase of Mars missions, the spacecraft must autonomously decelerate from approximately 12,000 mph to just over 0 mph in about six minutes. The lander or rover is located inside a protective aeroshell that uses a thermal protection system (TPS) in order to protect it from the extreme external temperatures, which can reach over 2,600° F (1,700 K). The EDL phase for all of the successful U.S. missions to Mars has consisted of an aeroshell, a parachute, and a touchdown attenuator, such as airbags, legs, or wheels. Figure 1.2 shows the EDL sequence for MSL, which is expected to reach Mars in 2012.

### 1.2.1 Mars EDL Challenges

EDL is a crucial phase of any Mars mission mainly due to several challenges that must be overcome in order to accomplish the mission scientific goals and objectives. One of these challenges is the Mars atmosphere. Figure 1.3 shows the density as a function of altitude for both the Mars and the Earth atmospheres [1]. Overall, the Mars atmosphere is approximately 100 times thinner in density than the Earth atmosphere. As a result, Mars-entry vehicles decelerate at much lower altitudes than Earth-entry vehicles and require more time to reach subsonic velocities, which may leave insufficient time to prepare for landing. Because of this thin atmosphere, it becomes increasingly more difficult to decelerate these vehicles as their size and mass increase. The Mars atmosphere, however, is thick enough to generate substantial heating to the surface of the aeroshell. As a result, Mars-entry aeroshells require a thermal protection system to protect them and their cargo from the harsh conditions encountered during EDL.



Figure 1.2: Entry, descent, and landing sequence for MSL (<http://jpl.nasa.gov>).

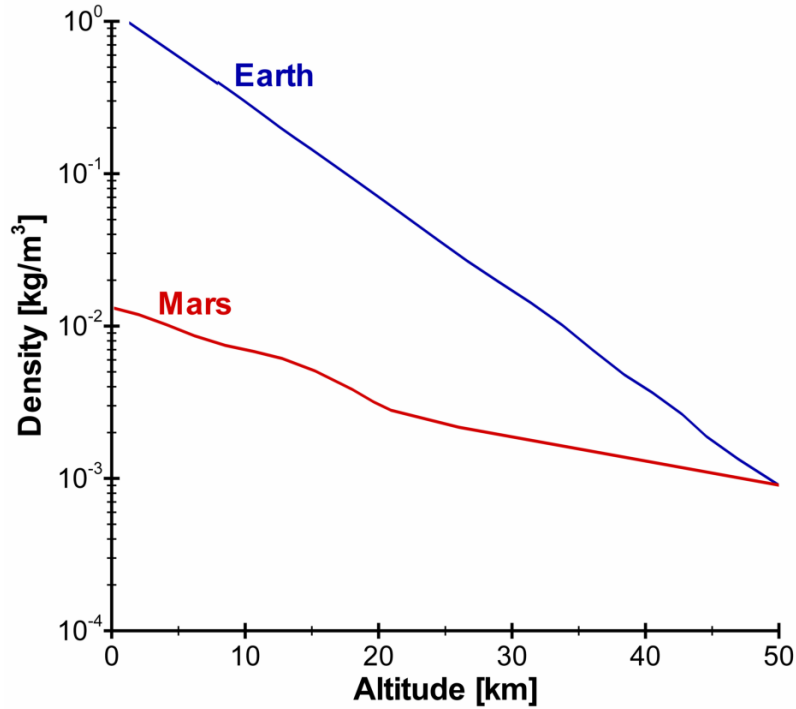


Figure 1.3: Earth and Mars atmospheric comparison. Data from Ref. [1].

Another challenge of the EDL phase is surface hazards on Mars. These hazards, such as rocks and sloped surfaces, pose tip-over threats, which would be devastating to mission success. As a result, all of the past successful Mars missions have avoided major rocky areas, as can be seen in Figure 1.4. The figure shows a MOLA topographic image, with blue regions representing relatively low elevations and red regions representing relatively high elevations. The figure also shows the landing sites of the six successful Mars missions, which are all located at relatively low elevations to provide the vehicle with more time to decelerate through the thin atmosphere. These sites are also relatively free of large rocks and small craters that can present hazardous surface conditions. The unguided EDL architectures of all of the successful missions require larger landing footprints to avoid hazardous regions and account for atmospheric uncertainties, such as wind conditions. Therefore, only a few landing sites are considered *a priori* that may not be as scientifically interesting as other, relatively riskier, sites.

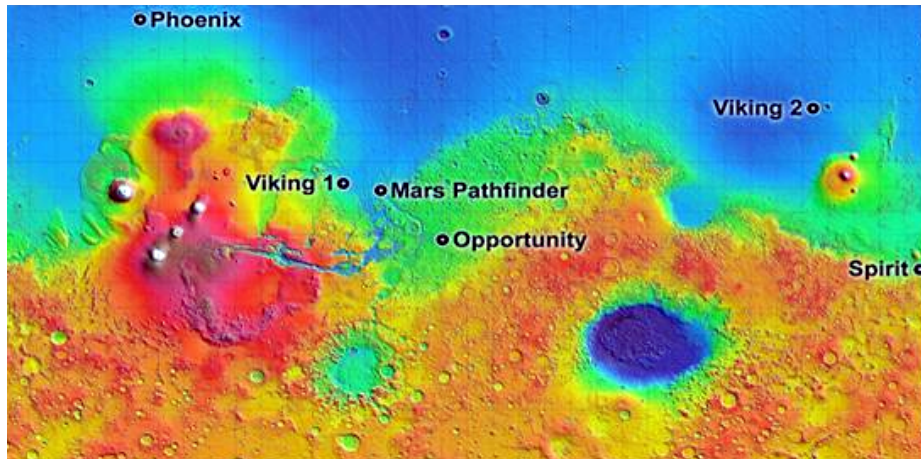


Figure 1.4: Landing sites of the successful Mars missions (<http://jpl.nasa.gov>).

### 1.2.2 Current Mars EDL Technology Limitations

Several of the EDL technology systems used in all of the Mars missions have stemmed from the Viking program of the 1960s and 1970s. These systems have remained mostly unchanged with appropriate scaling to meet the mission requirements. One such technology is the disk-gap-band (DGB) parachute, which is composed of a disk canopy, a gap, and a cylindrical band. Figure 1.5 shows the parachutes used for Viking, Pathfinder, and MER missions, which all employed a scaled-version of the Viking DGB parachute design. The Viking parachute system was qualified through a series of expensive qualification tests in the 1960s and 1970s to deploy between Mach numbers of 1.4 and 2.1, and between dynamic pressures of 400 Pa and 700 Pa [3]. This parachute design can remove about 0.98% of the vehicle's initial kinetic energy [4]. Subsequent missions to Mars have used scaled Viking DGB parachute designs without invalidating the deployment conditions in order to minimize cost. MSL will be the first mission with a parachute larger than what Viking used, but still within the qualification limits [3]. However, as the size and mass of future Mars entry systems increase, the deployment conditions of the Viking-era DGB parachute may not be reached until very close to the surface, which may not give enough time to prepare for a safe landing. Therefore, future, high-mass Mars missions will require either new

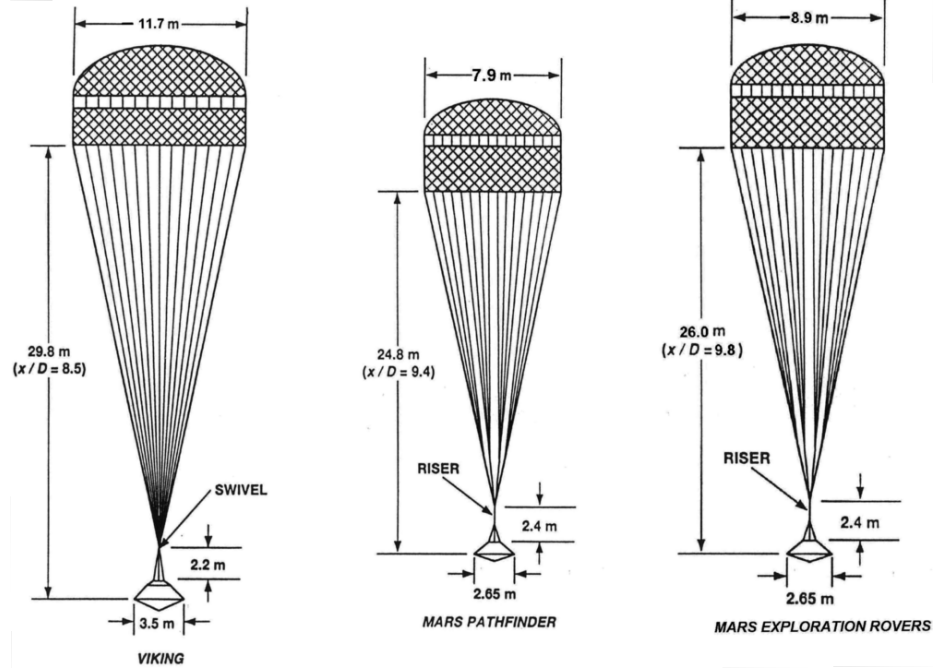


Figure 1.5: Supersonic disk-gap-band parachutes for Viking, Pathfinder, and MER. Figure from Ref. [3].

parachute designs that overcome the limitations of the Viking DGB parachute or additional deceleration techniques that can put the vehicle within the DGB parachute deployment limits at high enough altitudes.

Another technology that has been used on all successful Mars missions since the Viking program is the  $70^\circ$  blunt-cone aeroshell, which describes the angle of the forebody surface and is shown in Figure 1.6. The  $70^\circ$  blunt-cone is attractive for Mars missions because of the relatively large aerodynamic drag coefficient that it provides, which can remove approximately 90% of the vehicle's initial kinetic energy during the hypersonic regime [4]. The  $70^\circ$  blunt-cone is also attractive because of the large available aerodynamic database. The effects of the aeroshell shape on the EDL profile can be better understood by examining the ballistic coefficient,  $\beta$ , of the entry system which is defined as,

$$\beta = \frac{m}{C_D S} \quad (1.1)$$

where  $m$  is the mass of the vehicle,  $C_D$  is the drag coefficient of the aeroshell, and



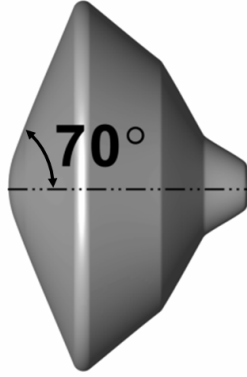


Figure 1.6: 70° blunt-cone aeroshell.

$S$  is the reference area (cross-sectional area). A Mars-entry vehicle with a low ballistic coefficient decelerates more at higher altitudes, which reduces both the peak deceleration rate and the peak heat flux, as well as provides the vehicle with more time to reach parachute deployment conditions before running out of altitude [3]. As can be seen from Table 1.1, the ballistic coefficient of previous successful Mars entry systems ranges from 63 kg/m<sup>2</sup> to 94 kg/m<sup>2</sup>. The MSL, however, has a ballistic coefficient of 115 kg/m<sup>2</sup>, mainly due to its relatively large mass of about 1 ton. In fact, future Mars missions, including possible manned missions, will continue this trend of carrying more mass to Mars. In order to minimize the ballistic coefficient, the size of the aeroshell must also increase since a different aeroshell forebody shape will not have a significant effect on the drag coefficient [1]. However, due to limitations on the launch vehicle size and integration, as well as restrictions on existing test facilities, the aeroshell diameter cannot increase beyond 5 m [3]. Therefore, future high-mass Mars missions will require either an overhaul of launch vehicle integration and ground facilities or new decelerator technology which will reduce the ballistic coefficient by either increasing the drag coefficient or the reference area of the entry capsule.

None of the previous robotic missions to Mars used a guided entry in order to perform pinpoint landing. As a result, the landing footprint for these systems was on the order of 10s to 100s of kilometers, as shown in Table 1.1. Viking flew a lifting

trajectory, but did not use the lift vector to adjust the vehicle flight path in real-time [1]. Mars Pathfinder, MER, and Phoenix all flew ballistic entries without any aerodynamic maneuvering. MSL will make the first attempt at performing precision landing on Mars. MSL is planned to land within 10 km of its target site using aerodynamic maneuvering (lift-to-drag ratio of 0.24), a reaction control system (RCS), and an entry guidance algorithm derived from the Earth reentry guidance design of the Apollo command module [5]. RCS can provide vehicle control and steering by inducing moments on the capsule using thrusters located on the aftbody of the aeroshell during entry to either guide or correct the flight path in real time. Although the new technology used in MSL will greatly improve the landing accuracy, future missions, especially human-exploration missions, will require pinpoint landing with an accuracy of meters [1]. Current plans for manned missions call for a rendezvous of the crew vehicle with pre-deployed cargo and exploration assets on Mars [6]. In order to accomplish this objective, the manned vehicle must land within 100 meters of the exploration assets, which can only be achieved by minimizing the delivery uncertainty of these systems through better guidance algorithms and RCS designs.

### **1.2.3 Alternative Mars EDL Technologies**

Alternative EDL technologies are required to overcome the limitations of the Viking-era systems. The first alternative is to develop new parachute designs with better and stronger materials [1]. The new designs should extend the parachute deployment conditions (e.g. deploy at higher altitudes) in order to provide future Mars entry systems with higher ballistic coefficients enough time to prepare for a safe landing.

Another alternative EDL technology is aerocapture, summarized in Figure 1.7(a). Aerocapture, which has never been used, is an orbit insertion maneuver in which the spacecraft flies through the Mars atmosphere in a single pass and uses the drag force

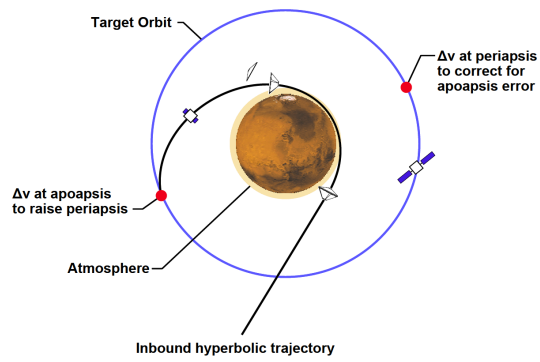
to decelerate to a target orbit around the planet. Unlike direct entry, aerocapture provides mission flexibility to accommodate for uncertainties in the Mars atmosphere, such as dust storms. Orbit insertion through aerocapture will also reduce the peak deceleration [7], which is particularly desirable for human-exploration missions. This maneuver can significantly enhance future Mars missions by placing larger spacecraft into a target orbit for approximately the same overall delivery cost as the best non-aerocapture alternative (e.g. conventional chemical propulsion orbit insertion) [8].

Inflatable or deployable entry aeroshells (usually referred to as “ballutes” in the literature) can also be considered an alternative Mars EDL technology. Figure 1.7(b) shows a forebody-attached inflatable aeroshell [9]. Ballutes are aerodynamic decelerators that increase the surface area of the aeroshell, which increases both the drag and lift forces and decreases the ballistic coefficient. As a result, ballutes are currently being considered for missions with aerocapture [10].

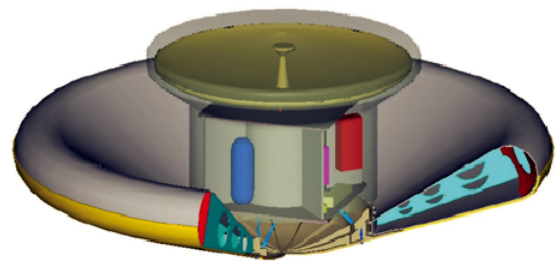
Future Mars-entry systems may also require the use of propulsive deceleration, in addition to the aerodynamic decelerators, to slow down during atmospheric descent. Propulsive deceleration works by directing thrust from engine(s) into the incoming hypersonic or supersonic freestream flow. Propulsive decelerator (PD) jets can be arranged in either a central configuration, with one jet located at the center of the aeroshell as shown in Figure 1.7(c), or a peripheral configuration, with several jets located on the forebody as shown in Figure 1.7(d). The use of these jets, however, can generate complex fluid interactions between the jets, the freestream, and the aeroshell that may have significant effects on the vehicle’s aerodynamic properties.

### **1.3 Review of Related Work**

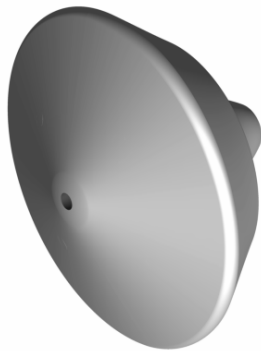
As described in Section 1.2.2, several of the Mars EDL technologies in use today were developed in the 1960s and 1970s for the Viking program. However, there has been a recent push to understand the effects of propulsive deceleration and reaction



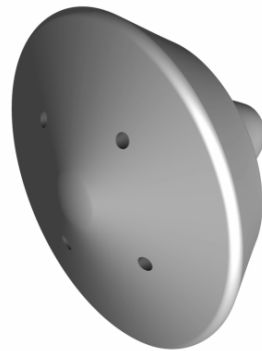
(a) Aerocapture [7]



(b) Inflatable decelerator [9]



(c) Propulsive deceleration (central)



(d) Propulsive deceleration (peripheral)

Figure 1.7: Alternative Mars EDL technologies.

control systems in order to achieve pinpoint-landing of high-mass entry vehicles on Mars. This section outlines some of the work that has been performed in order to analyze and mature these technologies.

### 1.3.1 Propulsive Deceleration

A substantial amount of experimental work was carried out from the 1950s to the 1970s on propulsive deceleration as part of the Viking program, which is mostly summarized in Ref. [11]. The majority of this work involved supersonic or sonic jets exhausting into supersonic or subsonic freestreams. Early work conducted in the 1950s focused mainly on the interaction between the PD jet and the boundary layer [12, 13] and between the PD jet and the shock that develops upstream of the test model [14, 15, 16, 17]. Although the aeroshell geometries used in these tests were not representative of the blunt-cone shapes of entry vehicles, this early work established fundamental physics of jet-shock interactions and motivated subsequent investigations of blunt-body entry vehicles.

By the 1960s and early 1970s, this work was extended to entry vehicle geometries and focused on two distinct PD configurations. The first configuration is the central PD jet, which gathered a lot of focus in the literature [18, 19, 20, 21, 22, 23]. Experimental visualizations for the central configuration showed that the flow is characterized by a bow shock, a PD jet terminal shock, and recirculation regions in front of the aeroshell [18, 20, 23]. These visualizations also showed that the flowfield structure transitions from stable to highly unstable and back to stable as the ratio of the jet total pressure to the freestream total pressure increases [18, 20]. Surface pressure measurements indicated that central PD jets can greatly reduce the aerodynamic drag force on the vehicle [20, 23, 24]. Figure 1.8 presents the variation in the coefficient of total axial force (i.e. sum of aerodynamic drag and PD thrust) for the central configuration with the PD thrust [11] (originally published in [24]). These results

are for supersonic PD jets of air at Mach 4.3 exhausting into a supersonic Mach 2.0 freestream. The plot shows that as the thrust from the PD nozzle increases, the total axial force acting on the capsule first decreases, and then increases mainly from the contribution of the thrust force.

Several experimental studies in the 1960s and early 1970s also looked at peripheral PD jets [22, 23, 24]. Flowfield visualizations from these studies showed that the peripheral PD jets are swept away by the opposing freestream [23], which minimizes the disturbance on the portion of the bow shock closest to the aeroshell nose. The visualizations also showed that the peripheral jets diffuse into the incoming freestream through mixing instead of a terminal jet shock at relatively low thrust conditions. Surface pressure measurements indicated that the peripheral PD jets can preserve the aerodynamic drag better than central jets at the same conditions, as shown in Figure 1.8. The results in this figure are for a 3-jet configuration of air at Mach 4.3 exhausting into a Mach 2.0 freestream.

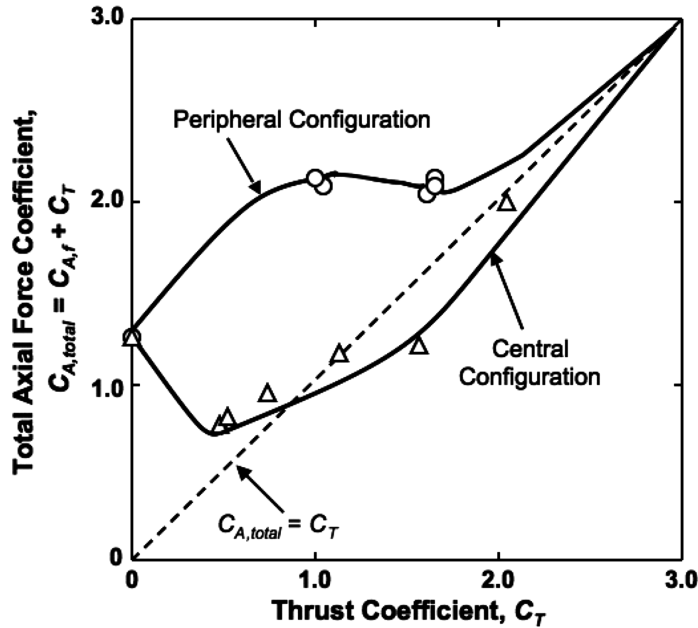


Figure 1.8: Total axial force coefficient as a function of PD nozzle thrust for central and peripheral (3 jets) PD configurations. Figure from Ref. [11].

After the selection of the Viking EDL architecture (i.e. 70° blunt-cone aeroshell

and DGB parachute), however, there has not been any extensive amount of work on propulsive deceleration until very recently. Interest in propulsive deceleration has been renewed due to the limitations of EDL technologies for future high-mass Mars missions. A 2008 Entry, Descent and Landing Systems Analysis (EDL-SA) study was commissioned by senior management at NASA to identify and roadmap EDL technology investments that the agency needed to make in order to successfully land large payloads on Mars for both robotic and human-scale missions [25]. This study established a suite of 8 candidate EDL architectures, shown in Figure 1.9, that NASA is considering for Exploration-class missions to Mars [26], with half of these architectures requiring propulsive deceleration in hypersonic or supersonic conditions. Exploration-class missions are defined as cargo or crewed missions requiring between 10 and 50 tons of landed payload [6]. As a result, there has been a significant push by engineers to mature propulsive deceleration to a point where it can be reliably used on Mars-entry vehicles [27]. This push includes experimental [28, 29, 30, 31] and numerical [32, 33, 34, 35, 36, 37, 38] studies to assess the validity of current computational models, as well as systems-level studies [39, 40] to understand the performance and mass requirements of propulsive deceleration. Most of this recent work focuses on using propulsive deceleration in a supersonic freestream (called supersonic retropropulsion) in order to reduce the propellant mass requirements. However, the EDL-SA study is considering an all-propulsive EDL architecture (#3 in Figure 1.9), which would utilize a nuclear thermal rocket (NTR) to place the spacecraft in an orbit around Mars and propulsive deceleration in the hypersonic regime. A fully-propulsive strategy was also shown to be capable of delivering approximately 9 tons of payload to Mars with Earth-launch masses as low as 25 tons when coupled with refueling resources in Earth and Mars orbit [40]. However, some of the major questions regarding an all-propulsive EDL strategy that still need to be addressed before using this technology are the flowfield interactions of the rocket plume firing into the atmosphere

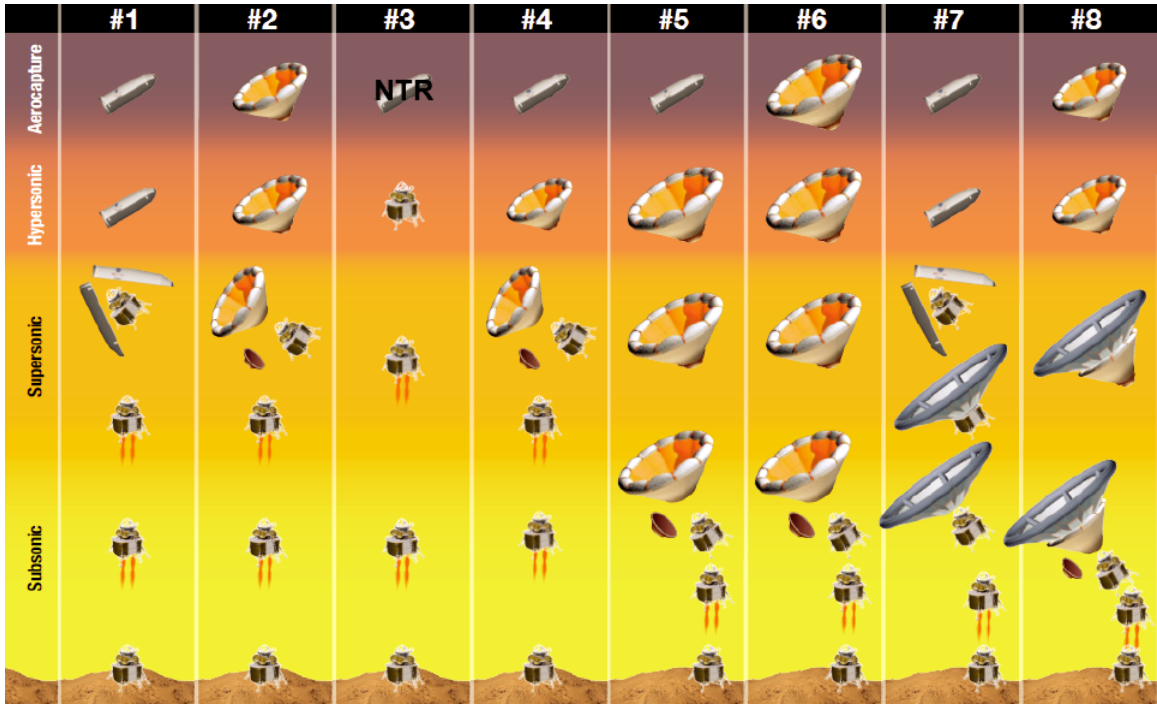


Figure 1.9: Candidate EDL architectures for Exploration-class missions to Mars. Figure from Ref. [26].

at hypersonic conditions and their effects on the resulting drag force on the vehicle [25]. Therefore, there is a need to analyze the effects of propulsive deceleration in hypersonic conditions.

### 1.3.2 Reaction Control Systems

Similar to propulsive deceleration, there is a significant generation gap in the development and analysis of reaction control systems for Mars-entry aeroshells. The Viking program, which was designed to use RCS thrusters for attitude control, attempted to measure experimentally the magnitude of the aerodynamic interference of the RCS jets in a Mach 20 wind tunnel [41]. Due to large uncertainties, however, this test was unable to infer any significant conclusions on the RCS jet aerodynamic interference. Following Viking, RCS development for subsequent Mars missions ceased in order to save on cost. However, there was a significant effort to understand the



effects of RCS thrusters on the Space Shuttle Orbiter. The Shuttle program carried out several wind tunnel experiments to examine the aerodynamic interference of the RCS jets [42, 43, 44, 45, 46]. By comparing the performance of the RCS jets in these wind tunnel tests to post-flight data, it was found that the ratio of the RCS jet momentum to the freestream momentum (i.e.  $(\dot{m}U)_{jet}/(\dot{m}U)_{\infty}$ ) is one of the key scaling parameters in the testing and development of RCS thrusters [47].

The scaling parameters used for the Space Shuttle Orbiter were also applied to test the RCS thrusters for Phoenix and MSL. The original EDL strategy for the Phoenix lander was to use RCS thrusters for attitude control and rate damping in order to reduce the landing footprint to approximately 10 km [48, 49]. However, numerical simulations indicated large uncertainties in the torque provided by the RCS jets due to significant interaction between the RCS plumes and the wake [50]. As a result, the deadbands (i.e. range of trajectory error around the ideal that is deemed acceptable and the thrusters do not fire) for the control system during hypersonic flight were widened to virtually remove the use of hypersonic guidance and rely on an unguided EDL architecture [49, 51]. Unlike Phoenix, the MSL will utilize RCS thrusters for a guided entry through the hypersonic phase [52]. As a result, there has been a significant amount of work, mainly using CFD, to analyze the aerodynamic interaction between the RCS jets and the wake [41, 2, 53, 54, 55]. As can be seen in Figure 1.10, the design of the MSL RCS thruster layout has evolved due to several constraints, including aerodynamic interference [41]. The final design of the MSL RCS layout uses eight thrusters arranged in four pairs, with each jet capable of providing roll, pitch, and yaw control [55]. Even with this work, however, there is still a need for further experimental tests and validated numerical methods to continue the development of RCS as an important part of Mars-entry systems [41].

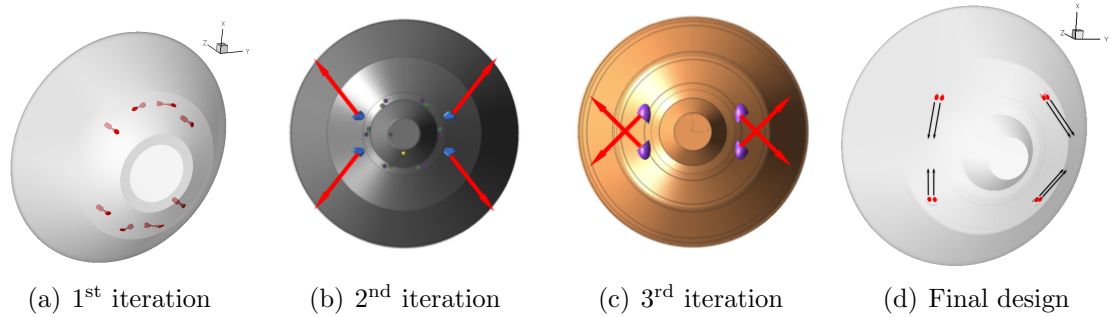


Figure 1.10: Design process for MSL RCS thrusters layout. Figure from Ref. [41].

## 1.4 Scope of Dissertation

### 1.4.1 Overview

The purpose of this dissertation is to examine the fluid interactions generated by propulsive decelerator and reaction control system thrusters on Mars-entry aeroshells in hypersonic freestream conditions. These interactions between the thrusters, the aeroshell, and a hypersonic freestream can have significant effects on the flowfield, surface, and aerodynamic properties of the capsule. Numerical results of an MSL-based aeroshell are obtained using the CFD code LeMANS. These results are compared to experimental measurements obtained at the University of Virginia using the planar laser-induced iodine fluorescence technique in order to assess the physical accuracy of the computational method. The first and second parts of this study examine the effects of central and peripheral propulsive deceleration, respectively, on the flowfield, surface, and aerodynamic properties of the aeroshell using LeMANS. The effects of a reaction control system used for vehicle control are investigated computationally in the third portion of this study. Finally, the study compares the numerical results obtained in the first, second, and third parts for propulsive deceleration and reaction control systems to experimental measurements and visualizations in order to assess the physical accuracy of the numerical method.

### 1.4.2 Outline

Chapter II outlines the technical approach used in this dissertation work. The chapter first provides a description of the experimental facility at the University of Virginia and the optical technique that is used to obtain the experimental measurements. The chapter then describes the CFD code that is employed in this dissertation and summarizes the governing equations solved by this code. Next, the chapter provides a detailed description of the boundary conditions that are implemented in the computational method to model the flow and match the conditions in the experimental facility. An assessment of the implementation of these conditions in the CFD code and their effect on the numerical solutions are also provided.

Chapter III presents a numerical study of central propulsive deceleration using sonic and supersonic jets at various thrust conditions. The chapter first describes the numerical setup followed in the study, including the aeroshell geometry and the PD jet conditions. The chapter then examines the flowfield, surface, and aerodynamic interactions generated by sonic central PD jets at different thrust conditions. These results are then compared to the results for supersonic PD jets in order to understand the effects of the central PD Mach number on the flowfield, surface, and aerodynamic properties of Mars-entry aeroshells. The chapter then concludes with a summary of the major discoveries of this study.

A numerical study of peripheral propulsive deceleration using sonic and supersonic jets at various thrust conditions is provided in Chapter IV. First, details on the aeroshell geometry and PD jet conditions are outlined. Then, the chapter describes the effects of the peripheral PD jet Mach number on the flowfield, surface, and aerodynamic properties of Mars-entry aeroshells. The chapter also examines the effects of the PD jet configuration on the properties and deceleration performance of the aeroshell by comparing the results for central and peripheral PD jets. Finally, the chapter summarizes the important conclusions of the study.

Chapter V describes a numerical investigation of the effects of reaction control systems on Mars-entry aeroshells. The chapter first outlines the numerical setup of the study, including the aeroshell geometry and RCS jet conditions. The chapter then describes the flowfield, surface, and aerodynamic properties of the aeroshell without the RCS jet at an angle-of-attack of  $20^\circ$ . Next, the chapter provides a discussion on how the flowfield, surface, and aerodynamic properties of the aeroshell are affected by the orientation of the RCS jet by presenting the results for parallel (jet exits parallel to the freestream flow) and transverse (jet exhausts perpendicular to the freestream flow) jets at different thrust conditions. The chapter also describes the effects of the fluid interactions induced by each jet orientation on the control effectiveness of the RCS. The chapter finally outlines the major conclusions of this study.

In Chapter VI, comparisons between the numerical results and experimental measurements are carried out in order to assess the physical accuracy of the computational method. The chapter first presents comparisons of the bow shock profile for the baseline configuration (i.e. without PD or RCS jets) at  $0^\circ$  and  $20^\circ$  angles-of-attack. The chapter then provides comparisons of bow shock profile and standoff distance for the central PD jets, as well as a comparison of the aerodynamic properties calculated by LeMANS for supersonic central PD jets with previously published experimental results. The chapter then provides similar qualitative bow shock profile and standoff distance comparisons, as well as quantitative jet species mole fraction comparisons between the numerical results and experimental measurements for the peripheral PD jets. Next, the chapter presents qualitative flowfield comparisons between the numerical results and experimental visualizations for RCS jets. The chapter concludes with a summary of the important findings of these comparisons.

Finally, Chapter VII summarizes all the conclusions drawn from each chapter and highlights the major contributions of this dissertation to the investigation of fluid interactions induced by propulsive deceleration and reaction control systems for

Mars-entry aeroshells. The chapter concludes with a recommendation of possible future directions for this research topic.

## CHAPTER II

### Technical Approach

One important goal of this dissertation is to compare numerical results from CFD to experimental measurements in order to assess the physical accuracy of the computational method in predicting the fluid interactions generated by propulsive deceleration and reaction control system jets for Mars-entry aeroshells. CFD can provide valuable understanding about how these interactions are produced and their impact on the properties of the aeroshell. However, due to the complexity of these flows, more insight on the physical models employed in the computational method can be gained by comparing the numerical results to what can be observed experimentally. By utilizing both computational and experimental methods, a more complete understanding can be achieved of propulsive deceleration and reaction control systems.

Therefore, this chapter describes the experimental and numerical approaches that are used to study the fluid interactions produced by propulsive deceleration and reaction control systems for Mars-entry aeroshells. The chapter first provides details on the experimental facility at the University of Virginia and gives an overview of the experimental technique employed to obtain both flowfield visualizations and fluid property measurements (e.g. jet mole fraction). The chapter then describes the CFD code used in this work and summarizes the governing equations that are solved by the numerical method. The chapter then provides an assessment of the boundary

conditions that are implemented in the CFD method to better model the flow in the experimental facility. Finally, the chapter concludes with a summary of the important findings.

## 2.1 Experimental Setup

Experimental visualizations and measurements are obtained at a hypersonic wind tunnel facility at the University of Virginia by Reed et al. [56] and Codoni et al. [57]. The facility also employs an optical technique called planar laser-induced iodine fluorescence that is capable of producing flowfield visualizations and measurements of fluid parameters, such as mole fraction, without disturbing the flow being investigated. This section describes the facility and technique that are used to obtain experimental data that will be compared to the numerical results in Chapter VI.

### 2.1.1 Hypersonic Wind Tunnel

The hypersonic wind tunnel is a low-density facility capable of providing Mach numbers and Knudsen numbers (based on the facility orifice) up to 16 and 1, respectively [58]. The freestream flow is produced by the expansion of a jet from a reservoir through a circular orifice with a diameter of 2 mm into a continuously evacuated vacuum chamber. The chamber, which constitutes the test section, is approximately cylindrical in shape with a diameter of 914 mm and a length of approximately 1350 mm. A Stokes MicroVac Pump, a Roots Rotary Vane Booster Pump, and a Roots Rotary Vane High Pressure Pump generate the vacuum conditions in the test section. These pumps can achieve back-pressures of approximately  $5 \times 10^{-4}$  atm at a freejet total pressure of 1.8 atm [56]. The total temperature of the freejet is 297 K. The underexpanded freejet can be either pure nitrogen, or iodine-seeded nitrogen. Nitrogen gas is used in the facility because it is cost efficient and exceptionally dry, which prevents the formation of iodic acid within the facility [59]. Figure 2.1 shows

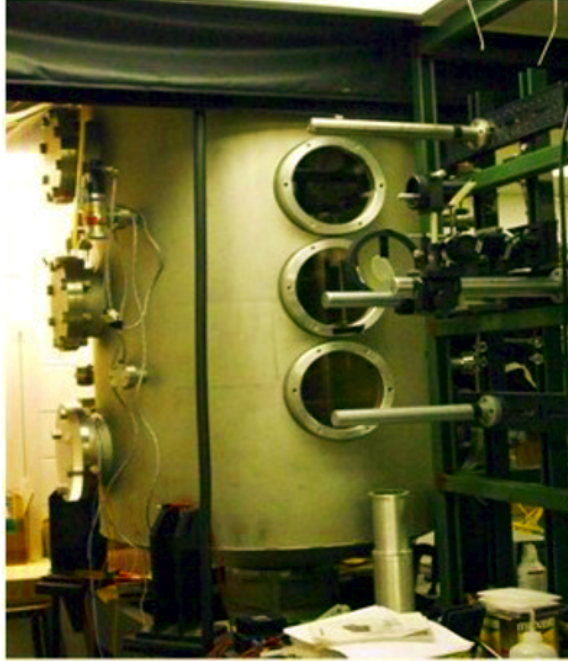


Figure 2.1: Image of the hypersonic wind tunnel at the University of Virginia. Figure from Ref. [56]

an image of the vacuum chamber [56]. The large quartz windows shown in the figure provide optical access to the underexpanded freejet flowfield.

Figure 2.2(a) shows a schematic of the experimental setup [57] and Figure 2.2(b) presents computed Mach number and Knudsen number distributions in the test section [59]. As the freejet expands through the sonic orifice, it creates a barrel shock in the vacuum chamber, which terminates at a Mach disk. Models are placed within the barrel shock at calibrated points for testing at specific Mach numbers and freestream conditions. After passing through the test section, the freejet flows through a liquid-nitrogen-cooled chevron baffle to condense the majority of the iodine from the gas before it enters the vacuum pumps. Then, the exhaust gas is passed through a charcoal filter to remove any remaining iodine particles before it leaves the facility. The gas supply in the wind tunnel is large enough to support continuous runs of about 15 hours [59]. Although this facility is capable of providing Mach numbers and Knudsen numbers that are similar to those encountered during atmospheric entry, it does not



generate enthalpy levels as high as those achieved during flights due to the relatively low stagnation temperature.

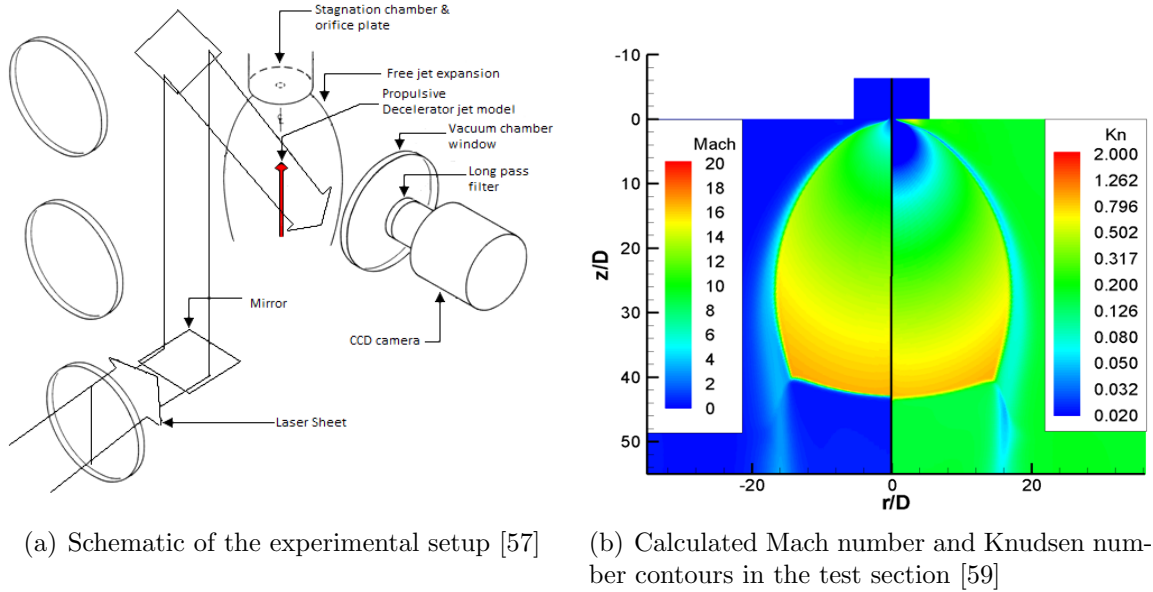


Figure 2.2: Experimental facility.

### 2.1.2 Planar Laser-Induced Iodine Fluorescence Technique

The experimental facility is capable of providing both qualitative and quantitative measurements using the planar laser-induced iodine fluorescence (PLIIF) technique. PLIIF is a non-intrusive, spatially resolved, time-averaged optical method for obtaining measurements in hypersonic flows. PLIIF has been extensively used at the University of Virginia to obtain measurements in both continuum internal flows [60, 61], and near-continuum or rarefied external flows [62, 56, 57]. Since PLIIF is an optical technique, it does not disturb the flowfield being investigated, unlike mechanical probes. PLIIF is also effective even at low flowfield densities unlike other optical methods, such as Raman scattering or Coherent Antistokes Raman Scattering [63]. PLIIF uses molecular iodine as the fluorescent gas because it is relatively easy to seed into nitrogen at room temperature. Iodine also has a dense absorption spectrum

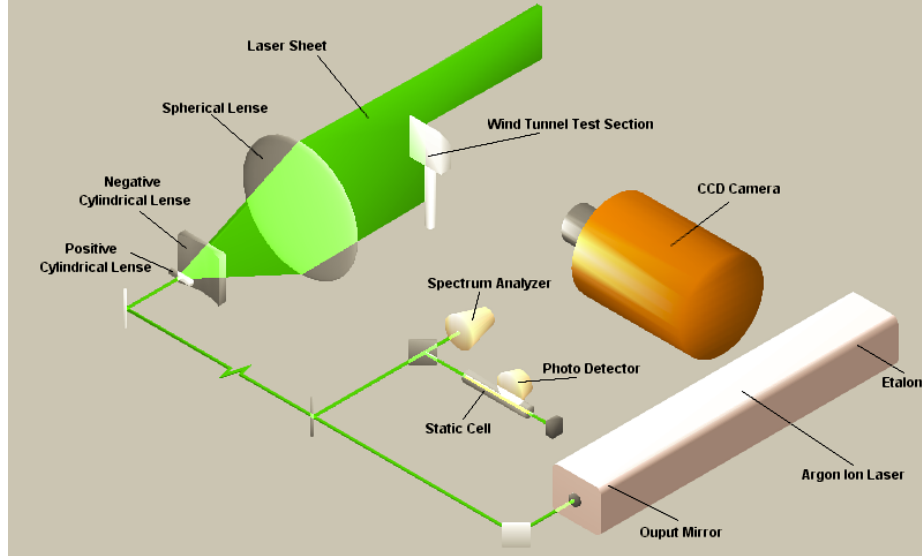


Figure 2.3: Schematic of the PLIIF setup. Figure from Ref. [63].

and fluoresces strongly in the visible [60], which does not require complicated optical systems. The iodine fluorescence can be collected using a standard scientific grade charge-coupled device (CCD) camera. Iodine, however, requires special experimental facilities and handling since it is corrosive and possibly toxic.

Figure 2.3 shows the optical setup for the PLIIF technique [63]. The main idea behind PLIIF is that when an iodine molecule is excited from a rotational and vibrational energy level in the ground state, it will return to equilibrium by emitting fluorescence. An argon ion laser operating at 514.5 nm provides the laser beam that excites the iodine. A portion of the beam is sent to the spectrum analyzer to monitor the laser frequency. The beam is then collimated into a laser sheet that is approximately 0.25 mm thick and directed into the vacuum chamber through one of the large quartz windows. The laser sheet impinges on the plane of the flowfield to be measured and the planar fluorescence is collected using an Andor iKon-L CCD camera with an array of  $2000 \times 2000$  active pixels that is perpendicular to the laser sheet [56]. The fluorescence images are time-averaged since the exposure times range from 4 to 17 seconds.

The PLIIF visualizations can be used to determine the flowfield structure and derive details about the bow shock that develops around a test-model, such as shock standoff distance. Jet mole fraction measurements can be also obtained by using two different PLIIF images [63, 64, 65]. The first image represents a PLIIF visualization with iodine seeding of the PD or RCS jet only, while the second image represents a visualization with iodine seeding of both the PD or RCS jet and the main freestream flow. The jet mole fraction is then directly proportional to the fluorescence ratio of the two images as shown in Equation 2.1,

$$X_{jet} = \frac{n_{jet}}{n_{total}} = C \cdot S_{F_{ratio}} \quad (2.1)$$

where  $X_{jet}$  is the PD or RCS jet mole fraction,  $n$  is the number density,  $S_{F_{ratio}}$  is the ratio of the fluorescence signal for the two PLIIF images, and  $C$  is a constant that is evaluated in the jet core where the mole fraction is equal to unity. This method provides quantitative jet mole fraction measurements and is valid in both viscous regions and across shock waves.

## 2.2 Navier-Stokes Solver

The main focus of this dissertation is to investigate the fluid interactions of propulsive deceleration and reaction control system jets on Mars-entry aeroshells using CFD. In order to achieve this, it is important to understand the physical and numerical models that are utilized in the computational method. Therefore, this section provides an overview of the CFD code that is used in this work and outlines the governing equations solved by the code.

### 2.2.1 LeMANS Overview

Numerical simulations are performed using the CFD code LeMANS, developed at the University of Michigan for simulating hypersonic reacting flows [66]. This general purpose, three-dimensional, parallel code solves the Navier-Stokes equations on unstructured computational grids, including thermo-chemical nonequilibrium effects with second-order spatial accuracy. The 0-equation algebraic Baldwin-Lomax turbulence model [67] is implemented in LeMANS to simulate hypersonic turbulent flows with thin attached boundary layers. The Baldwin-Lomax turbulence model, however, is not applicable to complex flows with large separation regions, and is, therefore, not used for the numerical simulations in this dissertation work. Several validation studies for LeMANS, including hypersonic capsule flows, have been conducted [66, 68, 69, 70]. In LeMANS, the flow is modeled assuming that the continuum approximation is valid and that the fluid is Newtonian. The set of partial differential equations solved by LeMANS to simulate flows with thermal nonequilibrium and finite-rate chemical reactions can be written as [66, 68, 69],

$$\frac{\partial \rho_s}{\partial t} + \nabla \cdot (\rho_s \mathbf{u} + \mathbf{J}_s) = \dot{w}_s \quad (2.2a)$$

$$\frac{\partial \rho \mathbf{u}}{\partial t} + \nabla \cdot (\rho \mathbf{u} \mathbf{u} + P \bar{\bar{I}} - \bar{\bar{\tau}}) = 0 \quad (2.2b)$$

$$\frac{\partial E}{\partial t} + \nabla \cdot \left( (E + P) \mathbf{u} - \bar{\bar{\tau}} \cdot \mathbf{u} + (\mathbf{q}_t + \mathbf{q}_r + \mathbf{q}_{ve}) + \sum_s (\mathbf{J}_s h_s) \right) = 0 \quad (2.2c)$$

$$\frac{\partial E_r}{\partial t} + \nabla \cdot \left( E_r \mathbf{u} + \mathbf{q}_r + \sum_s (\mathbf{J}_s e_{r,s}) \right) = \dot{w}_r \quad (2.2d)$$

$$\frac{\partial E_{ve}}{\partial t} + \nabla \cdot \left( E_{ve} \mathbf{u} + \mathbf{q}_{ve} + \sum_s (\mathbf{J}_s e_{ve,s}) \right) = \dot{w}_{ve} \quad (2.2e)$$

where  $\rho_s$  is the density of species  $s$ ,  $\mathbf{u}$  is the bulk velocity,  $P$  is the pressure,  $\bar{\bar{I}}$  is the identity matrix,  $h_s$  is the species enthalpy, and  $\mathbf{J}_s$  is the diffusion flux for species

$s$  modeled using a modified form of Fick's law [71].  $E$ ,  $E_r$ , and  $E_{ve}$  are the total, rotational, and vibrational-electron-electronic energies per unit volume of mixture, respectively, while  $e_{r,s}$  and  $e_{ve,s}$  are the rotational and vibrational-electron-electronic energies per unit mass, respectively.

The source term  $\dot{w}_s$  in Equation 2.2a is the species mass production and destruction rate due to chemical reactions. The term  $\dot{w}_r$  in Equation 2.2d includes the rotational energy relaxation and the gain and loss of rotational energy due to chemical reactions and can be written as [69],

$$\dot{w}_r = \sum_s (Q_{r,s}^{t-r} + \dot{w}_s e_{r,s}) \quad (2.3)$$

The rotational energy relaxation is modeled using a Landau-Teller model [72] as

$$Q_{r,s}^{t-r} = \rho_s \frac{e_{r,s}^* - e_{r,s}}{Z_{r,s} \tau_c} \quad (2.4)$$

where  $e_{r,s}^*$  is the rotational energy evaluated at the translational temperature,  $Z_{r,s}$  is the rotational collision number given in Equation 2.5, and  $\tau_c$  is the mean collision time, which is the inverse of the mean collision rate,  $\nu_s$ , shown in Equation 2.6 [73].  $Z_{r,s}$  and  $\tau_c$  together give the rotational relaxation time.

$$Z_{r,s} = \frac{Z_{r,s}^\infty}{1 + \frac{\pi^{3/2}}{2} \left(\frac{T^*}{T}\right)^{1/2} + \left(\frac{\pi^2}{4} + \pi\right) \left(\frac{T^*}{T}\right)} \quad (2.5)$$

$$\nu_s = \sum_r \left( n_r (d_{ref})_r^2 \left( \frac{8\pi k (T_{ref})_r}{m_r^*} \right)^{1/2} \left( \frac{T}{(T_{ref})_r} \right)^{1-\omega_r} \right) \quad (2.6)$$

where  $m^*$  is the reduced mass,  $k$  is the Boltzmann constant ( $1.38 \times 10^{-23}$  J/K), and  $Z_r^\infty$ ,  $T^*$ ,  $d_{ref}$ ,  $T_{ref}$ , and  $\omega$  are constants for each species and are given in Appendix A. Similarly, the source term  $\dot{w}_{ve}$  includes the energy transfer between nonequilibrium modes, the gain and loss of vibrational energy due to chemical reactions and an

approximation to the work done on electrons by the electric field induced by the electron pressure gradient. Full details of the source term in the vibrational energy equation are available in [66].

The shear stress,  $\bar{\tau}$ , is determined using Stokes' hypothesis [74],

$$\tau_{ij} = \mu \left( \frac{\partial u_j}{\partial x_i} + \frac{\partial u_i}{\partial x_j} \right) - \mu \frac{2}{3} \frac{\partial u_k}{\partial x_k} \delta_{ij} \quad (2.7)$$

where  $\mu$  is the mixture coefficient of viscosity, and  $\delta_{ij}$  is the Kronecker delta, which is equal to 1 if  $i = j$  and 0 otherwise. The heat fluxes in the energy conservation equations,  $\mathbf{q}_{t,r,ve}$ , are modeled according to Fourier's law as,

$$\mathbf{q}_{t,r,ve} = -\kappa_{t,r,ve} \nabla T_{t,r,ve} \quad (2.8)$$

where  $\kappa_{t,r,ve}$  is the mixture thermal conductivity for each energy mode. In LeMANS, the mixture transport properties can be computed using several options. In this study, Wilke's semi-empirical mixing rule [75] is used and is given in Equation 2.9,

$$\mu = \sum_s \frac{X_s \mu_s}{\phi_s} \quad \text{and} \quad \kappa = \sum_s \frac{X_s \kappa_s}{\phi_s} \quad (2.9)$$

where  $X_s$  is the mole fraction of species  $s$ ,  $\mu_s$  is the species coefficient of viscosity, and  $\kappa_s$  is the species thermal conductivity for each energy mode. The term  $\phi_s$  is given by

$$\phi_s = \sum_r X_r \left[ 1 + \sqrt{\frac{\mu_s}{\mu_r}} \left( \frac{Mw_r}{Mw_s} \right)^{1/4} \right]^2 \left[ \sqrt{8 \left( 1 + \frac{Mw_s}{Mw_r} \right)} \right]^{-1} \quad (2.10)$$

where  $Mw$  is the molecular weight. The coefficient of viscosity of each species is calculated using Blottner's curve fits [76] as

$$\mu_s = 0.1 \exp [(A_s \ln T + B_s) \ln T + C_s] \quad (2.11)$$

where  $A$ ,  $B$ , and  $C$  are constants determined for each species. The values of these constants for the species used in this study are listed in Appendix A. The coefficient of thermal conductivity for each internal energy mode can be calculated using Eucken's relation [77],

$$\kappa_{t,s} = \frac{5}{2}\mu_s C_{v_{t,s}} \quad \kappa_{r,s} = \mu_s C_{v_{r,s}} \quad \kappa_{ve,s} = \mu_s C_{v_{ve,s}} \quad (2.12)$$

where  $C_{v_{t,r,ve}}$  is the specific heat at constant volume for each internal energy mode.

The finite-volume method applied to unstructured grids is used to solve the set of governing partial differential equations. LeMANS can simulate two-dimensional and axisymmetric flows using any mixture of quadrilateral and triangular mesh cells, and three-dimensional flows using any mixture of hexahedra, tetrahedra, prisms, and pyramids. A modified Steger-Warming Flux Vector Splitting scheme is used to discretize the inviscid fluxes across cell faces, which is less dissipative and produces better results in boundary layers compared to the original scheme [78]. The viscous terms are computed using cell-centered and nodal values [79]. The boundary conditions implemented in LeMANS include pressure farfield (i.e. constant freestream conditions), supersonic pressure outlet, symmetry, and no-slip wall. Time integration in LeMANS can be performed using either an explicit, a point-implicit, or a line-implicit method with first-order accuracy. LeMANS is parallelized by domain decomposition, using METIS [80] to partition the computational mesh and the Message Passing Interface (MPI) to communicate the necessary information between processors. METIS divides the mesh such that each partition is assigned to a processor while maintaining a roughly balanced workload.

## 2.3 Numerical Boundary Conditions

CFD simulations using LeMANS of the entire experimental facility, including the aeroshell with PD and RCS jets, can be complex and computationally expensive. Therefore, the numerical cases only simulate the flow directly around the aeroshell in order to reduce computational cost and complexity. However, it is important that the conditions simulated in LeMANS match the conditions in the experimental facility since the numerical results will be compared to experimental measurements. Appropriate boundary conditions must be prescribed in the numerical simulations that accurately model the conditions of the underexpanded freejet in the experiments. This section describes how these freestream conditions are implemented in LeMANS, and how they affect the aeroshell properties compared to constant freestream conditions.

### 2.3.1 Implementation in LeMANS

In order to better simulate the flow in the experimental facility, I<sub>2</sub>-seeded N<sub>2</sub> gas is used in the numerical simulations with a seeding ratio of 200 ppm. Due to the low densities achieved in the freejet, the vibrational temperature in the numerical simulations is assumed to be frozen at the stagnation value of 297 K throughout this dissertation. The rotational temperature, on the other hand, is assumed to be different than the translational temperature. The freejet conditions in the experimental facility are modeled as freestream conditions in LeMANS using the relations of Ashkenas and Sherman [81]. These relations are based on the method of characteristics and can model both the axial and radial distributions of fluid properties in an underexpanded freejet. Based on the Ashkenas and Sherman relations, the Mach number at a distance  $z$  away from the orifice along the centerline of the freejet, shown



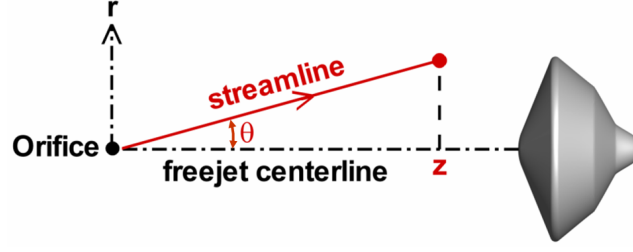


Figure 2.4: Schematic of the Ashkenas and Sherman relations.

schematically in Figure 2.4, is given by Equation 2.13,

$$M = A \left( \frac{z - z_0}{D} \right)^{\gamma-1} - \frac{1}{2} \left( \frac{\gamma + 1}{\gamma - 1} \right) \left[ A \left( \frac{z - z_0}{D} \right)^{\gamma-1} \right]^{-1} \quad (2.13)$$

where  $D$  is the diameter of the freejet orifice, and  $A$  and  $z_0/D$  are constants determined for values of the ratio of specific heats  $\gamma$ , and are equal to 3.65 and 0.40, respectively, for  $\gamma = 1.4$ . All other fluid properties along the freejet axis can be computed using the Mach number defined in Equation 2.13, the stagnation conditions of the freejet (i.e. 1.8 atm and 297 K) and the isentropic relations shown in Equation 2.14.

$$\frac{P}{P_0} = \left( 1 + \frac{\gamma - 1}{2} M^2 \right)^{\frac{-\gamma}{\gamma-1}} \quad (2.14a)$$

$$\frac{P}{P_0} = \left( \frac{\rho}{\rho_0} \right)^{\gamma} = \left( \frac{T}{T_0} \right)^{\frac{\gamma}{\gamma-1}} \quad (2.14b)$$

The density distribution at a fixed axial distance from the orifice exit is a function of the streamline angle  $\theta$  with respect to the freejet axis as shown in Equation 2.15,

$$\frac{\rho(\theta)}{\rho(0)} = \cos^2 \left( \frac{\pi\theta}{2\Phi} \right) \quad (2.15)$$

where  $\Phi$  is also a constant determined for each value of  $\gamma$ , and is equal to 1.662 for  $\gamma = 1.4$ . All other fluid properties can again be determined using the stagnation

conditions and the isentropic relations given in Equation 2.14. Note that the Ashkenas and Sherman relations assume that the flow is in thermal equilibrium (isentropic perfect gas), and, therefore, the freestream rotational and translational temperatures are set to the same value.

Table 2.1: Reference freestream conditions.

Parameter	Value
$M_{ref}$	12
$\rho_{ref}$ , kg/m <sup>3</sup>	$4 \times 10^{-4}$
$U_{ref}$ , m/s	776
$T_{ref}$ , K	10
$q_{ref}$ , Pa	127

In order to minimize the interaction between the bow shock that develops around the aeroshell and the barrel shock in the experimental facility, a reference leading-edge Mach number of 12 is used in both the experimental and numerical calculations. Based on Equation 2.13, this Mach number corresponds to placing the aeroshell approximately 42 mm away from the orifice. In order to specify this leading-edge Mach number in the numerical simulations, the distance of each cell in the upstream boundary to the orifice (i.e. the variable  $z$  in Equation 2.13) is scaled such that the distance of the leading-edge of the aeroshell to the orifice is equal to 42 mm. Using the isentropic relations and the stagnation conditions of the freejet, a set of reference freestream conditions based on this reference Mach number is used to compute non-dimensional quantities, such as the drag coefficient. These reference freestream conditions are given in Table 2.1 and are used throughout this dissertation.

Figure 2.5 shows temperature and density contours around a Mars-entry aeroshell computed by LeMANS. The freestream conditions for this simulation are calculated using the Ashkenas and Sherman relations for a leading-edge Mach number of 12. This figure illustrates the flow features generated by these freestream conditions. The flow is characterized by the bow shock that develops around the aeroshell and

the diverging streamlines that model the flow in the underexpanded freejet.

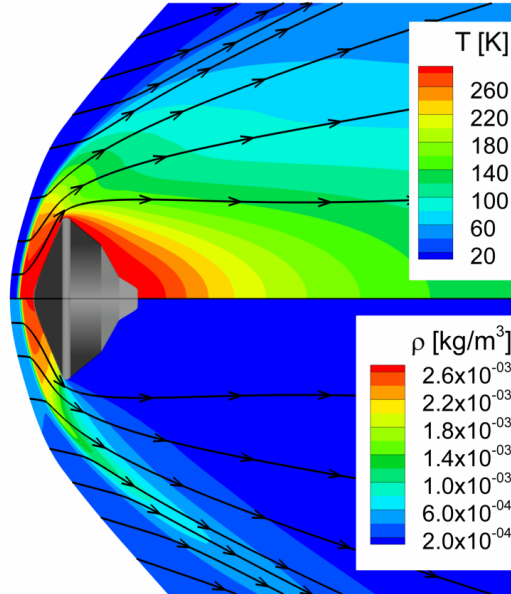


Figure 2.5: Temperature (top) and density (bottom) contours around a Mars-entry aeroshell with freestream conditions calculated using the Ashkenas and Sherman relations.

### 2.3.2 Assessment of the Ashkenas and Sherman relations

The Ashkenas and Sherman relations that are implemented in LeMANS to calculate the freestream conditions represent a convenient and inexpensive method of simulating the freejet conditions in the experimental facility. In an effort to assess the validity of the implementation of these relations in LeMANS, a numerical simulation of the entire experimental facility, including a 10 mm diameter Mars-entry aeroshell, is performed. Figure 2.6 presents the computational domain and the boundary conditions used in this simulation. Due to the symmetry of the flowfield, axisymmetric simulations are performed in order to reduce the computational cost. The stagnation conditions in the wind tunnel (i.e. 1.8 atm and 297 K) are specified at the farfield boundary. The temperature of the aeroshell and wind tunnel walls is assumed to be constant at 297 K. Since the current version of LeMANS does not include a subsonic pressure outlet boundary condition that can fix the downstream static pressure, the

back-pressure in the wind tunnel ( $5 \times 10^{-4}$  atm) is weakly imposed in the numerical simulation as the initial pressure in the computational domain. In order to reduce the effects of the supersonic pressure outlet boundary condition used in LeMANS, the computational domain is extended to 300 orifice diameters axially and over 210 orifice diameters radially.

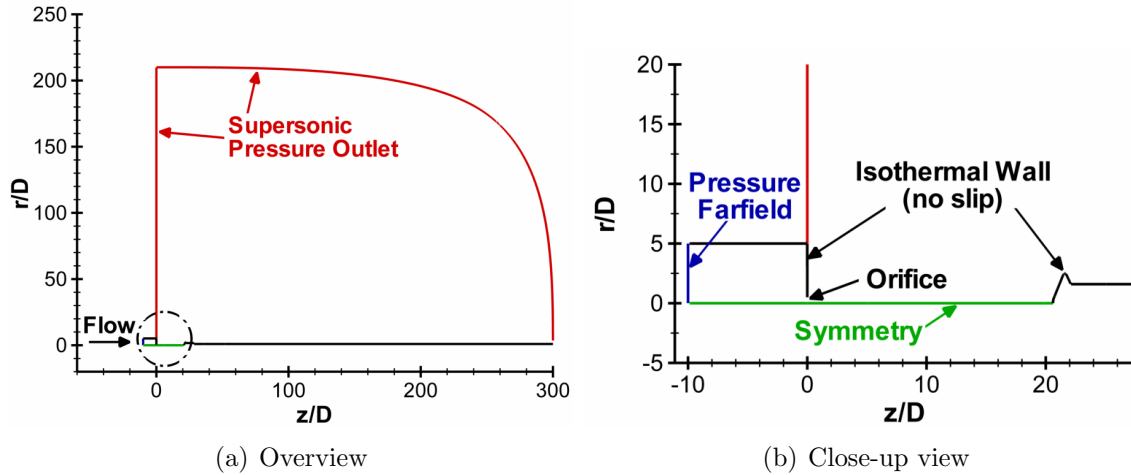


Figure 2.6: LeMANS boundary conditions for simulating the flow around a Mars-entry aeroshell in the experimental facility.

Figure 2.7 shows the final adapted grid used in the numerical simulations of the full experimental facility. The grid contains approximately 530,000 hexahedral cells with clustering near the freejet boundary and the surface of the aeroshell. The cells are manually aligned with the barrel and bow shocks based on preliminary simulations. A grid convergence study revealed that this grid size was adequate in capturing the important flowfield features and variations in the freejet and near the aeroshell. Due to the geometry of the computational domain, a point-implicit time integration method is used to march the solution to steady-state. This simulation takes approximately 2,850 CPU-hours, or 65,000 iterations, to reach a steady-state solution.

Figure 2.8 shows Mach number contours and velocity streamlines calculated by LeMANS in the experimental facility. The bottom half of the figure is a reflection of the top half for illustrative purposes, since these simulations are axisymmetric. The

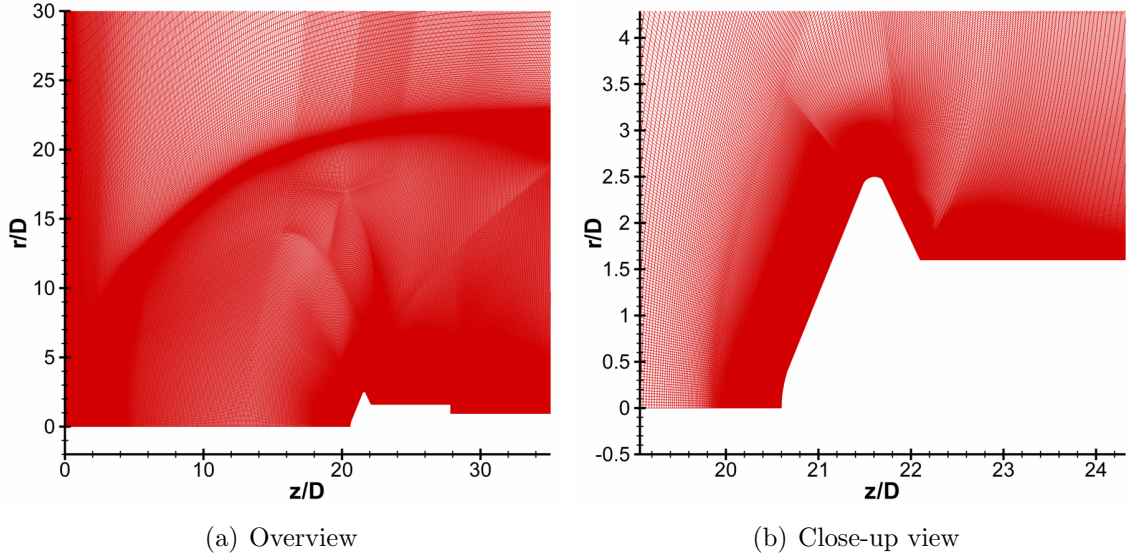


Figure 2.7: Computational grid for simulating the flow around a Mars-entry aeroshell in the experimental facility.

flow expands from sonic conditions at the orifice to Mach numbers as high as 15 in the test section. Upstream of the aeroshell centerline, the Mach number is slightly below the leading-edge reference Mach number of 12. A barrel shock develops at the entrance of the test section because the pressure of the underexpanded supersonic/hypersonic freejet is higher than the back-pressure in the facility. The barrel shock interacts with the bow shock around the capsule at approximately 15 orifice diameters downstream of the aeroshell. This interaction creates a third shock that links the barrel and bow shocks and is almost normal to the freejet flow. The streamlines in Figure 2.8(b) show a recirculation region in the wake downstream of the aeroshell that is characterized by relatively small Mach numbers (less than 0.5).

Due to the low densities achieved by the freejet in the experimental facility, rarefied flow regions can develop where the continuum approximation of the CFD method may become invalid. The gradient-length local Knudsen number [82, 83] can be used as a parameter to determine where continuum breakdown occurs in the numerical results

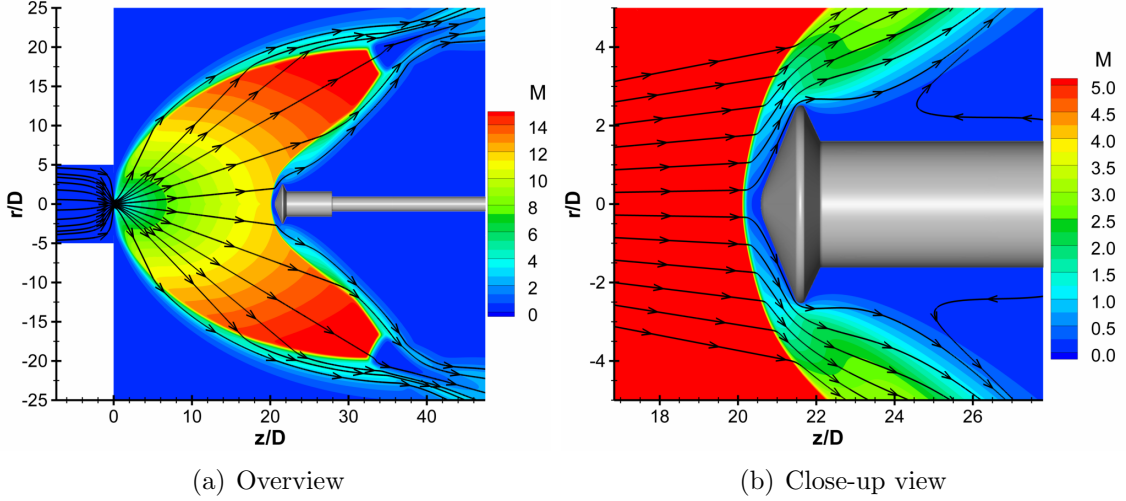


Figure 2.8: Mach number contours and velocity streamlines calculated by LeMANS around a Mars-entry aeroshell in the experimental facility.

and is defined as,

$$Kn_{GLL} = \max \left( \lambda \left| \frac{\nabla Q}{Q} \right| \right) \quad (2.16)$$

where  $\lambda$  is the local mean free path and  $Q$  is a flow quantity of interest: density, speed, and translational temperature. Previous studies found that for  $Kn_{GLL}$  values above 0.05, continuum breakdown may occur and the Navier-Stokes equations may not provide physically accurate solutions in those regions of the flow [82, 84]. This parameter is different than the Knudsen number shown in Figure 2.2(b) because it uses local fluid properties, instead of global properties (e.g. reference length scale) to determine continuum breakdown. The distribution of the local Knudsen number calculated by LeMANS in the test section is presented in Figure 2.9. The figure shows that most of the freejet flow is in the continuum regime. However, continuum breakdown may occur in certain regions of the test section. These regions include the barrel and bow shocks due to sharp gradients in the fluid properties, around the aeroshell shoulder due to the high flow expansion, and in the wake due to relatively low densities.

One of the assumptions of the Ashkenas and Sherman relations is that the flow is in

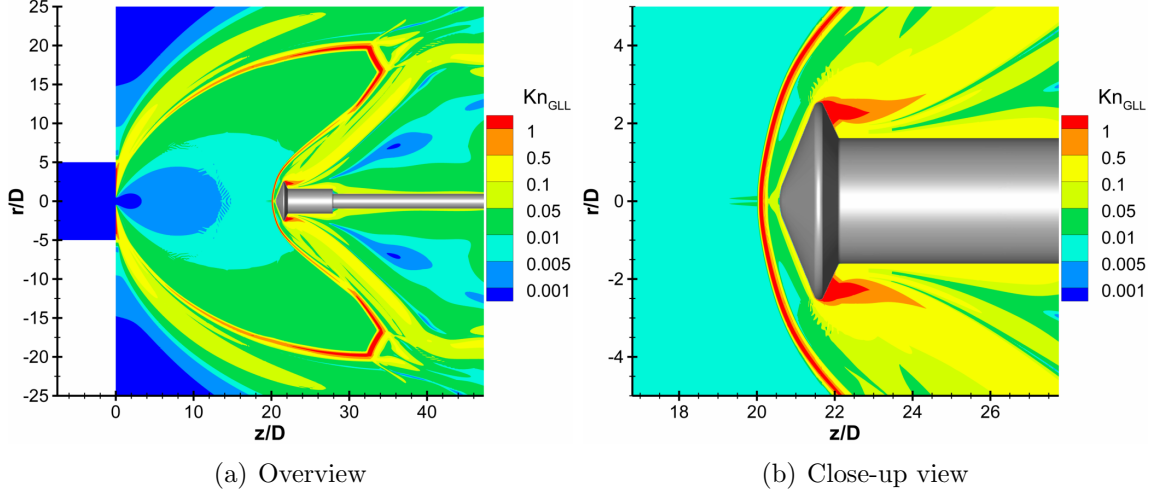


Figure 2.9: Gradient-length local Knudsen number contours calculated by LeMANS around a Mars-entry aeroshell in the experimental facility.

thermal equilibrium (isentropic perfect gas). However, strong thermal nonequilibrium effects may be present in the experimental facility due to the low densities achieved by the underexpanded freejet, which can cause the distributions of the translational and rotational temperatures to be different. The axial and radial distributions of the translational and rotational temperatures calculated by LeMANS in the freejet are presented in Figure 2.10. The figure shows very close agreement between the two temperature modes, which suggests that thermal nonequilibrium effects in the freejet are negligible. Therefore, the assumption that the translational and rotational temperatures are equal in the experimental facility upstream of the bow shock (i.e. freestream conditions) is valid.

Figure 2.11 presents axial ( $z/D$  at  $r/D = 0$ ) and radial ( $r/D$  at  $z/D = 15$ ) Mach number, translational temperature, and density distributions calculated by LeMANS in the experimental facility. The figure also compares the numerical results to the corresponding distributions given by the Ashkenas and Sherman relations (i.e. Equations 2.13 and 2.15). The plots show very good agreement between the numerical results and the Ashkenas and Sherman relations along the freejet centerline. The comparisons along the radial line, however, indicate large differences, with a maxi-

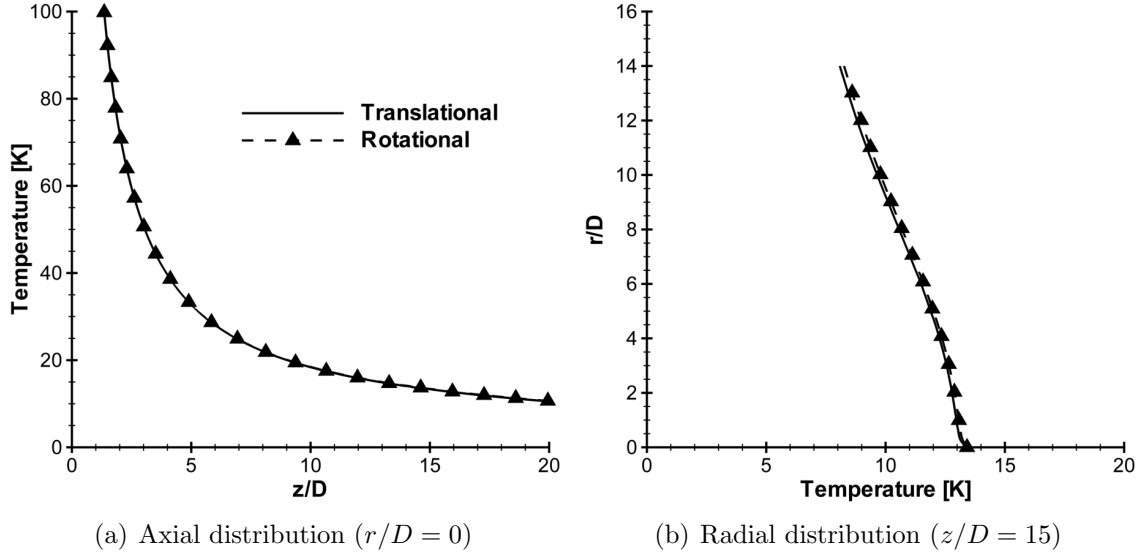


Figure 2.10: Comparison of translational and rotational temperature distributions computed by LeMANS in the experimental facility.

imum of approximately 14% in Mach number, 26% in temperature, and 82% in density, between the two sets of results. The differences in the radial distributions could be caused by several factors. The first factor is that the Ashkenas and Sherman relations may not be appropriate for streamline angles (i.e.  $\theta$  in Equation 2.15) greater than  $10^\circ$  [85]. At  $z/D = 15$ , a streamline angle of  $10^\circ$  corresponds to  $r/D = 2.6$ . At this radial location (i.e. 2.6), the difference between the numerical results and the Ashkenas and Sherman relations is approximately 1.5% for Mach number, 3% for temperature, and 13% for density. Another possible source for the disagreement in the radial distributions between the numerical results and the Ashkenas and Sherman relations is the boundary conditions in LeMANS, namely the supersonic pressure outlet and the pressure farfield, which may have an effect on the numerical solution.

The implementation of the Ashkenas and Sherman relations in LeMANS can be assessed by comparing the numerical results for the experimental facility to the results for the flow around the same aeroshell with freestream conditions calculated using the Ashkenas and Sherman relations. Figure 2.12 presents the boundary conditions and computational mesh for the axisymmetric simulation that uses the Ashkenas



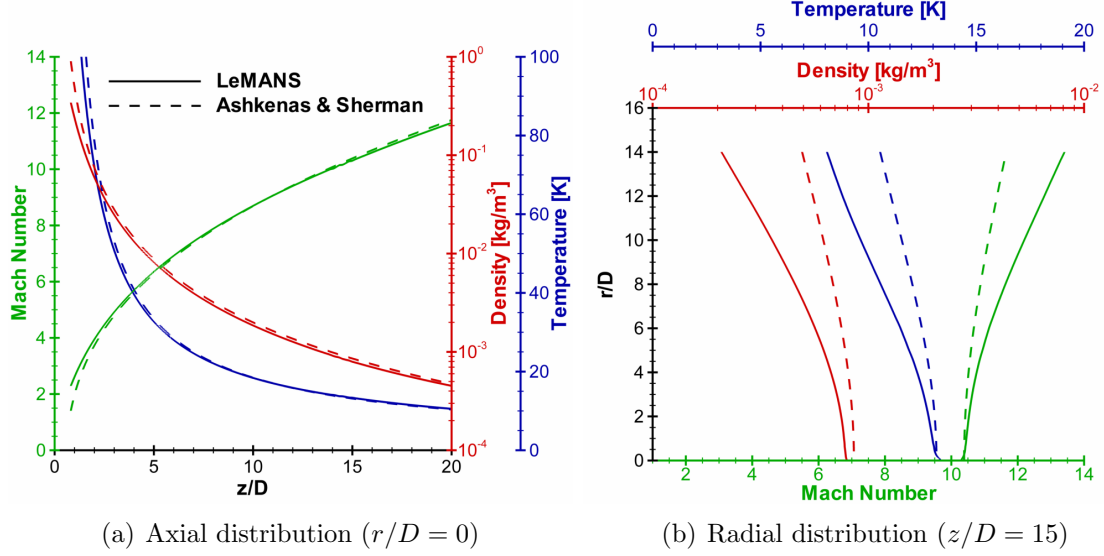


Figure 2.11: Comparison of the axial and radial Mach number, temperature, and density distributions calculated by LeMANS in the experimental facility and the Ashkenas and Sherman relations.

and Sherman-derived freestream conditions. The aeroshell wall is assumed to be at a constant temperature of 297 K. A grid convergence study showed that a mesh size of about 71,000 cells can adequately capture the flowfield features and aeroshell properties. This grid is approximately 7 times smaller than the mesh for the full experimental facility simulation. A line-implicit time integration method is used to march the solution to steady-state. This simulation takes approximately 32 CPU-hours, or 8000 iterations, to reach a steady-state solution, which is over 80 times faster than the full facility simulation. For the remainder of this section, the full experimental facility simulation will be referred to as the **EF** case and the simulation with the Ashkenas and Sherman-based freestream conditions will be addressed as the **AS** case.

Figure 2.13 presents Mach number and pressure contours for the **EF** (top) and **AS** (bottom) simulations. The figure shows overall close agreement between the two sets of results in the flowfield variations of Mach number and pressure, as well as the bow shock profile and standoff distance. However, there are some discrepancies between

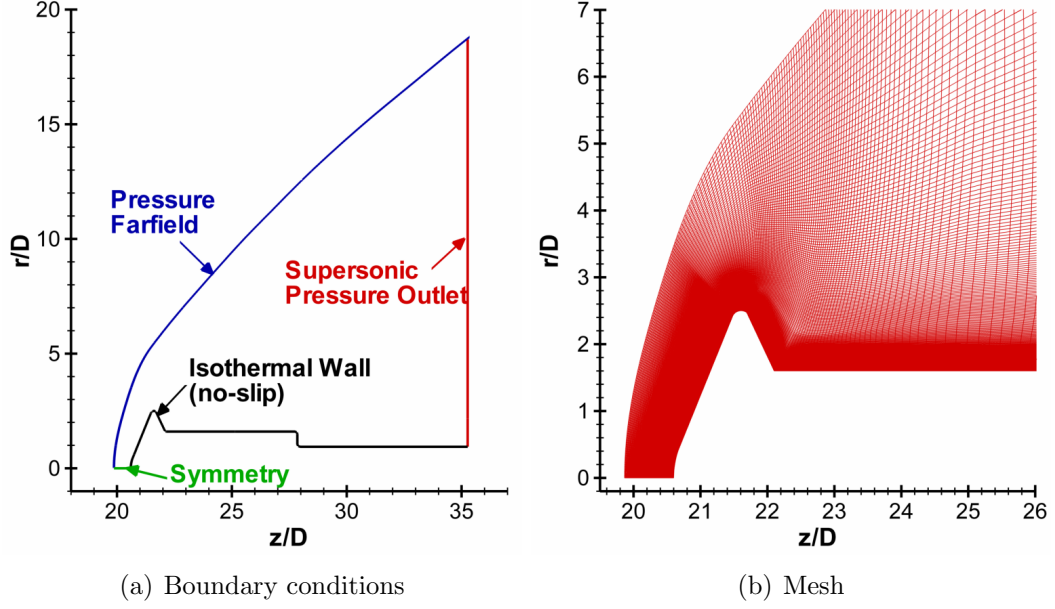


Figure 2.12: Boundary conditions and mesh for simulating flow around a Mars-entry aeroshell with Ashkenas and Sherman-derived freestream conditions.

the two cases. In the wake downstream of the aeroshell, the streamlines in Figure 2.13(a) indicate a recirculation region in the **EF** case that does not exist in the **AS** case. Due to this recirculation region, the contours show overall lower Mach numbers and higher pressures in the wake for **EF** simulation. The contours also show that the pressure along the forebody for the **AS** case is slightly higher, which is caused by the differences in the radial distributions of fluid properties between the Ashkenas and Sherman relations and the freejet conditions, as shown in Figure 2.11(b).

The aeroshell surface properties for the **EF** and **AS** simulations are shown in Figure 2.14. The surface properties are presented as non-dimensional pressure and skin friction coefficients calculated based on the reference freestream conditions given in Table 2.1 using Equations 2.17 and 2.18, respectively,

$$C_P = \frac{P}{(1/2) \rho_{ref} U_{ref}^2} \quad (2.17)$$

$$C_f = \frac{\tau}{(1/2) \rho_{ref} U_{ref}^2} \quad (2.18)$$

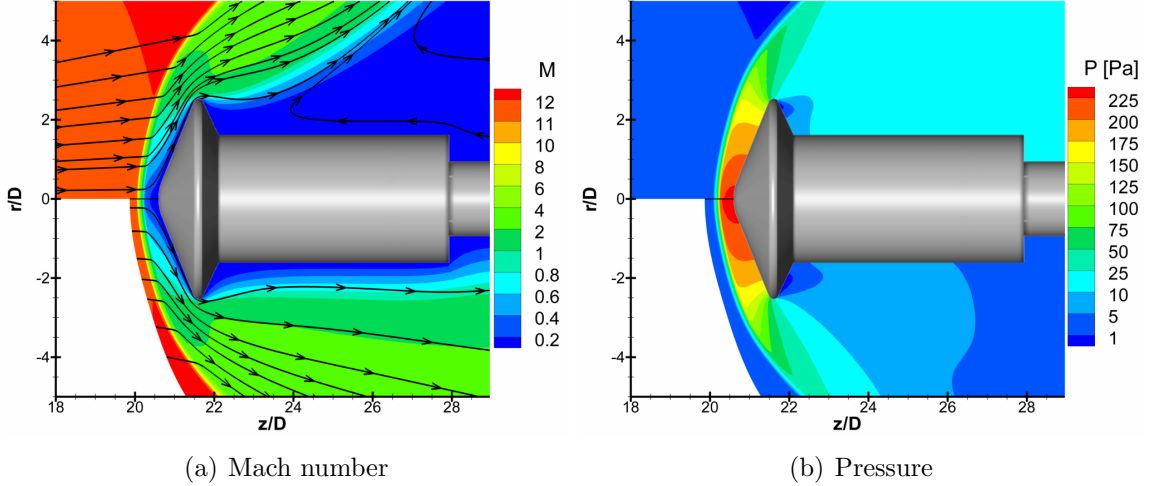


Figure 2.13: Comparison of Mach number and pressure contours around a Mars-entry aeroshell for the experimental facility simulation (top) and the simulation with the Ashkenas and Sherman-derived freestream conditions (bottom).

The figure shows overall close agreement between the two simulations, particularly with respect to the shear stress. However, Figure 2.14(a) shows that the overall pressure distribution along the forebody for the **AS** simulation is higher than the **EF** case, with a maximum difference of approximately 6% between the two sets of results. The plot also shows that the **AS** case predicts a 2% larger stagnation pressure compared to the **EF** simulation. These differences in the surface properties may also be caused by the numerical boundary conditions used in the full facility simulation and by possible inaccuracy of the Ashkenas and Sherman relations for large streamlines angles. As a result of the disagreement in the surface properties, the drag coefficient of the aeroshell, calculated using Equation 2.19, is approximately 7.5% larger for the **AS** simulation ( $C_D = 1.55$ ) than for the **EF** simulation ( $C_D = 1.44$ ). Even with these differences, however, the Ashkenas and Sherman relations still provide an attractive alternative to simulating the flow in the entire experimental facility. These relations reduce the grid size and computational runtime by a factor of 7 and 80, respectively, for these axisymmetric simulations. The computational savings by

the Ashkenas and Sherman relations are expected to increase for the simulations of complex, three-dimensional flows with PD and RCS jets.

$$C_D = \frac{F_D}{(1/2) \rho_{ref} U_{ref}^2 S} \quad (2.19)$$

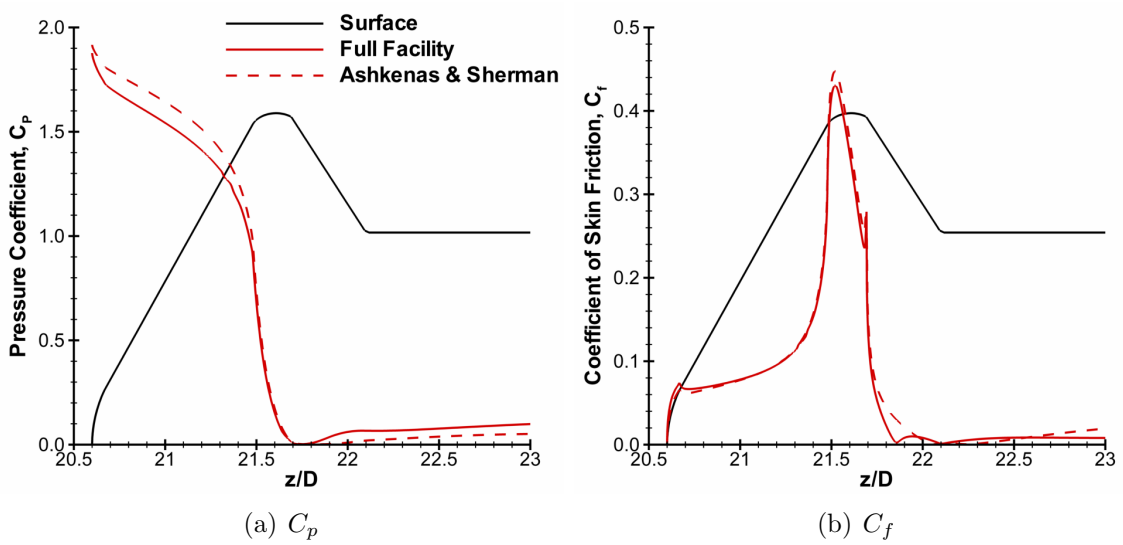


Figure 2.14: Comparison of pressure and skin friction coefficients for a Mars-entry aeroshell in the underexpanded freejet and in freestream conditions provided by the Ashkenas and Sherman relations.

### 2.3.3 Effects of the Ashkenas and Sherman relations

The Ashkenas and Sherman relations provide freestream conditions in LeMANS that simulate the freejet conditions in the experimental facility. However, it is important to understand how these nonuniform freestream conditions affect the properties of the aeroshell as compared to constant freestream conditions, which are typically used to simulate hypersonic entry flows. This can be achieved by comparing the numerical results for the Ashkenas and Sherman freestream conditions to the results for constant freestream conditions that are equal to the reference conditions given in Table 2.1 (i.e. Mach 12 flow). A scaled version of the MSL aeroshell is used for these simulations and is shown in Figure 2.15. The diameter of the aeroshell is equal

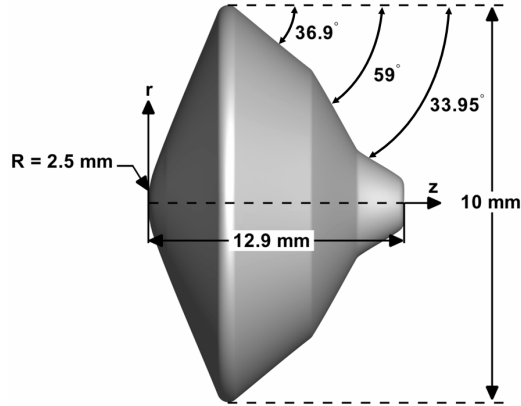


Figure 2.15: Geometry for the 10 mm diameter MSL-based aeroshell.

to 10 mm, which is equivalent to approximately 0.22% of the diameter for the MSL capsule. The grid size, based on a grid convergence study, for both simulations is approximately equal to 71,000 cells and each case takes roughly 32 CPU-hours using a line-implicit time integration method to reach a steady-state solution.

The flowfield Mach number and pressure distributions for the constant and the Ashkenas and Sherman freestream conditions are shown in Figure 2.16. The axial and radial distances are normalized by the aeroshell diameter (i.e.  $D_{model} = 10$  mm). The contours show overall similar flowfield structures for the two sets of results. However, the Ashkenas and Sherman freestream conditions reduce the bow shock standoff distance near the stagnation point and broaden the shock profile (i.e. larger distance from the aeroshell shoulder to the shock). The pressure contours in Figure 2.16(b) indicate that the bow shock strength decays faster for the Ashkenas and Sherman freestream conditions downstream of the capsule due to the diverging streamlines, as well as the interaction of the shock with a stronger expansion wave around the aeroshell shoulder.

Due to the similarities in the pressure variation upstream of the aeroshell, the surface properties for the two sets of freestream conditions can also be expected to be in close agreement. Indeed, the pressure distribution on the surface, which is presented as non-dimensional pressure coefficient in Figure 2.17(a), follows a similar

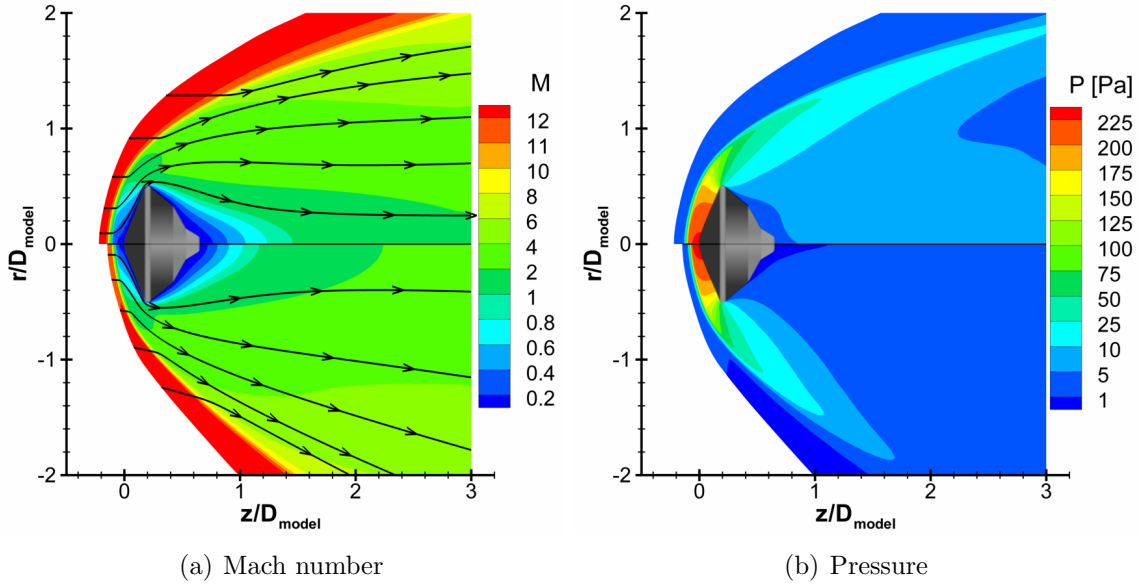


Figure 2.16: Comparison of Mach number and pressure contours around a Mars-entry aeroshell with constant (top) and Ashkenas and Sherman-derived (bottom) freestream conditions.

trend for both the constant and Ashkenas and Sherman freestream conditions. The figure shows that the stagnation pressure for the Ashkenas and Sherman conditions is approximately 5% larger than for the uniform freestream conditions due to the smaller bow shock standoff distance. However, downstream of the stagnation point along the aeroshell forebody, the pressure for the Ashkenas and Sherman conditions becomes lower than for the constant freestream conditions by roughly 4%. This is a consequence of the expanding freestream flow in the Ashkenas and Sherman case, which decreases the pressure away from the aeroshell centerline. The post-shock pressure for the Ashkenas and Sherman freestream conditions also decreases radially since the angle of the freestream flow with respect to the bow shock increases (i.e. more oblique shock). The overall similarities between the solution for the constant and the Ashkenas and Sherman freestream conditions also extend to the shear stress along the surface, plotted in Figure 2.17(b) as non-dimensional coefficient of skin friction. The figure, however, shows that the shear stress along the forebody is greater for the

Ashkenas and Sherman freestream conditions than the uniform conditions by as much as 50%. This difference can also be attributed to the radial variation of the freestream flow in the Ashkenas and Sherman relations. As a result of these discrepancies in the surface properties, the Ashkenas and Sherman freestream conditions cause approximately a 2% decrease in the drag coefficient of the aeroshell compared to the constant conditions.

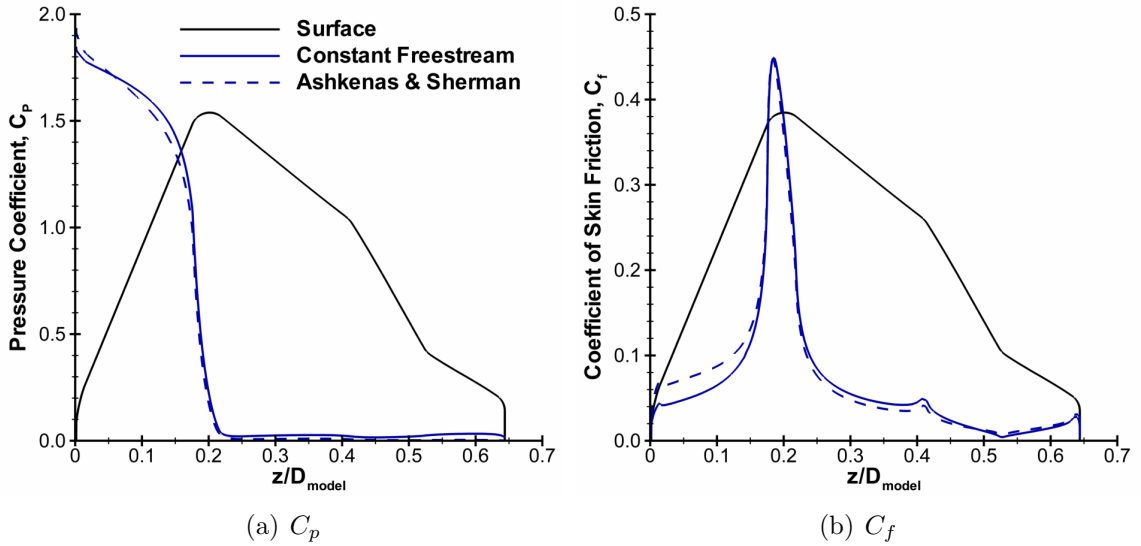


Figure 2.17: Comparison of pressure and skin friction coefficients for a Mars-entry aeroshell with constant and Ashkenas and Sherman-derived freestream conditions.

## 2.4 Summary

This chapter described the experimental facility and technique utilized at the University of Virginia to obtain flowfield visualizations and measurements of hypersonic flow around a Mars-entry aeroshell with propulsive deceleration and a reaction control system. The experiments are conducted in a low-density wind tunnel facility that is capable of providing Mach numbers up to 16. The hypersonic flow in this facility is produced by the expansion of a freejet through a thin sonic orifice. Experimental results are obtained using the PLIIF technique, which is a non-intrusive,

spatially-resolved, and time-averaged optical method. The chapter also described the numerical method used in this dissertation work to study the fluid interactions generated by propulsive deceleration and reaction control systems for Mars-entry aeroshells. The numerical simulations are performed using the parallel CFD code LeMANS, which solves the Navier-Stokes equations and can account for thermochemical nonequilibrium effects.

In order to better simulate the flow in the experimental facility, I<sub>2</sub>-seeded N<sub>2</sub> gas is used in the numerical simulations with a seeding ratio of 200 ppm. The Ashkenas and Sherman relations were implemented in LeMANS to calculate the freestream conditions in the numerical simulations. These relations model the axial and radial distributions of fluid properties in an underexpanded freejet, and can decrease the computational cost and complexity by reducing the need to simulate the entire experimental facility. The implementation was assessed by comparing the results for an axisymmetric simulation of a Mars-entry aeroshell in the experimental facility to the results for an axisymmetric simulation of the same aeroshell with freestream conditions given by the Ashkenas and Sherman relations. The flowfield, surface, and aerodynamic properties of the aeroshell for the two cases were overall similar, with small disagreement in the flowfield and surface distributions that caused a 7% difference in the aeroshell drag coefficient. This disagreement could be attributed to the numerical boundary conditions used in the full facility simulation and the fact that the Ashkenas and Sherman relations may not be appropriate for large streamline angles. The numerical results for the full experimental facility simulation also showed that thermal nonequilibrium effects in the freejet are negligible and the isentropic perfect gas assumption of the Ashkenas and Sherman relations is valid for these types of flows. The Ashkenas and Sherman relations were found to be an attractive alternative for simulating the flow in the entire experimental facility because they reduced the grid size and computational runtime by a factor of 7 and 80, respectively,



for axisymmetric simulations. These savings are expected to further increase for the simulations of complex, three-dimensional flows with PD and RCS jets.

The effects of the axial and radial fluid variations of the Ashkenas and Sherman relations were also examined by comparing the numerical results of flow over an MSL-based aeroshell with Ashkenas and Sherman freestream conditions to the results for constant freestream conditions. The Ashkenas and Sherman freestream conditions were found to decrease the bow shock standoff distance near the stagnation point and broaden the shock profile around the aeroshell. The Ashkenas and Sherman relations were also shown to decrease the overall pressure distribution along the aeroshell forebody, and consequently, decrease the drag coefficient of the aeroshell by 2%.

## CHAPTER III

# Central Propulsive Deceleration

Propulsive deceleration involves directing engine thrust into an incoming hypersonic or supersonic freestream. It is currently being considered as an enabling technology to slow future, high-mass, Mars-entry vehicles during atmospheric descent [25, 27]. The central configuration represents one possible layout of propulsive decelerator jets, in which a single thruster is placed at the center of the aeroshell forebody. Several studies, both recent and from the 1960s and 1970s, have investigated the fluid interactions produced by sonic or supersonic central PD jets exhausting into a supersonic freestream (i.e. supersonic retropropulsion). However, current plans for future Mars EDL architectures include an all-propulsive option that may require the use of central PD jets in hypersonic conditions [25]. As a result, it is important to understand the fluid interactions produced by central jets in a hypersonic freestream, and how the conditions of the PD jet influence these interactions.

This chapter outlines a numerical investigation conducted using the CFD code LeMANS to study the effects of central PD jets on the flowfield, surface, and aerodynamic properties of an MSL-based aeroshell in hypersonic freestream conditions. The chapter first outlines the numerical setup used in this study, including the aeroshell geometry and PD jet conditions. The chapter then presents the flowfield features generated by sonic, central PD jets and describes the fluid interactions induced by

these jets for various PD thrust conditions. The results for this configuration are then used to study how the jet Mach number for the central configuration affects these fluid interactions by comparing the flowfield, surface, and aerodynamic properties of the aeroshell with sonic and supersonic PD jets. Finally, a summary of the important conclusions from the study on central PD jets is presented.

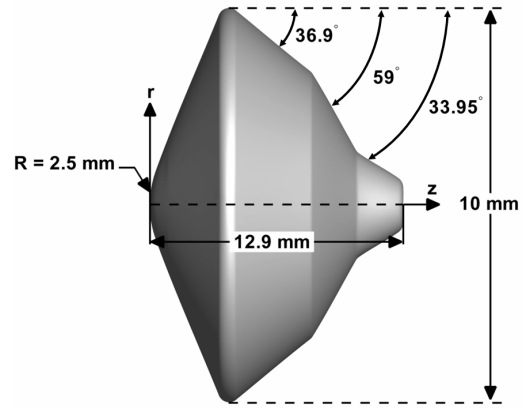
### 3.1 Numerical Setup

The conditions simulated by LeMANS in this work are based on the conditions used in experiments at the University of Virginia in order to compare the numerical results with experimental measurements. As previously described in Chapter II, the freestream conditions in LeMANS are provided by the Ashkenas and Sherman relations, which simulate the freejet conditions in the experimental facility. These relations can greatly reduce the complexity and cost of the numerical simulations of Mars-entry aeroshells with central PD jets. The aeroshell models are positioned in the experimental test section such that the Mach number at the leading-edge of the model is equal to 12. This position minimizes the interaction of the bow shock around the aeroshell and the barrel shock that develops in the wind tunnel. The leading-edge Mach number (for the aeroshell with the PD jet) is also used to compute a set of reference freestream conditions given in Table 2.1 that are used to calculate non-dimensional quantities, such as drag coefficient. In order to better match the conditions in the experimental facility, I<sub>2</sub>-seeded N<sub>2</sub> gas with a seeding ratio of 200 ppm is used as both the freestream and the PD jet gas in the numerical simulations. This section describes the aeroshell geometry and the conditions of the central PD jet used in this numerical investigation.

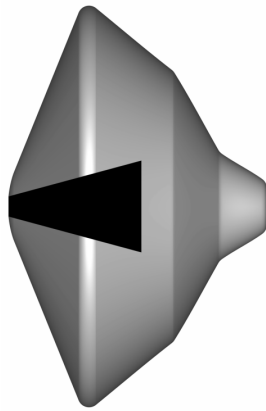
### 3.1.1 Aeroshell Geometry

The geometry of the aeroshell with the sonic and supersonic central PD jets is shown in Figure 3.1. The aeroshell is based on the MSL capsule and is similar to the test models used in the experiments. The aeroshell diameter is 10 mm, which is equivalent to approximately 0.22% the size of the MSL capsule. This diameter is chosen to further minimize the interaction of the bow shock and the barrel shock in the experiments. The Reynolds number and global Knudsen number based on the aeroshell diameter and the reference freestream conditions are 1,200 and 0.015, respectively, which suggest that the freestream flow is laminar and in the near-continuum regime. The PD jet is located at the center of the aeroshell forebody. A cross-sectional view of the aeroshell with the sonic central PD jet is given in Figure 3.1(b). The PD nozzle-exit diameter for the sonic jet is equal to 0.5 mm. Figure 3.1(c) shows a cross-sectional view of the aeroshell with the supersonic central PD jet. The throat and exit diameters of the PD nozzle are approximately 0.5 mm and 0.9 mm, respectively, which correspond to a design nozzle-exit Mach number of 2.66.

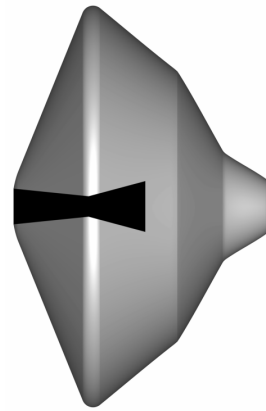
Due to the symmetry of the flowfield, axisymmetric simulations are performed using LeMANS in order to reduce the computational cost. The computational grids contain quadrilateral cells because the numerical results are sensitive to the alignment of the grid with the bow shock. These grids are adapted by hand from preliminary simulations in order to align the upstream boundary of the computational domain with the bow shock. Details regarding the adaptation process are provided in Appendix B. Cells are clustered near the wall and in the vicinity of the PD jet upstream of the aeroshell. The grid size varies from about 80,000 cells to approximately 110,000 cells based on the conditions of the PD jet. Figure 3.2 shows the computational mesh for the sonic and supersonic central PD jets at the lowest thrust conditions investigated in this study. The average computational runtime for these simulations is approximately 240 CPU-hours with about 12 Intel Xeon X5670 (Westmere) processors using



(a) Aeroshell geometry



(b) Sonic PD jet



(c) Supersonic PD jet

Figure 3.1: Aeroshell geometry with sonic and supersonic central PD jets.

a point-implicit time integration method.

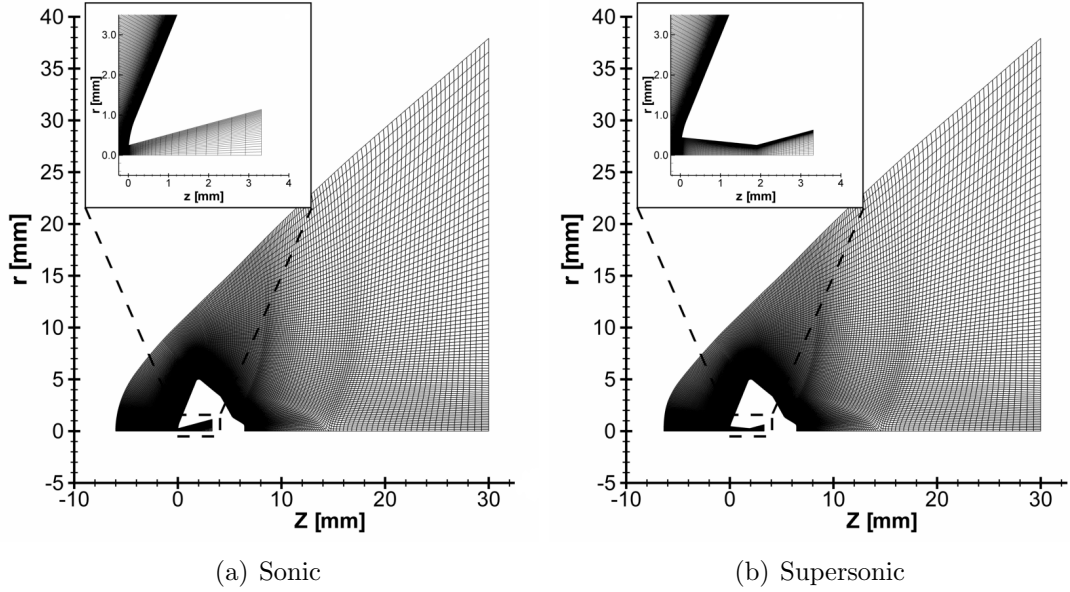


Figure 3.2: Computational mesh for sonic and supersonic central PD jets.

### 3.1.2 PD Jet Conditions

The boundary conditions for the PD jet are computed such that either sonic or supersonic conditions are obtained at the nozzle-exit using the isentropic relations. These conditions are non-dimensionalized using the thrust coefficient in order to compare the numerical results with experimental data from current and previous work. The thrust coefficient is defined as the ratio of the thrust force to the product of the dynamic pressure in the freestream and the aeroshell frontal area. This can be expressed as [20],

$$C_T = \frac{F_T}{q_{ref}S} = \left( 2 \frac{q_e}{q_{ref}} + \frac{P_e}{q_{ref}} - \frac{P_{amb}}{q_{ref}} \right) \left( \frac{S_e}{S} \right) \quad (3.1)$$

where  $P_{amb}$  is the post-bow-shock static pressure since the PD jet is exhausting into the flow that is downstream of the bow shock. The thrust coefficient can be also

expressed in terms of the mass flow rate from the PD nozzle as,

$$C_T = \frac{\dot{m}U_e + (P_e - P_{amb})S_e}{q_{ref}S} \quad (3.2)$$

Tables 3.1 and 3.2 present the design total pressure ratio, Reynolds number, and mass flow rate based on the nozzle-exit properties for the thrust coefficient values investigated in this study. The stagnation temperature of the PD jet is 297 K, which is equal to the value for the main freestream flow. The tables show that the mass flow rate at each thrust coefficient for the supersonic jets is about 15% lower than for the sonic jets, which can be an advantage since the required propellant mass for the supersonic jets at given thrust conditions could potentially be lower. The flow from the PD nozzle can also be assumed to be laminar because the jet Reynolds number for all the cases is less than  $10^4$  [86].

Table 3.1: Design conditions for sonic central PD jets.

$C_T$	$P_{0,jet}/P_0$	$Re$	$\dot{m}$ , mg/s
0.5	0.11	1,200	9.4
1.0	0.22	2,500	19
1.5	0.33	3,500	28
2.0	0.44	4,500	37
2.5	0.55	6,500	46

Table 3.2: Design conditions for supersonic central PD jets.

$C_T$	$P_{0,jet}/P_0$	$Re$	$\dot{m}$ , mg/s
0.5	0.09	1,000	7.9
1.0	0.18	2,000	16
1.5	0.27	3,100	24
2.0	0.36	4,100	31
2.5	0.45	5,100	39

The boundary conditions for the PD jet at a given thrust coefficient are computed using the isentropic relations such that the Mach number at the nozzle-exit is equal

to 1.0 for the sonic jets and 2.66 for the supersonic jets. However, due to viscous effects in the boundary layer along the nozzle walls, the actual Mach number at the nozzle-exit may be lower than the design value. Figure 3.3 presents Mach 1.0 and 2.66 contours in the PD nozzle for the sonic and supersonic central jets. Figure 3.3(a) indicates that the nozzle-exit Mach number for the sonic jet is approximately equal to the design value of 1.0. Figure 3.3(b), however, shows that the Mach number at the nozzle-throat for the supersonic jet is slightly less than 1.0 (approximately 0.8) for both thrust coefficients. The actual Mach number at the nozzle-exit for the supersonic jet is also lower than the design value of 2.66 by about 14% for both thrust conditions. Figure 3.3(b) also shows that the boundary layer thickness along the nozzle wall for the supersonic jet is smaller for  $C_T = 2.5$  than for  $C_T = 0.5$  by as much as 50% due to a larger favorable pressure gradient. The discharge coefficient of the nozzle, defined as the ratio of actual to design mass flow rate, is approximately equal to 0.93 and 0.94 for the sonic and supersonic central PD jets, respectively, as a result of the viscous effects along the nozzle walls.

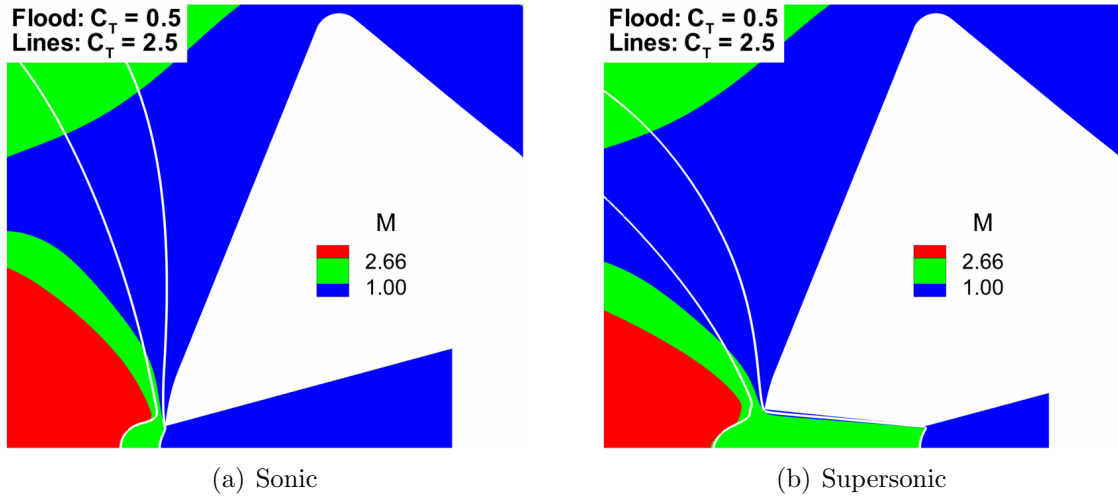


Figure 3.3: Mach number distribution in the nozzle for sonic and supersonic central PD jets.



## 3.2 Sonic PD Jets

This section describes the interactions generated by sonic central PD jets and their influence on the flowfield, surface, and aerodynamic properties of the aeroshell. The results presented in this section will also be used to understand how the PD jet Mach number and configuration affect the properties and deceleration performance of Mars-entry capsules.

### 3.2.1 Flowfield Features

Figure 3.4 presents Mach number contours for the 0.5 thrust coefficient conditions in order to illustrate the flow features generated by the sonic central PD jets. The jet expands from sonic conditions at the nozzle-exit to higher Mach numbers (i.e. supersonic) upstream of the aeroshell. The flow then first decelerates from supersonic to subsonic velocities through a jet shock, and then from subsonic to zero velocity at a stagnation point detached from the surface of the aeroshell. The freestream also decelerates from hypersonic to subsonic velocities through a bow shock and then to zero velocity at the same stagnation point. The PD jet mixes with the freestream flow in an interface region between the bow and jet shocks where the static pressures of the two streams become equal. The two streams then flow downstream of the aeroshell to the wake. The velocity streamlines indicate that the apparent size of the aeroshell perceived by the freestream flow increases due to the PD jet. The streamlines also show a region of separated flow between the PD jet boundary, the surface of the capsule and the mixed outflow, with a reattachment point near the shoulder of the aeroshell.

Mach number contours for PD nozzle thrust coefficient values of 0.5, 1.0, 2.0, and 2.5 are presented in Figure 3.5. The figure shows that the PD jet expands from sonic conditions at the nozzle-exit to supersonic conditions for all four thrust coefficients. The PD jet then decelerates to zero velocity at a detached stagnation point, first

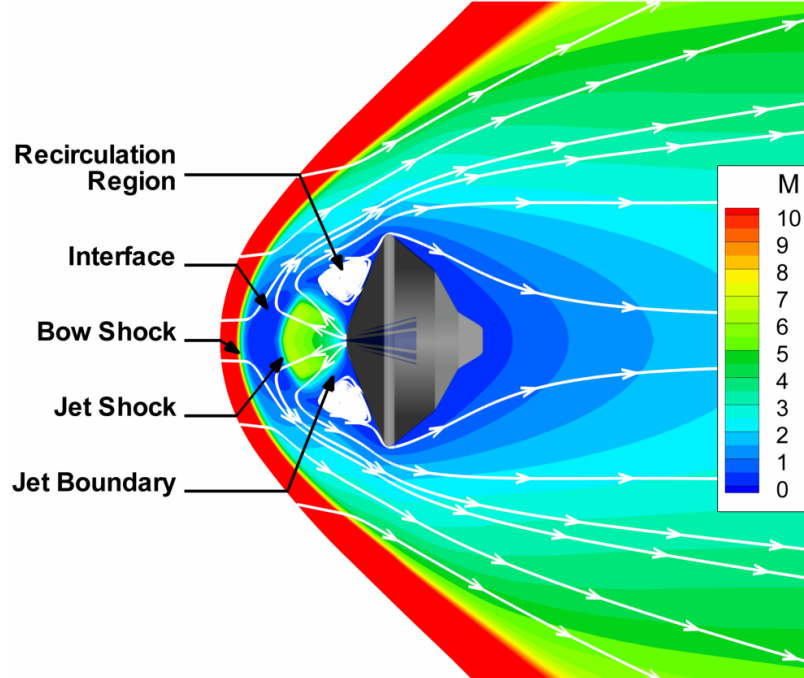


Figure 3.4: Flowfield features for sonic central PD jets ( $C_T = 0.5$ ).

through a shock and then subsonically. The figure also shows that all of the flowfield features shown in Figure 3.4 are affected by the PD thrust. The bow shock, interface region, and jet shock move upstream as the thrust coefficient increases in order to equalize the static pressure of the PD jet and the freestream flow. The recirculation regions along the aeroshell forebody decrease in size as the thrust increases until the flow becomes completely reattached around a thrust coefficient of 2.0. The reason for this is that the PD jet is able to expand more as its total pressure increases, and, therefore, can overcome the relatively sharp turning angle at the nozzle-exit.

Contours of the PD jet mole fraction for nozzle thrust coefficient values of 0.5, 1.0, 2.0, and 2.5 are presented in Figure 3.6. The PD jet species used in the simulations are tagged  $N_2$  molecules with the same properties as molecular nitrogen and only distinguishable by name. The size of the PD jet increases with the thrust coefficient, which is expected since the mass flow rate of the jet also increases. The width of the PD jet grows from approximately half the length of the aeroshell diameter for a

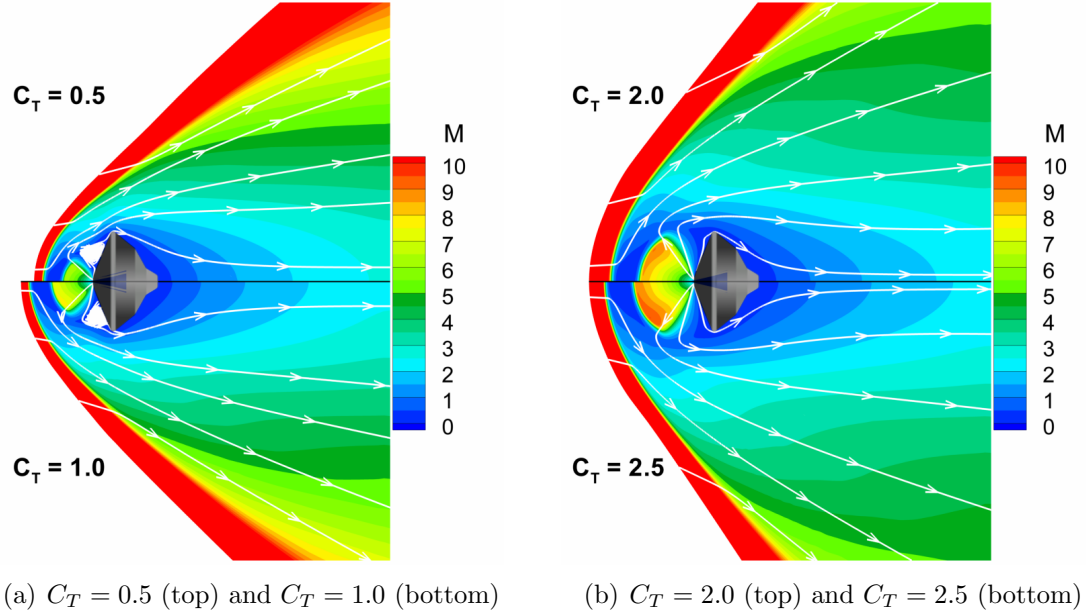


Figure 3.5: Mach number contours for sonic central PD jets at various thrust coefficients.

thrust coefficient of 0.5 to over a diameter length for a thrust coefficient of 2.5. The amount of PD jet species in the wake also increases as the thrust coefficient increases because more species are transported downstream by the main flowfield as the mass flow rate of the PD jet increases. This is important because the design of the thermal protection system of the backshell may need to consider the hot gases from the PD jet that will be transported downstream of the capsule.

Figure 3.7 shows gradient-length local Knudsen number contours for thrust coefficients of 0.5, 1.0, 2.0, and 2.5. The continuum approximation in the CFD method may be physically invalid for local Knudsen number values greater than 0.05. The figure shows continuum regions in the freestream and the PD jet core. The region in the PD jet core expands in size as the thrust coefficient increases due to the added mass. The contours also indicate that the local Knudsen number is higher than 0.05 in the bow shock and the wake, which is expected due to sharp gradients in fluid properties and relatively low densities. However, continuum breakdown may also occur along the forebody between the PD jet and the aeroshell surface. Despite the

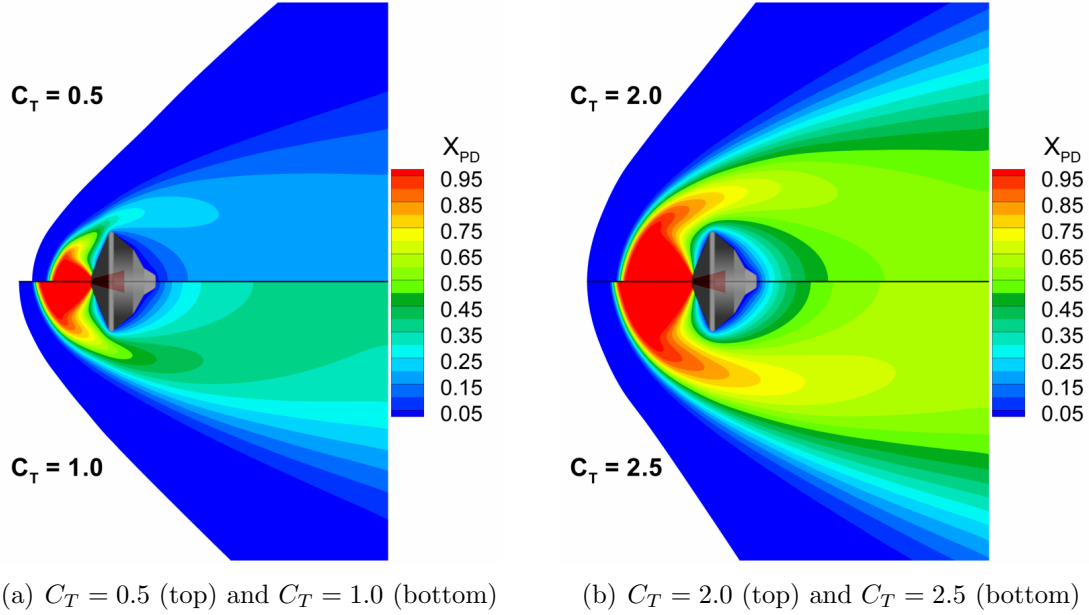


Figure 3.6: PD jet species mole fraction contours for sonic central PD jets at various thrust coefficients.

PD jet adding more mass to the flowfield as the thrust increases, the jet also induces larger gradients which increase continuum breakdown along the aeroshell forebody.

### 3.2.2 Surface Properties

The flowfield interactions generated by the sonic central PD jets also affect the surface properties of the aeroshell. Figure 3.8 presents the pressure and skin friction coefficients along the surface of the capsule for PD nozzle thrust coefficients of 0.5, 1.5, and 2.5, as well as for the no-jet case for comparison. The no-jet case uses a clean geometry without a nozzle cavity. The figure shows that both the surface pressure and shear stress are affected by the thrust coefficient of the PD. The pressure along the surface first decreases from a high value near the PD jet nozzle-exit. The pressure then increases to a peak near the shoulder of the aeroshell and sharply decreases along the aftbody before finally reaching a roughly constant small value. The magnitude of the peak decreases and the pressure along the forebody approaches an almost constant value equal to the aftbody value as the thrust coefficient increases. The

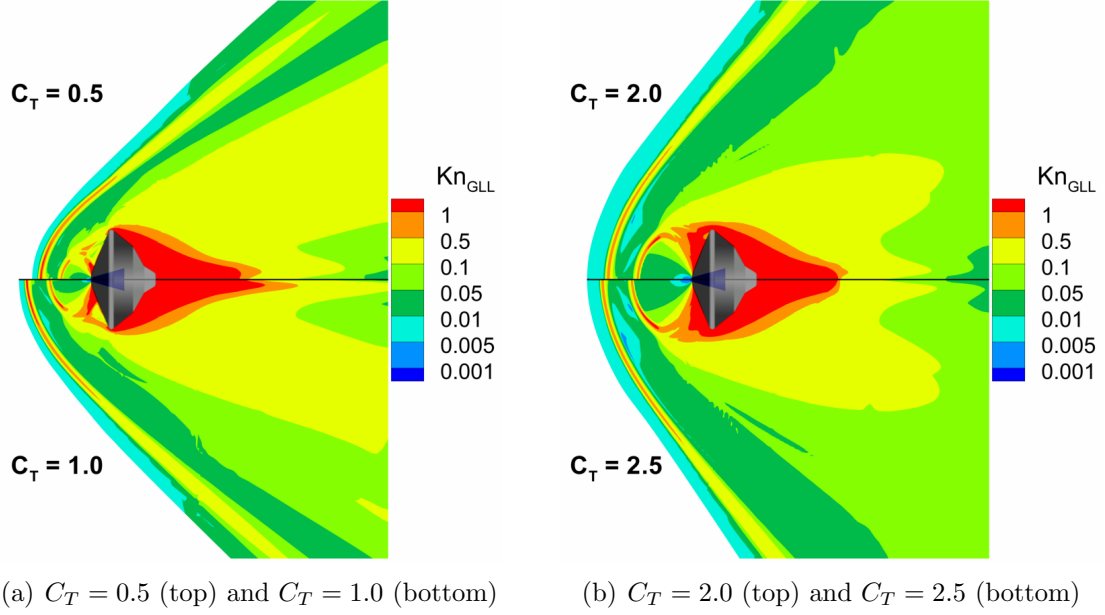


Figure 3.7: Gradient-length local Knudsen number contours for sonic central PD jets at various thrust coefficients.

coefficient of skin friction profiles also show that the shear stress along the surface first decreases from a maximum value near the PD jet nozzle-exit. The shear stress then decreases to negative values for thrust coefficients less than approximately 2.0 (i.e. flow reattachment begins near a thrust coefficient of 2.0), and then increases to a larger value at the shoulder before decreasing and finally reaching an almost constant small value along the aftbody of the aeroshell. Similar to the pressure, the overall magnitudes of the coefficient of skin friction decrease and approach a constant value along the entire aeroshell surface as the thrust coefficient increases. The effect of the thrust coefficient on the surface properties suggests that the aerodynamic properties of the aeroshell, in particular the drag force, may also be affected by the PD jet.

### 3.2.3 Aerodynamic Properties

The variation of the aerodynamic drag coefficient of the aeroshell with the sonic central PD thrust coefficient is shown in Figure 3.9. The figure also presents the total axial force coefficient of the aeroshell, which is equal to the sum of the aero-

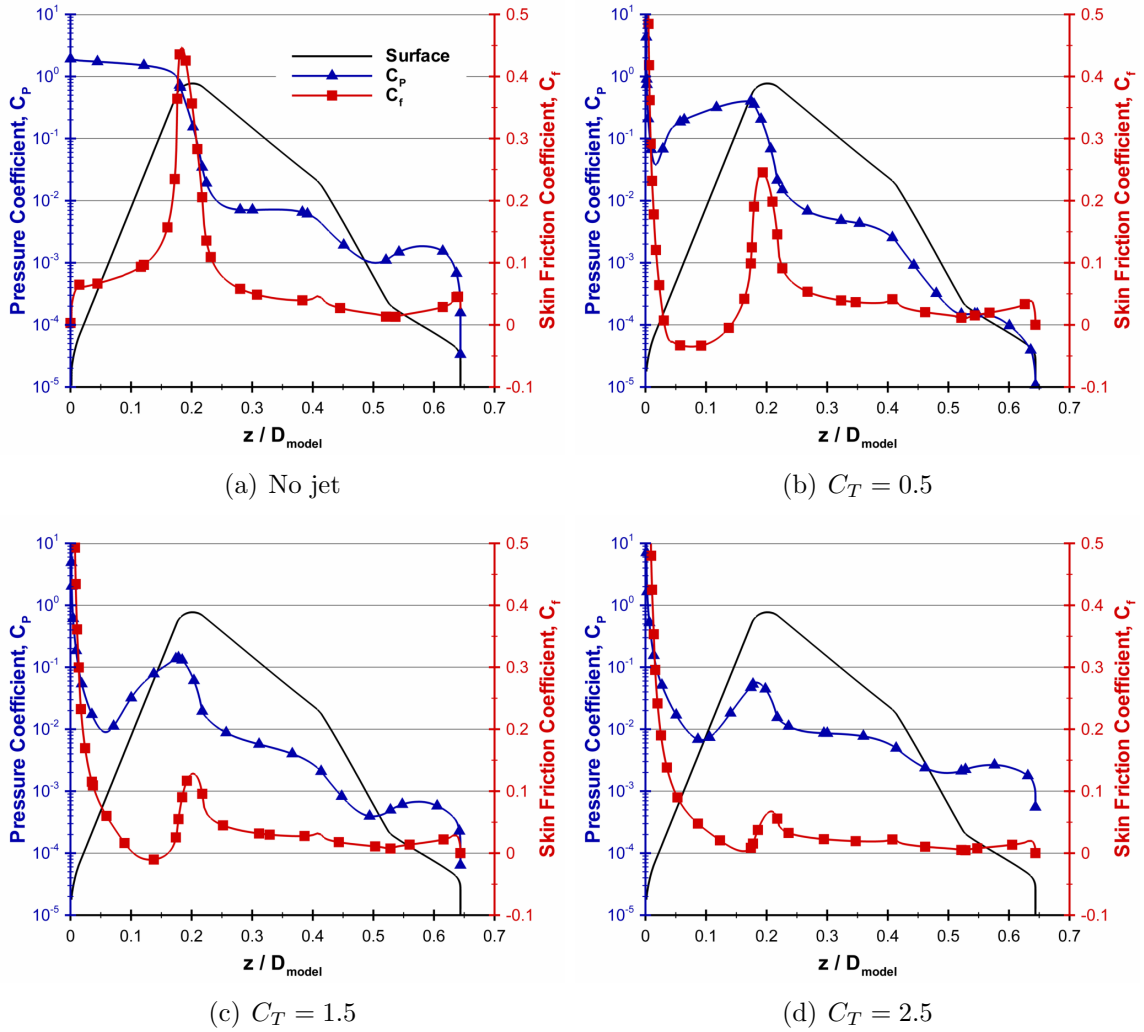


Figure 3.8: Coefficients of pressure and skin friction for sonic central PD jets at various thrust coefficients.

dynamic drag and thrust coefficients. The axial force coefficient is indicative of the aeroshell deceleration performance because it represents the total force experienced by the vehicle. As the thrust coefficient increases, the drag coefficient decreases and asymptotically approaches a constant value that is approximately equal to 7% of the value for the no-jet case ( $C_D = 1.55$  for  $C_T = 0$  and  $C_D = 0.11$  for  $C_T = 2.5$ ). The figure also shows that the total axial force coefficient first decreases as the thrust coefficient increases, and then begins to increase for thrust coefficient values greater than approximately 0.5. The total axial force coefficient value does not exceed the drag coefficient value for the no-jet case until the thrust coefficient is equal to about 1.5, where most of the contribution to the axial force is from the PD thrust. This suggests that propulsive deceleration using sonic PD jets in a central configuration may only be beneficial for relatively large thrust coefficient values that are greater than approximately 1.5. The total axial force coefficient increases by roughly constant increments for thrust coefficients greater than 1.5, since the drag coefficient is small and almost constant.

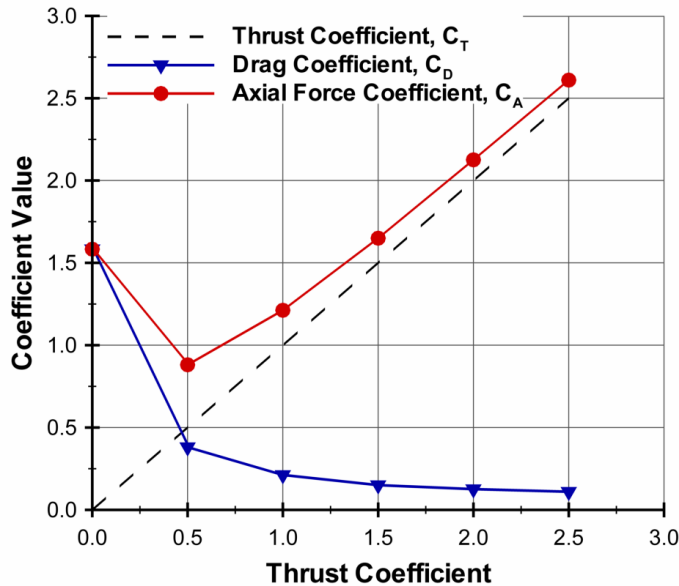


Figure 3.9: Drag and total axial force coefficients for sonic central PD jets.

The continuum breakdown regions along the aeroshell forebody shown in Figure

3.7 may have a significant effect on the surface and aerodynamic properties calculated by LeMANS (a continuum approach). However, a study by Deschenes et al. [87] showed that the deceleration performance predicted by LeMANS compares well with that predicted by a hybrid method that utilizes CFD in the continuum regions of the flow and the direct simulation Monte Carlo method (DSMC) in the rarefied regions for this particular configuration. The DSMC technique is a probabilistic particle approach that simulates the physical processes described by the Boltzmann equation. The study found that although the continuum approach (i.e. LeMANS) over-predicts the aerodynamic drag coefficient by a factor of 2.7 compared to the hybrid method for a thrust coefficient of 2.0, the difference in the axial force coefficient is less than 4% since most of the contribution is from the PD thrust. The study also found that the flowfield features predicted by LeMANS agree well with the results for the hybrid method, as can be seen in Figure 3.10. The figure shows Mach number and pressure contours for  $C_T = 2.0$  predicted by the two approaches.

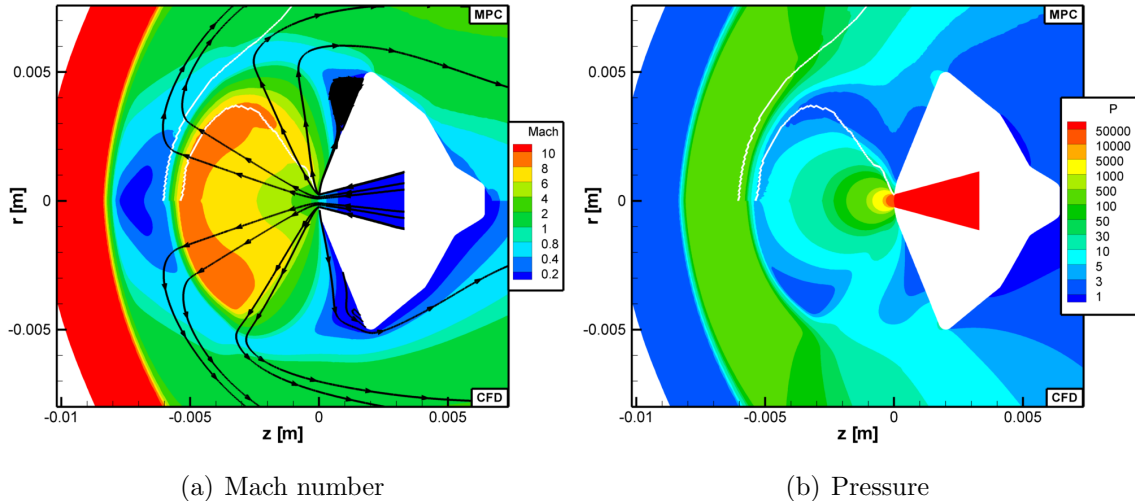


Figure 3.10: Comparison of Mach number and pressure contours predicted by continuum (bottom) and hybrid (top) methods for  $C_T = 2.0$ . Figure from Ref. [87].

The overall decrease in pressure along the surface, and consequently the drag co-



efficient of the aeroshell with increasing thrust coefficient, is caused by a shielding effect of the sonic PD jet in the central configuration that prevents mass and momentum in the main freestream flow from reaching the surface of the aeroshell. As the PD jet expands from the nozzle, it pushes the main freestream flow upstream and creates a low pressure region between the jet boundary and the surface. The size of this low pressure region expands and the flow around the aeroshell approaches a no-freestream, PD jet-only, configuration as the thrust coefficient increases. The location of the peak in the pressure profiles near the aeroshell shoulder shown in Figure 3.8 corresponds to the point at which the shielding effect of the PD jet becomes negligible. The magnitude of the peak is roughly equal to the value for the no-jet case shown in Figure 3.8(a). Figure 3.11 shows mass flux (i.e.  $\rho U$ ) and momentum flux (i.e.  $P + \rho U^2$ ) computed using the density of the main freestream flow (i.e. excluding the PD jet) for thrust coefficient values of 0.5 and 2.5 in order to quantify the amount of mass and momentum transferred to the surface. The figure shows that less mass and momentum from the freestream reach the surface of the aeroshell as the thrust coefficient increases, which decreases the overall pressure on the forebody and the drag coefficient of the aeroshell.

### 3.3 Effects of the Central PD Jet Mach Number

The results for the sonic jets can be compared to the results for supersonic jets in order to understand how the jet Mach number (and conditions) affect the fluid interactions produced by central PD jets. The mass flow rate for the supersonic jets is lower than for the sonic jets by approximately 15% at each thrust coefficient, which may have an important impact on the aeroshell properties. Therefore, this section examines the flowfield, surface, and aerodynamic effects of the PD jet Mach number at various thrust conditions.

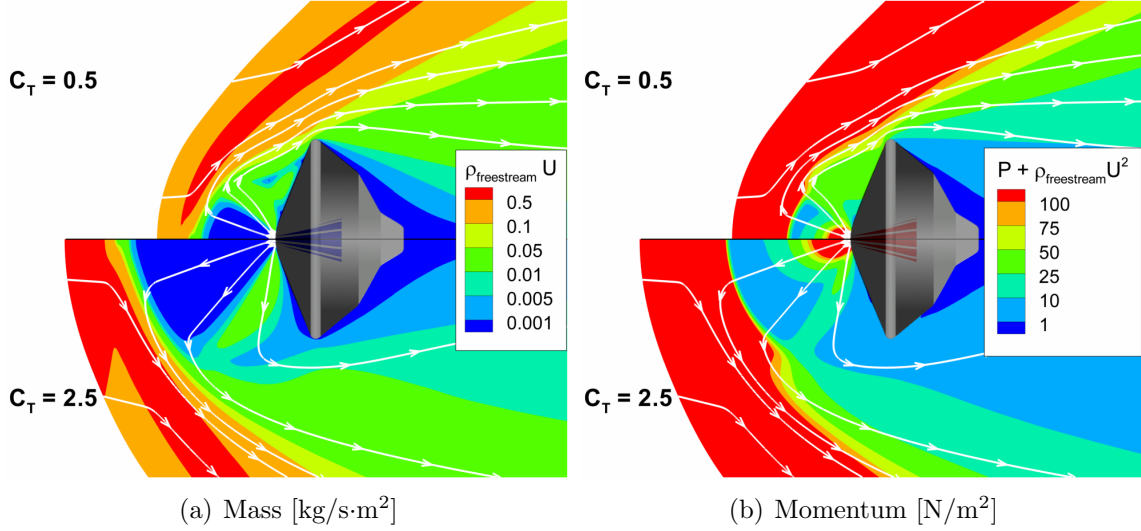


Figure 3.11: Mass and momentum transfer from the freestream to the surface of the aeroshell for sonic central PD jets at  $C_T = 0.5$  (top) and  $C_T = 2.5$  (bottom).

### 3.3.1 Flowfield Effects

Figure 3.12 presents Mach number contours for supersonic and sonic central PD jets for two different thrust coefficients, 0.5 and 2.5. The figure shows that both PD jet Mach numbers generate similar flowfield features, such as PD jet shock, interface region between the bow and jet shocks that contains the detached stagnation point, and recirculation zones between the jet boundary and the forebody. Several differences in these flowfield features can be observed, however, between the two PD jet Mach number cases. The figure shows that the supersonic PD jet penetrates farther upstream than the sonic jet for both thrust coefficients, which increases the standoff distances of the bow and jet shocks. The figure also shows that the width of the PD jet decreases as the Mach number increases, which is typical of supersonic jets. The recirculation region for the supersonic PD jets is also larger than for the sonic jets. Figure 3.12(b) shows that there is a separation region for the supersonic jet even at  $C_T = 2.5$ , whereas the flow around the forebody is completely attached at this thrust coefficient for the sonic jet.

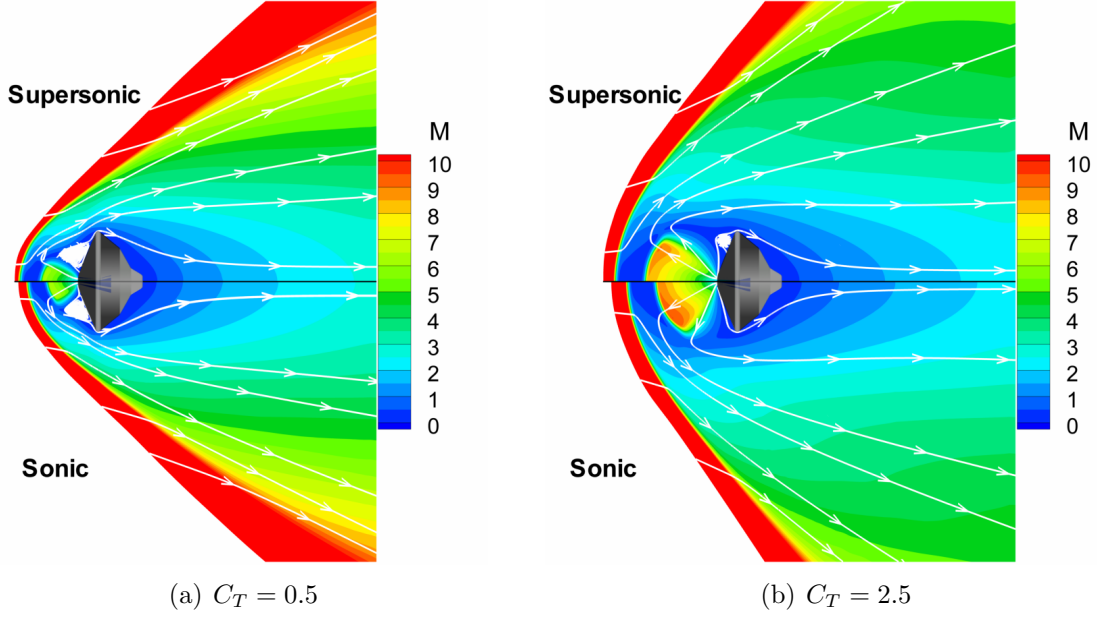


Figure 3.12: Comparison of Mach number contours for sonic (bottom) and supersonic (top) central PD jets at  $C_T = 0.5$  and  $C_T = 2.5$ .

PD jet species mole fraction (i.e. tagged  $N_2$  molecules) contours are shown in Figure 3.13 for supersonic and sonic PD jets at thrust coefficients of 0.5 and 2.5. As the thrust coefficient increases, the size of the PD jet also increases, since the mass flow rate from the PD nozzle is proportional to the thrust. The width of the supersonic PD jet increases from approximately an aeroshell-radius length to about 1.5 aeroshell diameters. The figure also shows that less jet species are transported downstream to the wake region by the main freestream flow for the supersonic jet than for sonic jets due to lower mass flow rates. Near the backshell, however, the PD jet mole fraction distribution is similar for the two central PD jet configurations.

The similarities observed in the flowfield properties also extend to the gradient-length local Knudsen number distribution, presented in Figure 3.14 for sonic and supersonic central PD jets. The high-density, continuum region within the PD jet core is longer and narrower for the supersonic PD jets because it follows the jet profile. Similar to the sonic jets, the supersonic PD jets also increase continuum breakdown

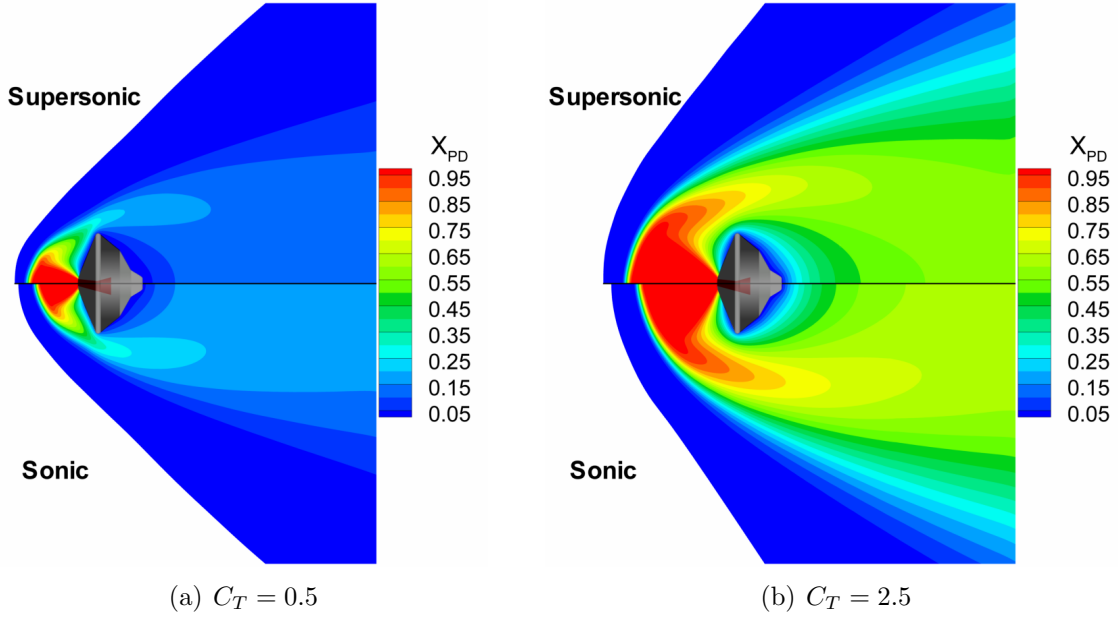


Figure 3.13: Comparison of PD jet species mole fraction contours for sonic (bottom) and supersonic (top) central PD jets at  $C_T = 0.5$  and  $C_T = 2.5$ .

along the aeroshell forebody as the thrust coefficient increases due to larger gradients in the fluid properties.

### 3.3.2 Surface Effects

The pressure and skin friction coefficients along the aeroshell surface for the supersonic and sonic PD jets at thrust coefficients of 0.5, 1.5, and 2.5, as well as for the no-jet case are presented in Figure 3.15. The figure shows that the overall trends for both surface pressure and shear stress are similar for the two jet Mach number cases. The figure also shows that there are some discrepancies in the magnitude of the surface properties, particularly in the pressure along the aeroshell aftbody. This difference, however, is insignificant with respect to the drag force acting on the aeroshell due to the relatively low pressures associated with wake flows. As previously observed in the flowfield results, the supersonic PD jet generates larger recirculation regions along the aeroshell forebody (i.e. areas of negative shear-stress) compared to the

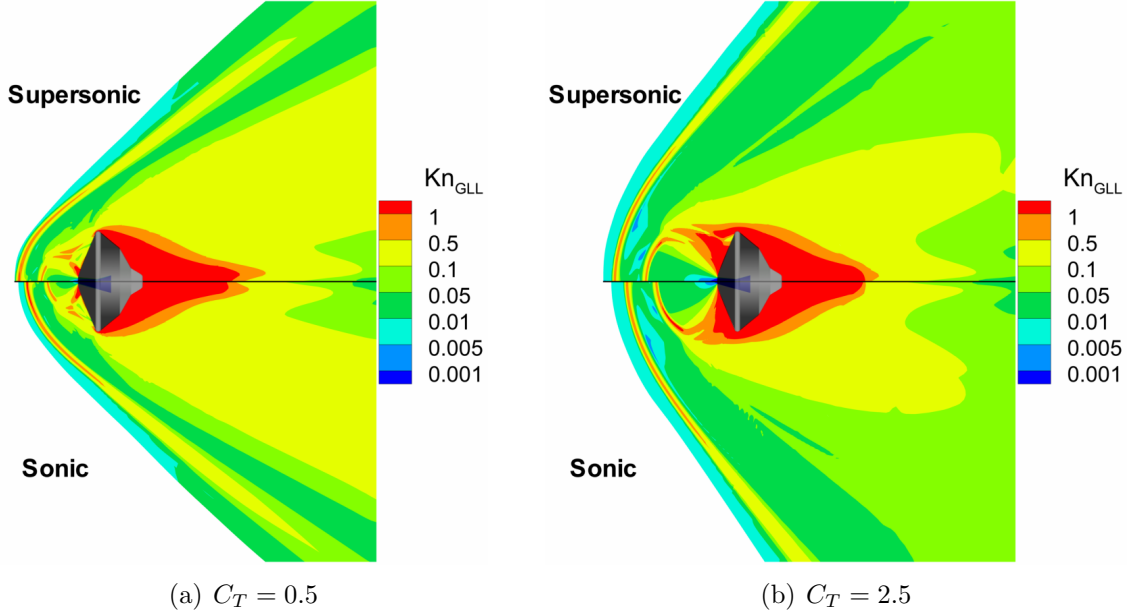


Figure 3.14: Comparison of gradient-length local Knudsen number contours for sonic (bottom) and supersonic (top) central PD jets at  $C_T = 0.5$  and  $C_T = 2.5$ .

sonic jets. This difference varies from about 3% for  $C_T = 0.5$  to approximately 90% for  $C_T = 1.5$ . For the highest thrust condition ( $C_T = 2.5$ ), the flow is attached along the entire surface for the sonic PD jet, but there is a small recirculation region that is roughly  $0.06 \times D_{model}$  long for the supersonic jet. The higher stagnation pressures and relatively lower Mach number delays the separation in the sonic PD jet cases because the flow can better overcome the sharp turning angle at the nozzle-exit. Another difference is that the surface pressure drops to a lower value downstream of the nozzle-exit for the supersonic jets. This difference can also be attributed to the lower stagnation pressures and higher Mach number of the supersonic jet compared to the sonic jets.

### 3.3.3 Aerodynamic Effects

The aerodynamic drag and total axial force (i.e. the sum of drag and thrust) coefficients of the aeroshell with supersonic and sonic central PD jets are presented

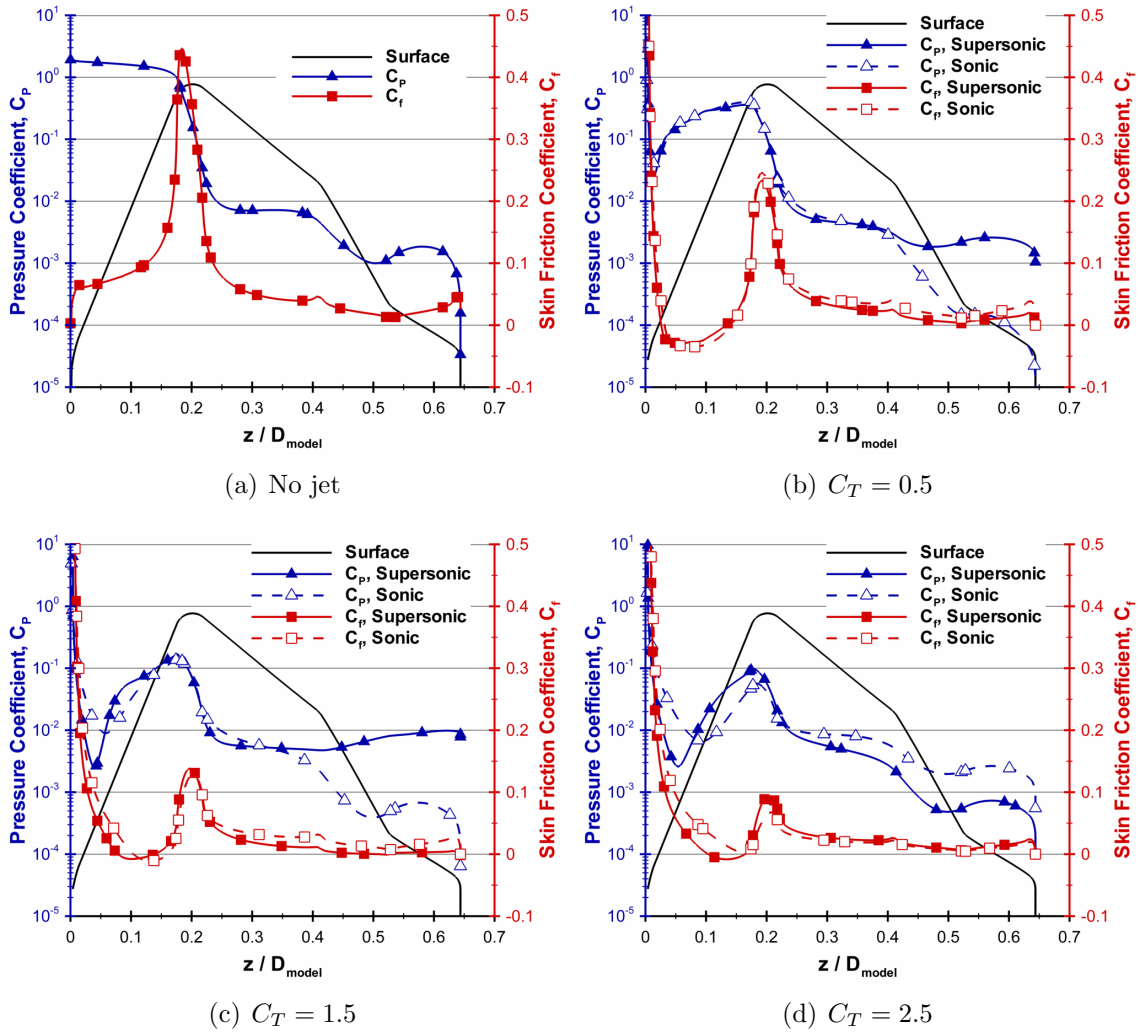


Figure 3.15: Comparison of coefficients of pressure and skin friction for sonic and supersonic central PD jets at various thrust coefficients.

in Figure 3.16 as functions of thrust coefficient. The figure shows that the trends of the aerodynamic properties of the aeroshell for the two PD jet Mach numbers are in overall close agreement. Similar to the sonic PD jets, the drag coefficient of the aeroshell with supersonic PD jets decreases and asymptotically approaches a constant value of 7% of the no-jet case as the thrust coefficient increases. The figure also shows that the axial force coefficient decreases up to  $C_T = 0.5$  by approximately 50% for both sonic and supersonic jets, then increases mainly due to the contribution from the PD thrust. The drag coefficient for the supersonic jet is approximately 10% and 25% lower than for the sonic jet for thrust coefficients of 0.5 and 2.5, respectively. However, since the aerodynamic drag is inversely proportional to the thrust, the total axial force coefficient for the supersonic jet is only 4% and 1% smaller than for the sonic jet for the same thrust coefficients.

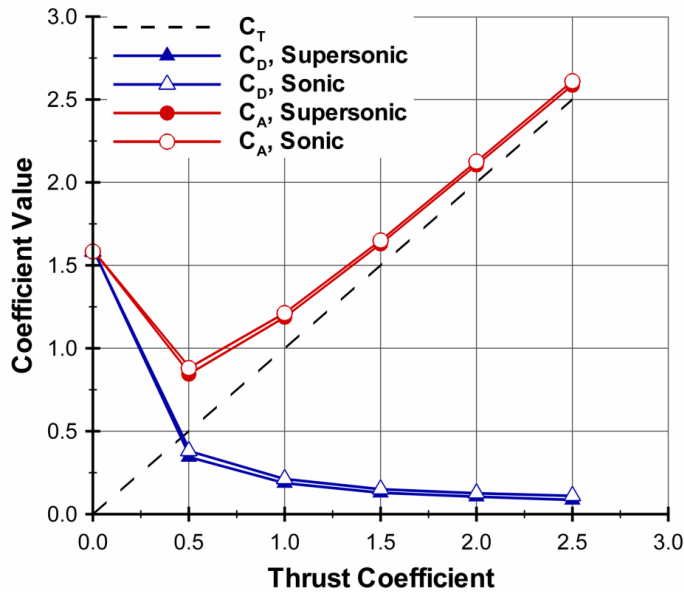


Figure 3.16: Comparison of drag and axial force coefficients for sonic and supersonic central PD jets.

Similar to the sonic central PD jets, the supersonic jets also create a shielding effect upstream of the aeroshell that prevents mass and momentum from the freestream to reach the aeroshell surface. In order to quantify this shielding effect, Figure 3.17

presents mass flux (i.e.  $\rho U$ ) and momentum flux (i.e.  $P + \rho U^2$ ) computed using the density of the main freestream flow (i.e. excluding the PD jet) for  $C_T = 2.5$  for supersonic and sonic PD jets. The figure shows a low mass and momentum region upstream of the aeroshell that decreases the pressure on the forebody. This region is produced by the expansion of the PD jet, which pushes the freestream flow upstream of the aeroshell. As the thrust coefficient increases, the influence of the PD jet also increases and the flow around the aeroshell resembles a jet-only, no-freestream configuration. The figure also shows an overall similar shielding effect between the sonic and supersonic central PD jets, which causes the similarities observed in the surface and aerodynamic properties of the aeroshell.

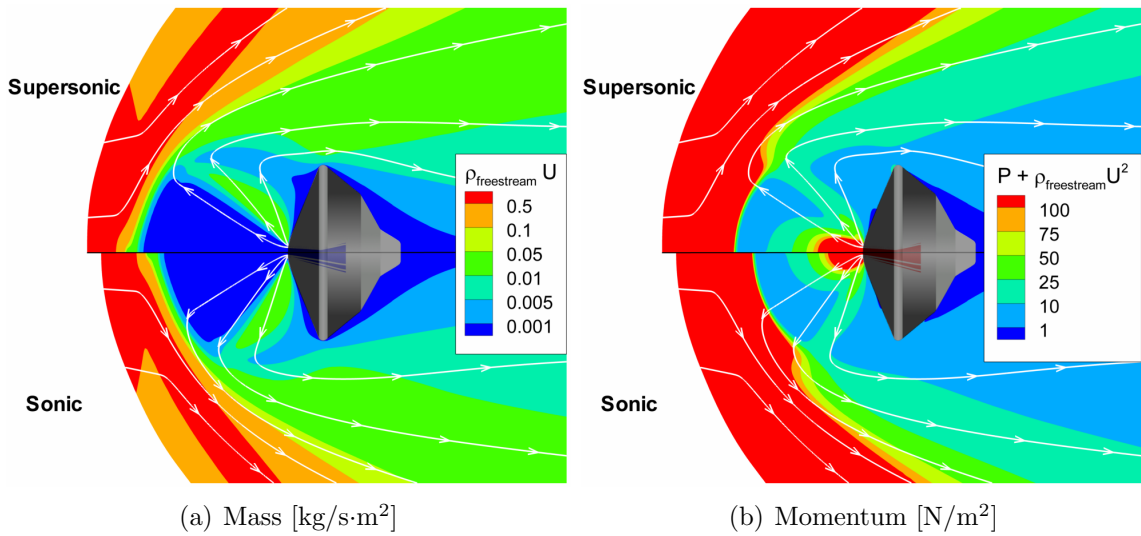


Figure 3.17: Comparison of mass and momentum transfer from the freestream to the surface of the aeroshell for sonic (bottom) and supersonic (top) central PD jets at  $C_T = 2.5$ .

The aerodynamic properties of the aeroshell with central PD jets are summarized in Figure 3.18. The figure presents the contribution from the aerodynamic drag and PD thrust to the axial force coefficient for sonic and supersonic PD jets for the range of thrust coefficients investigated in this study. The aerodynamic drag coefficient is virtually eliminated due to the shielding effect of the central PD jet, which reduces



the pressure on the aeroshell forebody by preventing mass and momentum from the freestream flow to reach the surface of the capsule. Even though the axial force for  $C_T = 2.5$  is approximately 60% larger for the sonic and supersonic PD jets than for the no-jet case, the contribution from the aerodynamic drag is less than 5% (the drag contribution is approximately 43% for  $C_T = 0.5$ ). Figure 3.18 also shows the close agreement in axial force coefficient between the sonic and supersonic PD jets. This agreement suggests that the PD jet Mach number may not have a significant effect on the overall deceleration performance of the aeroshell. Therefore, supersonic jets may be more advantageous than sonic jets for central propulsive deceleration since they can achieve the same deceleration performance with potentially less propellant mass requirements.

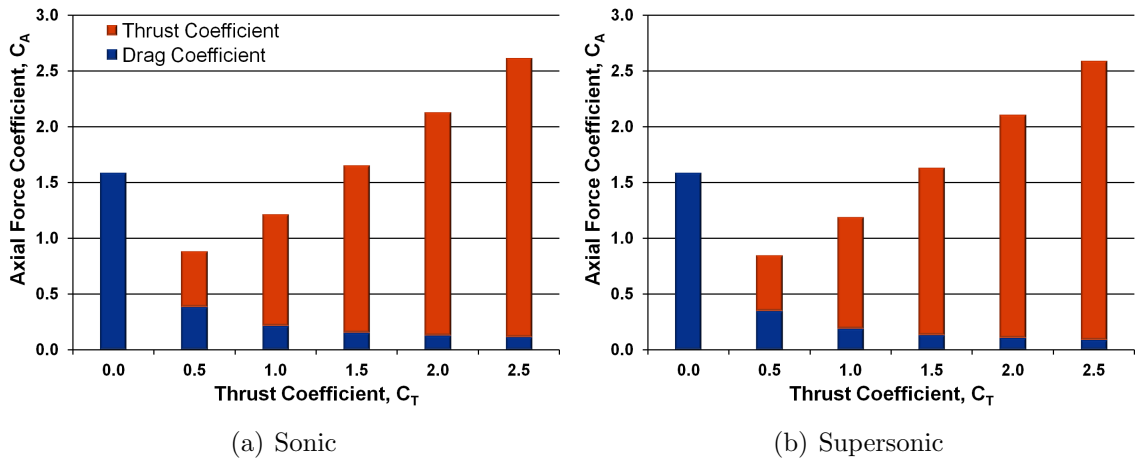


Figure 3.18: Drag and thrust contributions to the axial force on the aeroshell for sonic and supersonic central PD jets.

### 3.4 Summary

A numerical investigation of the interactions of sonic and supersonic central PD jets on Mars-entry aeroshells was performed using the CFD code LeMANS. The effects on the flowfield, surface, and aerodynamic properties of an MSL-based aeroshell

were evaluated for Mach 12 flow of I<sub>2</sub>-seeded N<sub>2</sub> gas using axisymmetric laminar simulations. The sonic and supersonic central PD jets were chosen to study the performance of central propulsive deceleration for Mars-entry vehicles, and how their flowfield, surface and aerodynamic properties are affected by the conditions of the PD jet.

The first part of this study focused on the fluid interactions produced by sonic central jets and their effects on the flowfield, surface, and aerodynamic properties of the aeroshell. The results showed that as the thrust provided by the PD nozzle increased, the bow shock, jet shock, and interface region moved upstream of the aeroshell, while the recirculation regions along the forebody became smaller in size until the flow became completely reattached around a thrust coefficient of 2.0. The results also showed that the size of the PD jet increased and more jet species were transported to the wake as the thrust coefficient increased. The level of continuum breakdown near the surface of the aeroshell forebody also increased with the PD thrust due to larger gradients in the fluid properties induced by the jet. Along the surface, the results showed that the overall magnitudes of the pressure and shear stress decreased and approached a roughly constant value along most of the aeroshell as the thrust coefficient increased. Due to this decrease in surface pressure on the forebody, the aerodynamic drag coefficient of the aeroshell was found to decrease and asymptotically reach a constant value of 7% of the no-jet case as the thrust coefficient increased. The axial force coefficient of the aeroshell was also found to not exceed the aerodynamic drag coefficient of the no-jet case until a thrust coefficient of 1.5, where most of the contribution to the axial force was from the PD thrust. The decrease in the overall surface pressure on the aeroshell, and consequently lower drag coefficients, with increasing PD thrust was shown to be caused by a shielding effect of the jet. The PD jet prevented mass and momentum from the freestream flow from reaching the surface of the aeroshell, which created low pressure regions close to the forebody. As

the thrust coefficient increased, the size of the PD jet also increased, which augmented the effects of the shield and expanded the size of the low pressure region near the aeroshell surface.

In the second part of the study, the effects of the central PD jet Mach number on the properties of the aeroshell were evaluated by comparing the results for sonic and supersonic jets. Similar features, such as PD jet shock and recirculation regions along the forebody, were observed for both the supersonic and sonic PD jets. The supersonic jets, however, were narrower and penetrated farther upstream for all thrust coefficients, which increased the standoff distances of these features compared to the sonic jets. The distributions of pressure and shear stress along the aeroshell surface were also found to be in close agreement between the sonic and supersonic PD jets, with some differences in the size of the recirculation region and the value of the pressure near the nozzle-exit. These differences extended to the aerodynamic drag coefficient for the two jet Mach number cases, which disagreed by 10% and 25% for thrust coefficients of 0.5 and 2.5, respectively. However, because the aerodynamic drag was shown to be inversely proportional to the thrust for both sonic and supersonic central PD jets, the difference in the axial force coefficient was less than 4%. Since the mass flow rate for the supersonic jets was approximately 15% lower than for the sonic jets at the same thrust coefficient, the similarities in the aerodynamic properties suggest that the supersonic jets may provide better deceleration performance for a given propellant mass. However, the trends in the axial force coefficient indicate that propulsive deceleration using central jets may only be beneficial at relatively high thrust conditions.

## CHAPTER IV

# Peripheral Propulsive Deceleration

The peripheral configuration represents another possible layout of propulsive decelerator jets for Mars-entry aeroshells. In this configuration, several PD jets (typically three or four) are placed on the periphery of the aeroshell forebody. Previous results for supersonic retropropulsion had shown that the peripheral configuration can preserve more aerodynamic drag and provide larger axial force compared to the central configuration [22, 23, 24]. However, similar to the central jets, this work mainly focused on sonic or supersonic peripheral PD jets exhausting into a supersonic freestream. As a result, there is a need to understand how the peripheral PD jets influence the aeroshell properties in hypersonic conditions before using this technology in an all-propulsive EDL architecture for future, high-mass, Mars-entry vehicles.

This chapter presents a numerical investigation of the effects of peripheral PD jets on the flowfield, surface, and aerodynamic properties of a Mars-entry aeroshell in a hypersonic freestream. The chapter first outlines the numerical setup used in this study. The chapter then describes the flow features produced by the peripheral PD jets. Next, the chapter presents the numerical results in two sections. The first section of this study examines the effects of the jet Mach number and conditions on the fluid interactions induced by the peripheral PD configuration by comparing the

numerical results for sonic and supersonic jets. In the second section, the numerical results for the peripheral jets are compared to the results for the central jets in order to examine the effects of the propulsive deceleration configuration on the properties and deceleration performance of Mars-entry aeroshells. Finally, the chapter presents a summary of the major conclusions drawn from this numerical study.

## 4.1 Numerical Setup

Similar to the central configuration, the Ashkenas and Sherman relations provide the freestream conditions for the peripheral PD jet simulations in order to model the freejet conditions in the experimental facility at the University of Virginia. The reference freestream conditions given in Table 2.1 for a leading-edge Mach number of 12 are also used in this study to calculate non-dimensional properties, such as drag coefficient. The freestream and PD jet gas used in the numerical simulations is molecular nitrogen seeded with 200 ppm of iodine. Details of the aeroshell geometry and peripheral PD jet conditions used in this numerical investigation are provided in this section.

### 4.1.1 Aeroshell Geometry

Figures 4.1 and 4.2 present the geometry for the aeroshell with sonic and supersonic peripheral PD thrusters, respectively. The geometry used in the numerical simulations is based on the test models utilized in the experiments. Both configurations use a 10 mm diameter,  $70^\circ$  blunt-cone aeroshell, which is representative of Mars-entry capsules. The Reynolds number and global Knudsen number based on the reference freestream conditions and the aeroshell diameter are 1,200 and 0.015, respectively, which suggest that the freestream flow is laminar and near-continuum. The computational geometry also includes a “sting” attached to the backshell that is used in the experiments to hold the model in the test section and supply the flow to

the PD jets. The sting is added in the numerical simulations because the PD jets are located relatively closer to the aeroshell aftbody, and, therefore, the jet plume can be influenced by the backshell geometry. Four PD nozzles are placed halfway between the aeroshell nose and shoulder, and are directed parallel to the capsule axis. The diameter of the PD nozzle-exit is 0.5 mm for the sonic peripheral jets and 0.9 mm for the supersonic jets. The diameter of the nozzle-throat for the supersonic jets is 0.5 mm, which corresponds to a nozzle-exit Mach number of approximately 2.66.

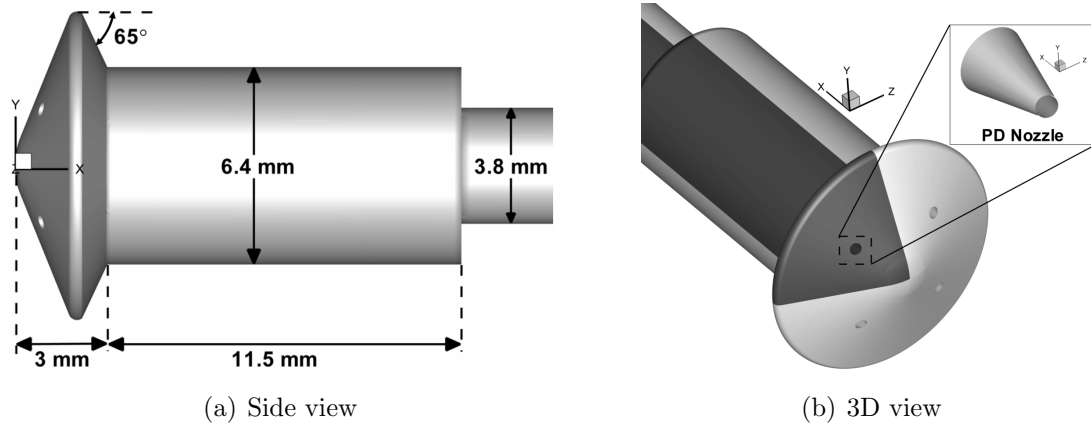


Figure 4.1: Aeroshell geometry for sonic peripheral PD jets (dark shade: geometry used in the computational simulations).

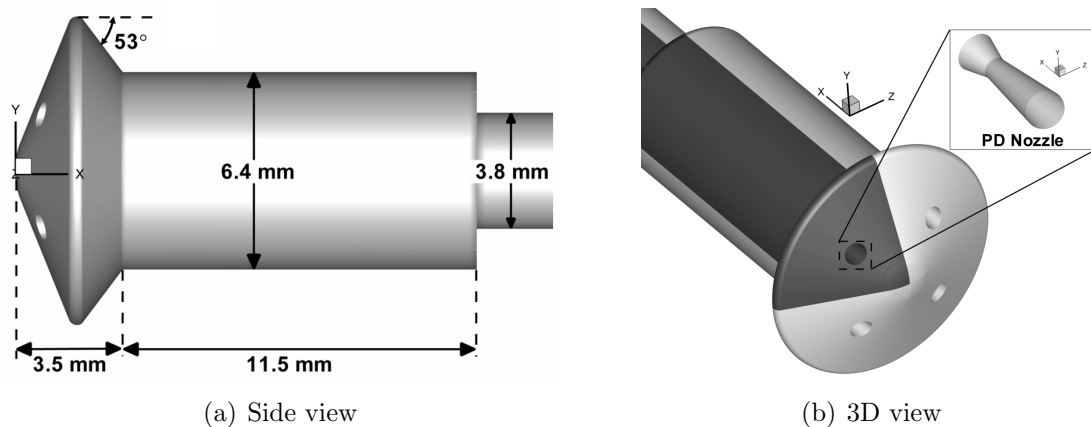


Figure 4.2: Aeroshell geometry for supersonic peripheral PD jets (dark shade: geometry used in the computational simulations).

Three-dimensional simulations are performed using LeMANS in order to study the interactions of the peripheral PD jets. The computational domain consists of only one quarter of the aeroshell (dark shaded sections in Figures 4.1 and 4.2) due to the symmetry of the flow. This assumption helps to reduce the computational cost and complexity of the simulations. The computational grids are adapted by hand from preliminary simulations in order to ensure adequate mesh resolution and to align the upstream boundary with the bow shock. Details regarding the adaptation process are provided in Appendix B. The grids use hexahedral cells with clustering near the wall and in the vicinity of the PD jet upstream of the aeroshell. The grid size varies from about 4.3 million cells to approximately 5.3 million cells based on the PD jet conditions. Figure 4.3 shows the surface mesh used in the simulations for the sonic and supersonic peripheral PD jets. Each simulation takes approximately 6,000 CPU-hours with about 100 Intel Xeon X5670 (Westmere) processors to reach a steady-state solution using a point-implicit time integration method.

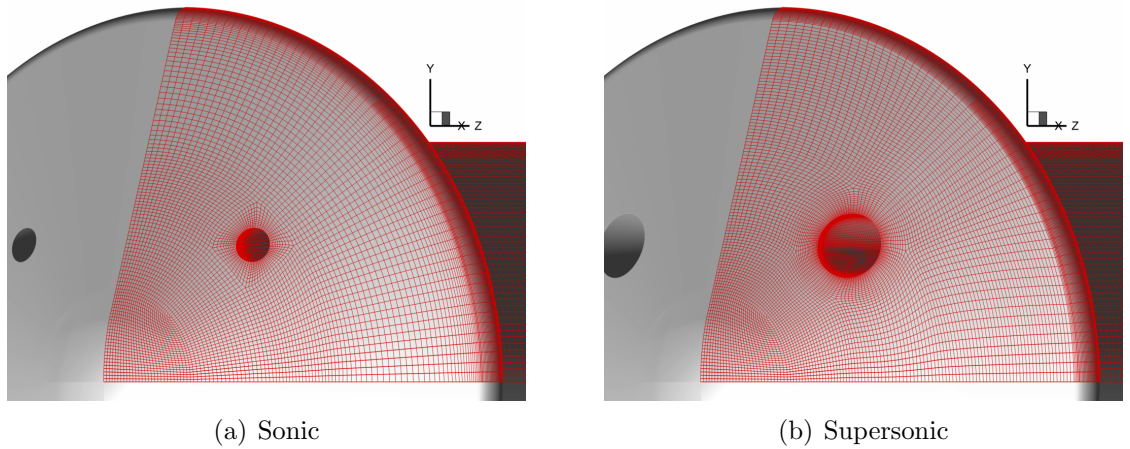


Figure 4.3: Surface mesh for sonic and supersonic peripheral PD jets.

#### 4.1.2 PD Jet Conditions

The boundary conditions for the peripheral PD jets are computed such that either sonic ( $M_{jet} = 1.0$ ) or supersonic ( $M_{jet} = 2.66$ ) conditions are obtained at the nozzle-

Table 4.1: Design conditions for sonic peripheral PD jets.

$C_T$	$P_{0,jet}/P_0$	$Re_{jet}$	$\dot{m}_{jet}$ , mg/s
0.5	0.03	370	2.4
1.0	0.06	720	4.6
1.5	0.08	1,050	6.9
2.0	0.11	1,450	9.2
2.5	0.14	1,800	11

Table 4.2: Design conditions for supersonic peripheral PD jets.

$C_T$	$P_{0,jet}/P_0$	$Re_{jet}$	$\dot{m}_{jet}$ , mg/s
0.5	0.02	280	2.1
1.0	0.05	530	4.0
1.5	0.07	780	5.9
2.0	0.09	1,040	7.8
2.5	0.11	1,300	9.7

exit. Similar to the central jets, the boundary conditions for the peripheral PD jets are non-dimensionalized using the thrust coefficient given in Equation 4.1,

$$C_T = \left( 2 \frac{q_e}{q_{ref}} + \frac{P_e}{q_{ref}} - \frac{P_{amb}}{q_{ref}} \right) \left( \frac{\sum_{jets} S_e}{S} \right) \quad (4.1)$$

This expression for the thrust coefficient includes the nozzle-exit area of all four PD jets. Tables 4.1 and 4.2 present the design total pressure ratio, Reynolds number, and mass flow rate based on the nozzle-exit properties for the sonic and supersonic peripheral PD jet configurations. These conditions are specified for each PD jet and are obtained such that the total thrust coefficient of all four peripheral jets is equal to the value shown in the tables. The stagnation temperature of the PD jets is 297 K. The flow from the PD nozzle is assumed laminar since the jet Reynolds number for all the cases is less than  $10^4$  [86]. Similar to the central jets, the lower mass flow rates provided by the supersonic peripheral jets may indicate potential savings in the required propellant mass compared to the sonic jets.



The PD nozzle-exit design Mach number and boundary conditions for the sonic and supersonic peripheral jets are calculated using the isentropic relations. However, the actual conditions at the PD nozzle-exit in the numerical simulations may be different due to viscous effects along the nozzle walls. Figure 4.4 presents Mach 1.0 and 2.66 contours in the PD nozzle for the sonic and supersonic peripheral jets. Figure 4.4(a) shows that the nozzle-exit Mach number for the sonic peripheral jet is equal to the design value of 1.0 for both  $C_T = 0.5$  and 2.5. However, Figure 4.4(b) shows that the actual Mach number for the supersonic jet is less than the design values of 1.0 at the nozzle-throat and 2.66 at the nozzle-exit by approximately 27% and 31%, respectively, for  $C_T = 0.5$ . The figure also shows that the larger favorable pressure gradient provided by the higher thrust coefficient increases the agreement between the actual and the design Mach numbers for the supersonic peripheral PD jets. The discharge coefficient of the PD nozzle for the sonic and supersonic peripheral jets is approximately 0.80 and 0.91, respectively.

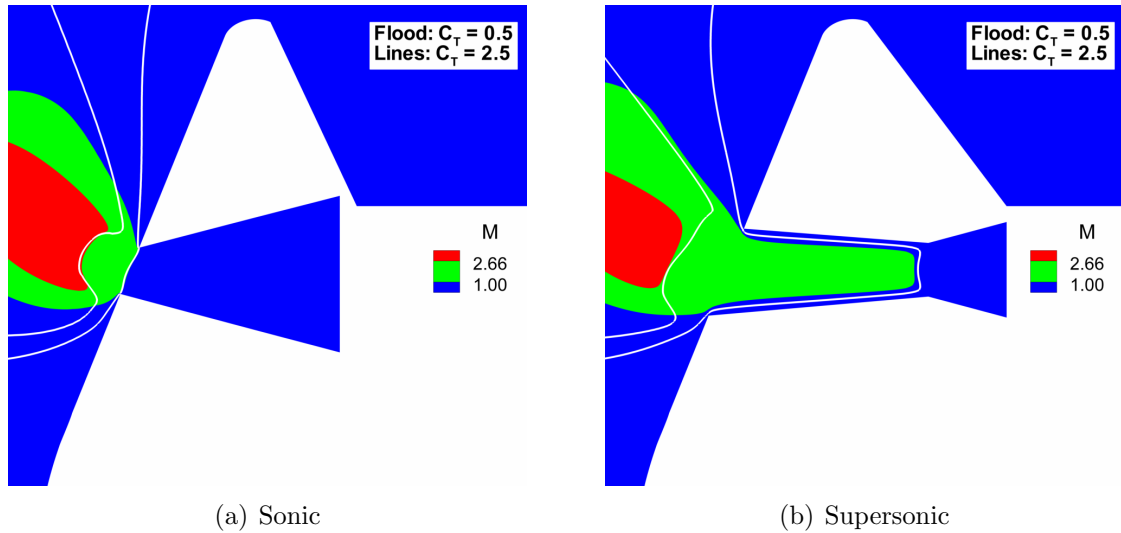


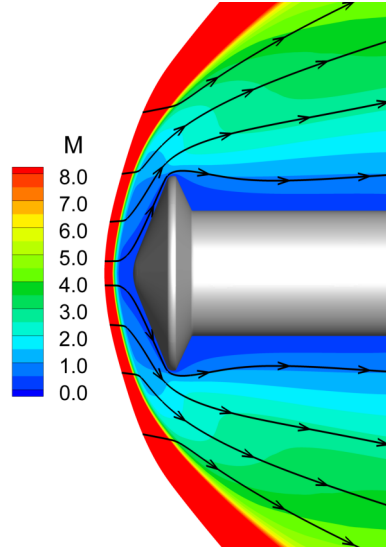
Figure 4.4: Mach number distribution along the nozzle for the sonic and supersonic peripheral PD jets.

## 4.2 Flowfield Features

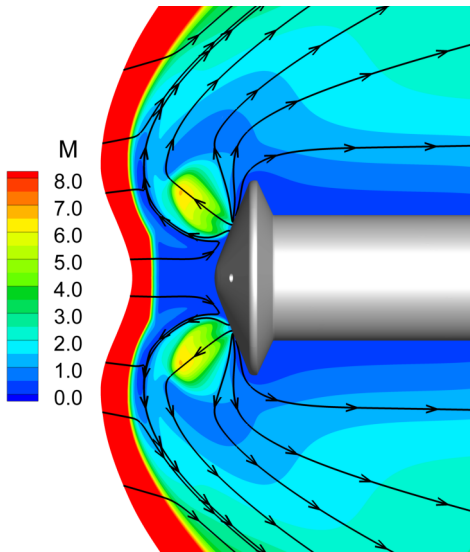
Figure 4.5 presents Mach number contours for the no-jet and the sonic peripheral PD jet with  $C_T = 1.5$  configurations. The no-jet case uses a clean geometry without the nozzle cavity. The bottom half is a reflection of the top half since only one quarter of the geometry is used in the numerical simulations. The flow for the no-jet case is characterized by a bow shock that develops around the aeroshell and a series of expansion and compression waves that occur along the aeroshell aftbody and sting. Figure 4.5(b) shows that the peripheral PD jet expands from sonic conditions at the nozzle-exit to supersonic and hypersonic conditions upstream of the aeroshell. The jet decelerates to subsonic conditions through a relatively weak jet shock before mixing with the freestream flow. The peripheral PD jet interacts with the bow shock by pushing the section close to the jet plume upstream and changing the shock profile to a “saddle” shape. As a result, some of the freestream flow between the peripheral PD jets upstream of the aeroshell nose passes through a nearly normal shock. Between two adjacent PD jets, the level of interaction of the jet with the bow shock diminishes, as can be seen in Figure 4.5(c). Although the bow shock standoff distance between two adjacent PD jets is still large, the shock recovers its shape and the overall flowfield features resemble the structure of the no-jet case.

## 4.3 Effects of the Peripheral PD Jet Mach Number

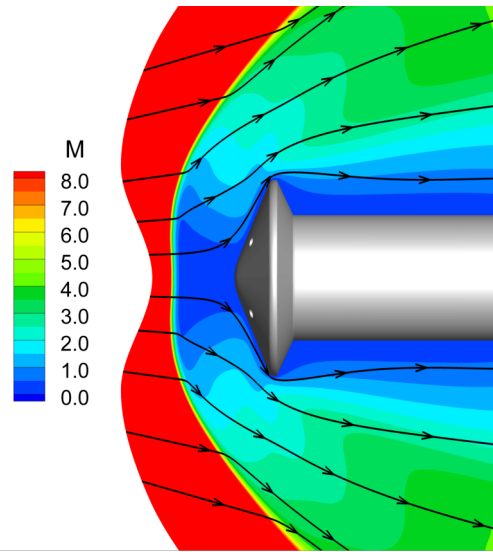
The flowfield properties of the peripheral PD jet described in the previous section can be affected by the Mach number and conditions of the jet. These effects may also extend to the surface and aerodynamic properties of the aeroshell. Therefore, this section compares the numerical results for sonic and supersonic peripheral PD jets in order to understand the effects of the jet Mach number and conditions on the flowfield, surface, and aerodynamic properties of a Mars-entry aeroshell.



(a) No jet



(b) Peripheral PD jet (cut-plane along the PD jet axis)



(c) Peripheral PD jet (cut-plane between 2 adjacent PD jets)

Figure 4.5: Comparison of Mach number contours for the no-jet and sonic peripheral PD jet ( $C_T = 1.5$ ) configurations.

### 4.3.1 Flowfield Effects

Figure 4.6 presents Mach number contours and velocity streamlines for sonic and supersonic peripheral PD jets at various thrust coefficients. The contours show that the supersonic PD jet is narrower and penetrates farther upstream than the sonic jet, particularly for the larger thrust coefficients. As a result, the interaction between the PD jet and the bow shock is stronger for the supersonic configuration. The bow shock standoff distance and curvature near the PD jet plume are also larger for the supersonic jets, which cause the normal portion of the bow shock between the PD jets upstream of the aeroshell nose to decrease in size.

The PD jet species mole fraction distribution for the sonic and supersonic peripheral jets at various thrust coefficients is shown in Figure 4.7. The size of the sonic and supersonic PD jets increases with thrust coefficient due to the added mass. The contours show that the PD jet is mainly swept away by the freestream flow. As a result, little to almost no PD jet species are transported to the aeroshell nose. The figure also shows overall close agreement between the sonic and supersonic peripheral jets. However, the supersonic jets are relatively narrower and penetrate farther upstream compared to the sonic jets.

The gradient-length local Knudsen number,  $Kn_{GLL}$ , is used to determine continuum-breakdown for the peripheral PD configuration. Figure 4.8 presents local Knudsen number contours for sonic and supersonic peripheral PD jets at various thrust coefficients. The contours indicate continuum-breakdown regions (i.e.  $Kn_{GLL} > 0.05$ ) in the bow shock due to sharp gradients in the flow properties and in the wake due to the relatively low densities. The figure also shows continuum-breakdown regions along the forebody between the PD nozzle-exit and the aeroshell shoulder which are caused by large gradients induced by the PD jet. Interestingly, Figure 4.8(b) shows an area of increased  $Kn_{GLL}$  upstream of the sonic PD jet plume that indicates the onset of a terminal jet shock. The magnitude of the local Knudsen number and the

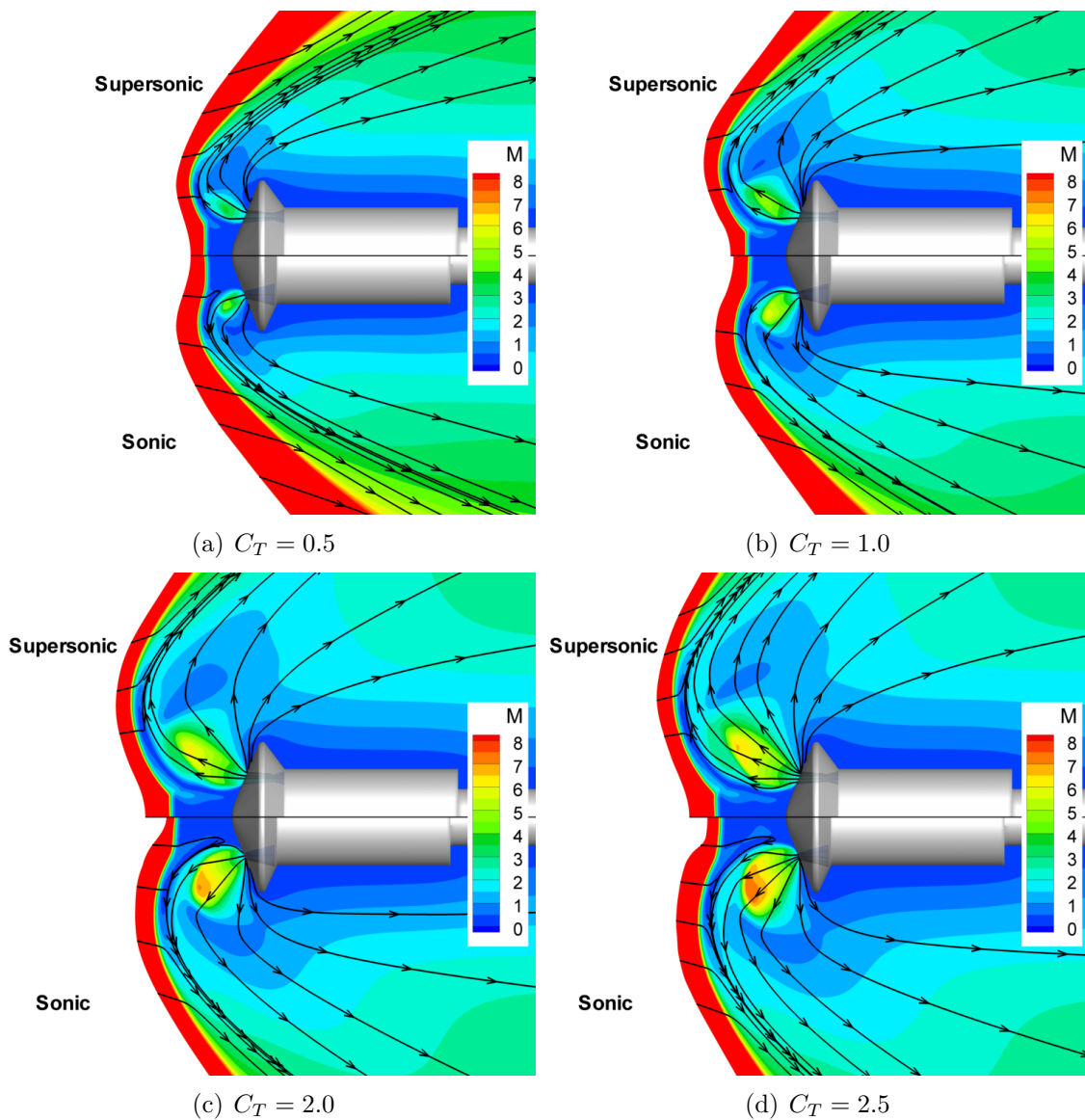


Figure 4.6: Comparison of Mach number contours for sonic (bottom) and supersonic (top) peripheral PD jets at various thrust coefficients.

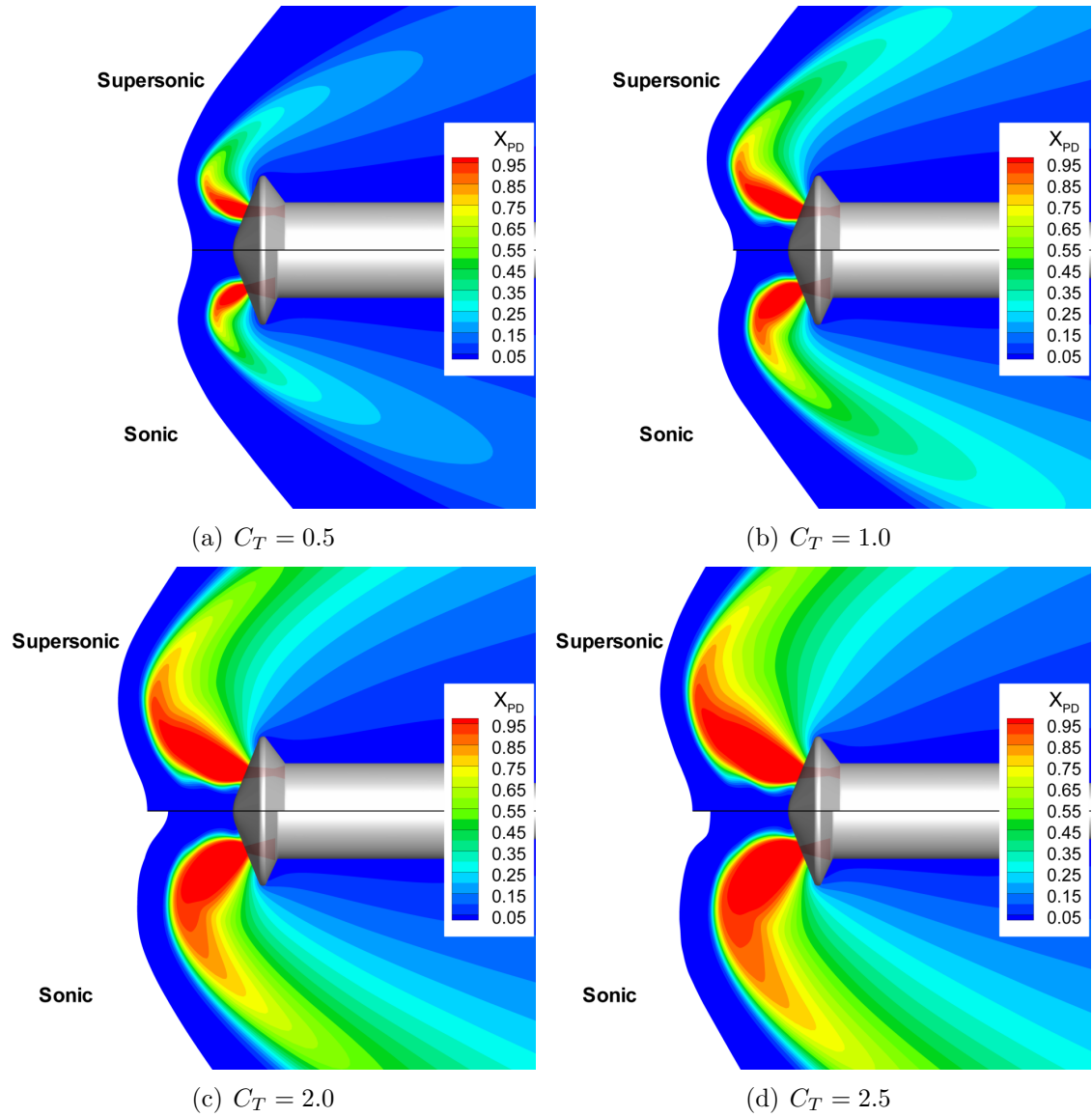


Figure 4.7: Comparison of PD jet species mole fraction contours for sonic (bottom) and supersonic (top) peripheral PD jets at various thrust coefficients.

size of the breakdown region increase with thrust coefficient, as can be seen in Figures 4.8(b)-4.8(d). This continuum-breakdown region, however, is not observed in the contours for the supersonic jets even at the highest thrust coefficient investigated in this study.

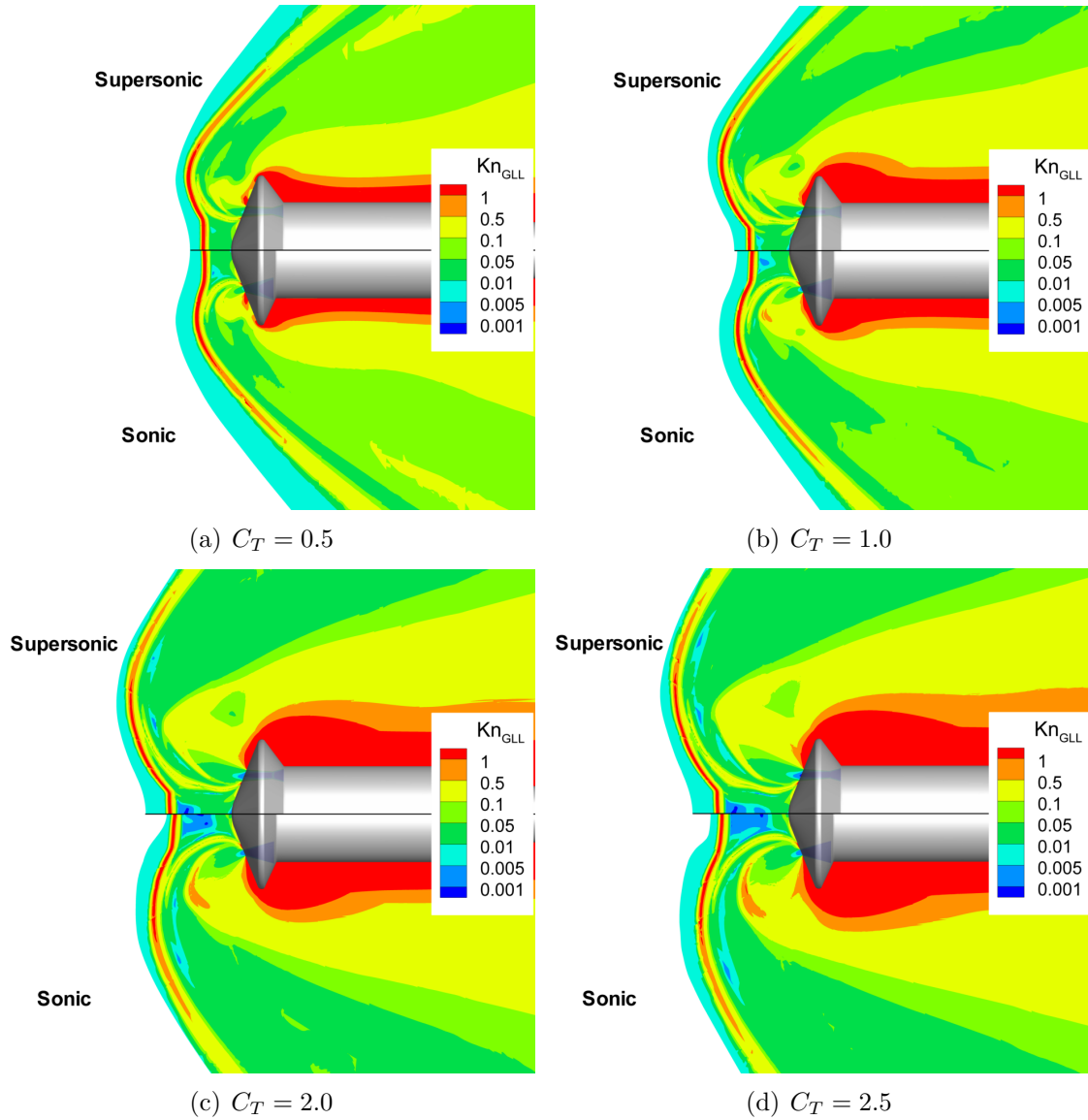


Figure 4.8: Comparison of gradient-length local Knudsen number contours for sonic (bottom) and supersonic (top) peripheral PD jets at various thrust coefficients.

### 4.3.2 Surface Effects

The surface properties for the sonic and supersonic peripheral PD jets are presented in Figure 4.9 as non-dimensional pressure coefficient. The figure also presents the distribution of the pressure coefficient for the no-jet case for comparison. The contours show overall similar pressure distributions on the aeroshell forebody for the sonic and supersonic jets. The distribution between two adjacent jets and near the aeroshell nose for the peripheral jets is similar to the no-jet case. This suggests that the peripheral jets can preserve some of the relatively high forebody pressures associated with the no-jet case. However, the figure also shows a low pressure region behind the jets (i.e. downstream of the nozzle-exit), which expands in size as the thrust coefficient increases for both sonic and supersonic jets.

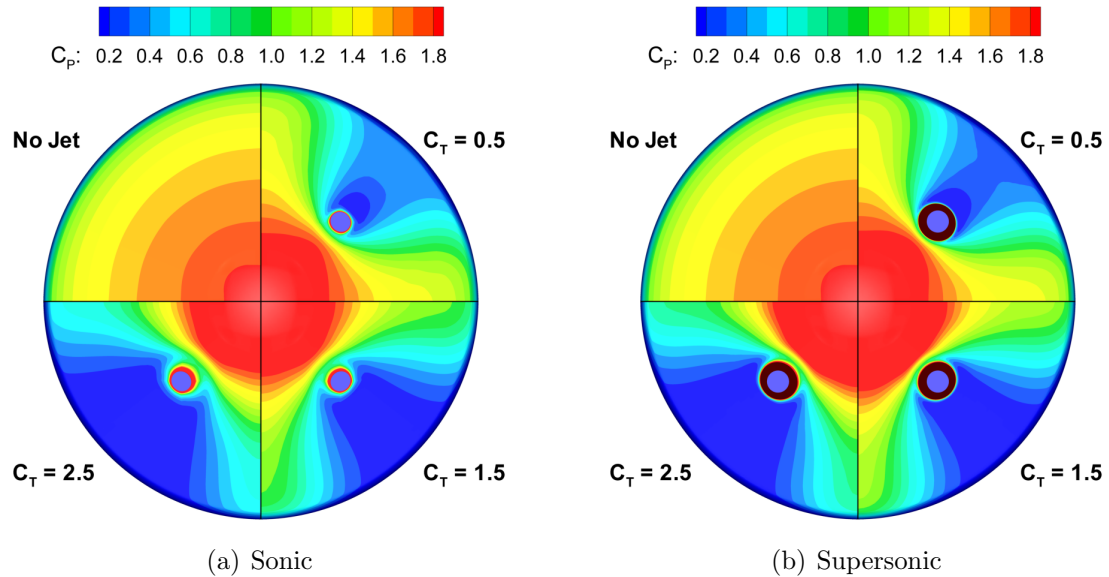


Figure 4.9: Comparison of forebody pressure coefficient contours for sonic and supersonic peripheral PD jets at various thrust coefficients.

### 4.3.3 Aerodynamic Effects

The drag and axial force coefficients for the sonic and supersonic peripheral PD jets are presented in Figure 4.10. The drag force is calculated by integrating the surface



pressure and shear stress along the aeroshell surface, excluding the sting. The figure shows very similar trends and overall similar values of drag and axial force coefficients for the sonic and supersonic peripheral jets. The drag for both configurations is inversely proportional to the PD thrust. The drag coefficient decreases from 1.55 for the no-jet case to approximately 0.76 for  $C_T = 2.5$  for the sonic jet, which corresponds to a 51% decrease, mainly due to the low surface pressure region downstream of the PD nozzle observed in Figure 4.9. The supersonic peripheral jet produces a slightly higher drag coefficient compared to the sonic jet for all thrust coefficients, with a maximum difference of approximately 8%. Unlike the aerodynamic drag, the axial force is proportional to the thrust coefficient. The axial force coefficient for  $C_T = 2.5$  is about 3.3 for the sonic jet, which is more than double the value of the no-jet case. The supersonic peripheral jet also generates slightly larger axial force coefficients due to larger drag coefficients compared to the sonic jet. The difference in the axial force coefficient between the two jet conditions, however, is small and does not exceed 2%.

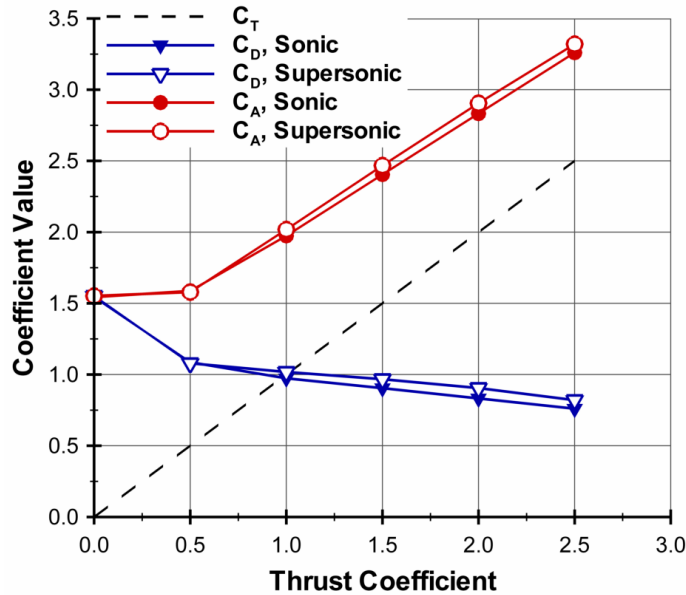
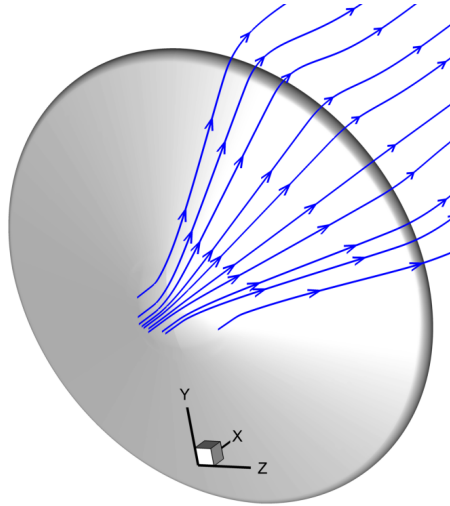


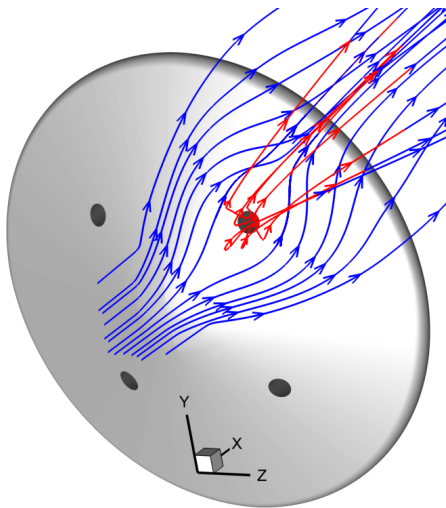
Figure 4.10: Comparison of drag and axial force coefficients for sonic and supersonic peripheral PD jets.

The low surface pressure regions downstream of the PD nozzle-exit are the main mechanism responsible for decreasing the aerodynamic drag coefficient. These regions are caused by an obstruction of the flow around the aeroshell by the PD jets. Figure 4.11 shows velocity streamlines for the no-jet and the sonic peripheral PD jet configurations in order to illustrate this obstruction. The blue streamlines represent particle paths originating from the freestream, while the red streamlines correspond to paths originating from the PD jet. The figure shows that the PD jet disrupts the path of the particles from the freestream along the aeroshell forebody and causes them to flow around the jet. This creates a wake-like region downstream of the PD jet, which is characterized by relatively low surface pressures. Figures 4.11(b) and 4.11(c) also show that the level of obstruction increases with thrust coefficient since the size of the PD jet increases. As a result, the size of the wake region (i.e. low pressure region) behind the PD jet expands and the aerodynamic drag coefficient decreases as the PD thrust increases. This result suggests that the peripheral PD jets may preserve more aerodynamic drag on the aeroshell forebody if they are placed closer to the shoulder, such that the low pressure region downstream of the PD nozzle created by the jet plume obstruction is moved away from the forebody to the backshell.

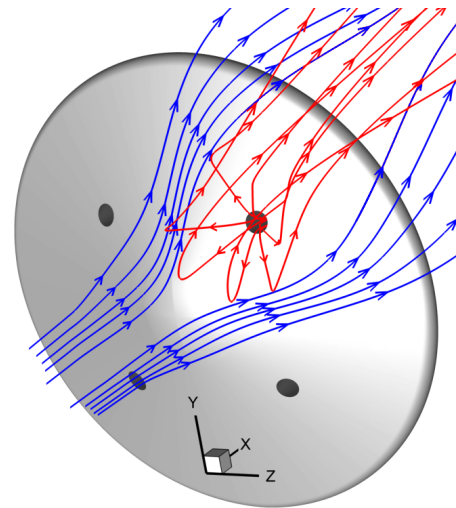
The aerodynamic properties of the aeroshell with sonic and supersonic peripheral PD jets are summarized in Figure 4.12. The figure presents the variation of the axial force coefficient with thrust coefficient, as well as the contributions to the axial force from the aerodynamic drag and thrust coefficients. The plots show overall similar axial force and aerodynamic drag for the sonic and supersonic peripheral PD jets. The axial force coefficient is proportional to the PD thrust for the range of thrust coefficient values investigated in this study due to the ability of the peripheral jets to preserve some the aerodynamic drag associated with the no-jet case. The drag contribution to the axial force ranges from approximately 70% to almost 25% for the 0.5 and 2.5 thrust coefficients, respectively. Similar to the central configuration, the



(a) No jet



(b)  $C_T = 0.5$



(c)  $C_T = 2.5$

Figure 4.11: Velocity streamlines along the aeroshell forebody for the no-jet and sonic peripheral jet configurations (blue: freestream flow; red: PD jet flow).

supersonic peripheral jets may have a potential advantage over the sonic peripheral jets with respect to the aerodynamic properties of the aeroshell and the propellant mass requirements because they provide 2% more axial force with an average of 15% less mass flow rate.

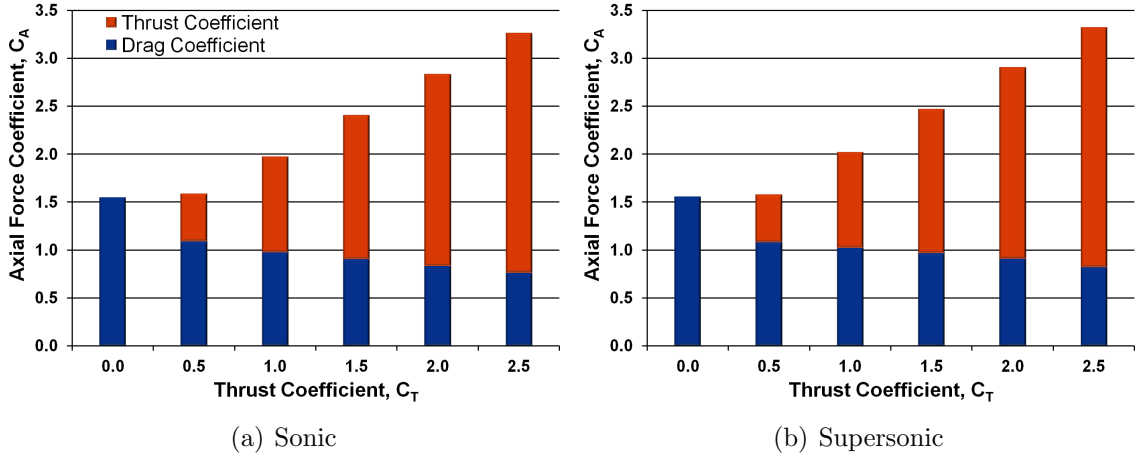


Figure 4.12: Drag and thrust contributions to the axial force on the aeroshell for sonic and supersonic peripheral PD jets.

#### 4.4 Comparisons Between Peripheral and Central PD Jets

It is clear based on the results presented in the previous section and in Chapter III that the propulsive deceleration configuration has a major impact on the properties of Mars-entry aeroshells. This section compares the numerical results for peripheral and central PD jets at various thrust conditions in order to examine how the PD configuration affects the flowfield, surface, and aerodynamic properties of the aeroshell. The comparisons mainly focus on sonic peripheral and central jets since it was shown in the previous section and in Chapter III that the PD jet Mach number does not have a significant effect on the aeroshell properties. The section also presents a discussion on the deceleration performance of Mars-entry aeroshells with central and peripheral PD jets.

#### 4.4.1 Flowfield Properties

Mach number contours and velocity streamlines for sonic peripheral and central PD jets are presented in Figure 4.13 for thrust coefficients of 0.5 and 2.5. The sting is also added for the central PD jet in order to provide a more consistent comparison between the two PD configurations. The central PD jets expand to higher Mach numbers upstream of the aeroshell before decelerating to subsonic conditions through a terminal jet shock compared to the peripheral jets. The reason for this is that the stagnation pressure of the central jets is higher than the stagnation pressure of *each* peripheral jet in order to obtain the same total thrust coefficient for the two configurations. The central jets move the stagnation point away from the aeroshell surface to the interface region between the bow and jet shocks, and increase the apparent size of the aeroshell as perceived by the main freestream flow based on the velocity streamlines. The peripheral jets, on the other hand, keep the stagnation point on the surface of the aeroshell and preserve the portion of the bow shock upstream of the aeroshell nose almost normal to the freestream flow. The central jets also generate a recirculation region along the aeroshell forebody that decreases in size until the flow is completely reattached at a thrust coefficient of approximately 2.0. The peripheral jets, however, do not generate any recirculation regions along the aeroshell forebody.

Figure 4.14 shows the PD jet species mole fraction flowfield distribution for the sonic peripheral and central configurations for the 0.5 and 2.5 thrust coefficients. The figure reveals that most of the jet species for the central PD configuration move upstream of the aeroshell to the interface region before being transported by the main freestream flow to the wake. The jet species for the peripheral configuration are swept away by the main freestream flow downstream of the aeroshell and only a small amount of the jet species move upstream of the aeroshell nose. This may be desirable during real entry flights because the peripheral configuration allows the hot exhaust

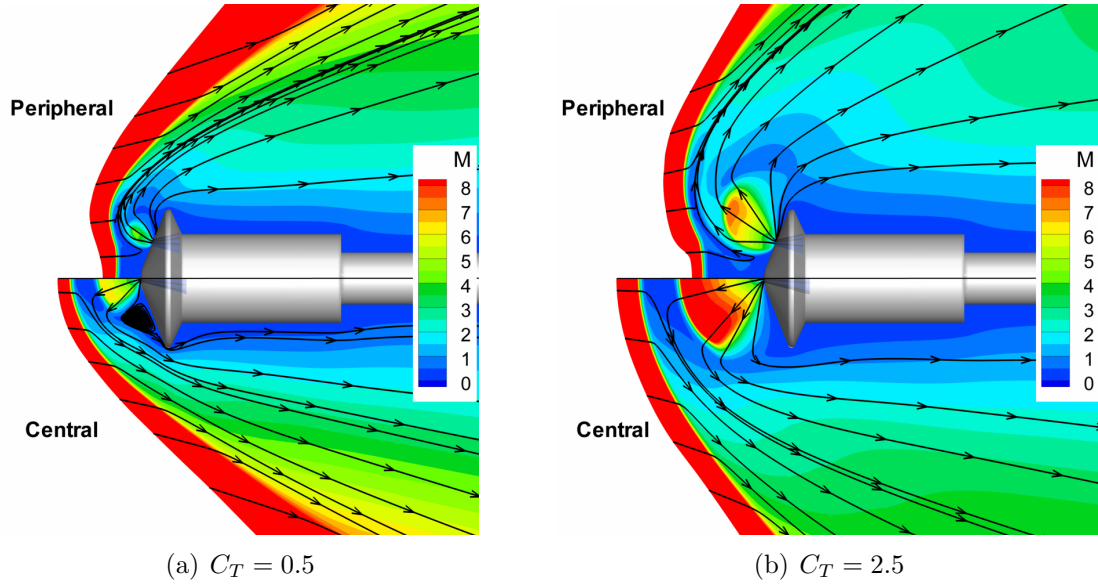


Figure 4.13: Comparison of Mach number contours for sonic peripheral (top) and central (bottom) PD jets at  $C_T = 0.5$  and  $2.5$ .

gases and the propellant by-products from the PD nozzle to be quickly transported away from the region near the aeroshell.

The distribution of the gradient-length local Knudsen number for the sonic peripheral and central configurations is presented in Figure 4.15 for  $C_T = 0.5$  and  $2.5$ . The figure shows significant continuum breakdown in the bow shock and the wake for both configurations. The contours also indicate larger continuum breakdown regions for the central configuration along the aeroshell forebody, especially near the nose. These regions are caused by the large gradients in the fluid properties induced by the central jet, particularly across the jet boundary, as well as the lower density near the aeroshell surface due to the shielding effect of the central configuration.

#### 4.4.2 Aerodynamic Properties

The differences between the peripheral and central PD jets also extend to the aerodynamic properties of the aeroshell. Figure 4.16 presents the drag and axial force coefficients for the peripheral and central PD configurations. The figure shows that

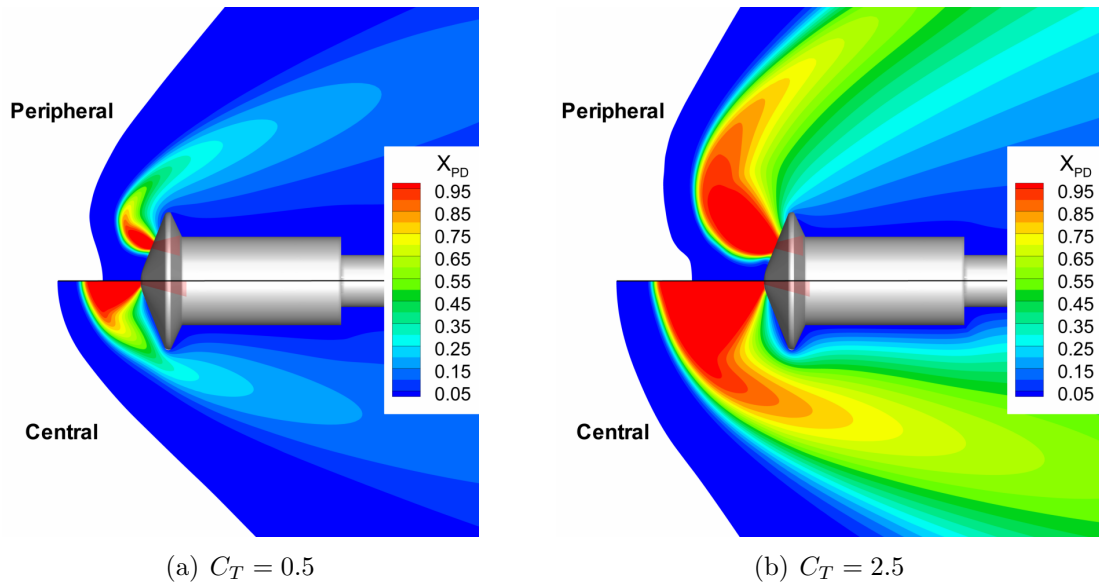


Figure 4.14: Comparison of PD jet species mole fraction contours for sonic peripheral (top) and central (bottom) PD jets at  $C_T = 0.5$  and  $2.5$ .

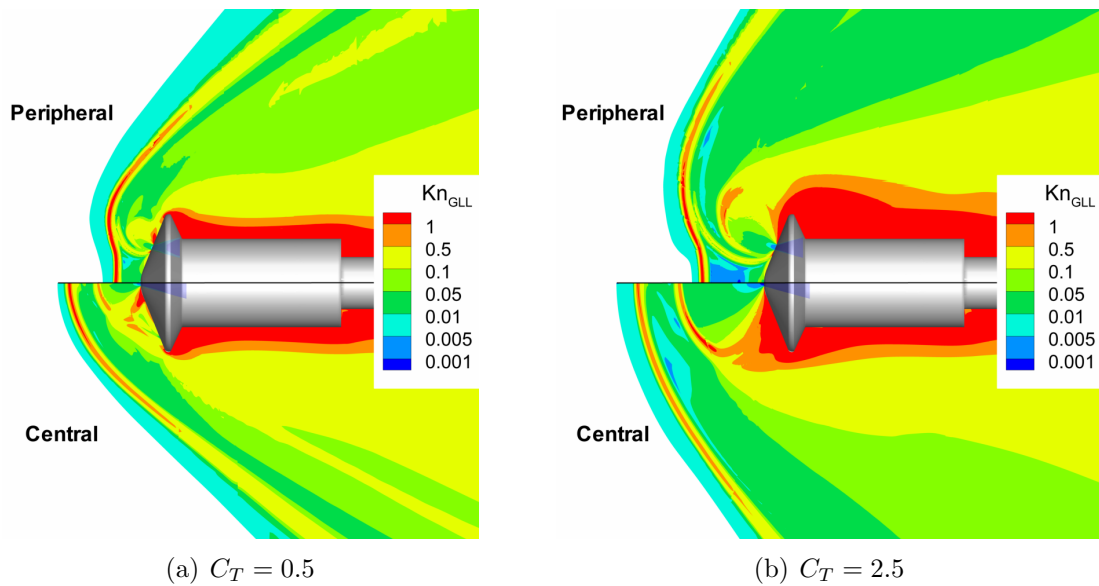


Figure 4.15: Comparison of gradient-length local Knudsen number contours for sonic peripheral (top) and central (bottom) PD jets at  $C_T = 0.5$  and  $2.5$ .

the aerodynamic drag is inversely proportional to the PD thrust for both configurations. However, the drag coefficient for the peripheral jets is larger than for the central jets for all thrust coefficients investigated in this study. The peripheral PD jets provide between 3 to 7 times more drag than the central jets for thrust coefficients of 0.5 and 2.5, respectively. The differences in the aerodynamic drag between the two configurations also affect the axial force trend. The axial force coefficient for the central PD jets initially decreases as the thrust coefficient increases, and then increases for thrust coefficients greater than 0.5 mainly due to the contribution from the thrust. As a result, the axial force coefficient for the central configuration does not exceed the drag coefficient for the no-jet case until  $C_T = 1.5$ . The axial force coefficient for the peripheral jets, however, increases for all thrust coefficients investigated in this study. This result suggests that the peripheral configuration with four PD jets is better than the central configuration with respect to the aerodynamic properties of a Mars-entry aeroshell because the peripheral jets can provide more force to decelerate the vehicle at a given thrust coefficient.

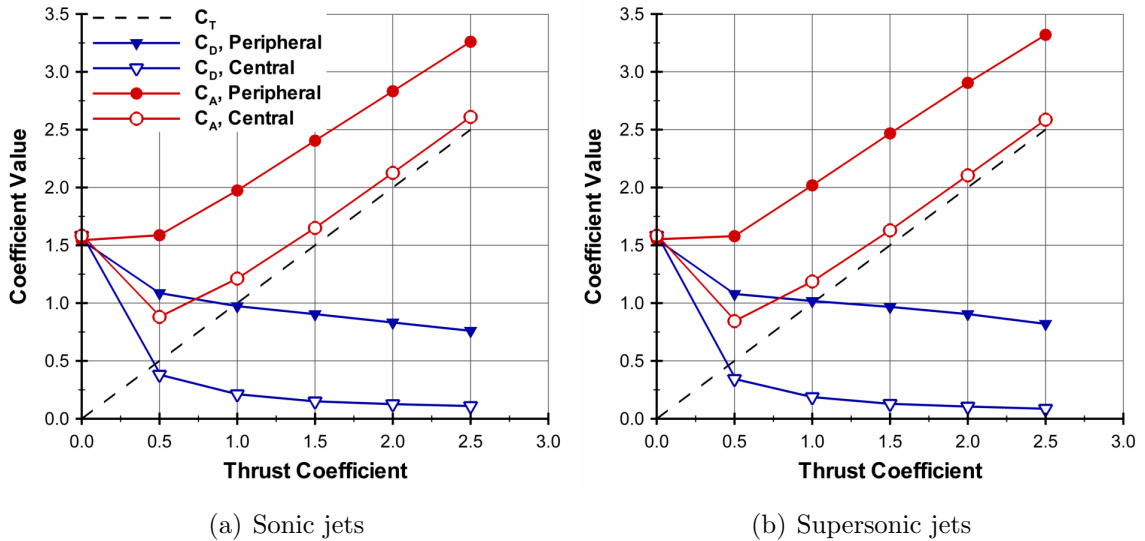


Figure 4.16: Comparison of drag and axial force coefficients for peripheral and central PD jets.



The trends observed in the aerodynamic properties of aeroshells with peripheral and central PD jets can be explained by examining the surface pressure distributions for the two PD configurations. Figure 4.17 shows forebody pressure coefficient contours for sonic peripheral and central PD jets at various thrust coefficients. The figure also compares these results with the no-jet case. As can be seen from Figure 4.17(b), the relatively high pressure on the aeroshell forebody for the no-jet case is replaced by low pressure values caused by the shielding effect of the central configuration. This shield prevents mass and momentum in the freestream from reaching the aeroshell surface. As the thrust coefficient increases, the size of the central jet, and hence the shielding effect, also increases. As a result, less mass and momentum from the freestream reach the aeroshell, which causes a decrease in the pressure values over the entire forebody surface. The peripheral PD jets, on the other hand, preserve some of the high forebody pressure of the no-jet case near the aeroshell nose and between adjacent PD jets. As a result, the peripheral PD jets can preserve more aerodynamic drag and produce larger axial force than the central jets.

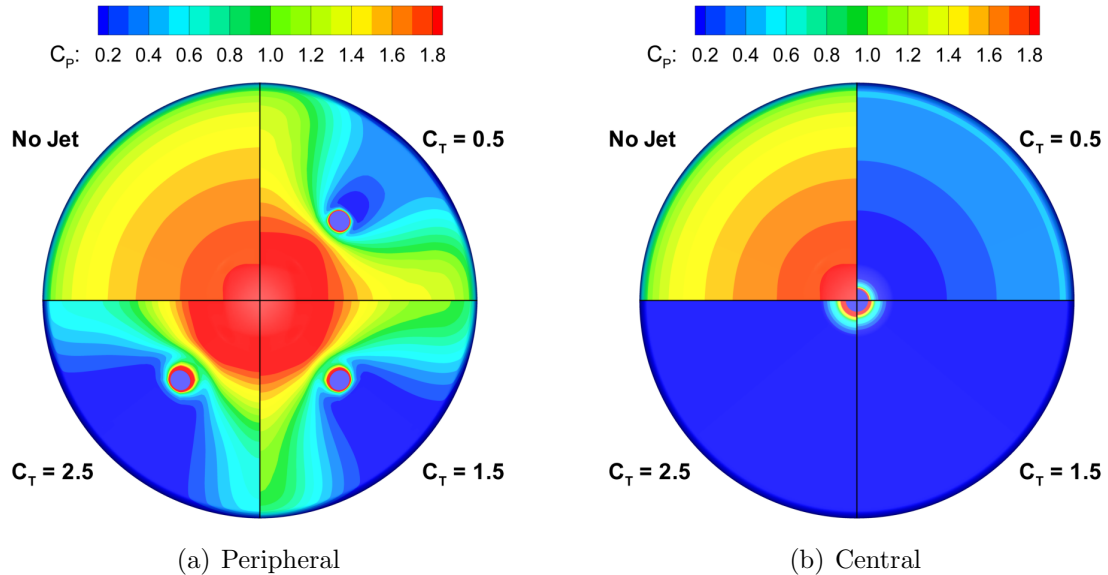


Figure 4.17: Comparison of forebody pressure coefficient contours for sonic peripheral and central PD jets.

### 4.4.3 Deceleration Performance

The deceleration performance for peripheral and central PD jets can be summarized using Figure 4.18. The figure shows the ratio of the axial force coefficient to an “ideal” axial force coefficient for the two propulsive deceleration configurations for the thrust coefficients investigated in this study. The ideal axial force coefficient is equal to the sum of the thrust coefficient and the drag coefficient for the no-jet case. This ratio indicates no change to the axial force on the aeroshell if it is equal to unity, drag augmentation if it is greater than 1, and drag reduction if it is less than 1. Both the peripheral and central PD jets produce axial force ratios that are less than unity since the drag is inversely proportional to the thrust. The axial force ratio for the peripheral jets is roughly constant at approximately 0.81 over most of the thrust coefficients investigated in this study for both sonic and supersonic jets. The ratio for the central configuration, however, increases from approximately 0.40 for  $C_T = 0.5$  to about 0.65 for  $C_T = 2.5$  for both sonic and supersonic jets. This suggests that the deceleration performance provided by the peripheral jets is roughly constant at 81% of an ideal performance, while the deceleration performance for the central jets is a function of the thrust coefficient and increases from 40% to 65% for the thrust coefficients investigated in this study. This result presents another advantage of the peripheral configuration because the deceleration performance can remain roughly constant and relatively large compared to an ideal performance over a range of thrust conditions.

## 4.5 Summary

This chapter presented a numerical investigation of the fluid interactions of peripheral propulsive deceleration for Mars-entry aeroshells. Both sonic and supersonic peripheral PD jets were considered in this study in order to quantify the effects of the

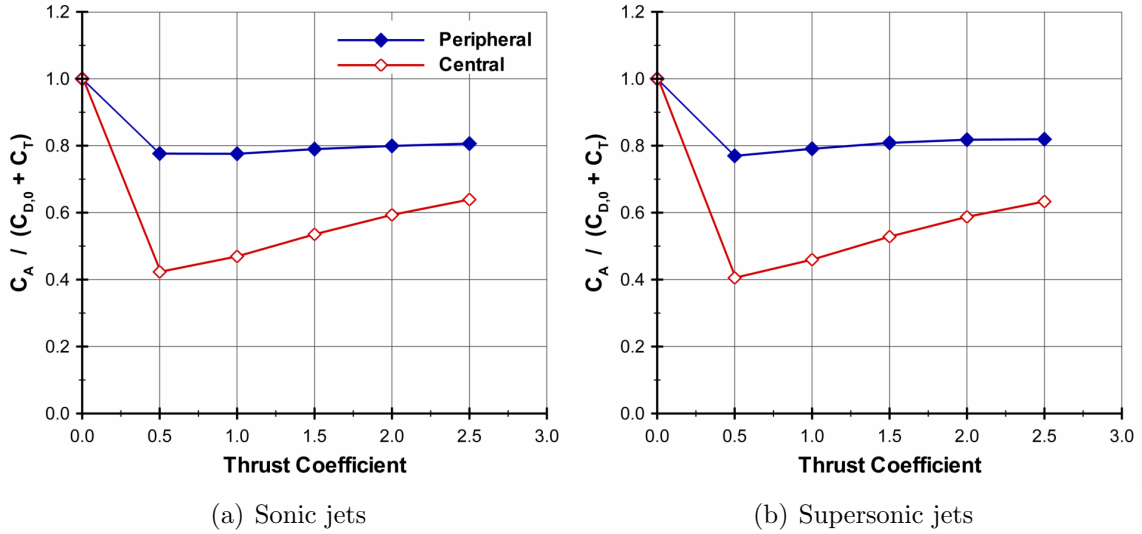


Figure 4.18: Deceleration performance for peripheral and central PD jets.

jet Mach number and conditions on the flowfield, surface, and aerodynamic properties of the aeroshell. A 10 mm diameter aeroshell with four PD jets located approximately halfway between the aeroshell nose and shoulder and directed parallel to the capsule axis was used in the numerical simulations. The aeroshell geometry was based on test models used in experiments in order to compare the numerical results with experimental measurements. I<sub>2</sub>-seeded N<sub>2</sub> gas was used in both the freestream flow and the PD jet. The Ashkenas and Sherman relations were also used to determine the freestream conditions in the numerical simulations based on a leading-edge Mach number of 12.

The first section of the study examined the effects of the peripheral jet Mach number on the aeroshell properties. The results showed that the overall flowfield features are similar for both sonic and supersonic peripheral PD jets. The jets change the bow shock profile around the aeroshell to a saddle shape by pushing the portion of the shock near the jet plume upstream. The PD jet species were swept away by the main freestream flow downstream of the aeroshell. The results also showed the onset of a terminal jet shock for the sonic jets that began at a thrust coefficient of

approximately 1.0. This shock, however, was not observed for the supersonic jets. The drag coefficient for the peripheral PD jets was inversely proportional to the thrust coefficient. This was found to be caused by the obstruction of the flow around the aeroshell by the peripheral PD jets, which created low surface pressure regions similar to wake flows downstream of the PD nozzle-exit. The results also showed that the Mach number of the peripheral PD jets had small effects on the aerodynamic properties of the aeroshell, with a maximum difference less than 2% in the axial force coefficient between the sonic and supersonic jets. However, the supersonic peripheral jets may have an advantage over the sonic jets because they utilized on average a 15% lower mass flow rate, which can produce propellant mass savings for future Mars missions with propulsive deceleration.

The second portion of the study examined the effects of the propulsive deceleration configuration by comparing the flowfield, surface, and aerodynamic properties of a Mars-entry aeroshell with peripheral and central PD jets. These comparisons revealed significant differences in the deceleration performance of the two configurations. Although the drag was inversely proportional to the thrust for both configurations, the peripheral PD jets provided 3 to 7 times more drag than the central PD jets for both sonic and supersonic jets. The reason for this was that the peripheral jets preserved some of the relatively high surface pressure associated with the no-jet case, particularly near the aeroshell nose and between adjacent PD jets. The axial force coefficient for the peripheral jets increased with the thrust coefficient, and, unlike the central PD jets, was always greater than the drag coefficient for the no-jet case. This is an important advantage of the peripheral jets because they improved the deceleration performance of the aeroshell over all thrust coefficients investigated in this study. Another advantage of the peripheral PD jets was that the deceleration performance compared to an ideal performance equal to the sum of the thrust and no-jet drag coefficients remained high and roughly constant over a range of thrust conditions.

## CHAPTER V

# Reaction Control System

Similar to propulsive deceleration, reaction control systems (RCS) are currently being investigated as an enabling technology for future Mars-entry vehicles. A reaction control system can provide vehicle control and steering during atmospheric descent by inducing moments using thrusters located on the aftbody of the capsule. The RCS can either guide the vehicle to the target landing site or correct the flight path in real-time. As a result, the RCS can reduce the landing footprint of Mars-entry systems and allow them to land at scientifically interesting sites while avoiding dangerous surface hazards (e.g. rocks). This added capability will be crucial for future robotic sample-return missions and human-exploration of Mars. The Mars Science Laboratory will make the first attempt at using RCS thrusters for a guided Mars entry through the hypersonic and supersonic phases of the EDL [52]. The layout of the RCS thrusters for MSL has gone through numerous designs due to several constraints, which include aerodynamic interference [41]. The analysis carried out for the MSL mission has also concluded that there is still a need for further development of reaction control systems as an important part of future Mars-entry vehicles [41].

This chapter presents a numerical study of the fluid interactions produced by RCS jets in hypersonic freestream conditions in an effort to continue the development of reaction control systems for Mars-entry aeroshells. The chapter first provides details

on the aeroshell geometry and RCS jet conditions used in this study. The chapter then describes the flowfield, surface, and aerodynamic properties of a Mars-entry aeroshell without an RCS jet (i.e. baseline configuration) at a  $20^\circ$  angle-of-attack. Next, the chapter presents the results for two different RCS jet configurations. The first configuration uses an RCS jet oriented almost parallel to the main freestream flow, while the second configuration uses a jet directed almost transverse to the freestream flow. The results for these two configurations are used to understand the effects of the RCS jet on the properties of the aeroshell, and how the orientation of the thrust force provided by the RCS influences the fluid interactions induced by the jet. The chapter then presents a discussion on the effects of these induced fluid interactions on the control effectiveness of each RCS configuration. Finally, the chapter summarizes the major conclusions of the numerical investigation.

## 5.1 Numerical Setup

The Ashkenas and Sherman relations are used in the numerical simulations to determine the freestream conditions in order to compare the results to experimental data obtained at the University of Virginia. Non-dimensional parameters, such as drag coefficient, are calculated using the reference freestream conditions given in Table 2.1 for a leading-edge Mach number of 12. The freestream flow and RCS jet are composed of molecular nitrogen seeded with 200 ppm of molecular iodine. The aeroshell is at an angle-of-attack of  $20^\circ$  in order to simulate the conditions of a lifting trajectory in which the lift vector can be utilized to provide some control of the vehicle during atmospheric descent. This section outlines the details of the aeroshell geometry and the RCS jet conditions used in this numerical study.

### 5.1.1 Aeroshell Geometry

The geometries for the Mars-entry aeroshell with parallel and transverse RCS jets are shown in Figures 5.1(a) and 5.1(b), respectively. The aeroshell is a scaled version of the MSL capsule, and is based on the test models used in the experiments at the University of Virginia [56]. The diameter of the aeroshell is equal to 20 mm, which is equivalent to approximately 0.44% of the MSL capsule. The Reynolds number and Knudsen number based on the aeroshell diameter and the reference freestream conditions are equal to 2,400 and 0.0075, respectively, which indicate that the flow is laminar and near-continuum. The aeroshell includes a “sting” attached to the leeward side of the backshell that is used in the experiments to hold the model in the test section and to supply the flow to the RCS jet. A single RCS jet is located about halfway along the windward side of the aeroshell aftbody, and is approximately directed either parallel or transverse to the main freestream flow. A single jet layout is chosen for this study to isolate the effects of each RCS thruster on the overall properties of the aeroshell. The jet for both configurations is supplied through a sonic nozzle with an exit diameter of 0.5 mm.

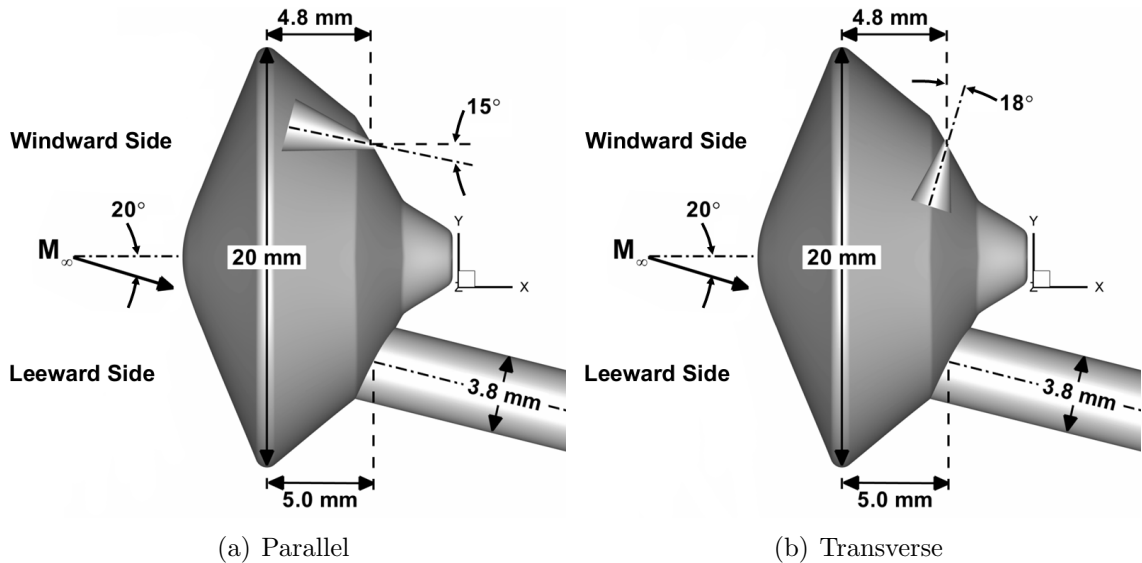


Figure 5.1: Aeroshell geometry with parallel and transverse RCS jets.

Three-dimensional simulations are performed using LeMANS to investigate the fluid interactions generated by parallel and transverse RCS jets. The computational domain consists of one half of the aeroshell geometry due to the symmetry of the flow in order to reduce the computational cost of the simulations. The upstream boundary of the domain is aligned with the bow shock around the aeroshell based on preliminary solutions. Details regarding the adaptation process are provided in Appendix B. The computational grid contains approximately 9 million hexahedral cells, with clustering near the aeroshell surface and in the vicinity of the RCS jet. Figure 5.2 presents the surface mesh along the aeroshell forebody and aftbody used in the computations. Each simulation takes approximately 14,000 CPU-hours with about 200 Intel Xeon X5670 (Westmere) processors to reach a steady-state solution using a point-implicit time integration method.

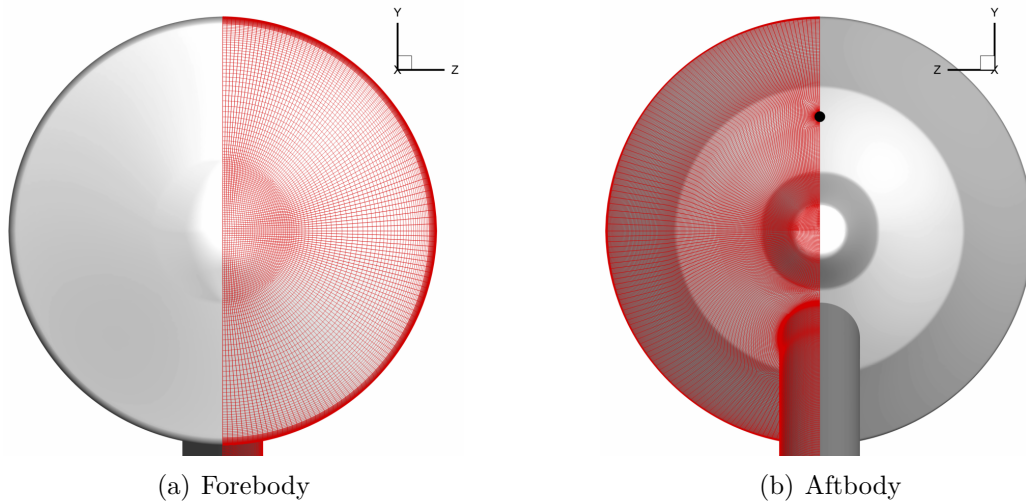


Figure 5.2: Surface mesh used in the RCS jet simulations.

### 5.1.2 RCS Jet Conditions

Early work on the Space Shuttle Orbiter had indicated that one of the main scaling parameters for testing of the reaction control system is the ratio of the RCS jet momentum to the freestream momentum (i.e.  $(\dot{m}U)_{jet}/(\dot{m}U)_{\infty}$ ) [42]. This scaling



parameter was also used to test the performance of the RCS jets for MSL [55]. The final design for the MSL RCS consists of eight total thrusters arranged in four pairs, with each thruster capable of delivering a maximum thrust force of 290 N [53]. The exit diameter for each MSL RCS nozzle is 65 mm. Table 5.1 presents freestream and RCS jet (nozzle-exit) conditions that MSL is expected to encounter during flight. The mass flow rate in Table 5.1 is based on the aeroshell frontal area and the nozzle-exit area for the freestream and RCS jet conditions, respectively.

Table 5.1: Expected freestream and RCS jet at maximum thrust conditions for MSL during flight. Data from Ref. [55].

Parameter	Freestream	RCS Jet
$\gamma$	1.313	1.346
$M$	10.0	4.47
$P_0$ , Pa	$1.8 \times 10^7$	$1.1 \times 10^6$
$\dot{m}U$ , N	$2.9 \times 10^5$	289

In order to match the ratio of jet momentum to freestream momentum expected to be experienced in flight, the stagnation pressure of the RCS jet for the current study can be calculated as,

$$P_{0,jet} = \left( \frac{\gamma_e M_e^2 P_e \sum_{jets} S_e}{\gamma_\infty M_\infty^2 P_\infty S} \right)_{flight} \left( \frac{\gamma_{ref} M_{ref}^2 S P_{0,jet} P_{ref}}{\gamma_e M_e^2 S_e P_e} \right) \quad (5.1)$$

where,

$$\frac{P_0}{P} = \left( 1 + \frac{\gamma - 1}{2} M^2 \right)^{\frac{\gamma}{\gamma - 1}} \quad (5.2)$$

Using these relations, the stagnation pressure of the RCS jet should be equal to 4,440 Pa for the current study in order to obtain the same momentum ratio as expected in flight. However, this pressure value is smaller than the smallest increment in the pressure gage used in the experimental setup at the University of Virginia, which is below the acceptable range of confidence. Therefore, in order to minimize

the uncertainty in the experimental setup to within an acceptable range, the stagnation pressure of the RCS jet for the current study is increased to 8,040 Pa, which corresponds to an 80% increase in the momentum ratio. A higher RCS jet stagnation pressure of 161,000 Pa is also considered in this study, which is well within the confidence range of the experimental setup. Similar to propulsive deceleration, the conditions of the RCS jet can be non-dimensionalized using the thrust coefficient given in Equation 3.1. Note, however, that the contribution of  $P_{amb}$  to the thrust coefficient is negligible since the RCS jet exhausts in the wake region where the pressure values are typically small. The two RCS jet stagnation pressures considered in this study correspond to thrust coefficient values of 0.05 and 1.0. Table 5.2 presents the design total pressure ratio, Reynolds number, mass flow rate, and momentum ratio based on the RCS nozzle-conditions for the two thrust coefficients investigated in this study. The relatively large Reynolds number for the 1.0 thrust coefficient case may indicate the potential transition of the jet from laminar to turbulent flow.

Table 5.2: Design conditions for the parallel and transverse RCS jets.

$C_T$	$P_{0,jet}/P_0$	$Re_{jet}$	$\dot{m}_{jet}$ , mg/s	$(\dot{m}U)_{jet}/(\dot{m}U)_{ref}$
0.05	0.04	570	4.0	0.014
1.0	0.88	11,000	81	0.284

The RCS jet conditions are calculated using the isentropic relations such that the Mach number at the nozzle-exit is equal to 1.0 for both the parallel and transverse configurations. However, it is important to understand how these conditions are affected by the viscous effects along the nozzle walls. Figure 5.3 presents Mach number contours in the RCS nozzle for the parallel and transverse RCS jets at  $C_T = 0.05$  and 1.0. The figure shows that the Mach number is equal to unity at the nozzle-exit for the parallel and transverse jets at both thrust coefficients. The figure also indicates that the boundary layer thickness along the nozzle walls is smaller for the higher thrust conditions due to the larger favorable pressure gradient. The discharge

coefficient of the RCS nozzles is approximately equal to 0.8 as a result of the viscous losses that occur along the nozzle walls.

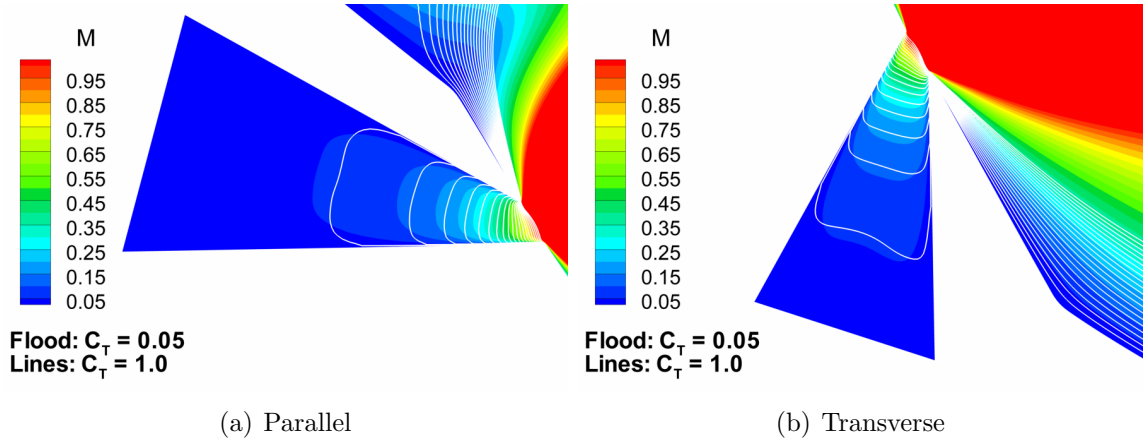


Figure 5.3: Mach number distribution in the nozzle for the parallel and transverse RCS jets.

## 5.2 Baseline Configuration

This section describes the flowfield, surface, and aerodynamic properties of the aeroshell without the RCS jet (i.e. baseline configuration) at an angle-of-attack of  $20^\circ$ . These results will be used in the following sections to understand how the fluid interactions produced by the RCS jets affect the properties of the aeroshell. Figure 5.4 presents Mach number and gradient-length local Knudsen number contours for the baseline configuration. Figure 5.4(a) shows that the flow around the aeroshell is characterized by the bow shock around the capsule and a series of expansion and compression waves that develop around the aeroshell shoulders. The local Knudsen number contours shown in Figure 5.4(b) indicate continuum breakdown regions (i.e.  $Kn_{GLL} > 0.05$ ) in the bow shock due to sharp gradients in the flow properties, and in the wake due to low densities.

Contours of the pressure coefficient along the aeroshell forebody and aftbody for the no-jet case at  $20^\circ$  angle-of-attack are presented in Figure 5.5. Figure 5.5(a)

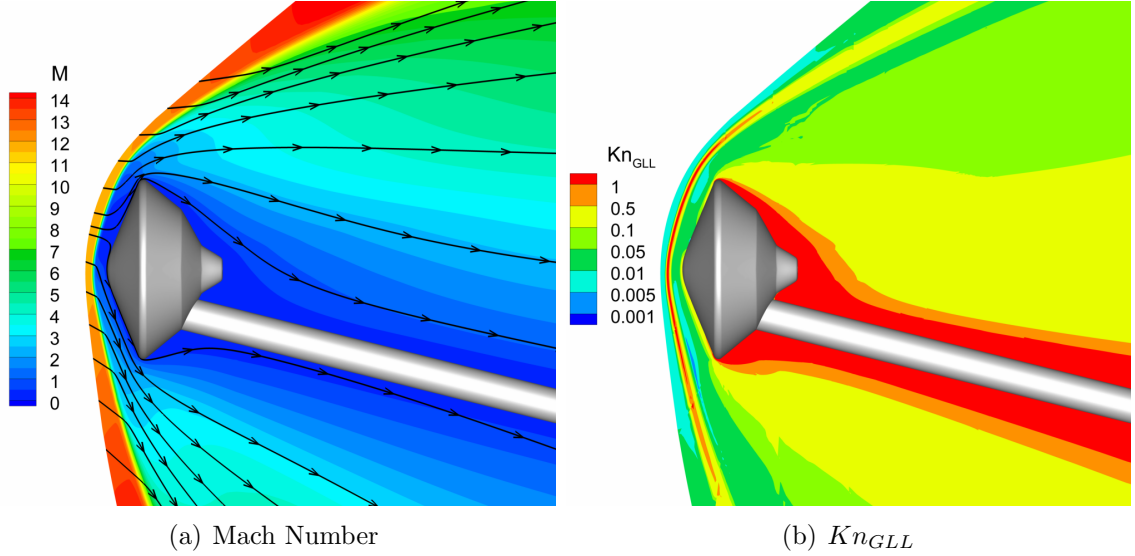


Figure 5.4: Mach number and gradient-length local Knudsen number contours for the no-jet case at 20° angle-of-attack.

shows a large high surface pressure region on the windward side of the aeroshell, with a maximum pressure coefficient value of approximately 2.0 at the stagnation point. The pressure distribution along the aeroshell aftbody shown in Figure 5.5(b) is characterized by very low pressure coefficient values relative to the forebody. In fact, the integrated aftbody pressure downstream of the aeroshell shoulder is over two orders of magnitude smaller than the integrated forebody pressure. This result suggests that the effects of the sting on the aerodynamic properties of the aeroshell are negligible since the force on the aftbody is very small compared to the forebody.

The aerodynamic properties of the aeroshell without the RCS jet at an angle-of-attack of 20° are provided in Table 5.3. The moment coefficient of the aeroshell is determined by,

$$C_M = \frac{M_z}{(1/2) \rho_{ref} U_{ref}^2 D_{model} S} \quad (5.3)$$

where  $M_z$  is the moment (about the  $Z$ -axis) given by,

$$M_z = (X - X_{CG}) F_N - (Y - Y_{CG}) F_A \quad (5.4)$$

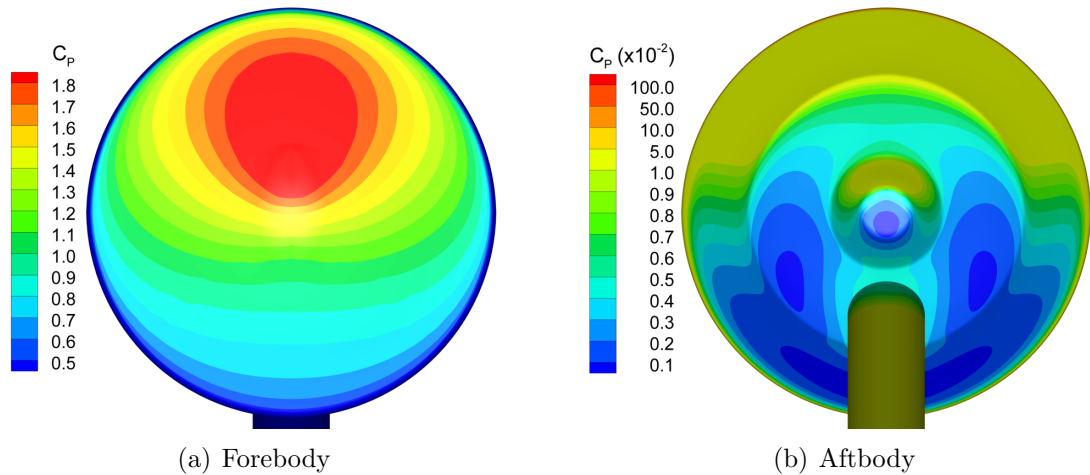


Figure 5.5: Forebody and aftbody pressure coefficient contours for the no-jet case at  $20^\circ$  angle-of-attack.

where  $F_N$  and  $F_A$  are the normal ( $Y$ -direction) and axial ( $X$ -direction) components of the aerodynamic force, respectively, and  $(X, Y)_{CG}$  is the location of the center of gravity of the aeroshell *without* the sting. This choice for the location of the center of gravity is appropriate since the presence of the sting has a negligible effect on the total aerodynamic forces acting on the aeroshell, which are shown schematically in Figure 5.6. The results given in Table 5.3 show that the normal force acting on the aeroshell is negative due to the large surface pressures on the windward side of the aeroshell forebody. The lift force on the aeroshell, however, is positive due to the contribution from the relatively large axial force. The results also show that the moment of the aeroshell is negative (i.e. clockwise-direction), which is also caused by the large surface pressures on the windward portion of the aeroshell forebody.

Table 5.3: Aerodynamic properties of the no-jet case at  $20^\circ$  angle-of-attack.

$C_A$	$C_N$	$C_D$	$C_L$	$L/D$	$C_M$
1.28	-0.17	1.26	0.28	0.22	-0.060

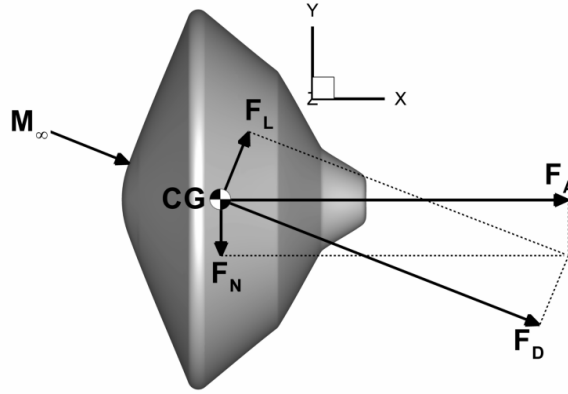


Figure 5.6: Schematic of the aerodynamic forces acting on the aeroshell at  $20^\circ$  angle-of-attack ( $X_{CG}/D_{model} = 0.26$ ,  $Y_{CG}/D_{model} = 0.0$ ).

### 5.3 Parallel RCS Jet

The reaction control system can have a significant impact on the properties of the aeroshell described in the previous section. Therefore, this section outlines the effects of the fluid interactions induced by the parallel RCS jet on the flowfield, surface, and aerodynamic properties of the aeroshell.

#### 5.3.1 Flowfield Properties

Mach number contours and velocity streamlines around the aeroshell with the parallel RCS jet are presented in Figure 5.7 for thrust coefficients of 0.05 and 1.0. The RCS jet at both thrust coefficients expands from sonic conditions at the nozzle-exit to supersonic and hypersonic conditions downstream of the aeroshell in the wake. The velocity streamlines indicate that the parallel RCS jet obstructs the path of the flow from the freestream around the aeroshell aftbody, particularly at  $C_T = 1.0$ , and causes it to move outward along the jet boundary. As a result, the Mach number decreases and the flow is compressed in the region along the aeroshell aftbody upstream of the RCS jet boundary. Figure 5.7(a) shows that the parallel jet at  $C_T = 0.05$  only disturbs the portion of the flow close to the aeroshell on the windward side, and does not have a significant effect on the overall structure of the flowfield. At  $C_T = 1.0$ , the

parallel RCS jet expands to higher Mach numbers and changes the flow in the entire windward portion of the wake region, as can be seen in Figure 5.7(b). The parallel jet, however, does not affect the profile of the bow shock around the aeroshell.

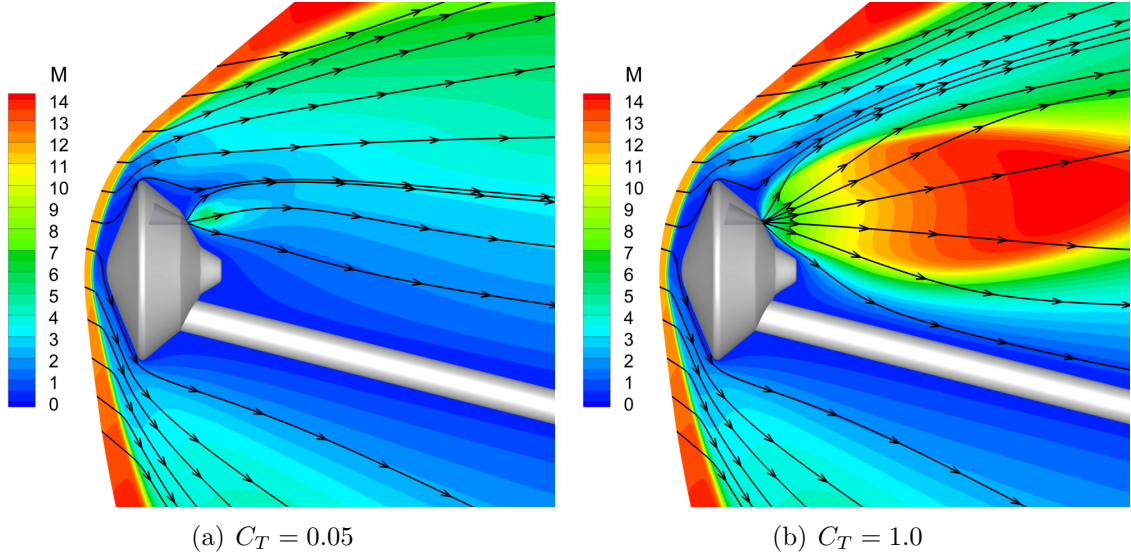


Figure 5.7: Mach number contours for the parallel RCS jet at  $C_T = 0.05$  and  $1.0$ .

The distribution of the RCS jet species mole fraction can be calculated by tagging the  $N_2$  molecules originating from the RCS (i.e. same properties as molecular nitrogen but different name), and is shown in Figure 5.8 for the parallel jet at  $C_T = 0.05$  and  $1.0$ . The contours for the lowest thrust condition presented in Figure 5.8(a) show that the mole fraction of the RCS jet is relatively high close to the aeroshell, and decreases downstream in the wake as the jet expands. At the higher thrust coefficient, the RCS jet mole fraction is large (greater than  $0.95$ ) in roughly the entire windward wake region of the computational domain. Figure 5.8(b) also shows that a significant amount of the jet species impinge on the surface of the aftbody downstream of the RCS nozzle. This impingement is important for the design of the aftbody thermal protection system since the hot exhaust from the RCS nozzle that may be experienced in flight can significantly increase the heat flux to the aeroshell surface.

The gradient-length local Knudsen number contours, shown in Figure 5.9 for the

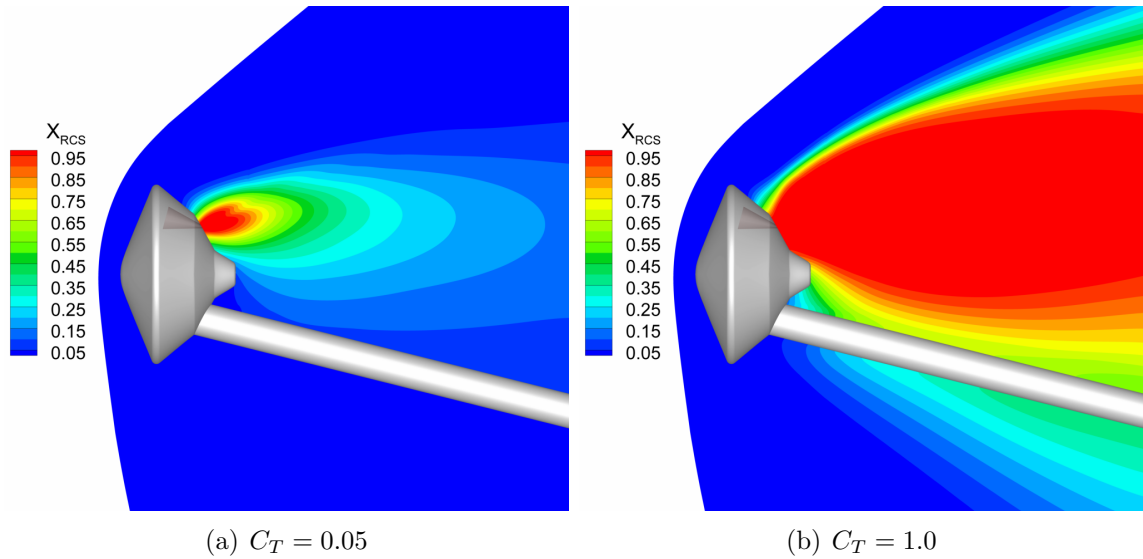


Figure 5.8: RCS jet species mole fraction contours for the parallel RCS jet at  $C_T = 0.05$  and  $1.0$ .

parallel RCS jet at  $C_T = 0.05$  and  $1.0$ , indicate that the RCS jet decreases the level of continuum breakdown around the aeroshell. The figure shows continuum breakdown regions in the bow shock and in the leeward portion of the wake similar to those observed for the no-jet case, as well as across the boundaries of the RCS jet due to the large gradients in the flow properties. However, the added mass from the RCS jet, particularly at the higher thrust conditions, reduces the size of the continuum breakdown regions in the windward side of the wake.

### 5.3.2 Surface Properties

The fluid interactions induced by the parallel RCS jet may also have a significant effect on the surface properties of the aeroshell. In order to examine these effects, Figure 5.10 presents pressure coefficient contours along the aeroshell forebody and aftbody for the parallel RCS jet at the  $0.05$  and  $1.0$  thrust coefficients. Figure 5.10(a) shows that the forebody pressure distribution is unaffected by the RCS jet, and is, in fact, identical to the forebody distribution for the no-jet case shown in Figure 5.5(a). Along the aftbody, however, the RCS jet alters the pressure distribution, particularly



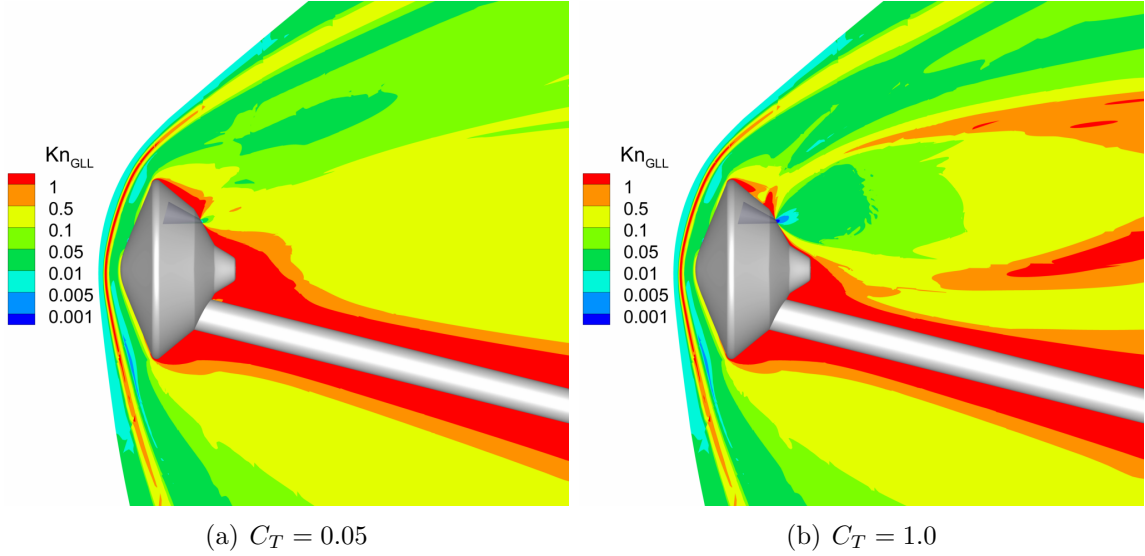


Figure 5.9: Gradient-length local Knudsen contours for the parallel RCS jet at  $C_T = 0.05$  and  $1.0$ .

at the higher thrust conditions. At  $C_T = 0.05$ , the RCS jet only affects the region directly around the nozzle-exit, where the impingement of the jet species causes an increase in the surface pressure. At  $C_T = 1.0$ , the RCS jet increases the pressure on most of the windward side of the aftbody compared to the baseline configuration, particularly downstream of the nozzle-exit near the parachute cone. As a result of the parallel RCS jet, the integrated pressure along the aeroshell aftbody increases by 31% and 520% for  $C_T = 0.05$  and  $1.0$ , respectively, compared to the no-jet case.

Figure 5.11 presents the distributions of the pressure and skin friction coefficients along the centerline of the aeroshell aftbody (excluding the RCS nozzle) for the parallel RCS jet at  $C_T = 0.05$  and  $1.0$ . The figure also presents the corresponding distributions for the baseline (i.e. no-jet) configuration for comparison. The pressure coefficient for the parallel RCS jet at  $C_T = 0.05$ , shown in Figure 5.11(a), sharply decreases from high values near the nozzle-exit to relatively small values comparable to the baseline configuration. At the high thrust coefficient, the pressure also decreases from high values near the RCS nozzle-exit, but then increases upstream of the nozzle to as much as twice as large as the corresponding value for the no-jet case.

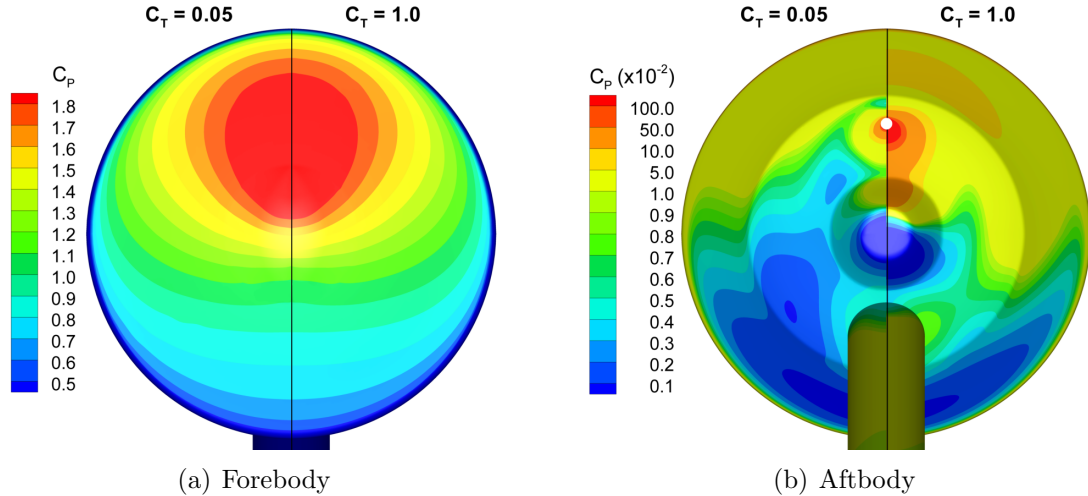


Figure 5.10: Forebody and aftbody pressure coefficient contours for the parallel RCS jet at  $C_T = 0.05$  and  $1.0$ .

This increase in pressure upstream of the nozzle-exit is caused by a combination of added mass from the RCS jet and the obstruction of the flow from the freestream by the parallel jet. Downstream of the nozzle-exit, the impingement of the jet species on the surface increases the surface pressure by approximately one order of magnitude compared to the baseline configuration.

The magnitude of the coefficient of skin friction for the parallel RCS jet at the two thrust conditions also decreases from high values near the nozzle-exit, as shown in Figure 5.11(b). The shear stress directly upstream of the nozzle-exit is negative at both thrust coefficients since the jet first moves upstream towards the aeroshell shoulder as it expands from the RCS nozzle. At the low thrust coefficient, the distribution of the shear stress away from the nozzle-exit is similar to the distribution for the no-jet case. At  $C_T = 1.0$ , however, the obstruction of the flow from the freestream by the parallel jet decreases the shear stress upstream of the RCS nozzle by approximately a factor of 2 compared to the no-jet case. Downstream of the nozzle-exit, the expansion of the parallel jet at  $C_T = 1.0$  along the aftbody increases the shear stress by roughly one order of magnitude compared to the baseline configuration.

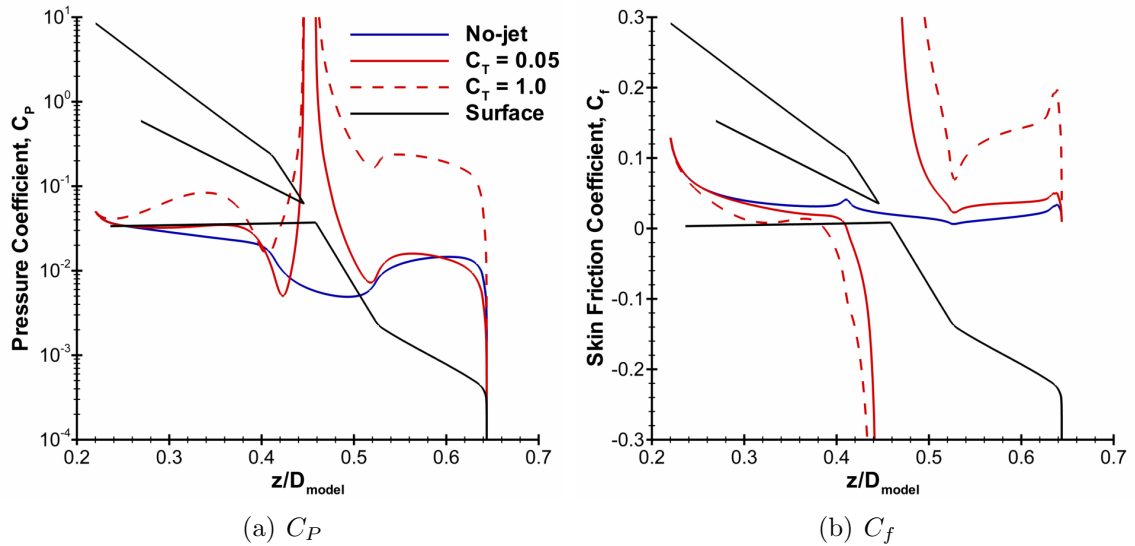


Figure 5.11: The distributions of pressure and skin friction coefficients along the centerline of the aeroshell aftbody for the parallel RCS jet at  $C_T = 0.05$  and 1.0.

### 5.3.3 Aerodynamic Properties

The changes in the surface properties along the aftbody caused by the parallel RCS jet may have an important effect on the aerodynamic properties of the aeroshell. Table 5.4 presents a summary of the aerodynamic properties of the aeroshell with the parallel RCS jet at  $C_T = 0.05$  and  $C_T = 1.0$ , as well as the properties for the no-jet case for comparison. Note that the axial and normal force coefficients presented in Table 5.4 do not include the thrust coefficient of the RCS thruster. The results indicate that the parallel RCS jet at  $C_T = 0.05$  has almost no effect on the aerodynamic properties of the aeroshell. At the higher thrust coefficient, however, the increased surface pressure on the windward side of the aeroshell aftbody decreases the aerodynamic axial force by approximately 4% and increases the modulus of the aerodynamic normal force by about 24%. As a result, the aerodynamic drag and lift forces acting on the aeroshell decrease by approximately 2% and 21%, respectively. The interactions produced by the RCS jet at the higher thrust coefficient also decrease the modulus of the moment by 5%, which may have an important effect on the control performance of the reaction

control system and will be discussed later in Section 5.5.

Table 5.4: Aerodynamic properties of the aeroshell with the parallel RCS jet.

$C_T$	$C_A$	$C_N$	$C_D$	$C_L$	$L/D$	$C_M$
No-jet	1.28	-0.17	1.26	0.28	0.22	-0.060
0.05	1.28	-0.17	1.26	0.28	0.22	-0.060
1.0	1.23	-0.21	1.23	0.22	0.18	-0.057

## 5.4 Transverse RCS Jet

The results presented in the previous section have shown that the parallel RCS jet produces fluid interactions that can affect the flowfield, surface, and aerodynamic properties of the aeroshell. In this section, similar results are presented for the transverse RCS jet in order to examine the effects of the induced fluid interactions on the properties of the aeroshell. The results presented in this section will also help in understanding the importance of the RCS jet orientation with respect to the freestream flow on the properties of the aeroshell.

### 5.4.1 Flowfield Properties

The Mach number distributions around the aeroshell with the transverse RCS jet for thrust coefficients of 0.05 and 1.0 are presented in Figure 5.12. The RCS jet at both thrust conditions exhausts almost normal to the flow around the aeroshell, and expands from sonic conditions at the nozzle-exit to hypersonic conditions downstream of the aeroshell. Similar to the parallel jet, the velocity streamlines shown in Figure 5.12 indicate that the transverse RCS jet obstructs the path of the flow from the freestream around the aeroshell aftbody, which decreases the Mach number and compresses the flow upstream of the jet boundary near the aftbody surface. This obstruction, however, is stronger for the transverse configuration since the jet can pen-

erate farther upstream than the parallel jet. Figure 5.12(b) also shows that the RCS jet impinges on the bow shock, which pushes the portion of the shock downstream of the RCS nozzle-exit away from the aeroshell.

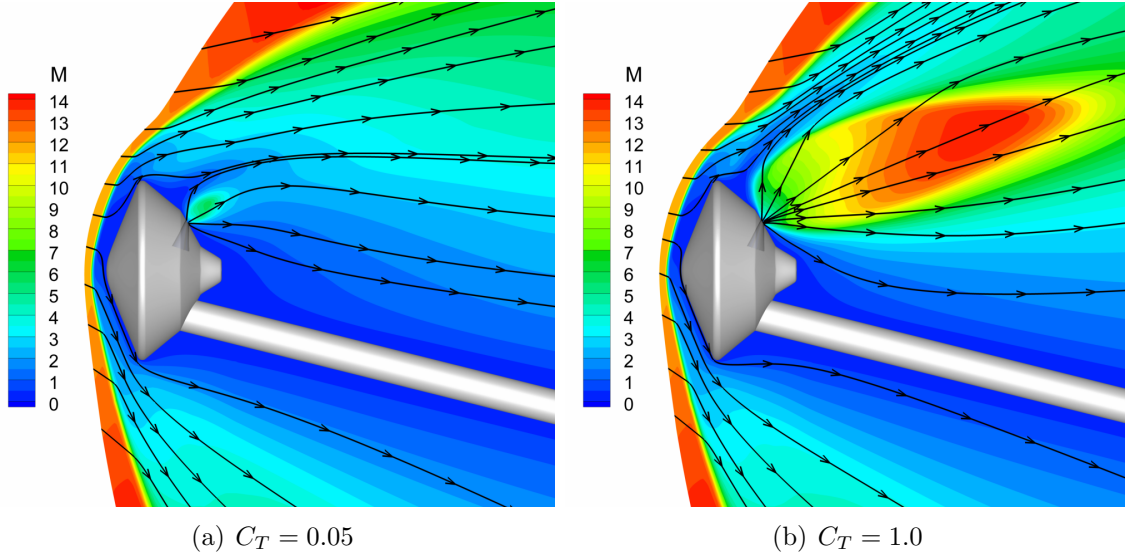


Figure 5.12: Mach number contours for the transverse RCS jet at  $C_T = 0.05$  and 1.0.

Figure 5.13 shows the jet species mole fraction for the transverse RCS jet at the two thrust conditions investigated in this study. Similar to the parallel jet, the mole fraction for the transverse RCS jet at the lower thrust coefficient is large relatively close to the nozzle-exit and decreases as the jet expands downstream of the aeroshell. At the higher thrust coefficient, the value of the jet species mole fraction remains large for approximately the entire windward portion of the wake that is included in the computational domain. Figure 5.13 also indicates that a larger amount of jet species is transported upstream of the nozzle-exit towards the aeroshell shoulder for the transverse RCS jet than previously observed for the parallel jet. For instance, the distance upstream of the nozzle-exit where the jet species molar fraction is equal to 0.5 is greater for the transverse jet by approximately 50% for  $C_T = 0.05$  and 65% for  $C_T = 1.0$  compared to the parallel jet. The figure, however, also shows that the amount of jet species downstream of the nozzle-exit near the parachute cone is

relatively smaller for the transverse jet than observed for the parallel jet.

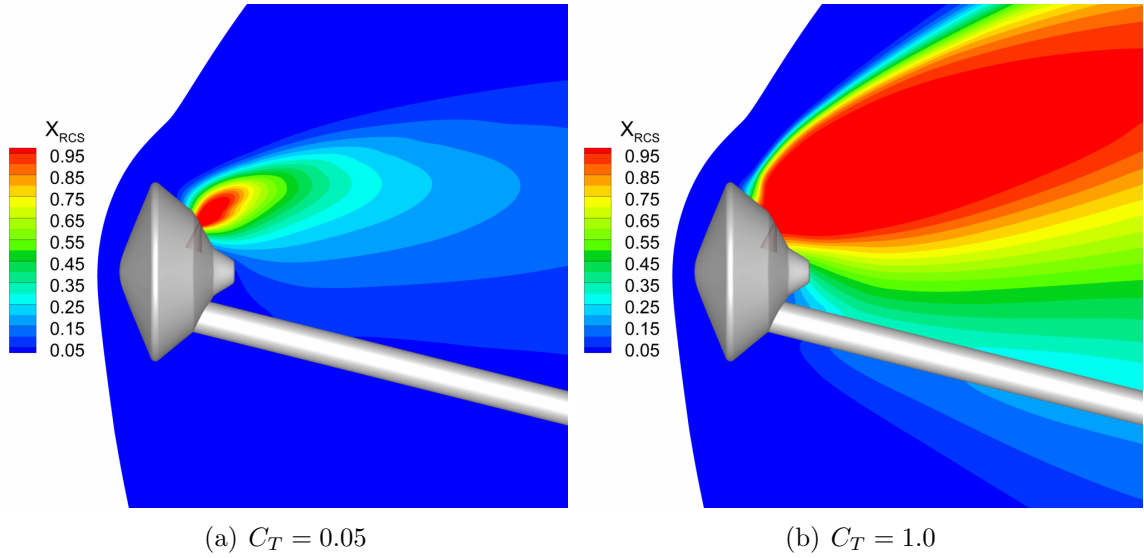


Figure 5.13: RCS jet species mole fraction contours for the transverse RCS jet at  $C_T = 0.05$  and  $1.0$ .

Similar to the parallel jet, the transverse RCS jet also reduces the level of continuum breakdown in the wake, especially at the higher thrust conditions, due to added mass. However, the distribution of the gradient-length local Knudsen number, shown in Figure 5.14, highlights continuum breakdown regions in the bow shock and in the wake, particularly on the leeward side. The contours also show continuum breakdown regions across the boundaries of the RCS jet due to large gradients in flow properties. The effect of the transverse RCS jet on the bow shock at the high thrust conditions can be clearly seen in Figure 5.14(b). The impingement of the RCS jet on the bow shock alters the profile of the portion of the shock downstream of the RCS nozzle-exit as it is pushed away from the aeroshell by the jet.

#### 5.4.2 Surface Properties

Figure 5.15 presents the distributions of pressure coefficient along the aeroshell forebody and aftbody for the transverse RCS jet at thrust coefficients of 0.05 and

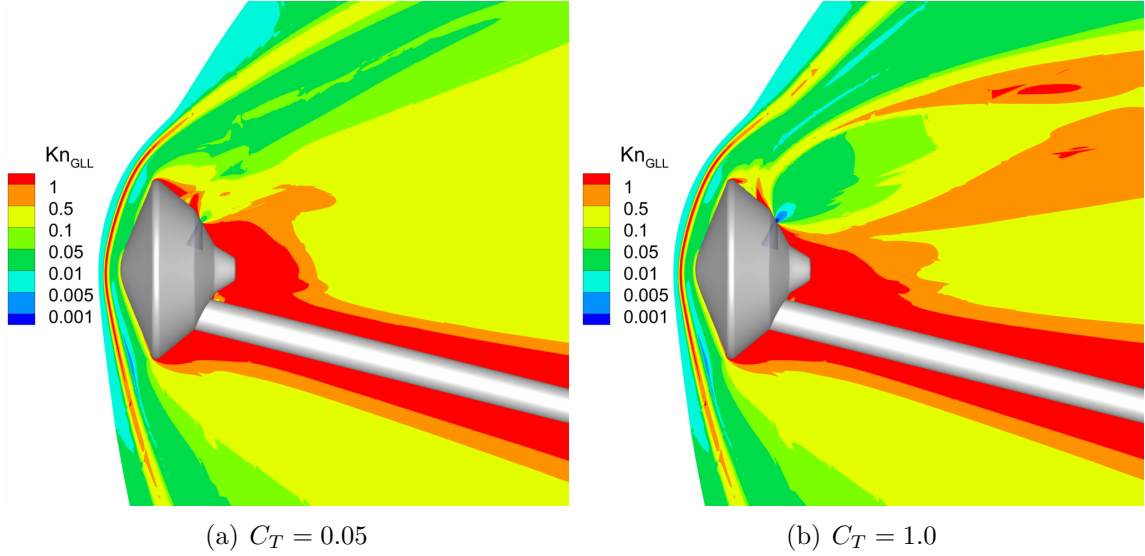


Figure 5.14: Gradient-length local Knudsen contours for the transverse RCS jet at  $C_T = 0.05$  and  $1.0$ .

1.0. Figure 5.15(a) shows that the transverse RCS jet does not affect the pressure distribution along the aeroshell forebody since the contours are identical to the ones shown in Figure 5.5 for the no-jet case. The transverse RCS jet, however, does affect the surface pressure along the aeroshell aftbody. Figure 5.15(b) indicates that the transverse RCS jet increases the pressure along the aftbody, particularly upstream of the nozzle-exit near the aeroshell shoulder compared to the baseline configuration. The figure also shows that the transverse jet at the higher thrust coefficient causes overall larger surface pressure values than the jet at the lower thrust conditions. As a result, the integrated pressure along the aeroshell aftbody increases by 43% and 560% for the transverse RCS jet at  $C_T = 0.05$  and  $1.0$ , respectively, compared to the no-jet case.

The coefficients of pressure and skin friction along the aftbody centerline for the transverse RCS jet at  $C_T = 0.05$  and  $1.0$  are presented in Figure 5.16. Upstream of the nozzle-exit, the pressure coefficient for the transverse jet at both thrust conditions, shown in Figure 5.16(b), first decreases and then increases due to a combination of

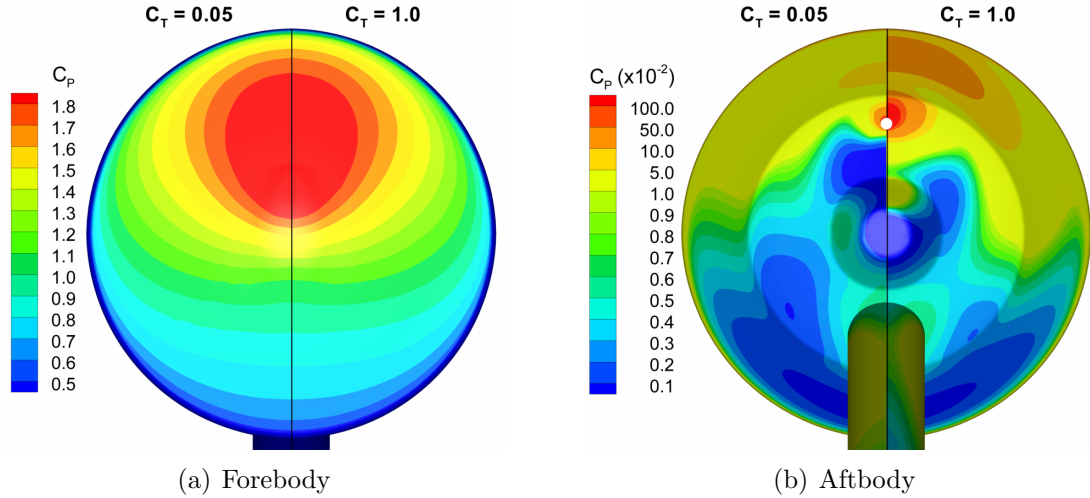


Figure 5.15: Forebody and aftbody pressure coefficient contours for the transverse RCS jet at  $C_T = 0.05$  and  $1.0$ .

added mass from the RCS and the compression of the flow near the surface caused by the obstruction of the flow from the freestream by the transverse jet. Downstream of the nozzle-exit, the transverse jet at  $C_T = 0.05$  decreases the pressure by approximately one order of magnitude compared to the no-jet case since only a relatively small amount of the jet species impinge on the surface. However, the pressure downstream of the nozzle-exit for the transverse RCS jet increases at  $C_T = 1.0$  to values comparable to the baseline configuration since more jet species are transported downstream.

Figure 5.16(b) shows that the coefficient of skin friction for the transverse RCS jet at both thrust conditions decreases in magnitude away from the nozzle-exit. The negative sign of the shear stress indicates that the transverse jet first flows upstream of the nozzle-exit before encountering the flow from the freestream. Upstream of the nozzle-exit, the shear stress for the transverse jet at both thrust conditions decreases from large values caused by the expansion of the transverse jet from the RCS nozzle to low values produced by the slow speeds of the flow from the freestream. Downstream of the nozzle-exit, the shear stress distributions for the transverse RCS jet at  $C_T =$



0.05 and 1.0 are similar to the distribution for the baseline configuration. However, the overall skin friction coefficients for the transverse jet at  $C_T = 1.0$  are approximately twice as large as the values for both  $C_T = 0.05$  and the no-jet cases.

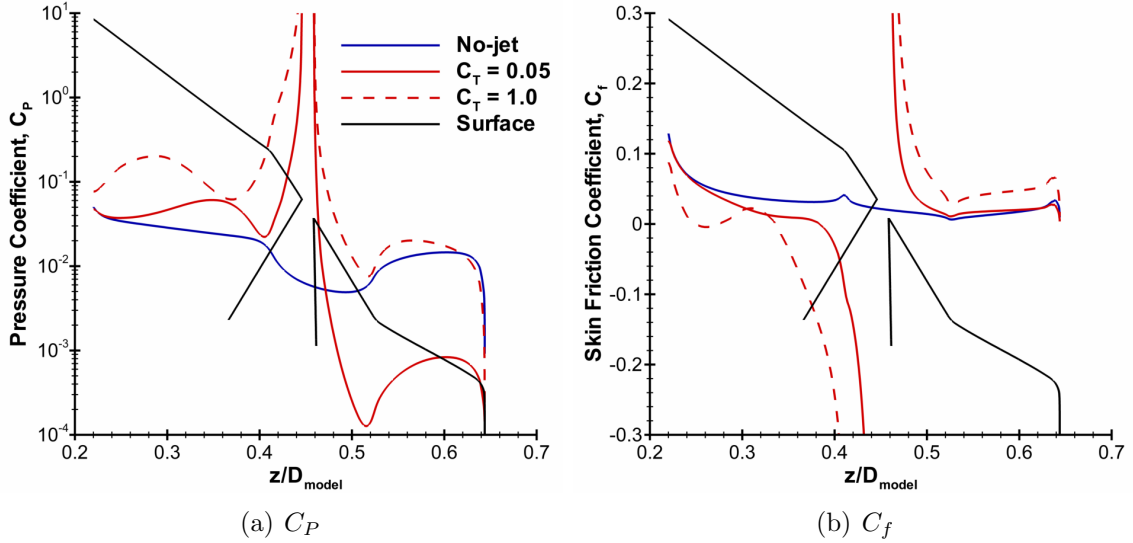


Figure 5.16: The distributions of pressure and skin friction coefficients along the centerline of the aeroshell aftbody for the transverse RCS jet at  $C_T = 0.05$  and 1.0.

### 5.4.3 Aerodynamic Properties

The fluid interactions produced by the transverse RCS jet may also affect the aerodynamic properties of the aeroshell. Table 5.5 presents the coefficients of the aerodynamic forces and moment acting on the aeroshell with the transverse RCS jet at  $C_T = 0.05$  and 1.0, as well as the coefficients for the baseline configuration for comparison. Similar to the parallel jet, the aerodynamic axial and normal forces do not include any contribution from the RCS thrust. The results show that for the lower thrust conditions, the larger aftbody pressures caused by the transverse RCS jet decrease the aerodynamic axial and drag forces acting on the aeroshell by less than 1%. The transverse jet at  $C_T = 0.05$  also decreases the modulus of the moment by approximately 3%. At the higher thrust conditions, the transverse RCS jet decreases

the axial force by approximately 5% and increases the modulus of the normal force by about 18% compared to the no-jet case. As a result, the drag and lift forces acting on the aeroshell decrease by 4% and 18%, respectively. The transverse RCS jet also decreases the modulus of the moment by about 22% at  $C_T = 1.0$  compared to the baseline configuration.

Table 5.5: Aerodynamic properties of the aeroshell with the transverse RCS jet.

$C_T$	$C_A$	$C_N$	$C_D$	$C_L$	$L/D$	$C_M$
No-jet	1.28	-0.17	1.26	0.28	0.22	-0.060
0.05	1.27	-0.17	1.25	0.28	0.22	-0.058
1.0	1.22	-0.20	1.21	0.23	0.19	-0.047

## 5.5 Performance of the Parallel and Transverse RCS Jets

The main function of the reaction control system is to provide vehicle control and steering by producing moments about the center of gravity of the capsule. Specifically, the parallel RCS jet investigated in this study generates a certain amount of positive moment (i.e. counter-clockwise direction) about the center of gravity, as can be seen in Figure 5.17. However, the aerodynamic interference induced by the RCS jet plume, particularly at the higher thrust condition, can have a significant impact on the performance of the RCS jet. Therefore, the effectiveness of the reaction control system can be examined by defining a “control gain” as,

$$\text{Gain} = \frac{C_{M_{thrust}} + C_{M_{interference}}}{C_{M_{thrust}}} \quad (5.5)$$

where,  $C_{M_{thrust}}$  is the moment generated by the thrust force of the RCS jet, and  $C_{M_{interference}}$  is the moment produced by the aerodynamic interference of the RCS jet, and is given by,

$$C_{M_{interference}} = C_M - C_{M_{no-jet}} \quad (5.6)$$

Ideally, the RCS jet does not generate any aerodynamic interference and the control gain is equal to unity. However, if the control gain is less than unity, then the aerodynamic interference creates a deficit of control authority. Similarly, if the control gain is greater than unity, then the aerodynamic interference causes a surplus of authority. A similar approach was also used to examine the effectiveness of the reaction control system for the Phoenix and MSL missions [50, 41].

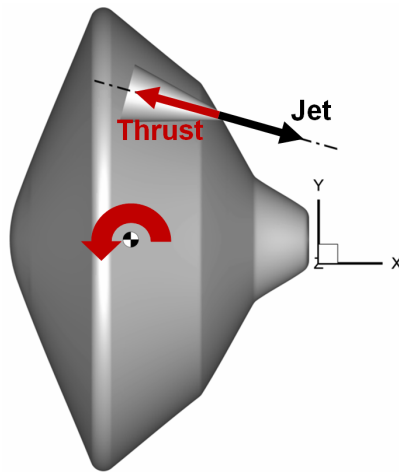


Figure 5.17: Direction of the moment due to the thrust force from the parallel RCS jet about the center of gravity of the aeroshell.

The moments due to the aerodynamic interference and the thrust force, as well as the control gain for the parallel RCS jet at  $C_T = 0.05$  and 1.0 are provided in Table 5.6. The results show that the moment caused by the aerodynamic interference of the RCS jet is small relative to the moment generated by the thrust force from the parallel RCS jet. As a result, the control gain for both thrust conditions is approximately equal to unity. This represents a desirable feature of the parallel RCS jet because the aerodynamic interference induced by the RCS plume does not alter the effectiveness and the performance of the control system.

Unlike the parallel jet, the thrust force obtained from the transverse RCS jet produces a negative moment (i.e. clockwise direction) about the center of gravity of the aeroshell, as shown in Figure 5.18. However, the aerodynamic effects summarized

Table 5.6: Control effectiveness of the parallel RCS jet.

$C_T$	$C_{M_{thrust}}$	$C_{M_{interference}}$	Gain
0.05	0.015	0.0	1.0
1.0	0.310	0.003	1.0

in Table 5.5 may have a significant effect on the effectiveness of the reaction control system using the transverse jet. Therefore, the control gain defined in Equation 5.5 can be used to quantify the performance of the transverse RCS jet. Table 5.7 presents the control gain, as well as the moment coefficients due to the thrust force and the aerodynamic interference (defined in Equation 5.6) for the transverse RCS jet at thrust coefficients of 0.05 and 1.0. The results show that the aerodynamic interference produces a moment that is opposite of the moment induced by the thrust force from the transverse RCS jet. The control gain for the transverse RCS jet is equal to 0.6 and 0.9 for the 0.05 and 1.0 thrust coefficients, respectively. This suggests that the aerodynamic interference induced by the transverse RCS jet causes a control deficit (i.e. gain less than unity) since a fraction of the moment produced by the thrust from the transverse RCS jet is used to counteract the moment generated by the aerodynamic interference. The control deficit, however, diminishes for relatively large thrust conditions because a smaller fraction of the thrust-induced moment is used to oppose the interference moment.

Table 5.7: Control effectiveness of the transverse RCS jet.

$C_T$	$C_{M_{thrust}}$	$C_{M_{interference}}$	Gain
0.05	-0.005	0.002	0.6
1.0	-0.097	0.013	0.9

The control performance of the transverse and parallel RCS jets are summarized in Figure 5.19. Figure 5.19(a) presents the ratio of the moment produced by the aerodynamic interference (defined in Equation 5.6) to the moment induced by the

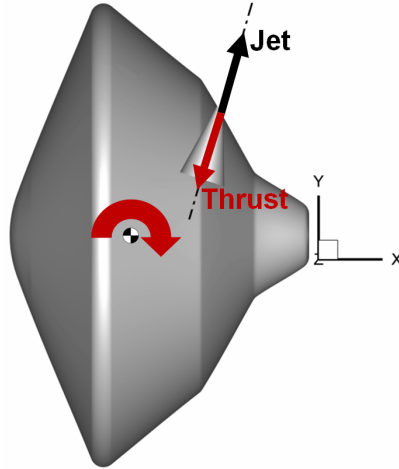


Figure 5.18: Direction of the moment due to the thrust force from the transverse RCS jet about the center of gravity of the aeroshell.

thrust force from the RCS for the parallel and transverse jets. The figure shows that the ratio is small for the parallel RCS jet and does not exceed 0.01 for both  $C_T = 0.05$  and 1.0. The ratio is also positive for the parallel jet, which implies that the two moments act along the same direction (counter-clockwise). As a result, the control gain for the parallel RCS jet, shown in Figure 5.19(b), is approximately equal to unity, which is ideal because the effectiveness of the reaction control system is similar to the design condition. For the transverse RCS jet, however, the ratio of interference moment to thrust moment is relatively large and equal to almost  $-0.40$  for  $C_T = 0.05$  and  $-0.14$  for  $C_T = 1.0$ . Figure 5.19(a) also shows that the interference moment (counter-clockwise) and the thrust moment (clockwise) act in opposite directions since the ratio of the two moments is negative. As a result, the aerodynamic interference induced by the transverse RCS jet creates a control deficit, as can be seen in Figure 5.19(b), which is not ideal because a fraction of the thrust is used to counteract the aerodynamic interference, and the effectiveness of the reaction control system diminishes. The combination of large thrust moment and small interference moment causes the effectiveness of the parallel RCS jet at these particular conditions to match the design performance. On the hand, the combination

of the relatively small thrust moment and large interference moment creates a control deficit for the transverse RCS jet.

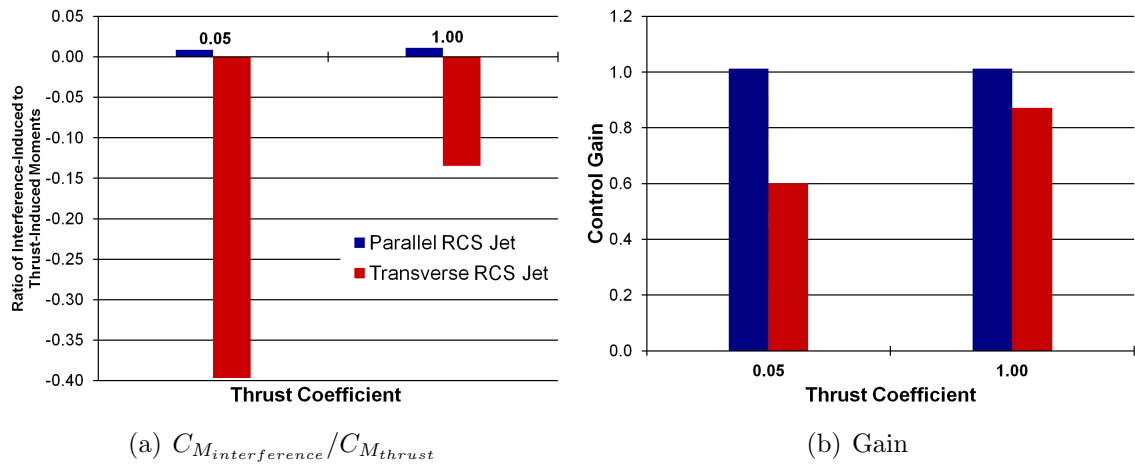


Figure 5.19: Comparisons of the ratio of interference moment to thrust-induced moment and the RCS control gain between the parallel and transverse RCS jets at  $C_T = 0.05$  and 1.0.

The trends observed in the performance of the reaction control system with parallel and transverse RCS jets are caused by two factors. First, the moment produced by the thrust force from the parallel RCS jet is approximately three times larger than the moment produced by the thrust from the transverse jet at both thrust conditions. This difference in the thrust-induced moment is caused by the contribution of the axial and normal components of the thrust force and the length of the moment arm. For the parallel RCS jet, both the axial and normal components of the thrust force contribute to a positive thrust-induced moment with respect to the center of gravity of the aeroshell. However, for the transverse RCS jet, the normal component of the thrust force produces a negative moment, while the axial component generates a positive moment about the center of gravity. The modulus of the moment produced by the axial component of the thrust force from the transverse jet is approximately equal to 45% of the modulus of the moment generated by the thrust component along the normal direction at both  $C_T = 0.05$  and 1.0. This means that the two components

of the thrust force from the transverse RCS jet provide counteracting moments that result in a smaller net thrust-induced moment. The parallel RCS jet also has a larger moment arm than the transverse jet. Figure 5.20 presents the lengths of the moment arm along the axial (i.e.  $X$ -axis) and normal (i.e.  $Y$ -axis) directions with respect to the center of gravity along the aeroshell surface. The midpoint of the RCS nozzle-exit is located approximately 0.2 and 0.3 aeroshell diameters away from the center of gravity of the aeroshell along the axial and normal directions, respectively, for both RCS configurations. Even though both RCS jets produce the same amount of thrust (at each given thrust coefficient), the parallel RCS jet has a larger moment arm than the transverse jet because most of the thrust force is directed along the axial direction. These results suggest that the control effectiveness of the reaction control system can be made close to ideal by selecting an orientation of the RCS jet such that the contribution to the thrust-induced moment by all of the components of the thrust force are along the same direction, and by maximizing the moment arm of each thruster.

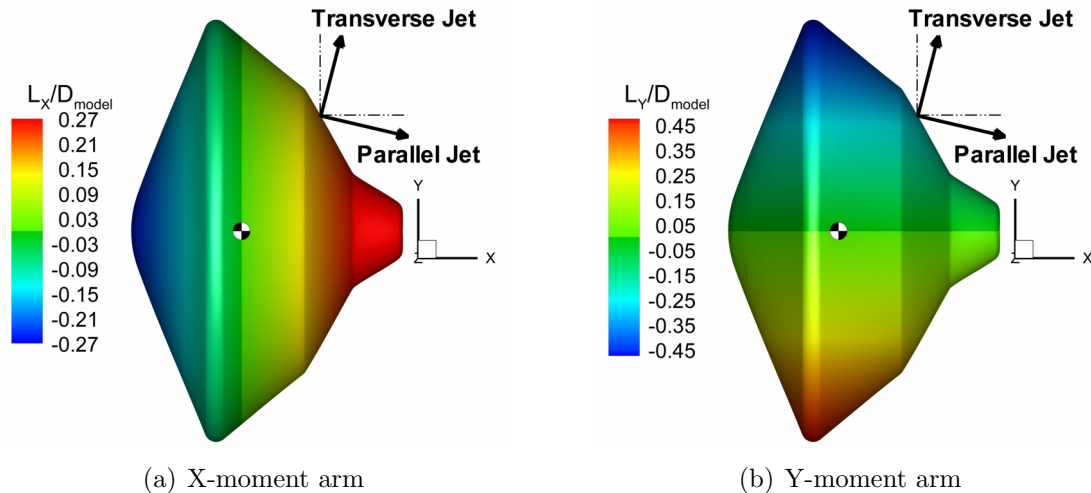


Figure 5.20: Lengths of the moment arm with respect to the center of gravity of the aeroshell along the  $X$  and  $Y$  directions.

The second cause of the trends observed in the performance of the RCS thrusters is

that the transverse jet produces a larger interference moment compared to the parallel jet. In order to understand the source of this interference, Figure 5.21 presents the distribution of the moment per unit area along the centerline of the aeroshell aftbody for the parallel and transverse RCS jets at the two thrust conditions investigated in this study. The figure also presents the corresponding distribution for the no-jet case for reference. The figure shows that the moment along the aftbody centerline is negative and relatively small for the baseline configuration. At the low thrust coefficient for the parallel RCS jet, the pressure and shear stress distributions produced by the jet generate a relatively large positive moment directly upstream of the nozzle-exit which is counteracted by a similarly large negative moment directly downstream of the nozzle. As a result, the integrated moment along the centerline for the parallel RCS jet is only 40% larger than the integrated moment for the no-jet case. For the transverse jet at  $C_T = 0.05$ , however, the augmented surface pressures upstream of the nozzle-exit create a relatively larger positive moment than the negative moment downstream of the nozzle-exit. Consequently, the integrated moment along the centerline for the transverse RCS jet is approximately three times larger than the value for the baseline configuration.

At the higher thrust coefficient, shown in Figure 5.21(b), the surface pressure and shear stress distributions caused by the parallel and transverse RCS jets produce a positive moment upstream of the nozzle-exit and a negative moment downstream of the nozzle-exit along the aftbody centerline. However, the figure shows that the transverse RCS jet induces a large positive moment over a longer distance upstream of the nozzle-exit compared to the parallel jet, which causes the integrated moment along the centerline for the transverse jet to be over twice as large as the value for the parallel jet. This result indicates that the parallel RCS jet produces relatively smaller net interference moments compared to the transverse jet because it can induce opposing moments with respect to the center of gravity of the aeroshell that can



counteract one another. Therefore, the control effectiveness of the reaction control system can be also improved by either minimizing the fluid interactions induced by the jet, or by designing the layout of the RCS such that the fluid interactions produce counteracting effects that result in a small net interference.

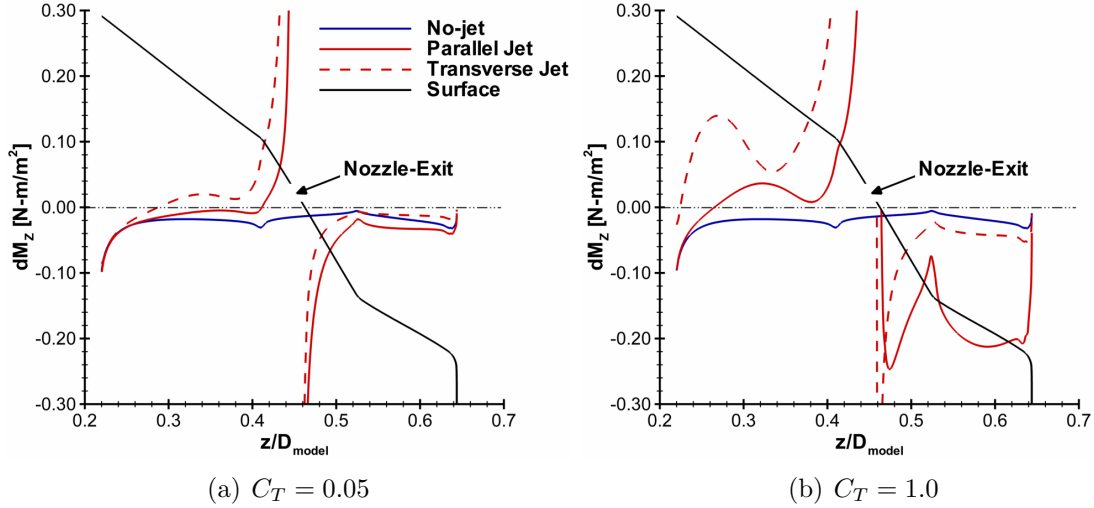


Figure 5.21: Comparison of the distribution of the moment per unit area along the centerline of the aeroshell aftbody between the parallel and transverse RCS jets at  $C_T = 0.05$  and  $1.0$ .

## 5.6 Summary

This chapter outlined a numerical investigation of the fluid interactions induced by the reaction control system of a Mars-entry aeroshell in hypersonic flow of  $I_2$ -seeded  $N_2$  gas. The aeroshell diameter used in the study is 20 mm and the angle-of-attack was set to  $20^\circ$  to simulate the conditions of a lifting trajectory. A single, sonic RCS jet was placed approximately half-way along the aeroshell aftbody. Two different RCS jet orientations were considered in this study to understand how the RCS configuration affects the flowfield, surface, and aerodynamic properties of the aeroshell. For the first configuration, the jet was directed almost parallel to the main freestream flow, while the second configuration used a jet that was almost normal to the flow. Two different

thrust coefficients were also considered for each RCS configuration. The lower thrust coefficient, equal to 0.05, was chosen to provide a ratio of RCS jet momentum to freestream momentum close to the value expected to be experienced in flight by MSL. A thrust coefficient of 1.0 was also chosen to compare the numerical results with experimental data in Chapter VI.

The results showed that the parallel RCS jet altered the flow on the windward side of the wake, particularly at  $C_T = 1.0$ . The jet expanded from sonic conditions at the nozzle-exit to higher Mach numbers downstream of the aeroshell, and obstructed the path of the flow from the freestream along the aftbody. The parallel jet also added mass to the wake region, which decreased the size of the continuum breakdown regions. However, some of the jet species, particularly at the higher thrust conditions, impinged on the surface, which may increase the heat flux experienced by the vehicle during flight and may influence the design of the aftbody thermal protection system. The results also showed that the parallel RCS jet did not have any effects on the pressure distribution along the aeroshell forebody. However, the parallel jet altered the surface properties and increased the overall pressure along the aeroshell aftbody by about 31% for  $C_T = 0.05$  and 520% for  $C_T = 1.0$ . The aerodynamic properties of the aeroshell with the parallel RCS jet at  $C_T = 0.05$  were overall similar to the properties for the baseline configuration. However, the parallel RCS jet at  $C_T = 1.0$  decreased the aerodynamic lift and drag forces acting on the aeroshell by 21% and 2%, respectively, and decreased the modulus of the moment by 5%.

Similar to the parallel jet, the transverse RCS jet also changed the flow on the windward side of the wake as it expanded from sonic conditions at the nozzle-exit to supersonic and hypersonic conditions downstream of the aeroshell. The transverse jet penetrated farther upstream than the parallel jet, which increased the obstruction of the flow from the freestream by the transverse jet near the aeroshell aftbody. The transverse RCS jet at  $C_T = 1.0$  also impinged on the bow shock and pushed

the portion of the shock downstream of the RCS nozzle away from the aeroshell. Although the forebody pressure distribution was not affected by the transverse RCS jet, the overall pressure along the aeroshell aftbody increased by 43% and 560% for  $C_T = 0.05$  and  $C_T = 1.0$ , respectively, compared to the no-jet case. The transverse RCS jet at  $C_T = 0.05$  did not have a significant effect on the aerodynamic forces acting on the aeroshell, but decreased the modulus of the moment by 3%. At  $C_T = 1.0$ , however, the transverse RCS jet decreased the aerodynamic lift and drag forces acting on the aeroshell by 18% and 4%, respectively, which is comparable to the effects of the parallel RCS jet. The transverse RCS jet, however, decreased the modulus of the moment by 22%, which is larger than the decrease produced by the parallel jet.

In the last section of the chapter, the control effectiveness of the parallel and transverse RCS jets was assessed. The results showed that the moment produced by the thrust force from the parallel RCS jet was three times as large as the moment produced by the thrust from the transverse jet. The large thrust-induced moment for the parallel RCS jet was due to the contribution of both the axial and normal components of the thrust force and a larger moment arm compared to the transverse jet. The parallel jet also induced relatively smaller net interference moments compared to the transverse jet because it generated opposing moments with respect to the center of gravity of the aeroshell that counteracted one another. This combination of large thrust-induced moment and small interference moment caused the performance of the parallel RCS jet to be close to an ideal performance at both  $C_T = 0.05$  and  $C_T = 1.0$ . The transverse RCS jet, however, suffered from a control deficit at both thrust conditions due to a combination of small thrust-induced moment and large interference moment. The results suggest that the control effectiveness of a reaction control system can be increased by selecting the orientation of the RCS jet with large moment arms such that the contribution to the thrust-induced moment by all of the components of the thrust force are along the same direction. The RCS control effec-

tiveness can be also increased by either minimizing the fluid interactions induced by the jet, or by designing the layout of the RCS such that the fluid interactions produce counteracting effects that result in a small net interference.

## CHAPTER VI

# Comparisons with Experimental Data

The numerical results presented in Chapters III, IV, and V provide valuable insight on the fluid interactions induced by propulsive deceleration and reaction control systems, as well as their effects on the flowfield, surface, and aerodynamic properties of Mars-entry aeroshells in hypersonic freestream conditions. These results, however, also reveal the complexity of these fluid phenomena, which include jet-shock interactions. Therefore, it is important to assess the physical accuracy of the computational method in capturing these induced fluid interactions by comparing the numerical results to experimental visualizations and measurements.

This chapter presents qualitative and quantitative comparisons between the numerical results described in the previous chapters and available experimental data. Most of the available experimental results are obtained from on-going work at the University of Virginia [56, 57, 63] using the planar laser-induced iodine fluorescence (PLIIF) technique for conditions similar to those used in the numerical simulations. The chapter is divided into four sections. The first section provides qualitative comparisons of the bow shock profile around the aeroshell without PD or RCS jets (i.e. baseline configuration) between the numerical results and experimental visualizations obtained using PLIIF. The second section provides qualitative comparisons of the bow shock profile, and quantitative comparisons of the bow shock standoff distance

and aeroshell aerodynamic properties between the numerical results and experimental data for central PD jets. The section also outlines similar qualitative comparisons of the bow shock profile, as well as quantitative comparisons of the bow shock standoff distance and the mole fraction of the jet species for peripheral PD jets. In the third section, qualitative bow shock profile comparisons between the CFD and experimental results for parallel and transverse RCS jets are described. Finally, the chapter outlines the major conclusions drawn from these comparisons.

## 6.1 Baseline Configuration

Qualitative comparisons between the CFD (LeMANS) results and experimental data of the bow shock profile around the aeroshell without PD or RCS jets (i.e. baseline configuration) is shown in Figure 6.1. The diameter of the aeroshell is 10 mm and the angle-of-attack is  $0^\circ$ . The image in Figure 6.1(a) is a PLIIF visualization obtained at the University of Virginia. The flow is from left to right and the freestream flow is seeded with iodine so that the flowfield features are visible. The sting used in the experiments to mount the capsule in the test section has been removed from the image and the aeroshell model has been superimposed for illustrative purposes. The fluorescence shown in the image is directly proportional to the iodine number density for regions of the flow where the Mach number is between 6 and 17 [63, 88], which means that each brightness level in the PLIIF image corresponds to a specific iodine density value in the hypersonic regions of the flow. The bow shock profile can be determined from this image as the region upstream and around the aeroshell where the brightness changes. Figure 6.1(b) presents velocity streamlines (top half) and a contour of iodine density (bottom half) obtained from the numerical results and overlaid on the PLIIF visualization. The contour level for the CFD results corresponds to the iodine density value at the point along the aeroshell centerline where the iodine density in the freestream begins to increase. This contour is representative of the

bow shock along the aeroshell since the fluorescence in the PLIIF image is directly proportional to the iodine density in this region of the flow. The bow shock profile for the numerical results can be also determined from the velocity streamlines as the location in the freestream where the slope of each streamline changes. Figure 6.1(b) shows good qualitative agreement in the bow shock profile between the numerical and experimental results for the no-jet case at  $0^\circ$  angle-of-attack.

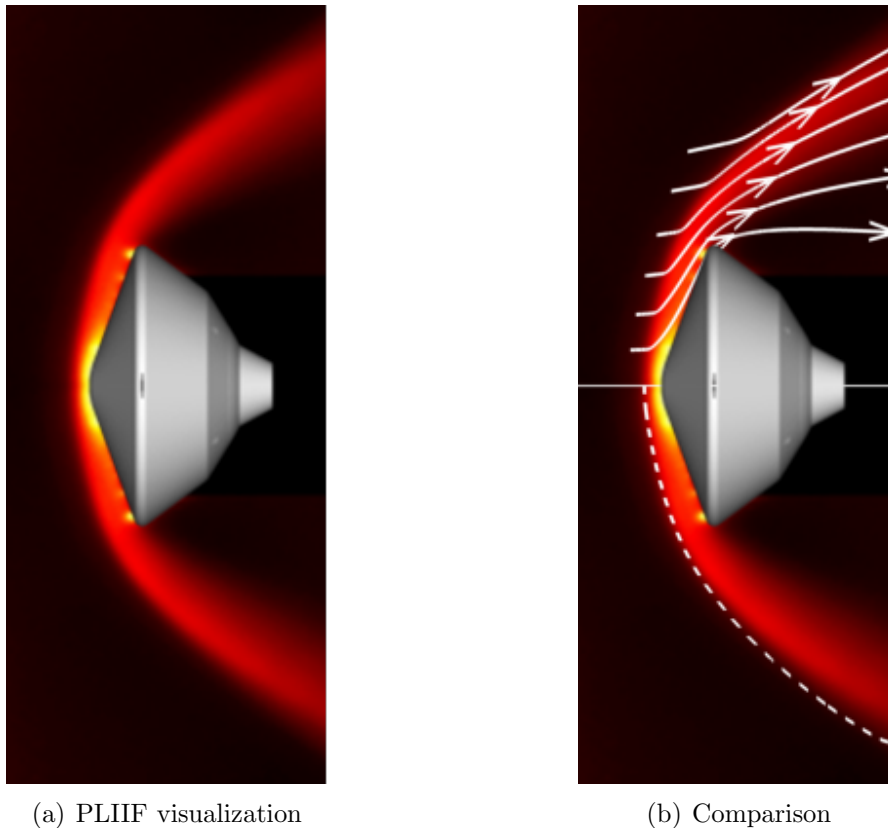


Figure 6.1: Comparison of the bow shock profile for the no-jet case at  $0^\circ$  angle-of-attack between the numerical and experimental results.

Similar qualitative comparisons of the bow shock profile for the baseline configuration at a  $20^\circ$  angle-of-attack are presented in Figure 6.2. The diameter of the aeroshell is 20 mm. Both the iodine density contour and the velocity streamlines indicate excellent agreement with the bow shock profile observed in the PLIIF visualization in the portion of the shock upstream of the aeroshell. However, the agreement between

the two sets of results decreases downstream of the aeroshell shoulder. The figure shows that the bow shock predicted by LeMANS is farther away from the aeroshell than observed experimentally.

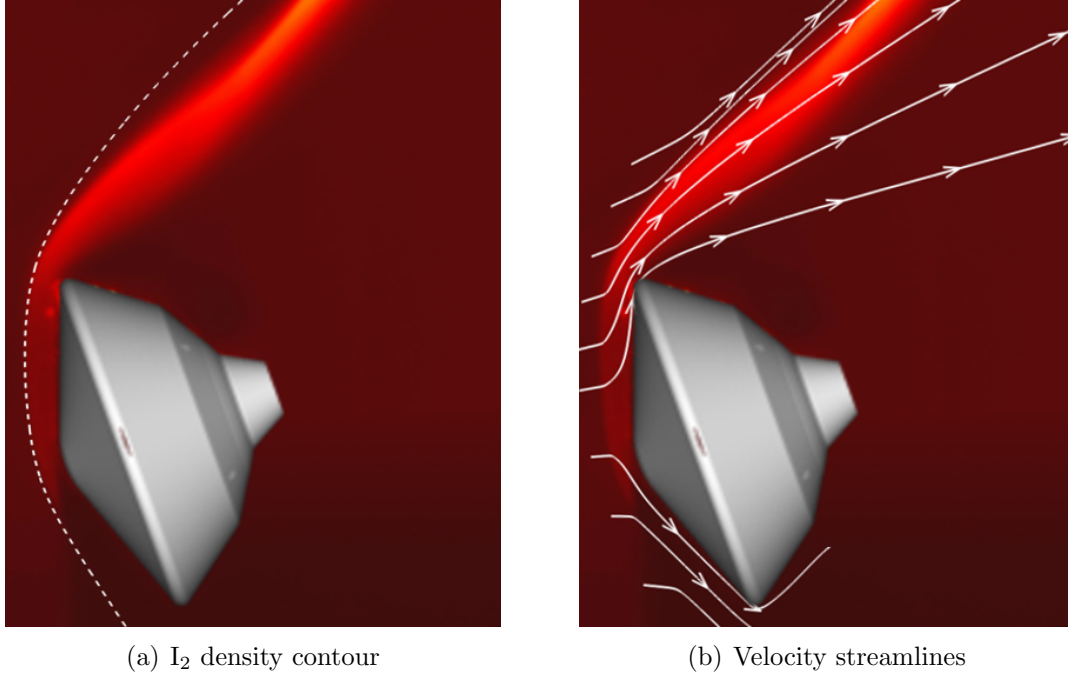


Figure 6.2: Comparison of the bow shock profile for the no-jet case at  $20^\circ$  angle-of-attack between the numerical ( $I_2$  density contour and velocity streamlines) and experimental (PLIIF image) results.

The disagreement in the bow shock profile between the numerical and experimental results for the 20 mm aeroshell at  $20^\circ$  angle-of-attack may be caused by several factors. The first possible source of the disagreement between the CFD result and the PLIIF visualization is the Ashkenas and Sherman relations that provide the freestream conditions in the numerical simulations, which may not be appropriate for large streamline angles [85]. In order to quantify this effect, Figure 6.3 presents the percent difference in total density between the Ashkenas and Sherman relations and the CFD solution for the flow in the experimental facility. The figure shows that the difference between the Ashkenas and Sherman relations and the computed solution in the experimental facility upstream of the bow shock increases as the angle of the



streamlines (i.e. angle with respect to the orifice) increases. Since the bow shock moves upstream as the size of the aeroshell increases, the disagreement between the freestream conditions in LeMANS given by the Ashkenas and Sherman relations and the conditions in the experimental facility along the same radial distance (i.e.  $r/D$ ) is greater for the 20 mm aeroshell than for the 10 mm aeroshell. Another possible cause of the disagreement between the numerical and experimental results is the interaction of the bow shock with the barrel shock in the experiments, which is shown in Figure 6.4. This interaction between the two shock structures in the experimental facility, referred to as the triple-point, is stronger for the larger aeroshell (i.e. 20 mm diameter) since the bow shock is pushed farther upstream. As a result, the interaction induces a greater influence on the bow shock and can change its profile around the aeroshell.

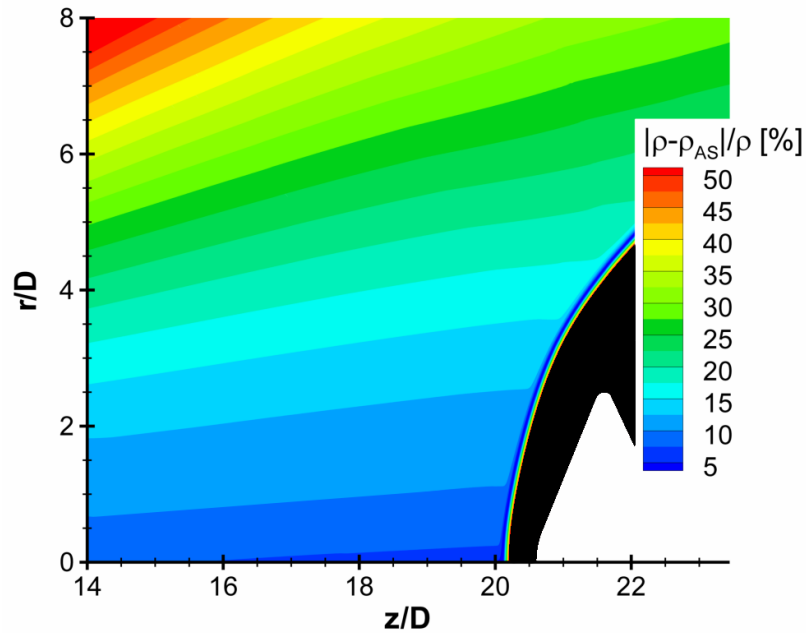


Figure 6.3: Percent difference in the density between the Ashkenas and Sherman relations and the CFD solution of the flow in the experimental facility.

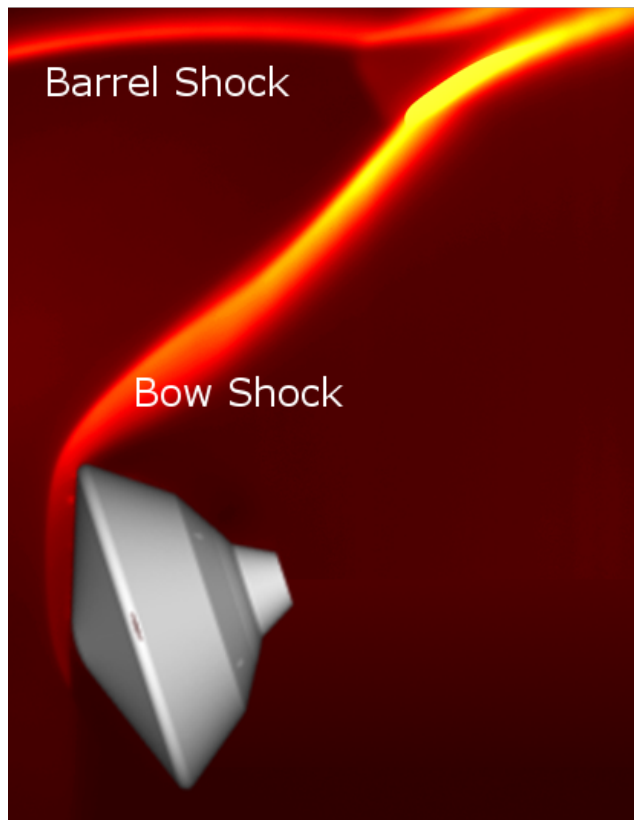


Figure 6.4: PLIIF image of the interaction between the bow shock and the barrel shock in the experimental facility.

## 6.2 Propulsive Deceleration

Qualitative and quantitative comparisons between the numerical results and experimental data for propulsive deceleration are described in this section. The section first presents qualitative bow shock profile comparisons, as well as quantitative bow shock standoff distance and aerodynamic drag and axial force comparisons for central PD jets between the CFD results and available experimental results. The section then provides similar qualitative bow shock profile comparisons, and quantitative bow shock standoff distance and jet mole fraction comparisons for peripheral PD jets.

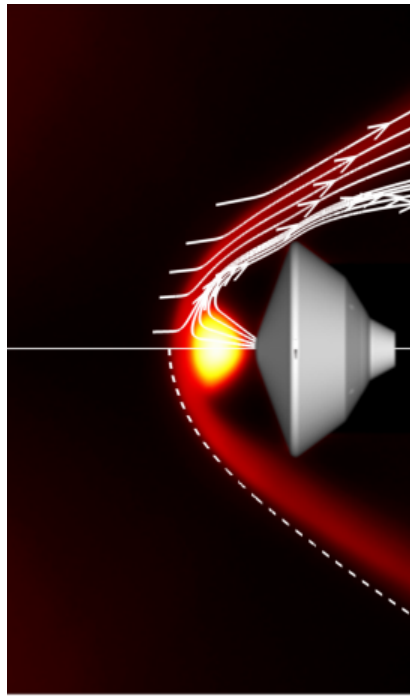
### 6.2.1 Central Configuration

Figure 6.5 presents qualitative bow shock profile comparisons for sonic central PD jets between the numerical results and experimental visualizations for thrust coefficients of 0.5, 1.0, 2.0, and 2.5. The images are PLIIF visualizations with iodine-seeding in both the freestream and the PD jet in order to display the flowfield features, which include the bow shock, PD jet core, and the jet shock. The images show that as the thrust coefficient increases, the PD jet core expands in size and the bow shock around the aeroshell is pushed upstream. The images also show that the bow shock becomes more normal as the thrust coefficient of the PD jet increases. The velocity streamlines and iodine density contour superimposed over the PLIIF images are calculated using LeMANS. The contour levels for the CFD results correspond to the iodine density values at the point along the aeroshell centerline where the iodine density in the freestream begins to increase. Note that the contour level is different for each case, as can be seen in Figure 6.6, due to the varying freestream conditions. Figure 6.6 shows the iodine number density along the aeroshell centerline for the sonic central PD jets at  $C_T = 0.5$  and 2.5. The iodine density in the freestream decreases away from the orifice (i.e. closer to the aeroshell) since the flow is expanding (i.e. underexpanded freejet). Therefore, as the thrust coefficient increases, the value of

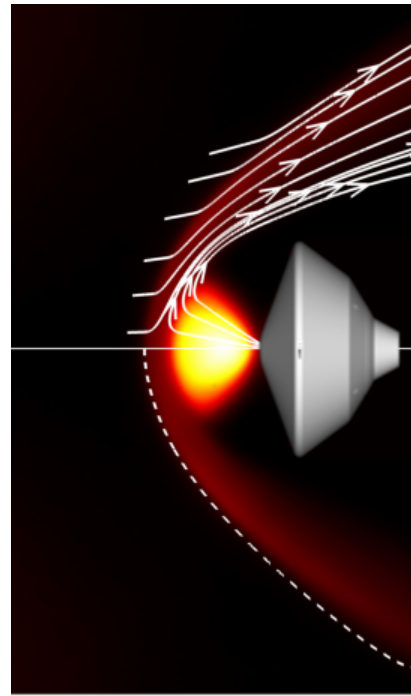
the iodine density contour level used in the profile comparisons increases since the bow shock is pushed farther upstream by the PD jet. Figure 6.5 indicates overall good qualitative agreement in the bow shock profile around the aeroshell between the CFD results and the experimental visualizations for all PD thrust conditions. The streamlines also indicate good agreement in the profile of the PD jet terminal shock between the two sets of results.

Similar qualitative bow shock profile comparisons between the CFD results and PLIIF visualizations for supersonic central PD jets are presented in Figure 6.7 for  $C_T$  values of 0.5, 1.0, 2.0, and 2.5. Like the sonic jets, the PLIIF visualizations for the supersonic PD jets show that the size of the PD jet core increases and the bow shock is pushed farther upstream and becomes more normal as the thrust coefficient increases. The supersonic jets also appear to penetrate farther upstream than the sonic jets. The velocity streamlines and iodine density contour from LeMANS indicate good qualitative agreement in the profiles of the bow shock and PD jet shock between the numerical and experimental results, particularly for the lower thrust conditions. For  $C_T = 2.0$  and 2.5, however, the agreement in the bow shock profile between the two sets of results decreases away from the capsule centerline. Figures 6.7(c) and 6.7(d) show that the distance of the bow shock to the aeroshell is smaller for the numerical results than observed experimentally. The disagreement in the bow shock profile away from the aeroshell centerline may also be caused by the Ashkenas and Sherman relations for large streamline angles, and the influence of the triple-point on the bow shock in the experimental facility. The influence of these two effects is more pronounced for the supersonic central PD jets than for the sonic jets because the supersonic jets push the bow shock farther upstream than the sonic jets.

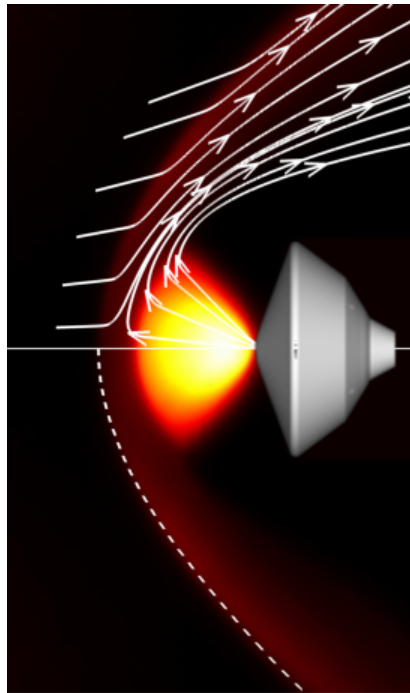
The bow shock standoff distance along the aeroshell centerline can be obtained from the PLIIF visualizations and compared to the distance calculated by the CFD results. Figure 6.8 presents comparisons between the numerical and experimental



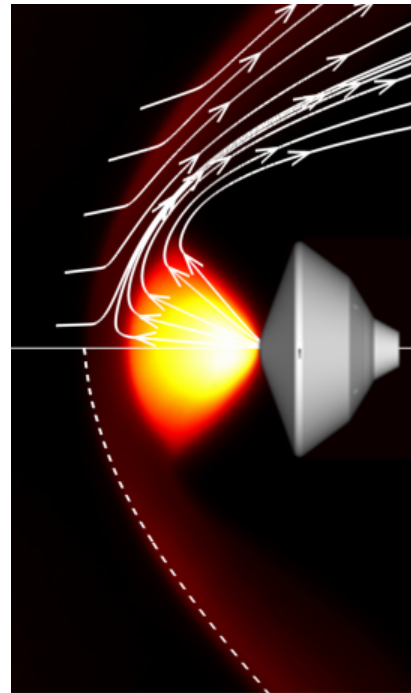
(a)  $C_T = 0.5$



(b)  $C_T = 1.0$



(c)  $C_T = 2.0$



(d)  $C_T = 2.5$

Figure 6.5: Comparison of the bow shock profile for sonic central PD jets between the numerical and experimental results.

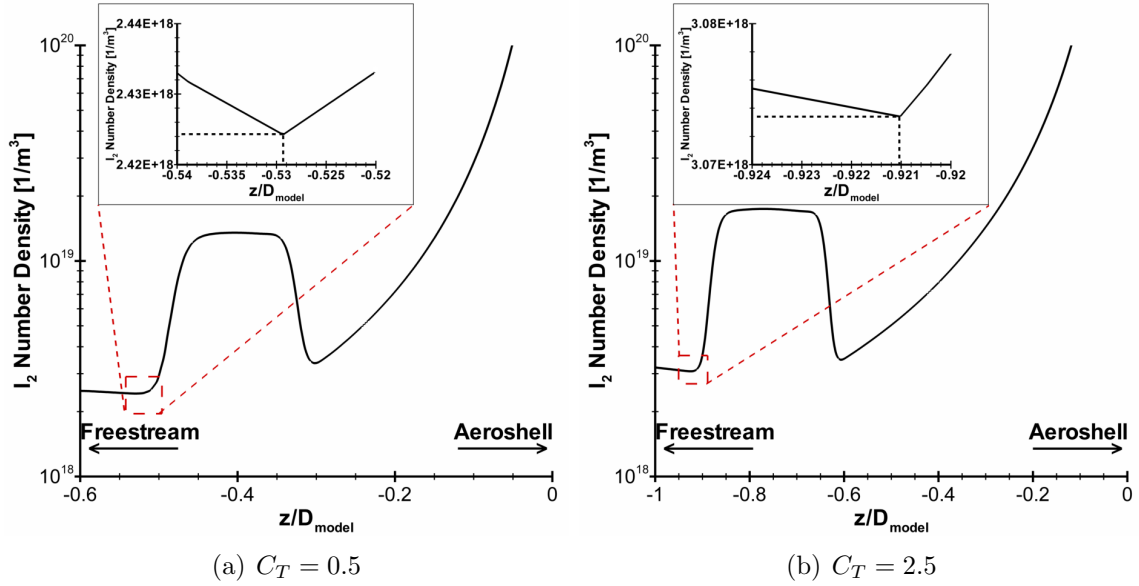


Figure 6.6: Distribution of the iodine number density calculated by LeMANS along the aeroshell centerline for the sonic central PD jet at  $C_T = 0.5$  and  $2.5$ .

results for the bow shock standoff distance normalized by the aeroshell diameter for sonic and supersonic central PD jets. The shock standoff distance is obtained from the PLIIF images by measuring the distance from the model to the location in the freestream where the brightness changes. The distance for the numerical results corresponds to the location in the freestream along the aeroshell centerline where the iodine density begins to increase, which is consistent with the experimental approach since the fluorescence in the PLIIF images is directly proportional to the iodine density in the hypersonic regions of the flow. The error bars for the experimental results are based on the uncertainty associated with the measurement of the shock standoff distance and the aeroshell diameter from the PLIIF visualizations. Figure 6.8(a) shows that the bow shock standoff distance calculated by LeMANS for the sonic central PD jets is in excellent agreement with the experimental results for all thrust coefficients investigated in this study. Good agreement in the bow shock standoff distance for the supersonic central PD jets between the two sets of results is also observed in Figure 6.8(b), with the difference ranging from 1% for  $C_T = 0.5$  to

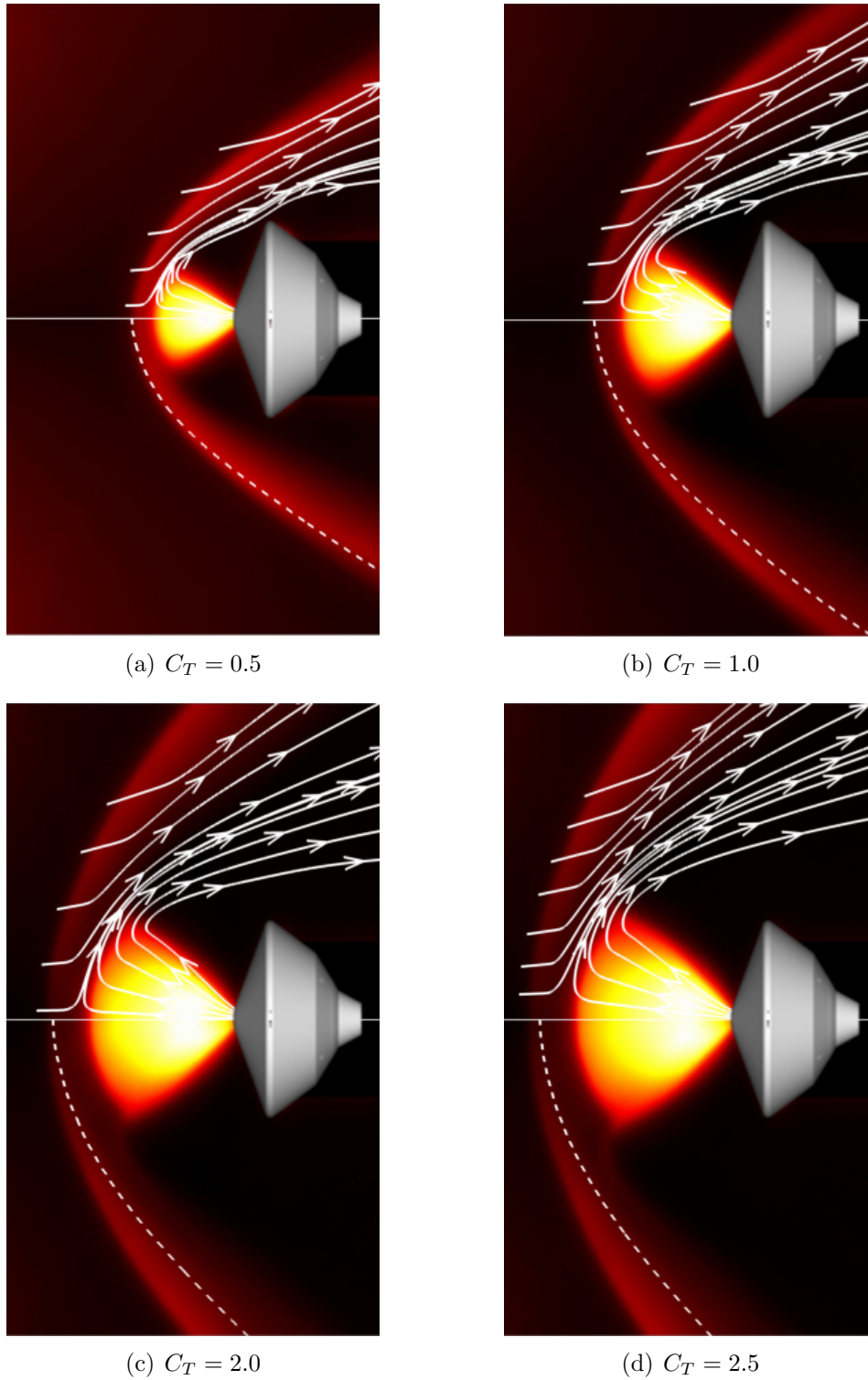


Figure 6.7: Comparison of the bow shock profile for supersonic central PD jets between the numerical and experimental results.

approximately 5% for  $C_T = 2.5$ .

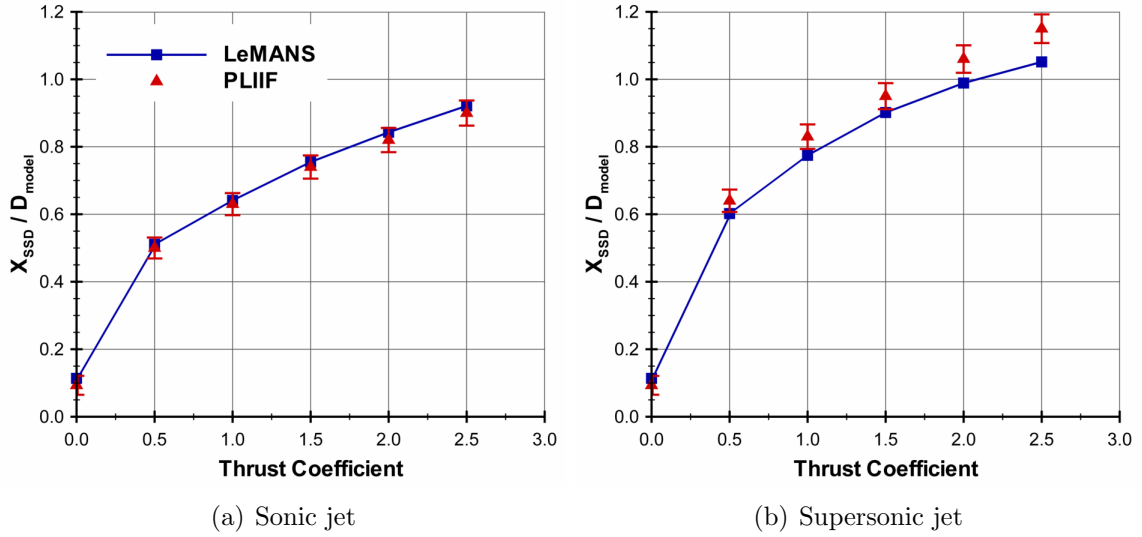


Figure 6.8: Comparison of the bow shock standoff distance for sonic and supersonic central PD jets between numerical (LeMANS) and experimental (PLIIF) results.

Figure 6.9 presents a comparison of the aerodynamic drag and total axial force coefficients for supersonic central PD jets between the numerical results and experimental measurements obtained by McGhee [20]. This experimental work investigated the aerodynamic interactions of central supersonic PD jets ( $M_{jet} = 3.0$ ) exhausting in hypersonic flow ( $M_\infty = 6.0$ ) for a  $70^\circ$  blunt-cone aeroshell. The experimental study reported a maximum variation of less than  $\pm 0.4$  in the Mach number and an accuracy better than 1% of the full-scale range (138,000 Pa) of the pressure transducers. However, the study did not provide any uncertainty values for the aerodynamic drag or total axial force measurements. Even though the freestream and PD jet Mach numbers are different between the numerical simulations and the experimental study, Figure 6.9 shows remarkably good agreement between the two sets of results with respect to the aerodynamic properties of the aeroshell. This agreement is an indication of hypersonic Mach number independence and suggests that the aerodynamic calculations obtained by LeMANS may be applicable even at lower freestream Mach



numbers.

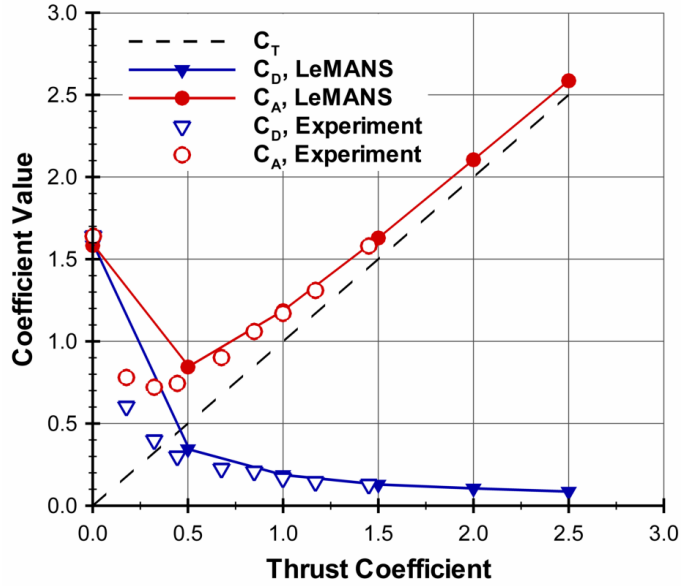


Figure 6.9: Comparison of drag and total axial force coefficients for supersonic central PD jets between numerical and experimental results. Experimental data obtained from Ref. [20]

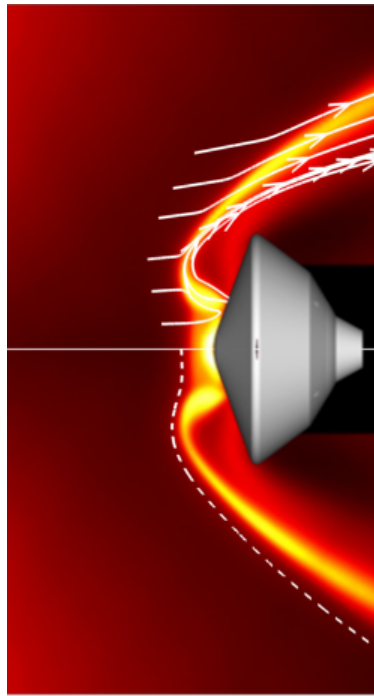
### 6.2.2 Peripheral Configuration

Qualitative bow shock profile comparisons between the numerical results and PLIIF visualizations for sonic peripheral PD jets are presented in Figure 6.10 for thrust coefficient values of 0.5, 1.0, 2.0, and 2.5. The contour levels for the CFD results correspond to the iodine density values at the point along the aeroshell centerline where the iodine density in the freestream begins to increase. Similar to the central PD jets, both the freestream flow and the PD jet are seeded with molecular iodine to reveal the features of the flow. The PLIIF images show that the bow shock is preserved between the PD jets upstream of the aeroshell nose, and is pushed away from the capsule as the thrust coefficient increases. The comparisons between the velocity streamlines and the iodine density contour calculated by LeMANS and the PLIIF visualizations show good qualitative agreement in the bow shock profile

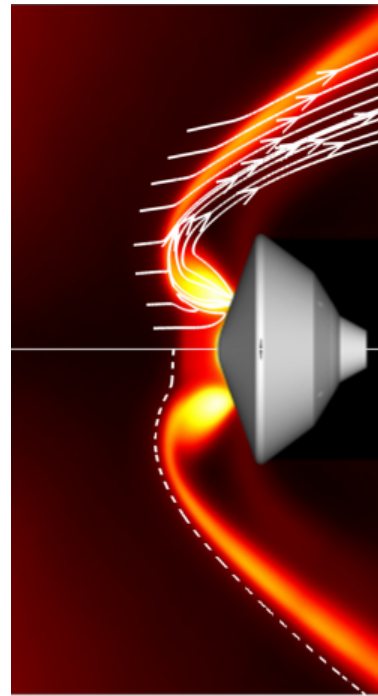
between the two sets of results, particularly between two PD jets upstream of the aeroshell nose.

Figure 6.11 shows similar bow shock profile comparisons for supersonic peripheral PD jets between the numerical and experimental results for thrust coefficient values of 0.5, 1.0, 2.0, and 2.5. The PLIIF visualizations indicate that the supersonic peripheral jets have a greater penetration depth than the sonic jets. As a result, the bow shock is pushed farther upstream by the PD jets. The recirculation regions predicted by LeMANS are caused by the projection of the three-dimensional flow around the plume of the PD jet onto a two-dimensional cut-plane. The figure shows good agreement between the CFD results and the experimental visualizations at the low thrust coefficients. Figures 6.11(c) and 6.11(d), however, indicate that the agreement between the two methods for  $C_T = 2.0$  and 2.5 is good upstream of the aeroshell nose, but decreases away from the capsule centerline. The figures show that the bow shock calculated by LeMANS is closer to the aeroshell than observed in experiments. This disagreement may also be caused by the effects of the Ashkenas and Sherman relations for high streamline angles and the triple-point interaction in the experimental facility, which are stronger for the supersonic than the sonic peripheral PD jets since the supersonic jets push the bow shock farther upstream of the aeroshell.

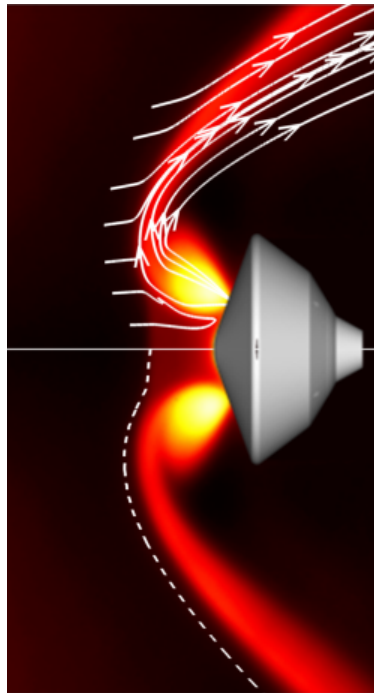
The bow shock standoff distance upstream of the aeroshell nose for the peripheral configuration can be measured from the PLIIF visualizations, similar to the central PD jets. Figure 6.12 shows the variation of the bow shock standoff distance normalized by the aeroshell diameter with thrust coefficient for the peripheral PD jets for the numerical and experimental results. The standoff distance is obtained from the PLIIF images by measuring the distance along the aeroshell centerline from the model to the location in the freestream where the brightness changes. For the CFD results, the bow shock standoff distance corresponds to the location in the freestream where the iodine density begins to increase. The error bars for the experimental results account



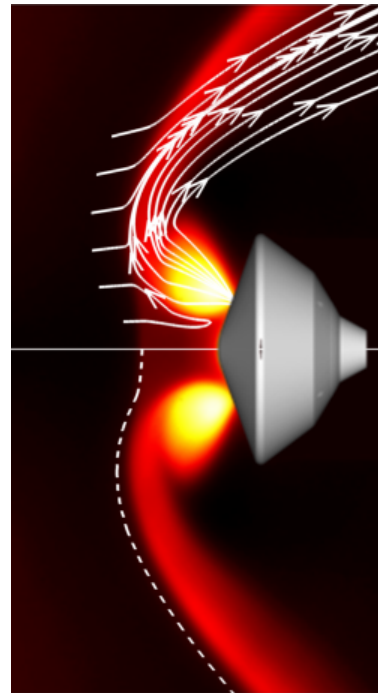
(a)  $C_T = 0.5$



(b)  $C_T = 1.0$

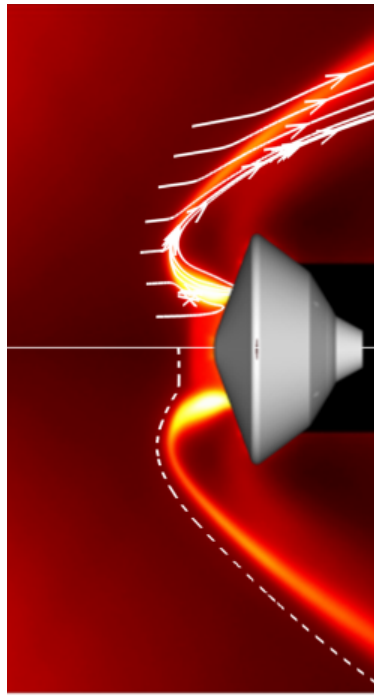


(c)  $C_T = 2.0$

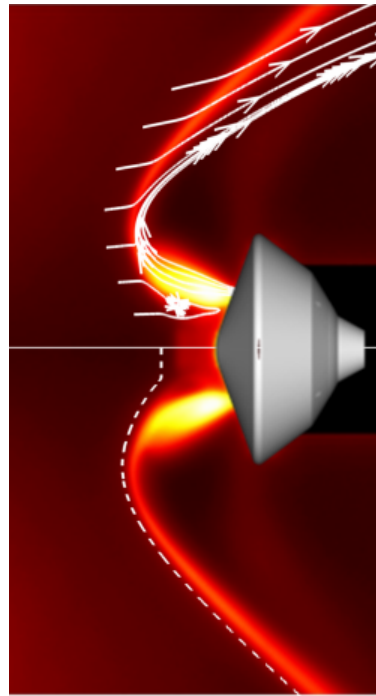


(d)  $C_T = 2.5$

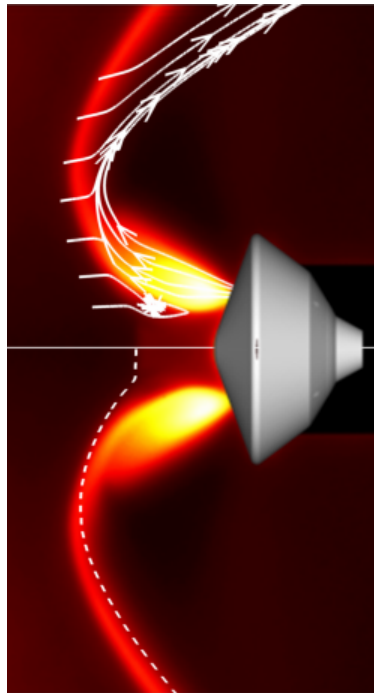
Figure 6.10: Comparison of the bow shock profile for sonic peripheral PD jets between the numerical and experimental results.



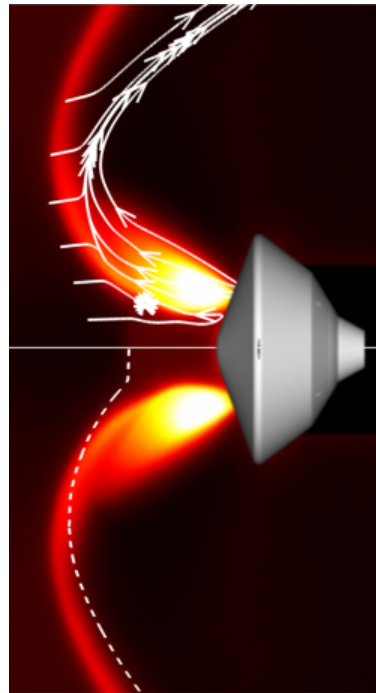
(a)  $C_T = 0.5$



(b)  $C_T = 1.0$



(c)  $C_T = 2.0$



(d)  $C_T = 2.5$

Figure 6.11: Comparison of the bow shock profile for supersonic peripheral PD jets between the numerical and experimental results.

for uncertainties in the measurements of the bow shock location and the aeroshell diameter from the PLIIF images. The figure shows that the agreement between the numerical and experimental results increases from 12% and 17% for the sonic and supersonic jets, respectively, at  $C_T = 0.5$  to within the experimental uncertainty at  $C_T = 2.5$ . This close agreement suggests that the differences in the bow shock profile away from the aeroshell centerline observed in Figure 6.11 may not have a significant effect on the flowfield properties near the aeroshell nose.

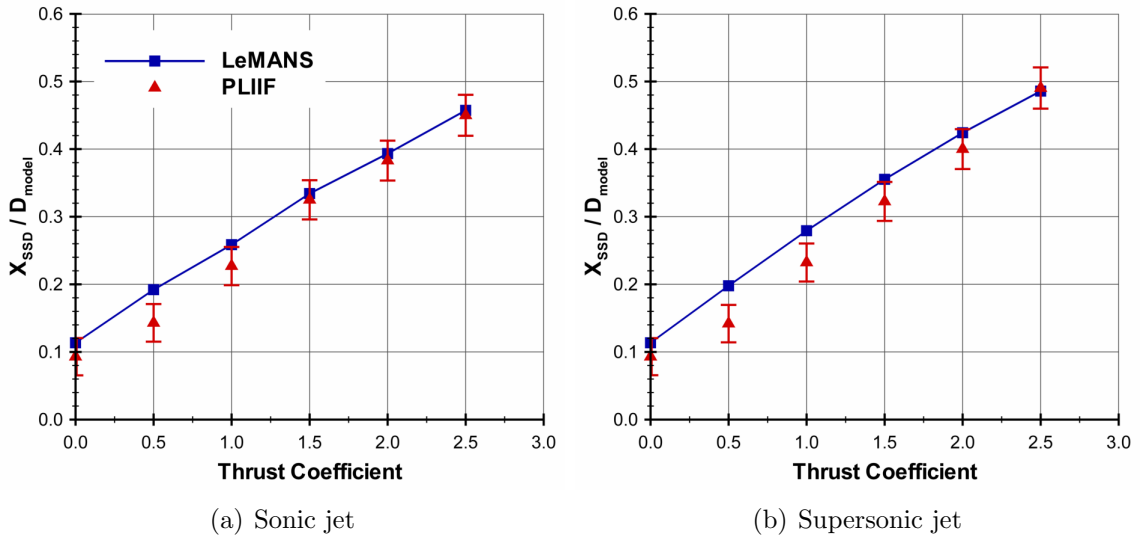


Figure 6.12: Comparison of the bow shock standoff distance for sonic and supersonic peripheral PD jets between the numerical (LeMANS) and experimental (PLIIF) results.

As previously described in Chapter II, the PD jet species mole fraction can be extracted from the PLIIF visualizations by calculating the fluorescence ratio of two images: one image of fully-seeded flow (i.e.  $I_2$  seeded in the freestream and the PD jet), and another image of  $I_2$ -seeding only in the jet. This fluorescence ratio is proportional to the fraction of iodine molecules that originate from the PD jet. Figure 6.13 presents contours of PD jet  $I_2$  mole fraction for the peripheral sonic PD jet at  $C_T = 1.5$  for numerical (top) and experimental (bottom) results. This mole fraction is calculated in the numerical simulations by tagging the  $I_2$  species from the PD jet

(i.e. same properties as molecular iodine but distinguishable by name). The figure indicates overall good agreement in the PD jet  $I_2$  mole fraction distribution between the numerical and experimental results. The contours, however, show that LeMANS calculates a more diffused PD jet plume around the aeroshell shoulder and in the wake compared to the experimental measurements. The contours also show that the width of the PD jet core upstream of the aeroshell calculated by LeMANS is slightly smaller than measured experimentally.

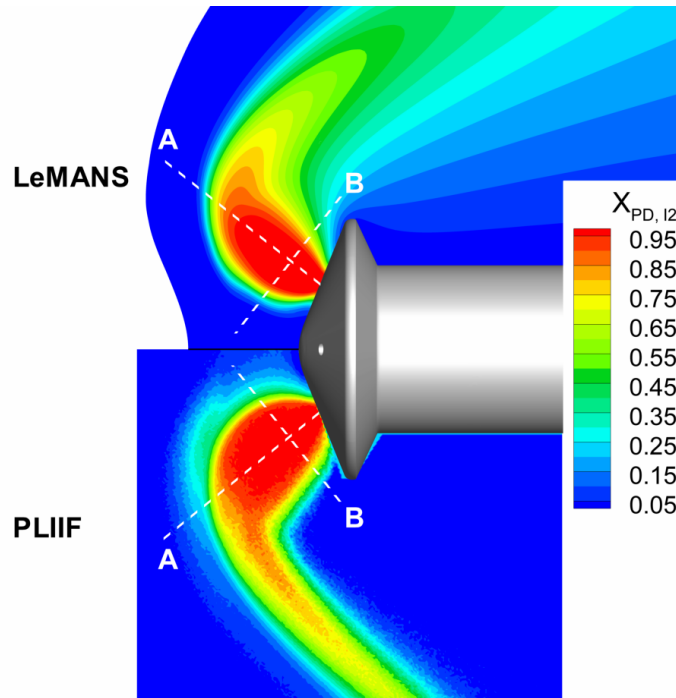


Figure 6.13: Comparison of the PD jet  $I_2$  mole fraction contours for sonic peripheral PD jet at  $C_T = 1.5$  between the numerical (LeMANS) and experimental (PLIIF) results.

Figure 6.14 presents the distribution of the PD jet  $I_2$  mole fraction along the cut-lines A and B shown in Figure 6.13 for the numerical and experimental results. The plots also include the distribution of the gradient-length local Knudsen calculated from the numerical results along the cut-lines. Line A begins at the nozzle-exit and ends approximately 0.8 aeroshell diameters (8 mm) along the core of the peripheral PD jet. Figure 6.14(a) shows that LeMANS predicts a relatively constant jet  $I_2$  mole

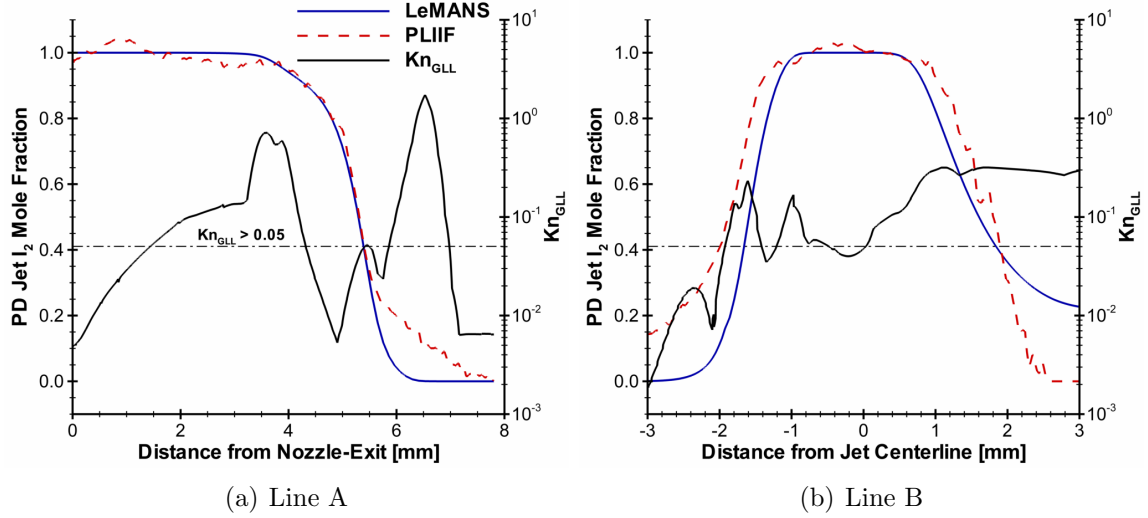


Figure 6.14: Comparison of PD jet I<sub>2</sub> mole fraction along extraction lines for sonic peripheral PD jet at  $C_T = 1.5$  between the numerical (LeMANS) and experimental (PLIIF) results.

fraction equal to 1.0 (i.e. all of the iodine is from PD jet) up to approximately 3.5 mm away from the PD nozzle-exit. Then, the jet I<sub>2</sub> mole fraction calculated by LeMANS decreases to 0.0 (i.e. all of the iodine is from the freestream flow) about 6.5 mm away from the nozzle-exit along the PD jet core. The figure also shows overall good agreement in the jet I<sub>2</sub> mole fraction distribution along the PD jet core between the numerical results and PLIIF measurements up to a distance of about 5.5 mm (0.55 aeroshell diameters) away from the nozzle-exit. From 5.5 mm to 7.5 mm (freestream) away from the nozzle-exit, however, the mole fraction calculated by LeMANS differs from the experimental measurements. Along this same portion of the cut-line, the local Knudsen number distribution indicates that continuum breakdown (i.e.  $Kn_{GLL} > 0.05$ ) may occur due to the sharp gradients across the bow shock. The difference between the numerical and experimental results may be caused by continuum breakdown effects on the CFD solution.

The PD jet I<sub>2</sub> mole fraction and the gradient-length local Knudsen number calculated from the numerical results along cut-line B are shown in Figure 6.14(b). Line

B crosses the PD jet at approximately 1.5 mm (0.15 aeroshell diameters) upstream of the nozzle-exit and is centered at its intersection with cut-line A. The distance along line B increases from negative values near the aeroshell centerline to positive values near the shoulder of the aeroshell. Figure 6.14(b) shows that the width of the PD jet calculated by LeMANS is approximately 30% smaller than that measured by PLIIF at this axial location. At the jet boundary near the aeroshell centerline, the PD jet  $I_2$  mole fraction decreases from 1.0 within the jet core to approximately 0.0 and 0.2 across the boundary for the numerical and experimental results, respectively. Near the aeroshell shoulder, the jet iodine mole fraction also decreases across the jet boundary from unity within the jet core to approximately 0.25 and 0.0 for the numerical and experimental results, respectively. These differences in the iodine distribution between the two methods may be caused by several factors, including continuum breakdown effects on the CFD solutions across the boundaries of the PD jet.

### 6.3 Reaction Control System

The planar laser-induced iodine fluorescence technique is also employed at the University of Virginia to obtain flowfield visualizations of flow around a Mars-entry aeroshell with parallel and transverse RCS jets. These visualizations are used in this section to conduct qualitative comparisons of the bow shock profile around the aeroshell with the numerical results. Figure 6.15 presents the iodine density contour representative of the bow shock profile and velocity streamlines obtained from the numerical results and overlaid on a PLIIF visualization for the parallel RCS jet at  $C_T = 1.0$ . The diameter of the aeroshell is 20 mm and the angle-of-attack is  $20^\circ$ . The PLIIF image indicates a small interaction between the parallel RCS jet and the bow shock because the jet does not impinge on the shock. The figure shows good qualitative agreement in the bow shock profile between the numerical and experimental



results, with some differences downstream of the aeroshell similar to those observed in the comparisons for the baseline configuration. These differences may be caused by the numerical freestream conditions (i.e. Ashkenas and Sherman relations) and the influence of the triple-point on the bow shock in the experimental facility.

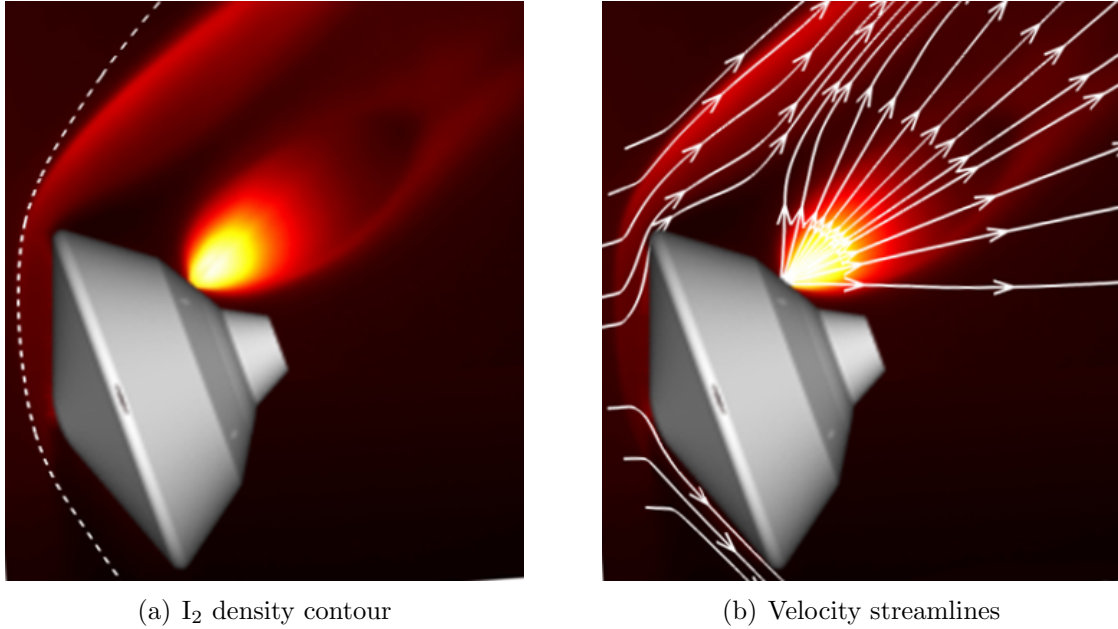


Figure 6.15: Comparison of the bow shock profile for the parallel RCS jet at  $C_T = 1.0$  between the numerical ( $I_2$  density contour and velocity streamlines) and experimental (PLIIF image) results.

Similar qualitative bow shock profile comparisons between the numerical results and experimental visualizations for the transverse RCS jet at  $C_T = 1.0$  are presented in Figure 6.16. The figure shows the iodine density contour indicative of the bow shock profile and velocity streamlines calculated by LeMANS and superimposed over a PLIIF visualization. The PLIIF image indicates that the plume of the transverse RCS jet impinges on the bow shock and changes its profile. This jet-shock interaction is greater than observed for the parallel RCS jet. Good agreement in the bow shock profile between the numerical results and the PLIIF image can be observed upstream of the aeroshell shoulder. Downstream of the capsule, however, LeMANS predicts a larger penetration depth of the transverse RCS jet, which increases the distance of

the bow shock from the aeroshell, compared to the PLIIF visualization. As a result, the distance of the bow shock from the aeroshell is greater for the CFD results than observed experimentally. The disagreement in the profile of the bow shock portion downstream of the aeroshell shoulder may again be caused by the Ashkenas and Sherman relations for large streamline angles and the interaction of the bow shock and the barrel shock in the experimental facility.

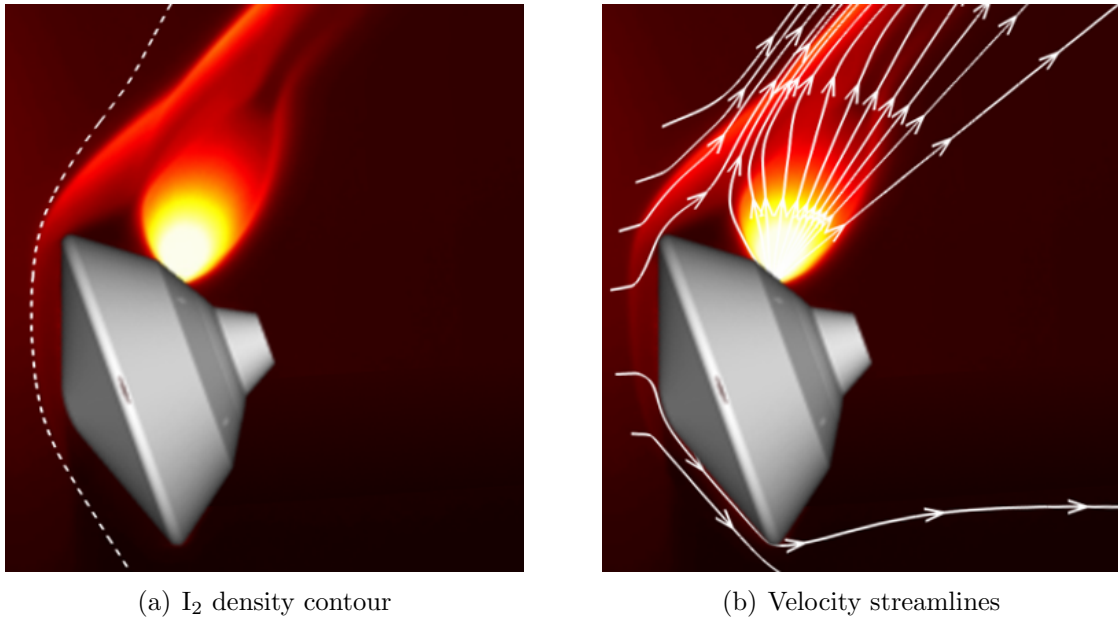


Figure 6.16: Comparison of bow shock profile for the transverse RCS jet at  $C_T = 1.0$  between the numerical ( $I_2$  density contour and velocity streamlines) and experimental (PLIIF image) results.

## 6.4 Summary

This chapter presented qualitative and quantitative comparisons between the numerical results obtained using the CFD code LeMANS and available experimental data for hypersonic flow around Mars-entry capsules with propulsive decelerator and reaction control system thrusters. These comparisons served to assess the physical accuracy of the computational method in predicting the complex fluid interactions

generated by PD and RCS jets. The comparisons indicated overall good qualitative agreement in the bow shock profile around the aeroshell with PD and RCS jets between the numerical results calculated by LeMANS and flowfield visualizations obtained at the University of Virginia using the planar laser-induced iodine fluorescence technique. The qualitative comparisons, however, showed some disagreement between the two methods in the portion of the bow shock away from the aeroshell centerline, particularly for the flow around the aeroshell with supersonic central and peripheral PD jets at high thrust conditions and the relatively larger aeroshell (20 mm diameter) with and without RCS jets. These differences are believed to be caused by the inaccuracy of the Ashkenas and Sherman relations in LeMANS for large streamline angles, and the influence of the triple-point on the bow shock profile in the experimental facility.

Quantitative comparisons were also carried out between the numerical results and available experimental data. The bow shock standoff distance calculated by LeMANS for central and peripheral PD jets was in overall close agreement with experimental measurements derived from PLIIF visualizations. The maximum difference in the shock standoff distance between the numerical and experimental results was less than 5% for the central PD jets and less than 17% for the peripheral PD jets. Quantitative comparisons of the jet  $I_2$  mole fraction between LeMANS and PLIIF for sonic peripheral PD jets at  $C_T = 1.5$  also indicated good agreement between the two methods. However, the numerical results showed a more diffused PD jet plume around the aeroshell shoulder and in the wake compared to the experimental measurements. These differences may be caused by several factors, including the effects of continuum breakdown on the CFD solutions. Finally, quantitative comparisons of the aerodynamic drag and axial force coefficients for supersonic central PD jets between the numerical results and experimental measurements showed remarkably good agreement between the two sets of results for a range of thrust conditions even though the

experimental study focused on Mach 3.0 jets exhausting in a Mach 6.0 freestream. This agreement demonstrated hypersonic Mach number independence and suggests that the numerical results may be applicable even at lower freestream Mach numbers.

## CHAPTER VII

### Conclusion

This chapter provides a summary of the results presented in this dissertation. The chapter also provides a list of the original contributions made to the field, and concludes with several recommendations for future research directions.

#### 7.1 Summary

Chapter I described the challenges of performing atmospheric entry, descent, and landing on Mars, and highlighted the limitations of the current EDL technology. The chapter showed how the six successful US robotic exploration missions to Mars have relied heavily on the heritage, Viking-era technology from the 1960s and 1970s to perform Mars EDL. All of these missions have had comparable landing masses of under 1.0 ton and relatively large landing ellipses on the order of 10s of kilometers. However, the chapter described how current plans for future sample-return and human-exploration missions to Mars call for landing masses of 40-80 tons and landing accuracy of within 10s of meters. The chapter also described how these requirements are beyond the capabilities of the current Viking-era EDL technologies, and presented some alternative technologies that are currently being investigated for these future missions. Two such alternatives are propulsive decelerator (PD) and reaction control system (RCS) thrusters, which are currently being considered as enabling technologies

for achieving pinpoint landing of high-mass Mars missions. The chapter cited several references that have mainly focused on examining the effects of propulsive decelerator jets exhausting into a supersonic freestream, and established the need to also investigate the fluid interactions induced by propulsive deceleration in a hypersonic freestream. The chapter also provided several references that promote the continued development of reaction control systems for Mars EDL.

Chapter II provided details on the technical approach used in this study. The chapter described the experimental hypersonic wind tunnel facility and the planar laser-induced iodine fluorescence (PLIIF) technique employed at the University of Virginia to obtain experimental results that are used to assess the physical accuracy of the computational method. The chapter also described the computational fluid dynamics code, LeMANS, used in this study to investigate the fluid interactions induced by PD and RCS jets in a hypersonic freestream. The chapter provided an overview of the governing equations solved by LeMANS and the relevant physical models used in the code. The chapter then outlined the implementation of the Ashkenas and Sherman relations in LeMANS as freestream boundary conditions in order to simulate the freejet conditions in the experimental facility. The Ashkenas and Sherman relations were shown to significantly reduce the computational complexity and runtime of the numerical simulations. The chapter finally presented the effects of the Ashkenas and Sherman relations on the flowfield, surface, and aerodynamic properties of a Mars-entry aeroshell compared to corresponding constant freestream conditions. The results showed that the Ashkenas and Sherman relations decreased the bow shock standoff distance near the stagnation point and broadened the shock profile around the aeroshell. The results also showed that the Ashkenas and Sherman relations decreased the overall pressure distribution along the aeroshell forebody, and consequently, decreased the drag coefficient of the aeroshell.

Chapter III presented a numerical investigation of the fluid interactions induced

by central PD jets on a Mars-entry aeroshell in a hypersonic freestream. The chapter first outlined details about the aeroshell geometry and central PD jet conditions used in the study. The chapter then described the fluid interactions induced by a sonic central PD jet. The results showed that the PD jet altered the structure of the flowfield upstream of the aeroshell. The results also showed that the aerodynamic drag on the aeroshell decreased with increasing thrust from the central PD jet, and asymptotically reached a constant value of 7% of the no-jet case. This decrease in the aerodynamic drag was shown to be caused by a shielding effect of the central PD jet that prevented mass and momentum in the freestream from reaching the surface of the aeroshell. The axial force acting on the aeroshell was also shown to initially decrease with PD thrust, and only exceeded the drag force for the no-jet case at relatively high thrust conditions. Finally, the chapter showed that the Mach number of the central PD jet did not have a significant effect on the deceleration performance of the aeroshell. However, the supersonic central PD jet may provide propellant mass savings compared to the sonic jet since it utilized a lower mass flow rate.

A numerical study of the fluid interactions produced by peripheral PD jets on a Mars-entry aeroshell in a hypersonic freestream was described in Chapter IV. The chapter began by providing details on the aeroshell geometry and peripheral PD jet conditions used in this study. Next, the chapter presented the numerical results in two sections. The numerical results in the first section showed that the peripheral PD jet changed the bow shock profile around the aeroshell to a saddle shape by pushing the portion of the shock near the jet plume upstream. The peripheral PD jet also decreased the drag force by obstructing the flow around the aeroshell and creating low surface pressure regions similar to wake flows downstream of the jet plume. However, the total axial force on the aeroshell was shown to be proportional to the thrust from the peripheral PD jet. The results also showed that the Mach number of the peripheral PD jets had small effects on the aerodynamic properties of the

aeroshell. In the second section, the numerical results indicated that the peripheral PD configuration provided between 3 and 7 times more drag than the central PD configuration depending on the thrust conditions. This was shown to be caused by the ability of the peripheral PD configuration to preserve some of the relatively high surface pressure associated with the no-jet case, particularly near the aeroshell nose and between adjacent PD jets. Finally, the chapter provided a discussion on the deceleration performance of peripheral and central PD configurations. The results showed that, unlike the central configuration, the deceleration performance of the peripheral PD configuration remained high and roughly constant over a range of thrust conditions for both sonic and supersonic jets.

Chapter V presented a numerical investigation of the fluid interactions induced by reaction control system jets on a Mars-entry aeroshell in a hypersonic freestream. The chapter first described the geometry of the aeroshell and the conditions of the reaction control system. The RCS jet was directed both parallel and transverse to the freestream flow in order to understand the effects of the jet orientation on the aeroshell properties. The chapter then presented the numerical results in four sections. The first section described the flow around the baseline configuration without the RCS jet at an angle-of-attack of  $20^\circ$ . The second and third sections of the chapter examined the effects of the parallel and transverse jet on the properties of the aeroshell. The numerical results showed that both the parallel and transverse jets obstructed the path of the flow from the freestream around the aeroshell aftbody, and altered the flowfield structure in the wake. The results also showed that both RCS jet configurations increased the overall pressure along the aftbody, particularly at high thrust conditions, which also affected the aerodynamic properties of the aeroshell. In the last section of the chapter, the control effectiveness of the parallel RCS jet was found to be comparable to an ideal performance, while relatively large aerodynamic interference caused a control deficit for the transverse RCS jet.



Chapter VI outlined comparisons between the numerical results for propulsive deceleration and reaction control systems and experimental data obtained from both previous and on-going work. These comparisons served to assess the physical accuracy of the computational method in capturing the complex fluid interactions produced by PD and RCS jets. Qualitative comparisons between the numerical results and flowfield visualizations obtained at the University of Virginia using PLIIF indicated overall good agreement in the bow shock profile around the aeroshell with PD and RCS jets. These comparisons, however, also showed some disagreement between the two methods in the portion of the bow shock away from the aeroshell centerline that might be caused by the inaccuracy of the Ashkenas and Sherman relations for large streamline angles, and the influence of the triple-point in the experimental facility on the bow shock. The chapter also presented quantitative comparisons between the numerical results and experimental measurements. Comparisons of bow shock standoff distance for central and peripheral PD jets showed overall good agreement between the numerical and experimental results. Comparisons of the jet  $I_2$  mole fraction for the sonic peripheral PD jet at  $C_T = 1.5$  also indicated overall good agreement between the two methods, with some differences possibly caused by the effects of continuum breakdown on the CFD solution. Finally, comparisons of the aerodynamic properties for supersonic central PD jets between the numerical results and experimental measurements for a Mach 6.0 freestream were remarkably good, which demonstrated hypersonic Mach number independence and suggested that the numerical results may be applicable even at lower freestream Mach numbers.

## 7.2 Contributions

The work presented in this dissertation advances the maturity levels of propulsive deceleration and reaction control systems as enabling technologies for pinpoint landing of future, high mass Mars missions. This work identified the effects of the fluid

interactions produced by propulsive deceleration and reaction control on the properties of Mars-entry aeroshells in hypersonic freestream conditions, and made several contributions to the continued development of these technologies. These contributions are provided in Refs. [89, 90, 91, 92, 56, 57, 93, 63, 87] and are summarized in this section.

1. Central propulsive deceleration can produce a shielding effect that prevents mass and momentum in the freestream from reaching the surface of the aeroshell. This shielding effect represents the main mechanism for the virtual elimination of the drag force acting on the aeroshell. The obstruction caused by the central PD jet creates a low pressure region near the aeroshell forebody. As the thrust from the central PD increases, the strength of this shielding effect also increases, which expands the size of the low pressure region and decreases the drag force acting on the aeroshell. As the thrust of the PD continues to increase, the flow around the aeroshell approaches a jet-only, no freestream configuration which causes the drag coefficient to asymptotically reach a constant small value. The decrease in the drag force also causes the total axial force acting on the aeroshell to initially decrease and then to increase mainly due to the contribution from the PD thrust. The trend in the axial force indicates that central propulsive deceleration may only be beneficial at relatively high thrust conditions.
2. Peripheral propulsive deceleration obstructs the flow around the aeroshell and generates wake-like regions downstream of the jet plumes, which are characterized by low surface pressures. As the thrust from the peripheral decelerators increases, the jet plumes obstruct more flow around the aeroshell which expands the size of the low surface pressure regions downstream of the PD nozzles. This represents the main reason for the decrease in the drag force acting on the aeroshell. However, unlike the central configuration, the peripheral PD jets can preserve some of the high forebody surface pressures associated with the no-jet

case, particularly near the aeroshell nose and between adjacent PD jets, which significantly reduces the elimination of the drag force. This drag preservation causes the total axial force acting on the aeroshell to increase with PD thrust, and the deceleration performance of the peripheral configuration to remain high and relatively constant over a range of thrust conditions.

3. The PD nozzle-exit Mach number may not have a significant effect on the performance of central and peripheral propulsive deceleration. For conditions similar to those investigated in this dissertation, the differences in the total axial force acting on the aeroshell for sonic and supersonic PD jets are small for both the central and peripheral configuration. Supersonic jets, however, require less mass flow rate than sonic jets, which can provide potential propellant mass savings for future Mars missions.
4. The comparisons between the numerical results and experimental data for central propulsive deceleration revealed hypersonic Mach number independence with respect to the aerodynamic properties of the aeroshell. This independence is significant for two reasons. The first reason is that the Mach independence indicates that the results presented in this dissertation for central propulsive deceleration may also be applicable for lower hypersonic freestream Mach numbers. The second reason is that the deceleration performance of a Mars-entry aeroshell with central propulsive deceleration may remain constant over a range of freestream Mach numbers during the hypersonic phase of Mars EDL.
5. The orientation of the thruster with respect to the aeroshell center of gravity can have a significant effect on the control effectiveness of the reaction control system. The orientation of the RCS jet has a direct impact on the moment generated by the thrust force from the jet, and can induce fluid interactions that produce interference moments. This aerodynamic interference can reduce

the control effectiveness of the RCS since a portion of the moment produced by the thrust from the jet is used to counteract the interference moment. Therefore, the performance of the reaction control system can be made close to an ideal performance by maximizing the moment induced by the thrust force and minimizing the moment produced by the aerodynamic interference. This can be achieved by selecting an orientation of the RCS jet that produces large moment arms for which all of the components of the thrust force contribute to moments along the same direction. The performance of the RCS can be also improved by either minimizing the fluid interactions induced by the jet, or by designing the layout of the RCS such that the fluid interactions produce counteracting effects that result in a small net interference.

### **7.3 Future Work**

This dissertation work identified several important fluid interactions produced by propulsive deceleration and reaction control system jets, and their effects on the properties of Mars-entry aeroshells. The physical accuracy of the computational method was assessed by qualitative and quantitative comparisons with available experimental data. These comparisons have shown that continuum breakdown may have an effect on the CFD results, which can be evaluated using a hybrid CFD-DSMC method. More experimental work is also needed that can provide further quantitative measurements for the continued assessment of the numerical method. The analysis presented in this dissertation can be extended to examine the effects of PD and RCS jets on the heat transfer to the aeroshell. The simulation of these complex flows in LeMANS can benefit from automatic mesh adaptation techniques that can significantly reduce the time spent on generating appropriate grids. Additionally, key performance parameters of propulsive deceleration and reaction control systems for future high-mass Mars missions can be estimated using system-level studies in order to raise the readi-

ness levels of these technologies. These parameters can then be used in simulations of representative conditions that may be encountered during atmospheric entry of a high-mass Mars capsule with PD and RCS jets.

### **Effects of Continuum Breakdown**

The numerical results presented in this dissertation have indicated possible continuum breakdown in some regions of the flow around the capsule. A previous study showed that the effects of these breakdown regions were not significant with respect to the deceleration performance calculated by LeMANS for the central PD jets [87]. The analysis can be extended to peripheral propulsive deceleration and reaction controls systems to identify and quantify the effects of continuum breakdown on the numerical results calculated by LeMANS. This can be achieved by using a hybrid particle-continuum technique, which utilizes the CFD method in the continuum regions of the flow and the DSMC method in the rarefied regions.

### **Further Comparisons with Experimental Data**

The experimental results described in Chapter VI provide valuable data that has been used to assess the physical accuracy of LeMANS. However, there is still a need for more quantitative experimental measurements of the effects of propulsive deceleration and reaction control systems to provide validation data for current CFD results. This need is currently being addressed by on-going work at the University of Virginia [56, 57, 63], which will provide flowfield measurements of several fluid properties, such as density, temperature, and velocity, using the planar-laser induced iodine fluorescence technique for flows around Mars-entry aeroshells with propulsive deceleration and reaction control systems. Quantitative comparisons with these experimental measurements will be crucial in the continued assessment of the numerical method in capturing the effects of PD and RCS jets on the properties of Mars-entry aeroshells.

## **Effects of PD and RCS Jets on the Heat Transfer to the Vehicle**

A major focus of this dissertation has been to examine the effects of propulsive deceleration and reaction control systems on the aerodynamic characteristics of Mars-entry capsules. The freestream conditions that have been used in this work are based on wind tunnel conditions at the University of Virginia that can replicate the high Mach numbers achieved during atmospheric entry. However, the freestream enthalpy levels achieved in the experimental facility and simulated in this work are approximately two orders of magnitude smaller than the enthalpy levels experienced during Mars entry. As a result, the heat transfer from the flow around the aeroshell to the capsule walls experienced in this work is significantly smaller than what is typically encountered during flight. However, propulsive deceleration and reaction control systems may have important effects on the heat transfer to the aeroshell, which may increase the temperature on the surface beyond acceptable limits. Therefore, these effects can be examined by matching the enthalpy in the freestream for the numerical simulations to levels similar to those experienced in flight.

## **Implementation of Automatic Mesh Adaptation Techniques in LeMANS**

Manual grid generation for flows around a Mars-entry capsule with PD and RCS jets can be difficult and very time-consuming due to the complexity of the flowfield. Uniform mesh refinement may also be inefficient since it can increase the grid resolution in regions of the flow that have small effects on the overall CFD solution. Therefore, automatic grid adaptation techniques present an attractive option to efficiently and accurately capture the flow features and interactions produced by propulsive deceleration and reaction control systems. These techniques can be divided into two main categories. Feature-based automatic grid adaptation techniques typically target local errors in the CFD solution due to gradients of a specific flow variable. Output-based grid adaptation methods refine the mesh based on error indicators that use the

adjoint solution of an output functional, such as lift or drag coefficient, to account for the effects of local errors as well as their transport throughout the computational domain to improve the calculation of that output functional [94]. The implementation of automatic grid adaptation techniques in LeMANS can significantly reduce the time spent on grid generation for these types of complex flows.

### **System-Level Studies**

System-level studies can identify and estimate the requirements for the performance of propulsive deceleration and reaction control systems for future, high mass, Mars missions. These requirements include estimating the thrust force that the propulsive decelerator or the moment that the RCS must provide to decelerate or control a capsule with a certain mass under specific trajectory constraints. Such system studies can also identify key performance parameters, which are defined as capabilities that are considered most essential for successful mission accomplishment [95], to track the maturity of propulsive deceleration and reaction control systems. Reference [27] provides a preliminary list of key performance parameters for propulsive deceleration, which include the PD engine thrust to weight ratio and the ability of the PD thruster to start in the expected environments. These studies are an important aspect of maturing and raising the technology readiness levels of propulsive deceleration and reaction control systems.

### **Mars Entry Simulations**

Once key performance requirements have been identified from system-level studies, numerical investigations of representative high-mass Mars entry systems with PD and RCS thrusters can be performed to evaluate the fluid interactions induced by these jets during Mars atmospheric entry. The freestream conditions in these simulations can be determined from EDL trajectory studies, and should account for the CO<sub>2</sub>

atmosphere that will be encountered during Martian entry, and reacting gas mixtures for the PD and RCS thrusters. Such numerical simulations, however, can be very complex because they need to include the effects of several other fluid phenomena, such as turbulence and chemical reactions. The conditions simulated in this dissertation represent flows in which viscous effects are important due to the relatively low densities and small length scales (i.e. small Reynolds numbers). These viscous effects can stabilize some flowfield features, such as the PD jet shock, which causes the flow to be overall steady. However, as the size of the entry-vehicle increases, the flow around the capsule with PD and RCS jets may become unsteady. As a result, future numerical simulations of Mars-entry vehicles with PD and RCS jets may require time-accurate solutions to capture the unsteady features of the flow, as well as the effects of PD and RCS engine-startup. Therefore, significant CFD code development, along with experimental testing, may be required to accurately simulate the fluid interactions induced by propulsive deceleration and reaction control systems during Mars atmospheric entry.



## APPENDICES

## APPENDIX A

### Species Data

#### Blottner Curve Fit Constants

Table A.1 presents the constants used in Equation 2.11 to determine the coefficients of viscosity for molecular nitrogen [66] and molecular iodine [96].

Table A.1: Blottner constants for molecular nitrogen and iodine.

	<i>A</i>	<i>B</i>	<i>C</i>
N <sub>2</sub>	0.027	0.318	-11.32
I <sub>2</sub>	-0.087	2.089	-17.99

#### Rotational Relaxation Coefficients

Table A.2 lists the coefficients used in the rotational relaxation model to calculate the rotational collision number,  $Z_{r,s}$ , given in Equation 2.5 and the mean collision rate,  $\nu_s$ , given in Equation 2.6 for molecular nitrogen [69] and iodine [97].

Table A.2: Rotational relaxation coefficients for molecular nitrogen and iodine.

	$Z_r^\infty$	$T^*$ , K	$T_{ref}$ , K	$\omega$	$d_{ref}$ , m
N <sub>2</sub>	18.1	91.5	273	0.740	$4.17 \times 10^{-10}$
I <sub>2</sub>	50.0	557	273	0.945	$8.80 \times 10^{-10}$

## APPENDIX B

### Manual Grid Adaptation Process

This appendix describes the process to manually adapt the computational grid to simulate hypersonic flow over Mars-entry aeroshells with propulsive deceleration (PD) and reaction control system (RCS) thrusters. This process is required to accurately capture the fluid interactions induced by these jets, as well as their effects on the properties of the aeroshell using the computational fluid dynamics (CFD) code LeMANS. Systematic grid convergence studies (i.e. mesh refinement until the solution becomes independent of the computational grid) are conducted for the simulations of the aeroshell without PD or RCS thrusters. However, such studies are very difficult and time consuming for the simulations of the aeroshell with PD and RCS jets due to the complexity of these flows. Therefore, the process described in this appendix provides an appropriate approach for manually generating suitable grids for such complex flows. Although this appendix mainly focuses on the sonic central PD jets, a similar process is used to generate the grids for all of the PD and RCS jet simulations investigated.

The grid adaptation process begins by generating a relatively coarse mesh with a large computational domain in order to adequately capture all of the flowfield features (e.g. the bow shock). Figure B.1 presents the preliminary grid for the sonic

central PD jets. This grid contains approximately 88,000 cells with clustering near the aeroshell surface in order to capture the sharp gradients in the boundary layer. The grid also uses quadrilateral elements because the numerical solution is sensitive to the alignment of the cells with the bow shock that develops around the aeroshell [66]. The grid contains 300 cells along the axial direction (i.e. along the  $z/D_{model}$  axis) and approximately 100 cells along the aeroshell forebody (i.e. along the radial direction,  $r/D_{model}$ ). This corresponds to a resolution of 190 and 200 cells per aeroshell diameter in the forebody region along the axial and radial directions, respectively.

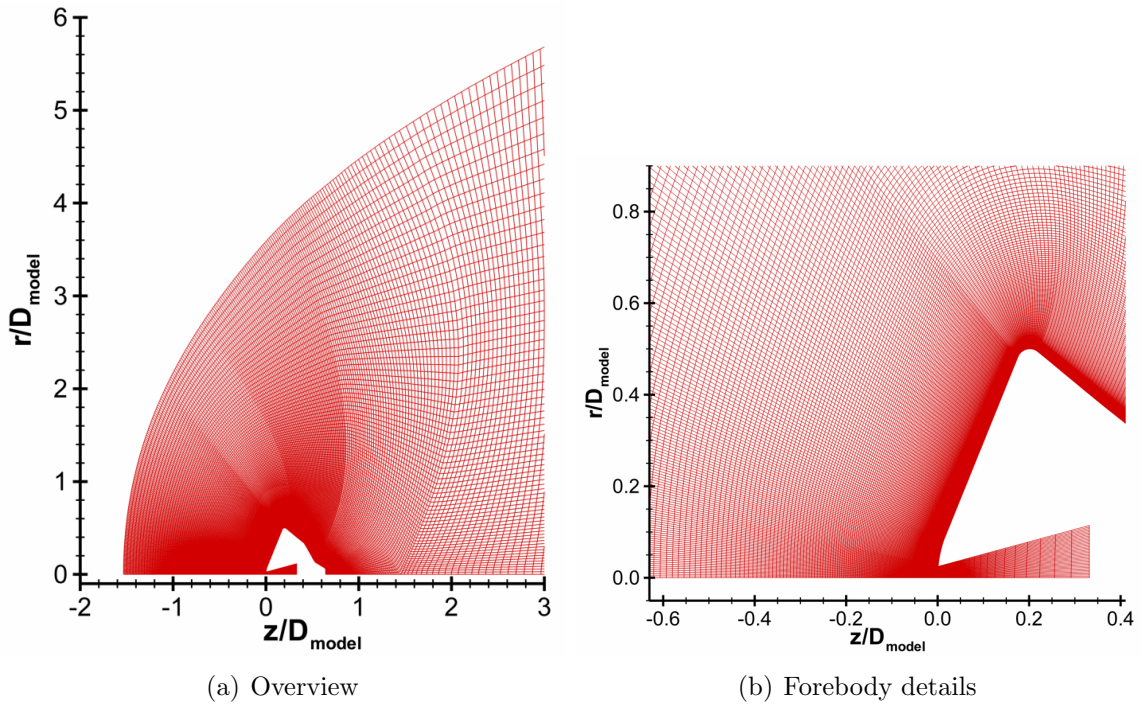


Figure B.1: Computational grid used to obtain preliminary numerical solutions for sonic central PD jets.

The grid presented in Figure B.1 is used to obtain the preliminary solutions for the sonic central PD jets at all of the thrust coefficients investigated in this work. These solutions are then used to manually adapt the upstream boundary of the computational domain and add grid points near flow features, such as the PD jet shock. The upstream boundary is aligned with the bow shock that develops around the aeroshell

based on the variation of the gradient-length local Knudsen number ( $Kn_{GLL}$ ), as shown in Figure B.2 for the sonic central PD jet at  $C_T = 0.5$ . The local Knudsen number is used because it provides a more conservative estimate of the bow shock profile since it is based on the density, temperature, and velocity distributions in the flowfield. The upstream boundary can be extracted from the preliminary solution as shown by the dashed line in Figure B.2.

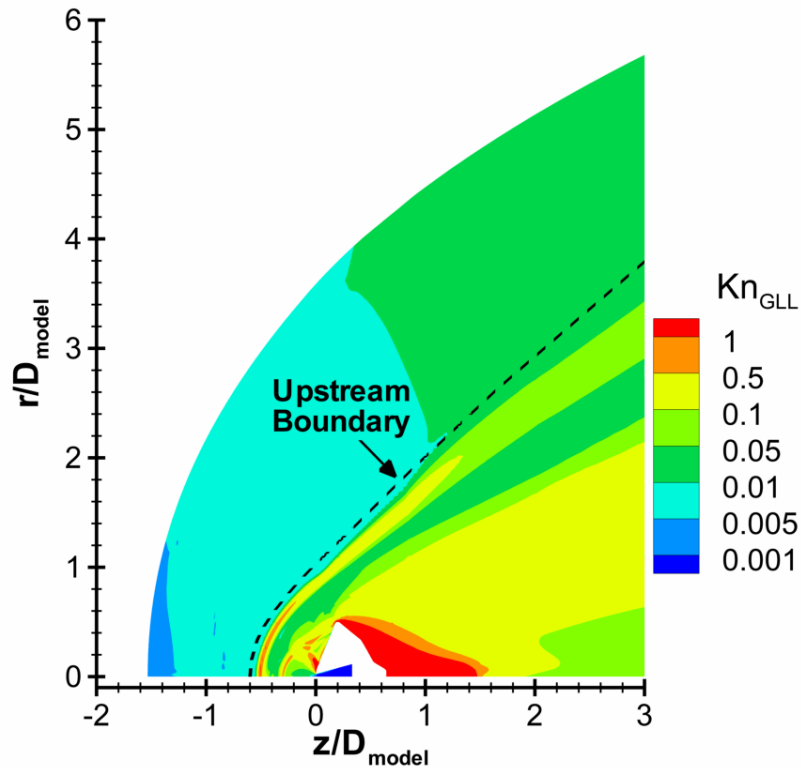


Figure B.2: Preliminary numerical solution ( $Kn_{GLL}$  contours) for sonic central PD jets at  $C_T = 0.5$ .

Figure B.3 presents the adapted computational grid for the sonic central PD jet at  $C_T = 0.5$ . Even though the grid contains approximately 86,000 cells, the mesh resolution for the adapted grid is higher than the resolution for the preliminary grid due to the smaller computational domain. For instance, the resolution for the adapted grid is approximately 500 and 300 cells per aeroshell diameter in the forebody region along the axial and radial directions, respectively. Figure B.4 presents comparisons of

Mach number contours and surface pressure and skin friction coefficients between the preliminary solution and the adapted grid for the sonic central PD jet at  $C_T = 0.5$ . The figure shows overall good agreement between the two solutions, even though the resolutions for the two grids are different.

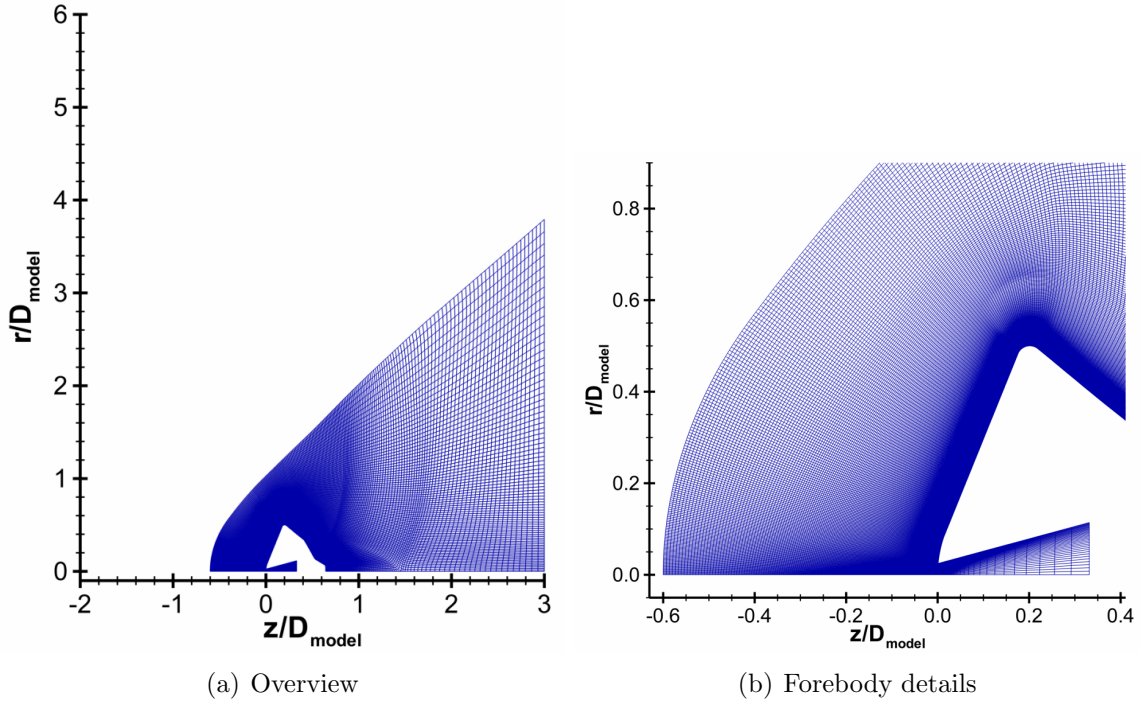


Figure B.3: Adapted computational grid for the sonic central PD jet at  $C_T = 0.5$ .

This grid adaptation process is repeated for sonic and supersonic central and peripheral PD jets, as well as for the RCS jets at all of the thrust coefficients investigated in this work. For the central PD configuration, the size for the adapted grids increases from 84,000 cells for  $C_T = 0.5$  to 110,000 cells for  $C_T = 2.5$  for both sonic and supersonic jets in order to maintain a roughly constant mesh resolution. The difference in the drag and total axial force coefficients between the solutions for the preliminary and adapted grids is less than 14% and 0.6%, respectively, for the central configuration (both sonic and supersonic jets). For the peripheral PD configuration, the mesh size for the preliminary grid is approximately 800,000 cells. The size for the adapted grids varies from about 4.3 million cells for  $C_T = 0.5$  to approximately 5.3 million

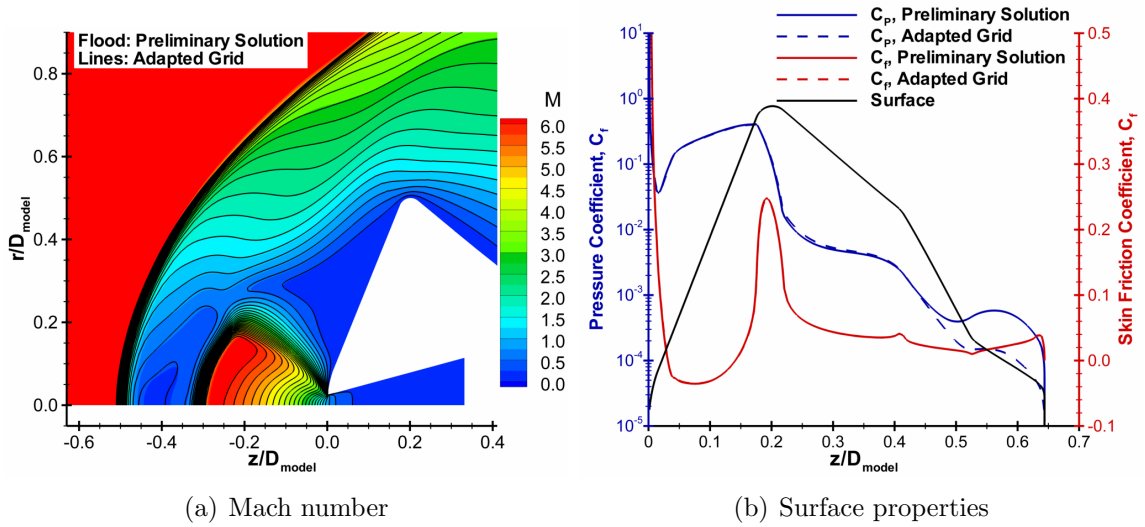


Figure B.4: Comparison of Mach number contours and surface properties between the preliminary and adapted grids for the sonic central PD jet at  $C_T = 0.5$ .

cells for  $C_T = 2.5$ . The difference in the drag coefficient between the preliminary and adapted grids increases with thrust coefficient from approximately 4% for  $C_T = 0.5$  to about 25% for  $C_T = 2.5$ . The difference in the total axial force coefficient, however, does not exceed 6%. Similar to propulsive deceleration, the computational grids for the simulations of the aeroshell with the RCS jet are also adapted using this process. The preliminary and adapted grids for the RCS simulations contain approximately 4 million and 9 million cells, respectively. The difference in the aerodynamic forces between the preliminary and adapted grids does not exceed 4%, and the difference in the aerodynamic moment is less than 5%.



## BIBLIOGRAPHY

## BIBLIOGRAPHY

- [1] Braun, R. D. and Manning, R. M., “Mars Exploration Entry, Descent, and Landing Challenges,” *Journal of Spacecraft and Rockets*, Vol. 44, No. 2, March-April 2007, pp. 310–323.
- [2] Edquist, K. T., Dyakonov, A. A., Wright, M. J., and Tang, C. Y., “Aerothermodynamic Environments Definition for the Mars Science Laboratory Entry Capsule,” *AIAA Paper 2007-1206*, January 2007.
- [3] Manning, R. M. and Adler, M., “Landing on Mars,” *AIAA Paper 2005-6742*, September 2005.
- [4] Rivellini, T., “The Challenges of Landing on Mars,” *The Bridge, National Academy of Engineering*, Vol. 34, No. 4, 2004, pp. 13–17.
- [5] Way, D. W., Powell, R. W., Chen, A., Steltzner, A. D., San Martin, A. M., Burkhart, P. D., and Mendeck, G. F., “Mars Science Laboratory: Entry, Descent, and Landing System Performance,” *IEEEAC Paper 1467*, February 2006.
- [6] Drake, G. B. (editor), “Human Exploration of Mars Design Reference Architecture 5.0,” NASA SP 2009-566, National Aeronautics and Space Administration, July 2009.
- [7] Wells, G., Lafleur, J., Verges, A., Manyapu, K., Christian, J., Lewis, C., and Braun, R., “Entry, Descent, and Landing Challenges of Human Mars Exploration,” *AAS Paper 06-072*, February 2006.
- [8] Hall, J. L., Noca, M. A., and Bailey, R. W., “Cost-Benefit Analysis of the Aerocapture Mission Set,” *Journal of Spacecraft and Rockets*, Vol. 42, No. 2, March-April 2005, pp. 309–320.
- [9] Moss, J. N., Glass, C. E., Hollis, B. R., and Van Norman, J. W., “Low-Density Aerodynamics for the Inflatable Reentry Vehicle Experiment,” *Journal of Spacecraft and Rockets*, Vol. 43, No. 6, November-December 2006, pp. 1191–1201.
- [10] Rohrschneider, R. R. and Braun, R. D., “Survey of Ballute Technology for Aerocapture,” *Journal of Spacecraft and Rockets*, Vol. 44, No. 1, January-February 2007, pp. 10–23.

- [11] Korzun, A. M., Braun, R. D., and Cruz, J. R., “Survey of Supersonic Retropropulsion Technology for Mars Entry, Descent, and Landing,” *Journal of Spacecraft and Rockets*, Vol. 46, No. 5, September-October 2009, pp. 929–937.
- [12] Moeckel, W. E., “Flow Separation Ahead of Blunt Bodies at Supersonic Speeds,” NACA TN 2418, National Advisory Committee for Aeronautics, 1951.
- [13] Moeckel, W. E., “Flow Separation Ahead of a Blunt Axially Symmetric Body at Mach Numbers 1.76 to 2.10,” NACA RM E51I25, National Advisory Committee for Aeronautics, 1951.
- [14] Love, E. S. and Grigsby, C. E., “Some Studies of Axisymmetric Free Jets Exhausting From Sonic and Supersonic Nozzles into Still Air and into Supersonic Freestreams,” NACA RM L54L31, National Advisory Committee for Aeronautics, 1955.
- [15] Love, E. S., Grigsby, C. E., Lee, L. P., and Woodling, M. J., “Experimental and Theoretical Studies of Axisymmetric Free Jets,” NASA TR R-6, National Aeronautics and Space Administration, 1959.
- [16] Love, E. S., “The Effect of a Small Jet of Air Exhausting from the Nose of a Body of Revolution in Supersonic Flow,” NACA RM L52I19a, National Advisory Committee for Aeronautics, 1952.
- [17] Huff, R. G. and Abdalla, K. L., “Mixing Characteristics Downstream of Core Region of High-Temperature Axisymmetric Jets Exhausting into Transonic and Supersonic Streams,” NASA TM X-151, National Aeronautics and Space Administration, 1960.
- [18] Finley, P. J., “The Flow of a Jet from a Body Opposing a Supersonic Free Stream,” *Journal of Fluid Mechanics*, Vol. 26, No. 2, 1966, pp. 337–368.
- [19] Romeo, D. J. and Sterrett, J. R., “Exploratory Investigation of the Effect of a Forward-Facing Jet on the Bow Shock of a Blunt Body in a Mach Number 6 Free Stream,” NASA TN D-1605, National Aeronautics and Space Administration, 1963.
- [20] McGhee, R. J., “Effects of a Retronozzle Located at the Apex of a 140° Blunt Cone at Mach Numbers of 3.00, 4.50, and 6.00,” NASA TN D-6002, National Aeronautics and Space Administration, 1971.
- [21] Charczenko, N. and Hennessey, K. W., “Investigation of a Retrorocket Exhausting from the Nose of a Blunt Body into a Supersonic Free Stream,” NASA TN D-751, National Aeronautics and Space Administration, 1961.
- [22] Keyes, J. W. and Hefner, J. N., “Effect of Forward Facing Jets on Aerodynamic Characteristics of Blunt Configurations at Mach 6,” *Journal of Spacecraft and Rockets*, Vol. 4, No. 4, April 1967, pp. 533–534.

- [23] Jarvinen, P. O. and Adams, R. H., “The Aerodynamic Characteristics of Large Angled Cones with Retrorockets,” NASA CR NAS 7-576, National Aeronautics and Space Administration, 1970.
- [24] Jarvinen, P. O. and Adams, R. H., “The Effects of Retrorockets on the Aerodynamic Characteristics of Conical Aeroshell Planetary Entry Vehicles,” *AIAA Paper 70-219*, January 1970.
- [25] Zang, T. A. (editor), “Entry, Descent and Landing Systems Analysis Study: Phase 1 Report,” NASA TM 2010-216720, National Aeronautics and Space Administration, July 2010.
- [26] Zang, T. A., Dwyer-Cianciolo, A. M., Kinney, D. J., Howard, A. R., Chen, G. T., Ivanov, M. C., Sostaric, R. R., and Westhelle, C. H., “Overview of the NASA Entry, Descent and Landing Systems Analysis Study,” *AIAA Paper 2010-8694*, August-September 2010.
- [27] Edquist, K. T., Dyakonov, A. A., Korzun, A. M., Shidner, J. D., Studak, J. W., Tigges, M. A., Kipp, D. M., Prakash, R., Trumble, K. A., and Dupzyk, I. C., “Development of Supersonic Retro-Propulsion for Future Mars Entry, Descent, and Landing Systems,” *AIAA Paper 2010-5046*, June-July 2010.
- [28] Palaszewski, B., Benic, T., and Field, L., “Mars Entry, Descent, and Landing: Experiments with Multiple Engine Supersonic Retro Propulsion Configuration,” *AIAA Paper 2010-6594*, July 2010.
- [29] Daso, E. O., Pritchett, V. E., Wang, T., Ota, D. K., Blankson, I. M., and Auslender, A. H., “Dynamics of Shock Dispersion and Interactions in Supersonic Freestreams with Counterflowing Jets,” *AIAA Journal*, Vol. 47, No. 6, June 2009, pp. 1313–1326.
- [30] Berry, S. A., Kleb, W. L., Rhode, M. N., Spells, C., Mccrea, A. C., Trumble, K. A., Schauerhamer, D. G., and Oberkampf, W. L., “Supersonic Retro-Propulsion Experimental Design for Computational Fluid Dynamics Model Validation,” *IEEEAC Paper 1499*, January 2011.
- [31] Berry, S. A., Rhode, M. N., Edquist, K. T., and Player, C. J., “Supersonic Retropropulsion Experimental Results from the NASA Langley Unitary Plan Wind Tunnel,” *AIAA Paper 2011-3489*, June 2011.
- [32] Kleb, W. L., Schauerhamer, D. G., Trumble, K., Sozer, E., Barnhardt, M., Carlson, J., and Edquist, K., “Toward Supersonic Retropropulsion CFD Validation,” *AIAA Paper 2011-3490*, June 2011.
- [33] Trumble, K. A., Schauerhamer, D. G., Kleb, W., Carlson, J., Buning, P. G., Edquist, K., and Barnhardt, M. D., “An Initial Assessment of Navier-Stokes Codes Applied to Supersonic Retro-Propulsion,” *AIAA Paper 2010-5047*, June-July 2010.

- [34] Trumble, K. A., Schauerhamer, D. G., Kleb, W. L., Carlson, J., and Edquist, K. T., “Analysis of Navier-Stokes Codes Applied to Supersonic Retro-Propulsion Wind Tunnel Test,” *IEEEAC Paper 1471*, March 2011.
- [35] Cordell, C. E., Clark, I. G., and Braun, R. D., “CFD Verification of Supersonic Retropropulsion for a Central and Peripheral Configuration,” *IEEEAC Paper 1190*, March 2011.
- [36] Bakhtian, N. M. and Aftosmis, M. J., “Parametric Study of Peripheral Nozzle Configurations for Supersonic Retropropulsion,” *Journal of Spacecraft and Rockets*, Vol. 47, No. 6, November-December 2010, pp. 935–950.
- [37] Bakhtian, N. M. and Aftosmis, M. J., “Analysis of Inviscid Simulations for the Study of Supersonic Retropropulsion,” *AIAA Paper 2011-3194*, June 2011.
- [38] Korzun, A. M., Cordell, C. E., and Braun, R. D., “Comparison of Inviscid and Viscous Aerodynamic Predictions of Supersonic Retropropulsion Flowfields,” *AIAA Paper 2010-5048*, June-July 2010.
- [39] Korzun, A. M. and Braun, R. D., “Performance Characterization of Supersonic Retropropulsion for High-Mass Mars Entry Systems,” *Journal of Spacecraft and Rockets*, Vol. 47, No. 5, September-October 2010, pp. 836–848.
- [40] Marsh, C. L. and Braun, R. D., “Fully-Propulsive Mars Atmospheric Transit Strategies for High-Mass Missions,” *Journal of Spacecraft and Rockets*, Vol. 48, No. 2, March-April 2011, pp. 271–282.
- [41] Dyakonov, A. A., Schoenenberger, M., Scallion, W. I., Van Norman, J. W., Novak, L. A., and Tang, C. Y., “Aerodynamic Interference Due to MSL Reaction Control System,” *AIAA Paper 2009-3915*, June 2009.
- [42] Rausch, J. R., “Space Shuttle Rear Mounted Reaction Control System Jet Interaction Study,” CASD-NSC-77-003, General Dynamics, 1977.
- [43] Brevig, O., Strike, W. T., and Fisher, R. R., “Aerothermodynamics of the Space Shuttle Reaction Control System,” *AIAA Paper 73-93*, January 1973.
- [44] Stechman, R. C. and Lynch, R. A., “Space Shuttle Reaction Control Thruster,” *AIAA Paper 74-1109*, October 1974.
- [45] Rausch, J. R. and Roberts, B. B., “Reaction Control System Aerodynamic Interaction Effects on Space Shuttle Orbiter,” *Journal of Spacecraft and Rockets*, Vol. 12, No. 11, 1975, pp. 660–666.
- [46] Sund, D. C. and Hill, C. S., “Reaction Control System Thrusters for Space Shuttle Orbiters,” *AIAA Paper 79-1144*, June 1979.
- [47] Scallion, W. I., Compton, H. R., Suit, W. T., Powell, R. W., Blackstock, T. A., and Bates, B. L., “Space Shuttle Third Flight (STS-3) Entry RCS Analysis,” *AIAA Paper 83-0116*, January 1983.

- [48] Edquist, K. T., Desai, P. N., and Schoenenberger, M., “Aerodynamics for Mars Phoenix Entry Capsule,” *Journal of Spacecraft and Rockets*, Vol. 48, No. 5, September-October 2011, pp. 713–726.
- [49] Grover III, M. R., Cichy, B. D., and Desai, P. N., “Overview of the Phoenix Entry, Descent, and Landing System Architecture,” *Journal of Spacecraft and Rockets*, Vol. 48, No. 5, September-October 2011, pp. 706–712.
- [50] Dyakonov, A. A., Glass, C. E., Desai, P. N., and Van Norman, J. W., “Analysis of Effectiveness of Phoenix Entry Reaction Control System,” *Journal of Spacecraft and Rockets*, Vol. 48, No. 5, September-October 2011, pp. 746–755.
- [51] Desai, P. N., Prince, J. L., Queen, E. M., Cruz, J. R., and Grover, M. R., “Entry, Descent, and Landing Performance of the Mars Phoenix Lander,” *AIAA Paper 2008-7346*, August 2008.
- [52] Prakash, R., Burkhart, P., Chen, A., Comeaux, K., Guernsey, C., Kipp, D., Lorenzoni, L., Mendek, G., Powell, R., Rivellini, T., San Martin, A., Sell, S., Steltzner, A., and Way, D., “Mars Science Laboratory Entry, Descent, and Landing System Overview,” *IEEEAC Paper 1531*, March 2008.
- [53] Edquist, K. T., Dyakonov, A. A., Wright, M. J., and Tang, C. Y., “Aerothermodynamic Design of the Mars Science Laboratory Backshell and Parachute Cone,” *AIAA Paper 2009-4078*, June 2009.
- [54] Johansen, C. T., Danehy, P. M., Ashcraft, S. W., Bathel, B. F., Inman, J. A., and Jones, S. B., “PLIF study of Mars Science Laboratory capsule reaction control system jets,” *AIAA Paper 2011-3890*, June 2011.
- [55] Schoenenberger, M., Dyakonov, A., Buning, P., Scallion, W., and Van Norman, J., “Aerodynamic Challenges for the Mars Science Laboratory Entry, Descent and Landing,” *AIAA Paper 2009-3914*, June 2009.
- [56] Reed, E. M., Codoni, J., McDaniel, J. C., Alkandry, H., and Boyd, I. D., “Investigation of the Interactions of Reaction Control Systems with Mars Science Laboratory Aeroshell,” *AIAA Paper 2010-1558*, January 2010.
- [57] Codoni, J. R., Reed, E. M., McDaniel, J. C., Alkandry, H., and Boyd, I. D., “Investigations of Peripheral 4-jet Sonic and Supersonic Propulsive Deceleration Jets on a Mars Science Laboratory Aeroshell,” *AIAA Paper 2011-1036*, January 2011.
- [58] Staack, D. A. and Del Vecchio, T. D., “The Design Building and Calibration of a Hypersonic Wind Tunnel,” *AIAA Paper 2000-0004*, January 2000.
- [59] McDaniel, J., Glass, C., Staack, D., and Miller, C., “Experimental and Computational Comparison of an Underexpanded Jet Flowfield,” *AIAA Paper 2002-0305*, January 2002.

- [60] Fletcher, D. G. and McDaniel, J. C., “Laser-Induced Iodine Fluorescence Technique for Quantitative Measurements in a Nonreacting Supersonic Combustor,” *AIAA Journal*, Vol. 27, No. 5, May 1989, pp. 575–580.
- [61] Hartfield, R. J., Hollo, S. D., and McDaniel, J. C., “Experimental Investigation of a Supersonic Swept Ramp Injector using Laser-Induced Iodine Fluorescence,” *Journal of Propulsion and Power*, Vol. 10, No. 1, January-February 1994, pp. 129–135.
- [62] Cecil, D. E. and McDaniel, J. C., “Planar Laser-Induced Iodine Fluorescence Measurements in Rarefied Hypersonic Flow,” *Rarefied Gas Dynamics: 24th International Symposium*, Toronto, Canada, 2005, pp. 1325–1350.
- [63] McDaniel, J. C., Codoni, J. R., Reed, E. M., Alkandry, H., and Boyd, I. D., “Propulsion Deceleration Studies using Planar Laser-Induced Iodine Fluorescence and Computational Fluid Dynamics,” *AIAA Paper 2011-2549*, May 2011.
- [64] Hartfield, R. J., Abbitt, J. D., and McDaniel, J. C., “Injectant Mole Fraction Imaging in Compressible Mixing Flows using Planar Laser-Induced Iodine Fluorescence,” *Optics Letter*, Vol. 14, August 1989, pp. 850–852.
- [65] Abbitt, J. D., Hartfield, R. J., and McDaniel, J. C., “Mole Fraction Imaging of Transverse Injection in a Ducted Supersonic Flow,” *AIAA Journal*, Vol. 29, No. 3, March 1991, pp. 431–435.
- [66] Scalabrin, L. C., *Numerical Simulation of Weakly Ionized Hypersonic Flow over Reentry Capsules*, Ph.D. thesis, University of Michigan, Ann Arbor, Michigan, 2007.
- [67] Baldwin, B. S. and Lomax, H., “Thin Layer Approximation and Algebraic Model for Separated Turbulent Flows,” *AIAA Paper 78-257*, January 1978.
- [68] Bisek, N. J., *Numerical Study of Plasma-Assisted Aerodynamic Control for Hypersonic Vehicles*, Ph.D. thesis, University of Michigan, Ann Arbor, Michigan, 2010.
- [69] Holman, T. D., *Numerical Investigation of the Effects of Continuum Breakdown on Hypersonic Vehicle Surface Properties*, Ph.D. thesis, University of Michigan, Ann Arbor, Michigan, 2010.
- [70] Deschenes, T. R., *Extension of a Modular Particle-Continuum Method for Nonequilibrium, Hypersonic Flows*, Ph.D. thesis, University of Michigan, Ann Arbor, Michigan, 2011.
- [71] Sutton, K. and Gnoffo, P. A., “Multi-Component Diffusion with Application to Computational Aerothermodynamics,” *AIAA Paper 1998-2575*, June 1998.
- [72] Landau, L. and Teller, E., “On the Theory of Sound Dispersion,” *Physikalische Zeitschrift der Sowjetunion*, Vol. 10, No. 34, 1936.

- [73] Bird, G. A., *Molecular Gas Dynamics and the Direct Simulation of Gas Flows*, Oxford University Press, 1994.
- [74] White, F. M., *Viscous Fluid Flow*, McGraw-Hill, 3rd ed., 2006.
- [75] Wilke, C. R., “A Viscosity Equation for Gas Mixtures,” *Journal of Chemical Physics*, Vol. 18 No. 4, 1950, pp. 517–519.
- [76] Blottner, F. G., Johnson, M., and Ellis, M., “Chemically Reacting Viscous Flow Program for Multi-Component Gas Mixtures,” SC-RR-70-754, Sandia National Laboratories, 1971.
- [77] Vincenti, W. G. and Kruger, C. H., *Introduction to Physical Gas Dynamics*, Krieger Publishing Company, 2002.
- [78] MacCormack, R. W. and Candler, G. V., “The Solution of The Navier-Stokes Equations Using Gauss-Seidel Line Relaxation,” *Computers and Fluids*, Vol. 17, 1989, pp. 135–150.
- [79] Jawahar, P. and Kamath, H., “A High-Resolution Procedure for Euler and Navier-Stokes Computations on Unstructured Grids,” *Journal of Computational Physics*, Vol. 164, 200, pp. 165–203.
- [80] Karypis, G. and Kumar, V., “METIS: A Software Package for Partitioning Unstructured Graphs, Partitioning Meshes, and Computing Fill-Reducing Orderings of Sparse Matrices,” *University of Minnesota*, 1998.
- [81] Ashkenas, H. and Sherman, F. S., “The Structure and Utilization of Supersonic Free Jets in Low Density Wind Tunnels,” *Proceedings of the 4th International Symposium on Rarefied Gas Dynamics*, Academic Press, 1966, pp. 84–105.
- [82] Boyd, I. D., Chen, G., and Candler, G. V., “Predicting Failure of the Continuum Fluid Equations in Translational Hypersonic Flows,” *Physics of Fluids*, Vol. 7, No. 1, January 1995, pp. 210–219.
- [83] Wang, W. and Boyd, I. D., “Predicting Continuum Breakdown in Hypersonic Viscous Flows,” *Physics of Fluids*, Vol. 15, No. 1, January 2003, pp. 91–100.
- [84] Schwartzenruber, T. E., Scalabrin, L. C., and Boyd, I. D., “A Modular Particle-Continuum Numerical Method for Hypersonic Nonequilibrium Gas Flows,” *Journal of Computational Physics*, Vol. 225, No. 1, 2007, pp. 1159–1174.
- [85] Legge, H., “Force and Heat Transfer Measurements in Hypersonic Free-Jet Flow,” *AIAA Paper 94-2633*, June 1994.
- [86] Pope, S. B., *Turbulent Flows*, Cambridge University Press, 2000.
- [87] Deschenes, T. R., Alkandry, H., and Boyd, I. D., “Application of a Modular Particle-Continuum Method to Hypersonic Propulsive Deceleration,” *AIAA Paper 2011-3137*, June 2011.



- [88] Hartfield, R. J., Hollo, S. D., and McDaniel, J. C., “Planar Temperature Measurement in Compressible Flows using Laser-Induced Iodine Fluorescence,” *Optics Letter*, Vol. 16, January 1991, pp. 106–108.
- [89] Alkandry, H., Boyd, I. D., Reed, E. M., Codoni, J. R., and McDaniel, J. C., “Interactions of Single-Nozzle Sonic Propulsive Deceleration Jets on Mars Entry Aeroshells,” *Journal of Spacecraft and Rockets*, Vol. 48, No. 4, July-August 2011, pp. 564–572.
- [90] Alkandry, H., Boyd, I. D., Reed, E. M., and McDaniel, J. C., “Numerical Study of Hypersonic Wind Tunnel Experiments for Mars Entry Aeroshells,” *AIAA Paper 2009-3918*, June 2009.
- [91] Alkandry, H., Boyd, I. D., Reed, E. M., Codoni, J. R., and McDaniel, J. C., “Interactions of Single-Nozzle Supersonic Propulsive Deceleration Jets on Mars Entry Aeroshells,” *AIAA Paper 2011-138*, January 2011.
- [92] Alkandry, H., Boyd, I. D., Codoni, J. R., Reed, E. M., and McDaniel, J. C., “Numerical Investigation of Multi-Nozzle Propulsive Deceleration Jets for Mars Entry Aeroshells,” *AIAA Paper 2011-3953*, June 2011.
- [93] McDaniel, J., Cecil, E., Reed, E., Codoni, J., Boyd, I., and Alkandry, H., “Planar Laser-Induced Iodine Fluorescence Technique for Flow Visualization and Quantitative Measurements in Rarefied Flows,” *Proceedings of the 27th International Symposium on Rarefied Gas Dynamics*, American Institute of Physics, May 2011, pp. 387–394.
- [94] Fidkowski, K. J. and Darmofal, D. L., “Review of Output-Based Error Estimation and Mesh Adaptation in Computational Fluid Dynamics,” *AIAA Journal*, Vol. 49, No. 4, April 2011, pp. 673–693.
- [95] “NASA Systems Engineering Processes and Requirements w/Change 1 (11/04/09),” NASA NPR 7123.1A, National Aeronautics and Space Administration, March 2007.
- [96] Svehla, R. A., “Estimated Viscosities and Thermal Conductivities of Gases at High Temperatures,” NASA TR R-132, National Aeronautics and Space Administration, 1962.
- [97] Boyd, I. D., Pham-Van-Diep, G. C., and Muntz, E. P., “Monte Carlo Computation of Nonequilibrium Flow in a Hypersonic Iodine Wind Tunnel,” *AIAA Journal*, Vol. 32, No. 5, May 1994, pp. 964–970.